**Universidad Complutense de Madrid**

**Facultad de Ciencias Físicas**


# Beta-decay spectroscopy of neutron-rich Cd isotopes

## Espectroscopía de desintegración beta de isótopos de Cd ricos en neutrones

MEMORIA PARA OPTAR AL GRADO DE DOCTOR PRESENTADA POR

**Marcos Llanos Expósito**

DIRECTORES
**Luis Mario Fraile Prieto**
**Jaime Benito García**

Madrid, 2025

© Marcos Llanos Expósito, 2026

UNIVERSIDAD
COMPLUTENSE
MADRID

Facultad de Ciencias Físicas

Programa de Doctorado en Física

# BETA-DECAY SPECTROSCOPY OF NEUTRON-RICH CD ISOTOPES

# ESPECTROSCOPÍA DE DESINTEGRACIÓN BETA DE ISÓTOPOS DE CD RICOS EN NEUTRONES

MEMORIA PARA OPTAR AL GRADO DE DOCTOR PRESENTADA POR

**Marcos Llanos Expósito**

Directores:
Luis Mario Fraile Prieto
Jaime Benito García

Madrid 2025

*A mi familia y a mis amigos*

# Agradecimientos

Mi agradecimiento a todas las personas que han contribuido, en mayor o menor medida, a la realización de este proyecto. A lo largo de estos años ha sido un camino en el que no solo he aprendido a nivel científico y profesional, sino también por lo especial y enriquecedor que ha sido toda esta etapa en mi vida a nivel personal. Por ello deseo expresar mi agradecimiento a todas las personas que han contribuido a que esta tesis haya sido posible. Sinceramente, muchas gracias.

A mi director Luis Mario muchas gracias por ofrecerme la gran oportunidad de poder hacer el doctorado en el grupo, por tu liderazgo y compromiso. Y sobre todo, gracias por tantas cosas que lo que me has enseñado y ayudado a lo largo de estos años. Te agradezco también enormemente la posibilidad de asistir y participar en tantos experimentos y congresos, que me han permitido enriquecerme como científico y conocer a personas maravillosas en todo el mundo dedicadas a la física nuclear. Por otra parte, me gustaría agradecerte que, aunque fuera festivo, quedaran apenas unos minutos para un plazo de entrega o surgiera cualquier imprevisto, siempre encuentras la manera de resolver el problema. Es una actitud que admiro profundamente y que intentaré mantener e inculcar siempre. Le deseo lo mejor en su etapa como director de ISOLDE.

Jaime, mi otro director, creo que debería de hacer una sección de agradecimientos a parte solo para agradecerte todo lo que me has ayudado durante la tesis, has tenido (y sigues teniendo) una paciencia infinita conmigo... jajajajajajaja. Me llama PODEROSAMENTE LA ATENCIÓN... y acto seguido en el 99% de las ocasiones tenías tu la razón jajajajjajaja Aún recuerdo la primera vez que tuve la oportunidad de conocerte, aunque fuera de manera virtual, durante la defensa de tu tesis, allá por diciembre de 2020. Desde ese momento pude apreciar claramente tu dominio del tema y pensé: "esta tío pilota bastante", y, efectivamente, no me equivoqué. Desde el primer minuto me mostraste los entresijos y triquiñuelas de el análisis y la física nuclear, pero no solo eso, sino también todo aquello que puede necesitar un doctorando: desde cuestiones administrativas hasta cómo se desarrolla un experimento,. Incluso después de todo este tiempo sigues ayudándome, y lo valoro profundamente. Pero, por encima de todo, me llevo un gran amigo y una persona noble. Hemos compartido muchas experiencias y fiestas que guardaré en el recuerdo. Por último, quiero destacar lo orgulloso que me siento de haber sido tu primer estudiante de doctorado y de poder seguir de cerca la trayectoria que estás construyendo como científico.

Creo que lo natural es continuar con mis "primos mayores académicos", ya que sus tesis han sido fundamentales para la elaboración de la mía. Bruno me enseñaste como funcionaba la beam gate y tus contribuciones han sido muy fructíferas para los artículos, así como tus consejos en general para la vida científica. Vadym, no he podido hablar contigo pero me gustaría agradecerte lo que me ayudó tu tesis para entender algunos conceptos que detallas muy bien en tu tesis. Vicky siempre con tu alegría intrínseca, gracias por optimizar los LaBr3(Ce) jejejejeje. Murias, sigo pensando que estás como una cabra, pero en el fondo eres una persona muy noble. Gracias por

todas las vivencias compartidas durante la tesis y por las anécdotas de los viajes, incluida aquella ocasión en la que salvaste mi mochila. A todos ustedes les deseo lo mejor.

Continúo ahora con el GFN (Grupo de Física Nuclear), espero no dejarme a alguien en el tintero, iré por despachos, al menos mi actualización de cuando escribo los agradecimientos implementando por los que he pasado. Comenzaré por el despacho de Joaquín, agradeciéndote que hayas aceptado ser el tutor de mi tesis y que siempre hayas estado dispuesto a ayudarme en todo lo posible. Clara (senior) me sigue haciendo gracia tener que llamarte clara senior. Siento siempre tardar tanto en contestarte pero que sepas que siempre me acuerdo de ti y que gran talento se perdió la investigación contigo yéndote a la privada... Nerea cuando te conocí y me hablabas de tus fiestas de tecno y tus característicos tatuajes pensé que eras una tía que estaría con muchos chicos, pero nada más lejos de la realidad. Madrileña de pura sangre agradezco enormemente todas las aventuras vividas y espero seguir viéndote crecer e ir finalmente a tu casa pero no de alquiler si no la tuya real. Jose Andrés, el otro canario del grupo, me parto siempre con las bromas que haces aunque muchas de ellas sean "out of context", eres la leche. Pablo Cabrales. una persona bastante metódica y comprometida, pero a la vez leal, al igual que le diré a Cayetano estás más que invitado a Tenerife. Pablo Galve Lahoz, digo tu segundo apellido porque me sigue flipando que tío me haya dado clases en la ULL. La persona más meticulosa, organizada y responsable del GFN sin duda (al menos desde mi perspectiva). Afortunadamente hemos podido vivir juntos muchos viajes y eventos tan especiales como la boda de Miguel, sin duda, podrás contar conmigo para lo que sea. Cinty y Mojahed no he podido hablar mucho pero lo poco que he hablado con ellos, no me cabe ninguna duda que están dispuestos a ayudar en lo que puedan, así que es totalmente recíproco. Mailyn y Paula, madres fundadoras del concepto de "gallinero". Me río mucho con ustedes y, al escuchar vuestras historias de cuando erais doctorandas, ahora puedo empatizar aún más con vosotras, tanto en los momentos más felices como en los más tensos. Ahora que estoy en este despacho, que yo también formé parte (otro de los 5 distintos de los que he estado), no puedo dejar de mencionar a un grande y una persona que ha marcado también mi doctorado: Victor Junior. Hemos vividos enormes parrandas y fiestas, así como horas hablando de la vida y partiéndonos todo el día de nuestras vidas también. También pude conocer a parte de tu círculo madrileño que están igual o más de tostados que tú. Te deseo lo mejor como postdoc en Boston, espero vernos pronto. Andrea, casi haces la tesis tan larga como Jaime, pude vivir todo el proceso en convertirse en Dra. Andrea. De las personas más trabajadoras que he conocido, pero también súper dulce y amable, no cambies nunca. Siempre tendrás mi apoyo para lo que necesites. Sara Lab, digna heredera de Miguel, siempre tan alegre y encantadora que hace que siempre ir a hablar contigo al laboratorio sea un ratito agradable. Por mucho que me quieran echar del grupo de WhatsApp ehh Barbara Díaz eh!!, forme parte y creación del 242. Javier, Alejandro y Barbara son unos excelentes compañeros de despacho/laboratorio. Dani, persona de la que he aprendido que siempre hay que reclamar y cosas tan curiosas como el método Insights. Adrían, un grande sin duda ninguna. Alguna burrada que otra se te escapa pero nunca con maldad, mil farras juntos, queda pendiente ir a los San Fermines a la "bajera". Claudia, Sara, en su estancia por el GFN y recientemente Vir. Se que hacen el laboratorio de Samuel aún más cañero. Susana y Barbara,

muchas gracias por ayudarnos con los temas administrativos incluso cuando se nos ha pasado el plazo. Cayetano, maestro y figura, con un don de oratoria magistral. Junto con Pablo Cabrales me han introducido en todo el tema de la inteligencia artificial y los nuevos gadgets que me han ayudado enormemente. Tenemos que salir más de fiesta. Javier García MARCOS que gran segundo apellido tienes verdad? jajajajajaja ahora en esta etapa en la que has regresado de Gante hemos incrementado la amistad. Nos partimos siempre hablando de chicas, fiestas y com no, nuestro temas estrellas, geopolítica e historia. Aunque no me guste el fútbol siempre iré con tal de compartir tu compañía. Finalmente, a mis recientes compañeros del 236. Iban con tus paridas se amenizan nuestras horas en el despacho. Clara y Charlie confío en ustedes que van a ser la nueva organización de planes, especialmente de festejos y actividades de ocio, así como los cañeros del grupo.

Continuaré con aquellos que han pasado por el GFN. Oli, también siempre tardo contigo un montón en contestar pero siempre estoy ahí. Es una pena que te hayas aliado con Gran Canaria y no con Tenerife pero se te quiere igual. Victor Senior, gracias a ti la estancia en 2023 se hizo bastante amena, al principio no te conocía tanto y pensé que era un poco Victoriano pero la estancia me hizo apreciar lo buena persona que eres y que aunque eres un poco. Tomás muchas gracias por acceder a ser tribunal de mi tesis, es todo un orgullo poder tener a alguien de tu nivel científico en el tribunal.

Le toca el turno al GFNspec. Briz, enormemente agradecido por todo el apoyo durante el depósito de la tesis, así como todas tus aclaraciones y enseñanzas a lo largo de estos años y sobre todo a dispuesto a ayudar siempre de forma noble. Andrés, aunque en ocasiones difiera de tu forma de expresar las cosas y de ciertos detalles, me has ayudado mucho, especialmente a ir a la raíz de los conceptos, a explorar nuevas ideas y a incorporar esos aspectos de orden de los que tanto me quejo, pero que, a la larga, terminan funcionando (no siempre). Victor 3, miembro fundamental del laboratorio, aunque reservado eres una persona bastante detallista y me quedé flipando con el regalo que le hiciste a Miguel. Cuando he requerido de tu ayuda siempre me la has dado. Miriam, siempre alegre y divertida, he aprendido bastante del manga y el anime gracias a ti, te deseo lo mejor en esta etapa. Nikita, gracias por darme consejos durante la tesis y en el postdoc. Odette, aunque de personalidad fuerte estás, siempre que esté en tu mano, dispuesta a ayudar. Finalmente, los auténticos sucesores del fast-timing Pin (Gabriel) y Pon (Pablo). No me olvido del IEM, CSIC. Dani, Jaime, Jesús y Samuel conn los que he compartido muchos experimentos y congresos.

Turno ahora para mi familia madrileña, quienes han dado pleno sentido a la frase «los sitios los hacen las personas». Nata, Esther y Miguel, tres personas muy especiales a las que quiero enormemente y que han contribuido enormemente a que esta etapa haya sido espléndida. Con ellos puedo ser yo mismo por completo, y saben que siempre podrán contar con mi apoyo para lo que necesiten. Me siento profundamente orgulloso de tenerlos en mi vida.. Nata, no sabría ni por dónde empezar. Hemos compartido tantas aventuras que algunas ya se confunden en la memoria. Hemos cerrado infinidad de bares hasta el punto de que, cuando nos preguntan a qué hora nos fuimos, siempre

podemos decir que aún no habíamos entrado. Sin ninguna duda, las experiencias más rocambolescas las he vivido a tu lado, así como innumerables momentos de apoyo y complicidad. Has sido una persona a la que siempre he podido llamar cuando se organizaba cualquier plan y quien me ha acercado a la cultura colombiana, a la que tanto cariño tengo ahora. Hemos viajado juntos a muchos lugares, lo que no ha hecho más que reforzar nuestra amistad, y aún nos quedan muchos destinos pendientes. Si lees esto, recuerda que seguimos teniendo en la lista Tomorrowland y, por supuesto, Colombia, la "tierra prometida", que ahora comparte ese papel con Zaragoza, ciudad que ya hemos tenido la oportunidad de visitar. Esther, mi niña querida. Me has ayudado enormemente y tus palabras, en muchas ocasiones, me han impulsado y motivado, especialmente en momentos complicados. Han sido incontables las cenas de estos años en las que hemos pasado horas y horas conversando. Aunque a veces choquemos en algunos debates y me acuses injustamente de ciertas cosas, en el fondo sé que eres una persona extraordinaria a la que siempre quiero ver brillar. Tu enorme nobleza te convierte en una persona bellísima. Te meto mucha caña, pero te quiero muchísimo y, al final, casi siempre termino haciendo lo que tú dices. Miguel, una de las personas más resilientes, luchadoras y divertidas que la vida me ha puesto por delante. Desde aquella broma de "¿tú eres bobo o te ha dado un haz en la cabeza?" supe que íbamos a conectar. Aunque los mensajes a veces tarden en llegar (no sé qué le ocurre a nuestro WhatsApp), sabes que siempre puedes contar conmigo, esté donde esté, y que allí donde yo esté tendrás siempre una casa. Admiro tu dedicación, tu férrea disciplina, incluso cuando intento sacarte un poco del tiesto y la resaca se prolonga más de lo que preferirías. Podría seguir escribiendo muchas líneas sobre ustedes, pero se haría interminable. Muchísimas gracias a los tres.

Carlitos, el otro canario fundamental en Madrid, fiel compañero y «vecino» del Pilar. Gracias por estar ahí en todas las aventuras madrileñas. No olvides los proyectos que tenemos en mente, aquellos de los que tantas veces hemos hablado entre cañas Jorge, aunque no sabía si incluirte en la parte de Tenerife, creo que fuiste y sigues siendo un apoyo fundamental de mi estancia en Madrid. Mira que hemos vivido farras, siendo la dupla galáctica. Gracias por tu apoyo siempre, ya que tu forma de ser es siempre de ayudar y sumar. Me alegro enormemente que con la gente de Tenerife hayas encontrado un huequito en el universo como quien dice. Continúo con dos personas especiales que llegaron a mi vida recientemente, al menos en 2025: Daniela y Elena. Poco a poco hemos ido construyendo una amistad muy sólida y, aunque siempre digan que los hombres mienten y son unos cabrones, espero haber contribuido, al menos como amigo leal, a matizar un poco esa opinión. Siempre tendrán Tenerife abierta para ustedes y, como le dije a Nata, aún nos quedan muchos viajes y aventuras pendientes.

Por supuesto, no me olvido de que este proyecto ha sido posible gracias al apoyo de mi gente de Tenerife. Esto incluye no sólo a quienes residen actualmente en la isla, sino también a quienes, habiendo pasado por ella, han dejado y siguen dejando una huella profunda en mí. Espero no olvidarme de nadie y, aunque solo escriba unas pocas palabras, mi agradecimiento es inmenso. Sabéis de sobra que sois un apoyo increíble para mí.

Comenzaré con una de mis amistades más longevas, el "Grupito Apapurcio".. Conocerles en la Oficial ha sido uno de los mayores regalos que la vida me ha dado. Hemos evolucionado muchísimo y me siento muy orgulloso de ustedes. Me han ayudado siempre y hemos compartido momentos muy complicados, pero también muchos momentos históricos. Óscar, Lucía, Claudia y Daniela, muchísimas gracias, les quiero.

Continuo con mi grupo de médicas favoritas, el "Gabinete nuevo". Vir, madre mía, como ha pasado el tiempo. Me siento muy orgulloso de tu trayectoria y cómo poco a poco estás construyendo un futuro sólido, gracias por ayudarme siempre con cualquier consulta médica al igual que Taty. Eres una persona mágnifica, no cambies nunca, tanto con tus amistades como con tu pasión por tu trabajo. Siempre me tendrás para lo que haga falta. Taty, mi niña querida. No sabría cómo agradecer el apoyo que has sido y sigues siendo a día de hoy para mí. Aunque últimamente no tengamos tanto contacto, cada vez que nos vemos somos capaces de ponernos al día sin ningún problema. Aunque muchas veces me meta contigo (y tú conmigo), al final eres una persona clave en mi vida. Siempre estaré ahí para lo que necesites. Vir y Taty, muchas gracias, las quiero.

Ahora continuo con "Okupa Madrileño" chicos que decirles, son la caña, la cantidad de vivencias, aventuras faltadas que hemos compartido son incontables. Jesu, aunque tu trayectoria en el grupo ha evolucionado especialmente mientras estaba en Madrid no pongo en duda que eres más que un fichaje para el grupo con lo cañero y liante que eres. Tito, el dios de olimpo, eres el papasito más papasito de todos, otro también que cuando el cohete despega no se queda atrás. Tocayo, que decirte viejo amigo. Desde la carrera supe que aunque medio manifa íbamos a tener una amistad duradera, es verdad que cuando estás en pareja te desconectas, pero siempre me tendrás para lo que necesites. Jesu, Tito y Toacyo muchas gracias, las quiero golfos!.

Ahora como no, no me puedo olvidar de la estancia en la terreta. Comenzaré como no con, Dr. Abian. Eternamente agradecido por todo tu apoyo durante mi estancia en Valencia. Te has convertido un amigo fundamental y por supuesto alguien de que me siento muy orgulloso. Sigue creciendo así. Javi Casañas, golfo jajajajajaja, aunque esté como una cabra eres una persona leal y noble, nos queda muchas farras y aventuras por vivir. Siempre me tendrán para lo que haga falta. Abian y Javi Casañas muchas gracias, las quiero golfos!.

Turno ahora para mis "hermanos de otra madre". Joaquín, eres un grande, aunque muy pocas veces te de tiempo de realizar todas las tareas que tienes en mente, se te quiere igual. Eres una persona fundamental para mi, parte de mi círculo cercano. Es imposible que no me salga una sonrisa con todas las aventuras y momentos que hemos vivido. Fiel, gracias por tu lealtad, por tu confianza y por haberme acompañado tanto en los momentos de celebración como en los de dificultad. Siempre en vanguardia y dispuesto a ir dónde fuera que yo estoy. Tu capacidad para escuchar, para relativizar los problemas y para hacerme reír incluso en los días más complicados ha sido un apoyo fundamental durante estos años. Esta tesis también es fruto de nuestras conversaciones, de tus ánimos constantes y de tu presencia discreta pero siempre firme.

Me siento profundamente afortunado de poder llamarte amigo. Joaquín y Fiel muchas gracias, las quiero golfos!.

Agradecer a mis primos. Mario, que ha sido siempre como un hermano mayor para mí. Gracias por cuidarme, aconsejarme y orientarme en momentos clave, por estar ahí cuando he tenido dudas importantes y por darme ejemplo con tu forma de ser y de afrontar la vida. Muchas de las decisiones que he tomado, y parte de la persona que soy hoy, están marcadas por tus consejos, tu apoyo y tu confianza en mí. Javi, contigo he compartido risas, confidencias, planes y conversaciones interminables, y siempre has sabido estar tanto para las bromas como para los momentos serios. Valoro muchísimo esa mezcla de familia E integrandonos en nuestras amistades y saber que puedo contar contigo como primo y como amigo es algo que aprecio de verdad. Sergio, por apoyarme siempre y por haber contribuido, desde pequeño, ese gusto por los videojuegos. Mario, Javi y Sergio muchas gracias, las quiero golfos!.

A mis tíos Benito, Bárbara y Fifa, por el cariño y el apoyo que siempre me han brindado. Gracias por interesarse por mi camino, por celebrar cada pequeño logro y por hacer que cada reunión familiar sea un espacio de desconexión, alegría y afecto sincero. Saber que cuento con ustedes, aunque a veces la distancia o las obligaciones nos lo pongan difícil, ha sido un respaldo muy importante durante estos años. Esta tesis también está dedicada a ustedes. Muchas gracias familia!

Agradecimientos especiales también a Elizabeth, Jenni y patricia como parte de la familia también, así como a todos mis tíos y primos.

Agradecimientos también a Casi, Andrea, Tina, Patricia, Alberto, Inma y David.

Finalmente, a mis padres, que han sido el pilar fundamental en todas las etapas de mi vida. Gracias por vuestro amor incondicional, por confiar en mí incluso cuando yo dudaba, y por todo el esfuerzo silencioso que hay detrás de cada oportunidad que he tenido. A mi padre, por su ejemplo de trabajo. Esta tesis es también suya: sin sus sacrificios, sus consejos y su apoyo, habría sido imposible llegar hasta aquí. A mi madre, por su cariño, su amor y esa capacidad de estar siempre ahí, en lo cotidiano y en lo difícil, sosteniéndome sin pedir nada a cambio. Me ha enseñado que las metas se alcanzan con esfuerzo y perseverancia. Muchas gracias, les quiero muchísimo!

# Contents

# Summary

This thesis investigates the nuclear structure of $^{128}$In, $^{128}$Sn, $^{128}$Te and $^{132}$In populated via $\beta$ decay of the neutron-rich cadmium isotopes $^{128,132,133}$Cd at the ISOLDE facility, CERN. The aim is to elucidate the evolution of nuclear shell structure near the doubly magic nucleus $^{132}$Sn ($Z = 50$, $N = 82$), a region of fundamental and astrophysical interest, particularly for the rapid neutron-capture $r$ process.

High-purity radioactive ion beams were produced by proton-induced fission of uranium carbide targets, followed by selective laser ionization with RILIS and high-resolution mass separation. The beams were implanted in the ISOLDE Decay Station (IDS) and studied with six High-Purity Germanium (HPGe) clover detectors for $\gamma$-ray spectroscopy and two $LaBr_3$(Ce) detectors combined with $\beta$ detectors for fast-timing measurements.

The fast-timing spectroscopy study of the $^{128}$Cd $\beta$-decay chain has yielded the first sub-nanosecond lifetime measurements in $^{128}$In, along with new and improved lifetime determinations for excited states in $^{128}$Te. In $^{128}$In, the lifetimes of the 315-, 488-, 710- and 1173-keV levels were measured using $\beta\gamma\gamma$(t) and $\gamma\gamma$(t) coincidence data. The experimental results support spin–parity assignments of $(2^-)$ for the 315- and 710-keV states, $(1^-)$ for the 488-keV state, and confirm the previous $1^+$ assignment for the 1173-keV level. In $^{128}$Te, the half-lives of the yrast $6^+$, $4^+$, and $2^+$ states were measured using both $\beta\gamma$(t) and $\gamma\gamma$(t) fast-timing techniques. These measurements enabled the extraction of $B(E2)$ transition strengths along the yrast cascade and their comparison with shell-model calculations.

A detailed investigation of the excited-state structure of $^{128}$Sn, selectively populated through the $\beta$ decay of $^{128g}$In, is presented. A total of 81 new $\gamma$ transitions and 30 new levels were identified providing a comprehensive update to the $^{128}$Sn level scheme. New ground-state half-lives were determined for $^{128g}$Cd$(0^+)$ and $^{128g}$In$(3^+)$: $T_{1/2} = 256(5)$ ms and $T_{1/2} = 814(9)$ ms, respectively, via the time distribution of the proton pulse respect to the time to detect the most intense $\gamma$ rays in the decay of $^{128}$Cd. The new level at 2164 keV has been established and is tentatively assigned as $(0^+)$ based on its de-exciting pattern and shell-model calculations. This is consistent with the systematics of the $0^+_2$ states in even-mass Sn isotopes. The lifetime of the $(4^+)$ state at 2001 keV was measured for the first time, giving $B(E2; 4^+ \rightarrow 2^+) = 2.1^{+2.3}_{-0.7}$ W.u., consistent with shell-model calculations and even-even Sn systematics. The half-life of the $(5^-)$ state at 2121 keV was measured, yielding $T_{1/2} = 10.5(3)$ ns, which differs from

the adopted value by more than two standard deviations and provides significantly improved precision. For the 2378 keV level, an upper limit of 40 ps was obtained for the lifetime; the $B(X\lambda)$ values computed for the $\gamma$-ray transitions that de-excite the level support a tentative $(4^-)$ assignment.

The nuclear structure of $^{132}$In, treated as a proton-hole neutron-particle configuration relative to the doubly magic $^{132}$Sn core, was investigated via the $\beta$ decay of $^{132}$Cd and the $\beta$-delayed neutron emission of $^{133}$Cd. Increased yields enabled, for the first time, provided confirmation of the level scheme through $\gamma\gamma$ coincidences. Observation of $\gamma$-ray transitions in $^{132}$In populated directly in the decay of $^{132}$Cd, is been measured for the first time. The level scheme is interpreted in terms of particle–hole configurations supported by shell-model calculations and regional systematics. Beta-feeding intensities and $\beta$-delayed neutron emission data are obtained for the decays of $^{132}$Cd and $^{133}$Cd. New values for the $T_{1/2}[^{132}\text{Cd}]$and $P_{1n}[^{132}\text{Cd}] = 97.8(10)\,\%$ was extracted from $\gamma$-ray intensities.

In conclusion, this thesis provides new experimental information on the structure of isotopes near the $Z = 50$, $N = 82$ shell closure. Results on $^{128}$Sn were published in Ref. [LEBF$^+$25a], and findings on $^{128}$In and $^{128}$Te in Ref. [LEFB$^+$24]. A manuscript on $^{132}$In is in preparation for submission to a high-impact journal.

# Resumen en español

Esta tesis investiga la estructura nuclear de $^{128}$In, $^{128}$Sn, $^{128}$Te y $^{132}$In poblados mediante desintegración $\beta$ de los isótopos de cadmio ricos en neutrones $^{128,132,133}$Cd en la instalación ISOLDE del CERN. El objetivo es dilucidar la evolución de la estructura de capas nucleares cerca del núcleo doblemente mágico $^{132}$Sn ($Z = 50$, $N = 82$), una región de interés fundamental y astrofísico, en particular para el proceso $r$ de captura rápida de neutrones.

Se produjeron haces de iones radiactivos de alta pureza mediante fisión inducida por protones de blancos de carburo de uranio, seguida de ionización láser selectiva con RILIS y separación de masas de alta resolución. Los haces se implantaron en la Estación de Decaimiento de ISOLDE (IDS) y se estudiaron con seis detectores clover de germanio de alta pureza (HPGe) para espectroscopía de rayos $\gamma$ y dos detectores $LaBr_3$(Ce) combinados con detectores de $\beta$ para medidas de cronometraje rápido.

El estudio de espectroscopía de cronometraje rápido de la cadena de desintegración $\beta$ de $^{128}$Cd ha proporcionado las primeras medidas de tiempos de vida subnanosegundo en $^{128}$In, junto con nuevas y mejoradas determinaciones de tiempos de vida para estados excitados en $^{128}$Te. En $^{128}$In, los tiempos de vida de los niveles de 315, 488, 710 y 1173 keV se midieron utilizando datos de coincidencias $\beta\gamma\gamma$(t) y $\gamma\gamma$(t). Los resultados experimentales respaldan las asignaciones de espín-paridad de $(2^-)$ para los estados de 315 y 710 keV, de $(1^-)$ para el estado de 488 keV, y confirman la asignación previa de $1^+$ para el nivel de 1173 keV. En $^{128}$Te, las semividas de los estados yrast $6^+$, $4^+$ y $2^+$ se midieron empleando técnicas de cronometraje rápido $\beta\gamma$(t) y $\gamma\gamma$(t). Estas medidas permitieron extraer las intensidades de transición $B(E2)$ a lo largo de la cascada yrast y su comparación con cálculos de modelo de capas.

Se presenta una investigación detallada de la estructura de estados excitados de $^{128}$Sn, poblado selectivamente mediante la desintegración $\beta$ de $^{128g}$In. Se identificaron en total 81 nuevas transiciones $\gamma$ y 30 nuevos niveles, proporcionando una actualización exhaustiva del esquema de niveles de $^{128}$Sn. Se determinaron nuevas semividas del estado fundamental para $^{128g}$Cd($0^+$) y $^{128g}$In($3^+$): $T_{1/2} = 256(5)$ ms y $T_{1/2} = 814(9)$ ms, respectivamente, a partir de la distribución temporal del pulso de protones con respecto al tiempo de detección de los rayos $\gamma$ más intensos en el decaimiento de $^{128}$Cd. El nuevo nivel a 2164 keV ha sido establecido y se asigna tentativamente como $(0^+)$ en función de su patrón de desexcitación y de cálculos de modelo de capas. Esto es coherente con la sistemática de los estados $0_2^+$ en los isótopos de Sn de masa par. El

tiempo de vida del estado $(4^+)$ a 2001 keV se midió por primera vez, obteniéndose $B(E2; 4^+ \rightarrow 2^+) = 2.1^{+2.3}_{-0.7}$ W.u., en concordancia con los cálculos de modelo de capas y la sistemática de Sn par-par. La semivida del estado $(5^-)$ a 2121 keV se midió, dando $T_{1/2} = 10.5(3)$ ns, lo que difiere del valor adoptado en más de dos desviaciones típicas y proporciona una mejora significativa en la precisión. Para el nivel de 2378 keV se obtuvo un límite superior de 40 ps para el tiempo de vida; los valores $B(X\lambda)$ calculados para las transiciones de rayos $\gamma$ que desexcitan el nivel apoyan una asignación tentativa de $(4^-)$.

La estructura nuclear de $^{132}$In, tratada como una configuración protón-hueco partícula de neutrón respecto al núcleo doblemente mágico $^{132}$Sn, se investigó mediante la desintegración $\beta$ de $^{132}$Cd y la emisión retardada de neutrones por $\beta$ de $^{133}$Cd. Los mayores rendimientos permitieron, por primera vez, confirmar el esquema de niveles mediante coincidencias $\gamma\gamma$. Se observaron por primera vez transiciones de rayos $\gamma$ en $^{132}$In pobladas directamente en el decaimiento de $^{132}$Cd. El esquema de niveles se interpreta en términos de configuraciones partícula–hueco sustentadas por cálculos de modelo de capas y la sistemática regional. Se obtuvieron intensidades de alimentación beta y datos de emisión de neutrones retardados por $\beta$ para los decaimientos de $^{132}$Cd y $^{133}$Cd. A partir de las intensidades de rayos $\gamma$ se extrajeron nuevos valores para $T_{1/2}[^{132}\text{Cd}]$ y $P_{1n}[^{132}\text{Cd}] = 97.8(10)\,\%$.

En conclusión, esta tesis aporta nueva información experimental sobre la estructura de isótopos próximos al cierre de capas en $Z = 50$, $N = 82$. Los resultados sobre $^{128}$Sn se publicaron en la Ref. [LEBF$^+$25a], y los relativos a $^{128}$In y $^{128}$Te en la Ref. [LEFB$^+$24]. Un manuscrito sobre $^{132}$In está en preparación para su envío a una revista de alto impacto.

# Chapter 1

# Introduction

What is matter made of and how does it originate? Atomic nuclei, containing nearly the entire mass of the atom, constitute complex quantum systems governed by the strong, electromagnetic, and weak interactions, and display a broad spectrum of single-particle and collective phenomena. Historically, the development of the nuclear shell model by Maria Goeppert-Mayer and Hans Jensen [Gug34], which introduced spin-orbit coupling to explain the existence of magic numbers, marked a foundational advancement in nuclear structure theory. The so-called magic numbers (2, 8, 20, 28, 50, 82, and 126) correspond to closed shells of nucleons and are associated with an extra binding energy for nuclei that have these numbers of protons or neutrons. However, this framework must be critically assessed in exotic regions of the nuclear chart, where traditional shell closures may weaken or disappear and new ones may emerge. The evolution of shell structure far from stability is one of the key questions that drives nuclear structure research.

The region around the doubly-magic $^{132}$Sn isotope [JAB$^{+}$10, RSR$^{+}$18] is one of the most thoroughly studied, since it is within reach of current experimental facilities. Understanding of nuclear structure in this region requires systematic investigation of nuclei around the double $Z = 50$ and $N = 82$ shell closure, where collective effects appears just with only few extra nucleons. Large-scale shell-model calculations have been developed to describe the structure of nuclei in the vicinity of $^{132}$Sn [CCGI13, HXL$^{+}$20, Eva21], achieving good agreement with experimental data. Furthermore, exotic nuclei near $^{132}$Sn are of particular astrophysical interest, as their nuclear properties can influence the rapid neutron-capture $r$-process path [AGT07, HAC$^{+}$19], which influences the predicted isotopic abundances.

One of the missing pieces of information are reduced transition probabilities $B(X\lambda; J_i \rightarrow J_f)$, which are key measurements for probing nuclear wave functions, and can be obtained from the direct measurement of excited-state lifetimes. The aim of this thesis is the determination of nuclear level lifetimes through advanced fast-timing techniques, including the Advanced Time-Delayed $\beta\gamma\gamma$(t) method [MGM89, Fra17]. These allow for the extraction of reduced transition probabilities.

This thesis focuses on the nuclear structure of $^{128}$In, $^{128}$Sn, $^{128}$Te and $^{132}$In

populated via $\beta$-decay of the neutron-rich $^{128,132,133}$Cd isotopes. The high-purity Cd beams were produced at the ISOLDE (Isotope Separator On-Line DEvice) facility at European Organization for Nuclear Research (CERN) in the framework of the IS685 experiment [FBL$^+$20]. The data taking was conducted in two campaigns of which we will label IS685 and IS685_II, conducted in 2022 and 2023, respectively. The measurements were carried out at the ISOLDE Decay Station (IDS). An array of six High-Purity Germanium (HPGe) clover detectors were used for high-resolution $\gamma$-ray spectroscopy. Three $\beta$ detectors surrounded the implantation point in the tape in combination with two $LaBr_3$(Ce) crystals with the shape of truncated cones fitted with fast photomultiplier tubes (PMTs), was also employed for fast-timing measurements. A XIA Pixie16 data acquisition (DAQ) system was used to digitize all the signals used for this analysis. The fast-timing signals were subject to analog processing via constant fraction discriminators and time-to-amplitude converters prior to being fed to the digitizers, while slow and logic signals were directly input to the DAQ.

The thesis is structured as follows: Chap. 2 introduces the fundamentals relevant to nuclear structure, $\beta$ and $\gamma$ decay, and transition probabilities. Chap. 3 presents an overview of the ISOLDE facility, detailing the production of high-purity Cd beams. Chap. 4 describes the experimental setup, the calibration procedures and the timing analysis methodologies. Chap. 5 presents fast-timing lifetime measurements in the $\beta$-decay chain of $^{128}$Cd, aimed at extracting reduced transition probabilities in $^{128}$In and $^{128}$Te. Chap. 6 offers a comprehensive investigation of the nuclear structure of $^{128}$Sn, based on the selective population via $\beta$ decay of $^{128}$Cd $\rightarrow$ $^{128}$In $\rightarrow$ $^{128}$Sn, aiming to construct a new level scheme and determine lifetimes of excited states. Chap. 7 provides the investigation of the exotic nucleus $^{132}$In nucleus through $\beta$ decay of $^{132}$Cd and $\beta$-delayed neutron emission of $^{133}$Cd, leading the construction of a level scheme supported by $\gamma\gamma$ coincidence data and interpreted within the nuclear shell-model framework. Finally, Chap. 8 summarizes the conclusions of this work.

# Chapter 2

# Introduction to nuclear structure

The investigation of exotic nuclei located far from the line of stability in the nuclear chart provides essential insights into the evolution of nuclear shell structure. Nuclei with a large neutron-to-proton ratio ($N/Z$) predominantly undergo $\beta^-$ decay, characterized by short lifetimes. The de-excitation of the resulting excited nuclear states generally occurs through the emission of $\gamma$ radiation. The analysis of these emitted particles constitutes a fundamental tool for obtaining detailed information on the nuclear structure and properties of such nuclei. This chapter presents the theoretical foundation for the nuclear shell model and the decay properties of exotic nuclei, with special focus on the region around the doubly magic $^{132}$Sn nucleus.

## 2.1 The nuclear shell model

During the 20$^{\text{th}}$ century, nuclear experiments conducted by K. Guggenheimer [Gug34] and W. Elsasser [Els34] revealed that nuclei composed of specific numbers of protons ($Z$) or neutrons ($N$) exhibit enhanced stability. Experimental evidence showed that such nuclei have larger binding energies. These specific numbers are referred to as *magic numbers*, namely: 2, 8, 20, 28, 50, 82, and 126. Nuclei that contain both proton and neutron numbers equal to magic numbers are termed *doubly magic* and are particularly stable. This anomaly bears a resemblance to the stability observed in noble gases, where specific electron configurations (2, 10, 18, 36, 54, 86) result in chemically inert atoms.

The *nuclear shell model* was developed to explain the increased stability associated with magic numbers. In principle, the description of the system requires solving the nuclear many-body Schrödinger equation for $A$ interacting fermions. The nuclear Hamiltonian for the $j^{\text{th}}$ nucleon is expressed as:

$$H = -\sum_{j=1}^{A} \frac{\hbar^2}{2m_N}\nabla_j^2 + \sum_{i<j}^{A} v(\vec{r}_i, \vec{r}_j) = T + V_{m-b} \tag{2.1}$$

where $A$ is the total number of nucleons, $m_N$ is the nucleon mass, $\vec{r}_j$ denotes the spatial coordinate of the $j$-th nucleon, $\nabla_j^2$ is the Laplacian operator acting on that coordinate, $T$ is the total kinetic energy, $V_{m\text{-}b}$ is the many-body interaction term, and $v(\vec{r}_i, \vec{r}_j)$

denotes the nucleon–nucleon interaction between particles $i$ and $j$. The key theoretical assumption of the shell model is that each nucleon moves independently in an average potential generated by all other nucleons. Thus, the many-body interaction can be approximated by a mean-field potential, reducing the problem to a one-body system. Consequently, the Hamiltonian in Eq. 2.1 can be rewritten as:

$$H = \left[\sum_{j=1}^{A}\left(-\frac{\hbar^2}{2m_N}\nabla_j^2 + V_0^j\right)\right] + \sum_{i<j}^{A}\left(v(\vec{r}_i,\vec{r}_j) - V_0^j\right) = H_0 + V_{\text{int}} \tag{2.2}$$

Here, $V_0$ is the one-body mean-field potential, and $V_{\text{int}}$ represents the residual two-body interaction, which can be treated using perturbation theory. Several forms have been proposed for the one-body potential $V_0$, including the harmonic oscillator and the Woods-Saxon potential. The Woods-Saxon potential is given by:

$$V_{WS}(r) = -\frac{V_i}{1+\exp\left(\dfrac{r-R_i}{a}\right)} \tag{2.3}$$

where $V_i \sim 50$ MeV, $a \sim 0.55$ fm, and $R_i = r_0 A^{1/3}$ (with $r_0 \sim 1.2$ fm) is the nuclear radius. These potentials, however, initially failed to reproduce the observed magic numbers.

In 1949, Maria Göppert-Mayer, Otto Haxel, Hans Suess, and Hans Jensen [May49] introduced the concept of *spin-orbit coupling* to the shell model. The intrinsic spin of a nucleon is $s = \frac{1}{2}$, leading to a splitting of the orbital angular momentum states into total angular momenta $j = l \pm \frac{1}{2}$. This splitting reflects the dependence of the nuclear potential on the relative orientation of the spin and orbital angular momentum of the nucleon. The magnitude of the splitting increases with $l$, and the energy difference is approximately proportional to $(2l+1)$:

$$\Delta E \propto \frac{\hbar^2}{2m}(2l+1)$$

When a shell corresponding to a magic number is completely filled, the nucleons form a highly stable configuration and the nucleus exhibits a spherically symmetric wavefunction, showing minimal collective motion. Significant nuclear collectivity and deformation typically arise only when valence nucleons are present away from magic numbers.

In the *Single Particle Model* (SPM), the residual interaction $V_{int}$ is neglected ($V_{int} = 0$). This approximation is valid primarily for nuclei near the Valley of Stability, where two-body interactions are not dominant. The model assumes that nucleons occupy the lowest available single-particle states, and it has been successful in predicting low-energy level properties of nuclei with proton and neutron numbers near magic numbers. For instance, total angular momentum and parity ($J^\pi$) of the ground-state of a nucleus can often be determined by the valence nucleon occupying a specific $Nl_j$ orbital. Moreover, in even-even nuclei, all closed shells contribute zero total angular momentum, leading to a ground state with $J^\pi = 0^+$. For an even $Z$-odd

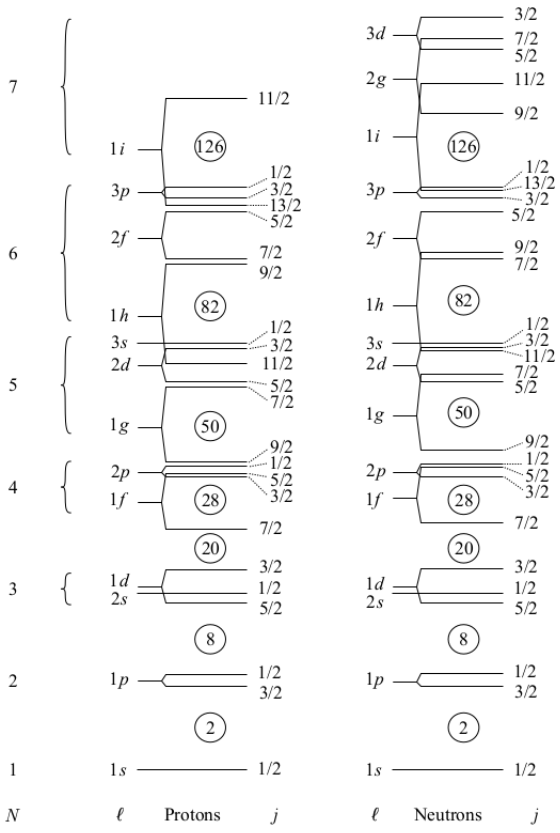


**Figure 2.1.** Energy levels calculated with potential $V_0$. $N$ the principal quantum number, $l$ orbital angular momentum($s(l = 0)$, $p(l = 1)$, $d(l = 2)$, $f(l = 3)$, $g(l = 4)$, $h(l = 5)$, $i(l = 6)$...), and $j$ the total angular momentum. Each level is represented as $Nl_j$ and can be occupied by (2j + 1) nucleons. Image taken from [Kli52].

$N$ or odd $Z$-even $N$ nucleus, the properties of the ground state are defined by the total angular momentum $j$ and parity $(-1)^l$ of the level of the unpaired proton or neutron. For an odd-odd nucleus, the coupling of the unpaired proton and neutron determines the possible spin-parity combinations for the ground state.

However, this simple shell-model configuration fails to account for the experimentally excited states in exotic nuclei, indicating the need to consider configuration mixing and residual interactions. For exotic nuclei with $Z/N \ll 1$ (neutron rich), such as around $Z = 50$ and $N = 82$, the nuclear mean-field potential is modified, leading to single-particle levels with energies that deviate from those observed in stable nuclei. This shift reflects the evolving nature of the underlying nucleon-nucleon interactions in exotic nucleus.

### 2.1.1 Interacting shell model and shell structure around the $^{132}$Sn region

The interacting shell model considers the residual interaction ($V_{int} \neq 0$). Calculations for the interacting shell model divide the proton and neutron orbitals in three spaces: a non-interacting core, a valence space and an external space. The *effective Hamiltonian* $H_{\text{eff}}$ is a simplified representation of the full many-body Hamiltonian, restricted to a finite model space defined by the active valence nucleons outside the inert core. It incorporates both single-particle and residual two-body interactions (including proton-proton, neutron-neutron, and proton-neutron components), renormalized to account for the effects of the excluded configurations in the external space.

The general form of the effective Hamiltonian in second quantization is:

$$H_{\text{eff}} = \sum_i \varepsilon_i \, a_i^\dagger a_i + \frac{1}{4} \sum_{ijkl} \langle ij \,|\, \bar{V}_{\text{eff}} \,|\, kl \rangle \, a_i^\dagger a_j^\dagger a_k a_l \tag{2.4}$$

where:

- $\varepsilon_i$ are the single-particle energies (SPEs) of the orbitals in the model space,
- $a_i^\dagger$ and $a_i$ are the fermionic creation and annihilation operators,
- $\langle ij \,|\, \bar{V}_{\text{eff}} \,|\, kl \rangle$ are the matrix elements of the effective two-body interactions (TBMEs), antisymmetrized and restricted to the valence space.

The effective Hamiltonian in the region of $^{132}$Sn is generally obtained from realistic nucleon–nucleon CD-Bonn interactions through renormalization of the G matrix [BSS$^+$05, CCGI13, Eva21], ensuring that the excluded space contributions are implicitly included. Additional effective interactions have also been developed for this region to improve agreement with experimental observables. The specific shell-model interactions adopted for each isotope discussed in this work are detailed in Chaps. 5, 6, and 7. For calculations in the model space between $28 < Z \leq 50$ and $50 < N \leq 82$, the four proton orbitals, $\pi(0f_{5/2}, 1p_{3/2}, 1p_{1/2}, 0g_{9/2})$, and six neutron orbitals, $\nu(1f_{7/2}, 2p_{3/2}, 2p_{1/2}, 0h_{9/2}, 1f_{5/2}, 0i_{13/2})$ were used. Including these orbitals as part of the valence space means that the Hamiltonian takes into account the interactions of the nucleons in these orbitals with all other nucleons in the valence space orbitals via the respective two-body matrix elements (TBMEs). This Hamiltonian is used as input for large-scale shell-model codes such as NUSHELLX [BR14], or KSHELL [Shi13], which solve the Schrödinger equation restricted to the model space and provide theoretical predictions for level schemes, electromagnetic transition rates, magnetic moments, spectroscopic factors, and other nuclear structure observables.

When the effective Hamiltonian is applied, the orbital SPEs shift to effective single-particle energies $\tilde{\varepsilon}_i$ (ESPE). The ESPE of an occupied orbit is calculated by taking the average of the one-nucleon separation energies weighted by the probability to reach the corresponding $A \pm 1$ eigenstates by adding/removing a nucleon to/from a single-particle state $|i\rangle$. The ESPE, defined as the opposite of the nucleon separation energy for the

given orbital, depends linearly on the occupation number and accounts for the energy shift due to the interaction. It can be expressed as:

$$\tilde{\varepsilon}_i = \varepsilon_i(A) + \sum_j \langle ij \,|\, \bar{V}_{\text{eff}} \,|\, ij \rangle \, n_j, \tag{2.5}$$

where:

- $\tilde{\varepsilon}_i$ is the effective single-particle energy of orbital $i$,
- $\varepsilon_i$ is the SPEs,
- $\langle ij|V_{\text{eff}}|ij\rangle$ is the monopole matrix element of the effective interaction (antisymmetrized),
- $n_j$ is the occupation number of orbital $j$ in the considered configuration.

The quantity $\tilde{\varepsilon}_i - \varepsilon_i(A)$ is commonly referred to as the *monopole drift*, and it is employed to characterize the evolution of shell structure in exotic regions of the nuclear chart. This phenomenon can be sufficiently pronounced to induce the breakdown of established magic numbers and the appearance of new ones.

## 2.2 Beta decay

The $\beta$-decay is the first manifestation of the weak interaction, converts nucleons inside the nucleus to the other kind, emitting a $\beta$ particle and a neutrino in the process. It was first theoretically postulated by E. Fermi in 1934 in order to explain the experiments in 1920 about the electron emission after radioactive decay, and using W. Pauli's ideas about the existence of a new particle called the neutrino two years earlier. It is one of the most common decay processes that may occur to exotic nuclei outside of the stability. In this section, the theoretical foundations and the operational principles of the method are presented.

The weak interaction allows three processes of nuclear beta decay. When a neutron changes into a proton and an electron ($e^-$) with an electron antineutrino ($\bar{\nu}e$) is emitted, it is called negative $\beta$ decay ($\beta^-$). Positive $\beta$ decay ($\beta^+$) is the opposite process, occurring when a proton changes into a neutron, emitting a positron ($e^+$) and an electron neutrino ($\nu_e$). Finally, a third process takes place when an electron from an inner atomic shell is captured by the nucleus. This is called the electron capture process ($\epsilon$). It usually occurs in proton-rich nuclei and competes with $\beta^+$ decay.

Schematically, the three processes for an initial nucleus $X$ that decays to a decay product $X'$ can be represented by the following equations:

$$\beta^- : {}^A_Z X_N \rightarrow {}^A_{Z+1} X'_{N-1} + e^- + \overline{\nu}_e \tag{2.6}$$

$$\beta^+ : {}^A_Z X_N \rightarrow {}^A_{Z-1} X'_{N+1} + e^+ + \nu_e \tag{2.7}$$

$$\epsilon : {}^A_Z X_N + e^- \rightarrow {}^A_{Z-1} X'_{N+1} + \nu_e \tag{2.8}$$

### 2.2.1 Energy balance $Q_\beta$

The mass difference between the initial and final nuclear masses, including the emitted particles is know as the $Q_\beta$ value. This value has to be positive for $\beta$-decay to be energetically possible. This means that starting with an initial nucleus we move to the final one with higher binding energy and thus more stable. The emitted $\beta$ particles have a continuous energy distribution, contrary to the discrete spectrum of $\alpha$ or $\gamma$ decay. This is due to the 3-body interaction between the proton or neutron, electron or positron and neutrino or anti-neutrino respectively (Fig. 2.2).

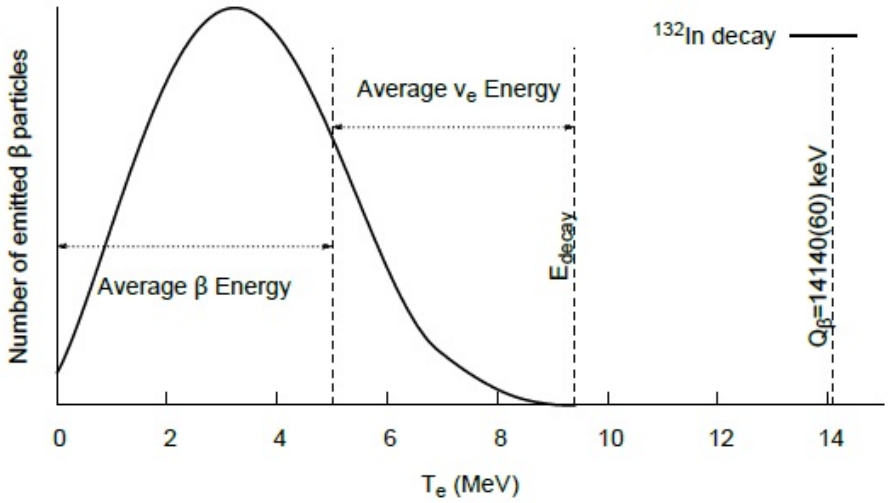


**Figure 2.2.** Energy distribution of the electrons emitted during $\beta$-decay. Image taken from Ref. [Ben20]

The decay energy is of the order of MeV so relativistic kinematics must be used (the non-relativistic approximation $T << mc^2$ is not valid). Using Eq. 2.6 $Q_{\beta^-}$ has the following expression:

$$Q_{\beta^-} = \left[M(^A_Z X) - M(^A_{Z+1} X')\right] c^2 - m_e c^2 - m_\nu c^2 \tag{2.9}$$

Where $M$ corresponds to the nuclear mass than can express in terms of atomic mass $m$ applying the following expression:

$$m(^A_Z X) = M(^A_Z X)c^2 + Z m_e c^2 - \sum_{i=1}^{Z} B_i \tag{2.10}$$

Where $B_i$ is the Binding energy of the electron that is defined as the minimum energy that must be supplied to an electron to displace it from its shell and separate it from the atom. Neglecting the neutrino's mass and taking 2.10:

$$Q_{\beta^-} = \left\{ \left[ m(^A_Z X) - Z m_e \right] - \left[ m(^A_{Z+1} X') - (Z+1) m_e \right] - m_e \right\} c^2 + \left\{ \sum_{i=1}^{Z} B_i - \sum_{i=1}^{Z+1} B_i \right\} \tag{2.11}$$

Neglecting the binding energy between electrons and nucleons, the expression above results:

$$Q_{\beta^-} = \left[ m(^A_Z X) - m(^A_{Z+1} X') \right] c^2 \tag{2.12}$$

If it is considered that the resulting nucleus is much more heavier compared with them the conservation of momentum requires that the recoil energy of the nucleus is negligible ($T_{X'} = 0$), and Eq. 2.12 can then be written as:

$$Q_{\beta^-} = T_e + E_{\bar{\nu}} \tag{2.13}$$

In the $\beta^+$-decay process it is used an analogous procedure from Eqs. 2.6 and 2.8:

$$Q_{\beta^+} = \left[ M(^A_Z X) - M(^A_{Z-1} X') - 2m_e \right] c^2 \tag{2.14}$$

$$Q_{EC} = \left[ M(^A_Z X) - M(^A_{Z-1} X') \right] c^2 - B_e \tag{2.15}$$

Where $B_e$ is the binding energy of the captured electron of the corresponding orbital. It can be observed that whenever $\beta^+$-decay is energetically possible, electronic capture will be possible, but the opposite affirmation is not true. For this to occur, the mass difference between the initial and final states must be at least 1.022 MeV (twice the mass of the electron).

As can be observed in Fig. 2.2, the energy spectrum of the $\beta$-particle goes from 0, when all the energy is received by the neutrino, to the maximum defined by $Q_\beta$, when all the energy is taken by the $\beta$-particle. All $Q_\beta$ values described above refer to decays between the ground states (g.s.). If the final nuclear state is not the ground state, the maximum energy is thus defined by the energy difference with lowest lying excited state $f_i$ that can be populated. The total released energy $E_{decay}$, corresponds to the $Q_{\beta g.s.}$ minus the excitation energy of $E_{f_i}$ of the populated level:

$$E_{decay} = Q_{\beta g.s.} - E_{f_i} \tag{2.16}$$

### 2.2.2 Fermi theory of $\beta$

In the framework of perturbation theory, Fermi considered the assumption that the interaction that causes the transition is weak in comparison with the nuclear interaction the generates the quasi-stationary states in the nucleus so the transition rate can be described using Fermi's golden rule:

$$d\lambda = \frac{2\pi}{\hbar} |M_{fi}|^2 \rho(E_f) \tag{2.17}$$

where $M_{fi} = \langle f | M_{fi} | i \rangle$ is the matrix element of the weak interaction potential between the initial and final states and $\rho(E_f) = \dfrac{dn}{dE_f}$ is the density of final states.

$|i\rangle = |J_i, m_i\rangle$ is the initial nuclear stationary state with angular momentum and parity well defined $J_i^\pi$. The matrix elements $M_{fi} = G_F O_X$ is composed of the Fermi constant $G_F$ and the axial-vector nuclear operator $O_X$. The final nuclear state contains well-defined angular momentum and parity $J_f^\pi$ and the electron and neutrino wave function can be approximated to a plane wave and normalized in a volume $V$:

$$|f\rangle = \frac{1}{\sqrt{V}} e^{i\vec{p}\cdot\vec{r}/\hbar} \frac{1}{\sqrt{V}} e^{i\vec{q}\cdot\vec{r}/\hbar} |J_f, M_f; \xi_f\rangle \tag{2.18}$$

Where $\vec{p}$ is the electron momentum and $\vec{q}$ is the neutrino momentum.

The angular momentum $l$ of the two particles is 0. Due to that reason, the only change in the angular momentum $J$ of the the daughter nucleus is given by the spin of the electron and the neutrino. This is the so-called *allowed approximation*. Both particles, electron and neutrino, have spin 1/2 therefore there are two possibilities. If the spins are anti-parallel coupled ($\vec{S} = \vec{S_e} + \vec{S_\nu} = 0$) it is called a Fermi transition, in the other case is the Gamow-Teller (GT) transition where the spins are coupled in parallel ($\vec{S} = \vec{S_e} + \vec{S_\nu} = 1$). These two type of transitions are defined in the transition nuclear matrix by the operator $O_X$. It is an operator that has a vector component (Fermi component) and an vector axial component (GT component):

$$O_{V-A} = \sum_{j=1}^{A} (\overbrace{\tau_\pm(j)}^{Fermi} + \overbrace{g_A \sigma(j) \tau_\pm(j)}^{GT}) \tag{2.19}$$

Where $\tau_\pm(j)$ is the Fermi isospin operator that only produces changes in the third component of isospin $I_3$ (it changes a neutron into a proton and vice versa). $\sigma(j)$ is the Pauli spin operator that changes the isospin $I$ one unit. The parity of the electron and the neutrino is defined by the angular momentum ($\pi = (-1)^l$). For that reason, for allowed decays there is no parity change. There also exists the so called *superallowed Fermi transitions*, that is a special case of Fermi transitions $0^+ \rightarrow 0^+$. In general, *allowed transition* are most probable to occur and more intense. Taking all these into account, the $\beta$-decay are expressed in Tab. 2.1.

**Table 2.1.** Selection Rules for allowed $\beta$-decay transitions. $I$ is the isospin and $I_3$ is the third isospin component

| | **Fermi Transition** | **Gamow-Teller Transition** |
|---|---|---|
| $\boldsymbol{\Delta J}$ | 0 | $0, \pm 1$ ($\cancel{0^+ \longrightarrow 0^+}$) |
| $\boldsymbol{\Delta \pi}$ | $+1$ | $+1$ |
| $\boldsymbol{\Delta I}$ | 0 | $0, \pm 1$ ($\cancel{0^+ \longrightarrow 0^+}$) |
| $\boldsymbol{\Delta I_3}$ | $\pm 1$ | $\pm 1$ |

The electron and neutrino plane wave function can be expressed in terms of Spherical harmonics and the angular momentum $l$ as follow:

$$e^{i\vec{k}\cdot\vec{r}/\hbar} = \sum_{l=0}^{\infty} i^l \sqrt{4\pi(2l+1)} j_l(kr) Y_{l0}(\theta) \tag{2.20}$$

Upon performing a Taylor expansion of Eq. 2.20, each term corresponds to a spherical harmonic with definite angular momentum. Decays with angular momentum greater than one $l_{e-\nu} \geq 1$ are called *Forbidden transitions*. The forbidden decays are less probable than the allowed decays and it is common to have longer state half-lives based on how far we must take the expansion of the plane wave to find a nonvanishing nuclear matrix element. The degree of the *Forbidden transitions* are classified depending on the value of the angular momentum. Transitions with $l_{e-\nu} = 1$ are called *First-Forbidden*, $l_{e-\nu} = 2$ *Second-Forbidden* and so forth. Introducing Eq. 2.20 into the nuclear transition matrix $M_{fi}$:

$$\begin{aligned} M_{fi} = \overbrace{\sum_{M_f} = \langle J_f, M_f; \xi_f | \underbrace{\left(1 + i\vec{k}\cdot\vec{r} + \frac{1}{2}(\vec{k}\cdot\vec{r})^2 + ...\right)}_{forbiddenness\ degree} \sum_{j=1}^{A} \tau_{\pm}(j) | J_i, M_i; \xi_i \rangle}^{Fermi} \\ \overbrace{+ g_A \sum_{M,\mu} = \langle J_f, M_f; \xi_f | \underbrace{\left(1 + i\vec{k}\cdot\vec{r} + \frac{1}{2}(\vec{k}\cdot\vec{r})^2 + ...\right)}_{forbiddenness\ degree} \sum_{j=1}^{A} \sigma(j)\tau_{\pm}(j) | J_i, M_i; \xi_i \rangle}^{GT} \end{aligned} \tag{2.21}$$

The density of final states $\rho(E_f)$ within a phase-space volume $V$ can be expressed in terms of the decay $Q$-value and the electron kinetic energy $T_e$ as follows:

$$\frac{dn}{dT_e} = \frac{V^2}{4\pi^4\hbar^6 c^3} (Q - T_e)^2 p^2 dp \tag{2.22}$$

Using Eq. (2.22) and noting that the electron's total energy satisfies $E_e^2 = (T_e + m_e c^2)^2$, Eq. (2.17) can be written as:

$$\lambda = \frac{2\pi}{\hbar} |\langle f | M_{fi} | i \rangle|^2 = \frac{G_F^2}{2\pi^3\hbar^7 c^3} |M_{fi}|^2 \sqrt{(Q - T_e)^2 m_\nu^2 c^4} (Q - T_e) p^2 dp \tag{2.23}$$

The distribution of the emitted particles can be expressed based on the momentum $p$:

$$N(p) = \frac{d\lambda}{dp} = \frac{G_F^2}{2\pi^3\hbar^7 c^3} |M_{fi}|^2 \sqrt{(Q - T_e)^2 m_\nu^2 c^4} (Q - T_e) p^2 \tag{2.24}$$

The Coulomb potential inside the nucleus modifies the spectrum by introducing an additional factor, caused by the $\beta$ particle and the resulting nucleus, the *Fermi function* $F(Z', p)$, where $Z'$ is the atomic number of the resulting nucleus. On the other hand, the nuclear matrix element $|M_{fi}|^2$, which accounts for the effects of particular initial

and final nuclear states and which may include an additional electron and neutrino momentum dependence $S(p,q)$ from forbidden terms. The function $S(p,q)$ is known as the *shape factor*. The $\beta$ spectrum Eq. 2.25 includes three factors: 1. *Statistical factor*, 2. *Fermi function*, 3. *Shape factor*:

$$N(p) = \frac{G_F^2}{2\pi^3\hbar^7 c^3} \overbrace{\left[\sqrt{(Q-T_e)^2 m_\nu^2 c^4}\,(Q-T_e)\,p^2\right]}^{1} \overbrace{F(Z',p)}^{2} \overbrace{\left[|M_{fi}|^2 S(p,q)\right]}^{3} \tag{2.25}$$

### 2.2.3 The Total Decay Rate

The total decay rate in term of momentum $p$ (for allowed transitions) is obtained integrated Eq. 2.25

$$\lambda = \int_0^{p_{max}} \frac{d\lambda}{dp} dp = \frac{G_F^2 |M_{fi}|^2}{2\pi^3\hbar^7 c^3} \int_0^{p_{max}} F(Z',p) p^2 \left(Q - T_e\right)^2 dp \tag{2.26}$$

This integral depends on $Z'$ and the maximum electron total energy $E_o$ ($p_{max} = \sqrt{E_o^2 + m_e^2 c^4}$). Accordingly, the *Fermi integral* is defined as

$$f(Z',Q) = \frac{1}{m_e^5 c^7} \int_0^{p_{max}} F(Z',p) p^2 \left(Q - T_e\right)^2 dp \tag{2.27}$$

where the constants are chosen such that $f(Z',Q)$ is dimensionless. This integral has been tabulated. Consequently, the total transition rate is given by:

$$\lambda = \frac{m_e^5 c^4}{2\pi^3\hbar^7} G_F^2 |M_{fi}|^2 f(Z',Q) \tag{2.28}$$

A very useful parameter is the *comparative half-life* or *ft* value. Considering the relationship between $\lambda$ and the half-life of the parent nucleus $t_{1/2}$:

$$\lambda = \frac{\ln 2}{t_{1/2}} \tag{2.29}$$

The Fermi integral can be expressed as follow:

$$ft_{1/2} = \ln 2 \frac{2\pi^3\hbar^7}{m_e^5 c^4 G_F^2 |M_{fi}|^2} \tag{2.30}$$

As can be seen from Eq. (2.30), variations in $ft$ imply changes in the nuclear matrix element $|M_{fi}|$ and hence differences in the nuclear wave function. Therefore, the $ft$ value classify $\beta$ transitions. It is common to use the logarithm in base 10 of $ft$ ($\log ft_{1/2}$) due to the enormous range of half-lives in $\beta$-decay $ft$ (about $10^{-3}$ to $10^{20}$ s) (see Tab. 2.2). It is still unknown if there are transitions with $\log ft_{1/2} > 26$.

Fig. 2.3 presents the distribution of $\log ft$ values corresponding to well-characterized $\beta$-decay transitions. The data represent experimental determinations for forbidden transitions between nuclear states with well-defined spin and parity quantum numbers.

**Table 2.2.** Classification of transitions in the $\beta$-decay. L is the angular momentum of electron

| $\log ft_{1/2}$ | L | Type | Fermi/GT | $\Delta J$ | $\Delta\pi$ |
|---|---|---|---|---|---|
| 2.9-3.7 | 0 | Super-allowed | Fermi | 0 ($0^+ \longrightarrow 0^+$) | +1 |
| 3.8-6.0 | 0 | Allowed | Fermi<br>GT | 0<br>$0, \pm1$ (~~$0^+ \longrightarrow 0^+$~~) | +1 |
| 6.0-8.0<br>8-10 | 1 | First-forbidden | Fermi<br>GT | $0, \pm1$ (~~$0^+ \longrightarrow 0^+$~~)<br>$0, \pm1, \pm2$ | -1 |
| 11.0-13.0 | 2 | Second-forbidden | Fermi<br>GT | $\pm2$<br>$\pm2, \pm3$ | +1 |
| 17.0-19.0 | 3 | Third-forbidden | Fermi<br>GT | $\pm3, (\pm4)$<br>$\pm3, \pm4, (\pm5)$ | -1 |
| $> 26$ | 4 | Fourth-forbidden | | | +1 |

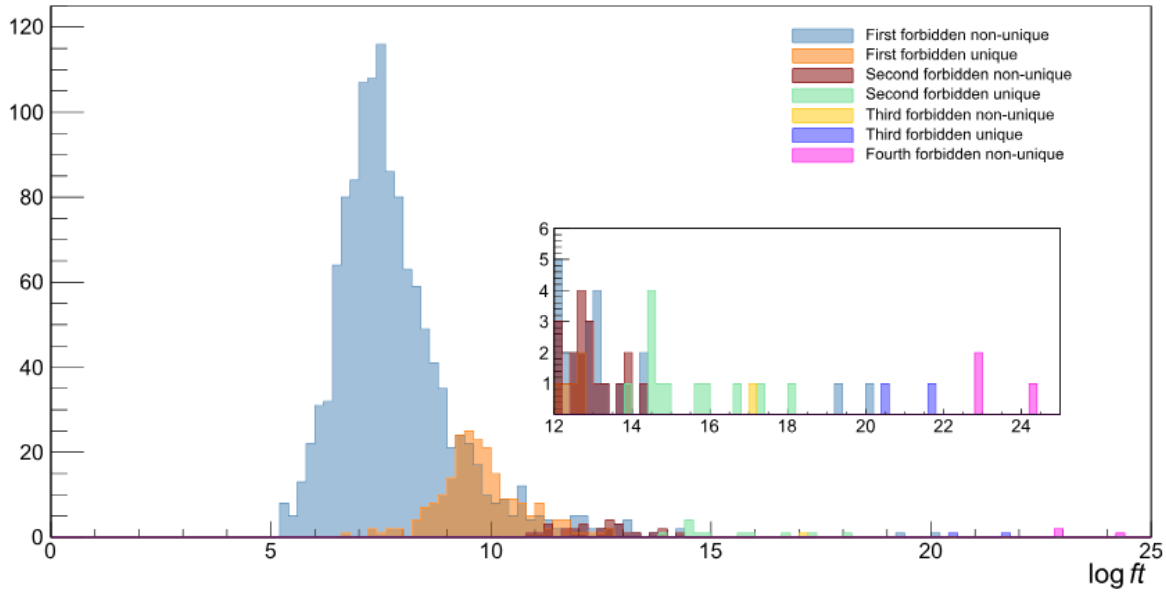


**Figure 2.3.** Distribution of all forbidden log$ft$ values, which fulfill the selection criteria. The distributions are shown in greyish blue and orange in case of first forbidden non-unique and unique transitions, respectively. Different shades might appear due to the overlap of different transparent colors. Image taken from Ref. [TMSZ23]

## 2.3 $\beta$-delayed neutron emission

In the neutron-rich region of the nuclei chart, the $Q_{\beta^-}$ value is quite high, especially in the exotic nuclei $^{132}$Cd and $^{133}$Cd studied during the IS685_II experimental campaign. This makes it possible to overcome the energy required to extract one or a few nucleons from the daughter nucleus may lead to the subsequent emission of one or more neutron after the emission of the $\beta$ particle. This energy is called neutron separation energy $S_n$ and is determined by:

$$S_n \left({}^{A}_{Z}X_N\right) = \left[m \left({}^{A-1}_{Z}X_{N-1}\right) + m_n - m \left({}^{A}_{Z}X_N\right)\right] c^2 \tag{2.31}$$

When the $\beta$-delayed neutron emission processes is possible, various competing

processes can take place. These include $\gamma$ de-excitations originating from states within the emitter or $\beta$-decays to lower levels in the emitter that cannot undergo decay through particle emission. Theoretical methods typically presume that levels situated above the neutron separation energy primarily undergo decay through neutron emission [Mie14, MKM16].

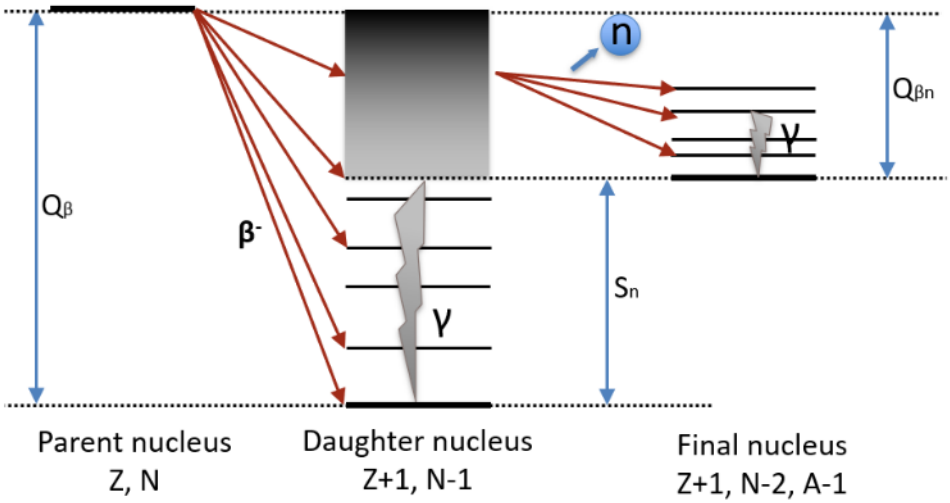


**Figure 2.4.** Schematic representation of the $\beta$ decay and $\beta$-delayed neutron emission processes [Ber18]

It is possible for more than one neutron to be emitted, therefore, the neutron separation energy is denoted as $S_{2n}$ for 2 neutrons, for 3 neutrons, $S_{3n}$ and so on. Therefore, the final nucleus from a $\beta$-delayed neutron emission ($\beta$n) has ${}^{A-1}_{Z+1}X_{N-2}$, ($\beta$2n) ${}^{A-2}_{Z+1}X_{N-3}$, ($\beta$3n) ${}^{A-3}_{Z+1}X_{N-4}$ etc. respectively. The delayed neutron emission probability $P_n$, depends on the difference between the $Q_{\beta^-}$ value of the parent and the $S_n$ of the daughter.

$$Q_{\beta^- n} = Q_{\beta^-} - S_n \tag{2.32}$$

Following a similar approach, the probability of $\beta$-delayed emission of $x$ neutrons ($P_{xn}$).

## 2.4 Gamma decay

After $\beta$-decay, the resulting nucleus might be in an excited state. In most cases, de-excitation to the ground state (g.s.) occurs with the emission of monoenergetic $\gamma$ rays, which correspond to a specific transition between two particular levels (the recoil has been assumed negligible).

$${}^{A}_{Z}X_N{}^{*} \rightarrow {}^{A}_{Z}X_N + \gamma \tag{2.33}$$

The transitions probabilities follows Fermi's golden rule between the initial and final state:

$$\Gamma_{i\to f} = \frac{2\pi}{\hbar} |\langle\psi_i|H_{int}|\psi_f\rangle|^2 \rho \tag{2.34}$$

Thanks to the electromagnetic nature of gamma radiation, the matrix elements $m_{fi}(X\lambda)$ can be described in terms of electric $m_{fi}(X\lambda = E\lambda)$ and magnetic $m_{fi}(X\lambda = M\lambda)$ multipoles where $\lambda$ is the angular momentum of the $\gamma$-ray and $X$ could be $E$ for Electric transitions and $M$ for Magnetic transitions [MM89]. Therefore Eq. 2.34 becomes:

$$\Gamma_{i\to f}(X\lambda) = \frac{8\pi(\lambda+1)}{\lambda[(2\lambda+1)!!]^2}\left(\frac{E_\gamma}{\hbar c}\right)^{2\lambda+1}[m_{fi}(X\lambda)]^2 \tag{2.35}$$

$$m_{fi}(X\lambda) = \int \psi_f^* M(X\lambda)\psi_i dv \tag{2.36}$$

If the internal composition of the nucleons is neglected and it is assumed that the wavelength of the $\gamma$-ray is much larger than the size of the nucleus (the transitions studied in this thesis are of the order of MeV and therefore satisfy this approximation) Eq. 2.35 and Eq. 2.36 can be written as follow:

$$M(E\lambda,\mu) = \int \rho(\boldsymbol{r}) r^\lambda Y_{\lambda\mu}(\hat{\boldsymbol{r}}) dr \tag{2.37}$$

$$M(M\lambda,\mu) = \frac{-1}{c(\lambda+1)}\int \overrightarrow{j}(\boldsymbol{r})\cdot(\boldsymbol{r}\times\overrightarrow{\nabla}) r^\lambda Y_{\lambda\mu}(\hat{\boldsymbol{r}}) dr \tag{2.38}$$

Where $\rho(\boldsymbol{r})$ is the charge distributions, $\overrightarrow{j}(\boldsymbol{r})$ is the current distributions and $\lambda\mu$ order spherical harmonics $Y_{\lambda\mu}$.

The conservation of parity and angular momentum combined give the $\gamma$ **decay selections rules**. These selections rules determine the parity of the transitions, depending if is electric E or magnetic M, and the total angular momenta as follows:

$$\Delta\pi(E\lambda) = (-1)^\lambda \quad \Delta\pi(M\lambda) = (-1)^{\lambda+1} \tag{2.39}$$

and

$$|J_i - J_f| \leq \lambda \leq J_i + J_f \quad \lambda \neq 0 \tag{2.40}$$

The case $\lambda = 0$ is not allowed because $\gamma$ rays have spin 1 and monopole transitions $0^+ \to 0^+$ are forbidden. Tab. 2.3 is an schematic view for the $\lambda = 3$ first orders. If there is no parity change ($\Delta\pi = +1$) then E$\lambda$ is even and M$\lambda$ is odd. As a general view, transitions with higher $\lambda$ are less probable and if it is the same order electric dominate in comparison with magnetic transitions, and in most cases can be suppressed. Taking this into account, the transitions E($\lambda$+1) competes with M($\lambda$). In the $^{132}$Sn region the competition mostly occurs between E2 and M1 transitions and is described by the mixing ratio $\delta = \frac{\Gamma_\gamma(X\lambda)}{\Gamma_\gamma(X'\lambda')}$, which the set-up used in the experiment of this thesis can not measure.

**Table 2.3.** Spin and parity selection rules for gamma-ray transitions up to order $\lambda = 3$.

| $\Delta J = \lvert J_f - J_1 \rvert$ | **1** | **2** | **3** |
|---|---|---|---|
| $\Delta\pi$ = -1 | $E1$ | $M2$ | $E3$ |
| $\Delta\pi$ = +1 | $M1$ | $E2$ | $M3$ |

To understand the parity of electromagnetic transitions we need to recall that each of the initial and final states of the nucleus involved in the transition can be viewed as having a definite distribution of matter and charge. When the excited nucleus makes a transition from the excited state to a lower energy state, the distribution of matter and charge will change in some way. For example, a nucleus that is spinning with a certain value of angular momentum will slow down as it de-excites and reaches the ground state. Thus, the emission of the photon can be associated with the change in the overall distribution of neutrons and protons but we can identify two different changes that are analogous to classical antennas. A shift in the distribution of charge (for example, the transition of a proton from one orbital to another) will give rise to an electric field but a shift in the distribution of current in the nucleus (for example, the shift of the direction of a proton) will give rise to a magnetic field. The parity of the photon depends on both the angular momentum and the type (electric or magnetic). Notice that electric and magnetic radiation with a given multipole character have opposite parities.

### 2.4.1 Electromagnetic transition multipolarities

The initial $|J_i M_i\rangle$ and the final nuclear $\langle J_f M_f|$ states are characterized by total angular momenta $J$ and their projections $M$ on the chosen quantization axis. To compute the transition matrix elements for certain $\gamma$ transition and obtain the reduced transition probabilities $B(X\lambda; J_i \rightarrow J_f)$ all the final level projections $M_f = M_i + \mu$ are to be summed:

$$B(X\lambda; J_i \rightarrow J_f) = \sum_{\mu, M_f} |\langle J_f M_f | M(X\lambda, \mu) | J_i M_i \rangle|^2 \tag{2.41}$$

Thanks to Wigner-Eckhart theorem it is possible to avoid the M projections dependence. Thus, applying this theorem to Eq. 2.41:

$$B(X\lambda; J_i \rightarrow J_f) = \frac{1}{2J_i + 1} |\langle J_f | M(X\lambda) | J_i \rangle|^2 \tag{2.42}$$

To compute $M(X\lambda)$ it is necessary to give a specific theoretical nuclear model. However, by experimentally knowing the $\gamma$-ray energy $E_\gamma$, the mean lifetime of the level $\tau$ and the spin of the initial and final state ($J_i \rightarrow J_f$), it is possible to determine the reduced transition probability:

$$B(X\lambda; J_i \rightarrow J_f) = \frac{1}{\tau_\gamma} \left[ \frac{\lambda((2\lambda+1)!!)^2}{8\pi(\lambda+1)} \hbar \left( \frac{\hbar c}{E_\gamma} \right)^{2\lambda+1} \right] \tag{2.43}$$

Eq. 2.43 contains the nuclear structure information because reduced transition probabilities are very sensitive to the detailed wave functions. The dimensions depends

on whether it is an electrical or magnetic transition. For electric transitions $[e^2\text{fm}^{2\lambda}]$ and for magnetic transitions $[\mu_N^2\text{fm}^{2\lambda-2}]$. The first four multipoles for electric and magnetic are calculated in Tab. 2.4.

**Table 2.4.** First four order of electric and magnetic reduced transition probability. $\tau_\gamma$ in s and $E_\gamma$ in MeV

| $X\lambda$ | E | M |
|---|---|---|
| **1** | $B(E1) = 6.29 \cdot 10^{-16} E_\gamma^{-3} \tau^{-1} e^2\text{fm}^2$ | $B(M1) = 5.68 \cdot 10^{-14} E_\gamma^{-3} \tau^{-1} \mu_N^2$ |
| **2** | $B(E2) = 8.20 \cdot 10^{-10} E_\gamma^{-5} \tau^{-1} e^2\text{fm}^4$ | $B(M2) = 7.41 \cdot 10^{-8} E_\gamma^{-5} \tau^{-1} \mu_N^2\text{fm}^2$ |
| **3** | $B(E3) = 1.76 \cdot 10^{-3} E_\gamma^{-7} \tau^{-1} e^2\text{fm}^6$ | $B(M3) = 1.59 \cdot 10^{-1} E_\gamma^{-7} \tau^{-1} \mu_N^2\text{fm}^4$ |
| **4** | $B(E4) = 5.92 \cdot 10^{3} E_\gamma^{-9} \tau^{-1} e^2\text{fm}^8$ | $B(M4) = 5.34 \cdot 10^{5} E_\gamma^{-9} \tau^{-1} \mu_N^2\text{fm}^6$ |

Considering Eq. 2.43, the transition probability for a gamma transition can be obtained as follows:

$$\Gamma_\gamma(X\lambda) = \left[ \frac{8\pi(\lambda+1)}{\lambda((2\lambda+1)!!)^2} \hbar \left( \frac{E_\gamma}{\hbar c} \right)^{2\lambda+1} \right] B(X\lambda; J_i \to J_f) \tag{2.44}$$

The selection rules may allow more than one $\Gamma_\gamma(X\lambda)$ at certain $\gamma$ transitions. In these cases, all possible $\Gamma_\gamma(X\lambda)$ must be added together. Higher order contributions are usually less relevant and can be ignored.

### 2.4.2 Internal conversion

In the region below 300 keV (although it is possible to take place at energies above this limit), an electromagnetic phenomenon called internal conversion has an important role to play and competes with the $\gamma$ emission. This process occurs when the energy between two excited levels of the nucleus is transferred to an atomic electron of a specific atomic layer of the nucleus (K, L, M...). This atomic electron is emitted from the atom, which can be experimentally measured to determine the X$\lambda$.

$$^A_Z X^*_N \to {}^A_Z X_N + e^- \tag{2.45}$$

The internal conversion coefficient $\alpha_{IC}$ is defined as the probability of internal conversion electron emission relative to the $\gamma$ emission:

$$\alpha_{IC} = \frac{\Gamma_{IC}}{\Gamma_\gamma} \tag{2.46}$$

An internal conversion ratio can be defined for each atomic shell or sub-shell ($\alpha_{IC} = \alpha_{IC}^K + \alpha_{IC}^L + \alpha_{IC}^M + ...$). Therefore, the total transition rate can be expressed as:

$$\Gamma = \Gamma_\gamma + \Gamma_{IC} = \Gamma_\gamma(1 + \alpha_{IC}) \tag{2.47}$$

In general $\alpha_{IC}$ increases with the $Z$-value of the isotope, the $\lambda$ of the multipolarity and as the atomic level decreases. On the other hand decreases with $E_\gamma$. Only $0^+ \to 0^+$ transitions can decay by pure internal conversions.

### 2.4.3 Lifetimes of excited states

Experimentally measuring the lifetime $\tau$ of the level provides easy access to the transition rate $\Gamma$ since $\Gamma = \frac{1}{\tau}$. The relation between the half-life $T_{1/2}$ is simply $\Gamma = \frac{1}{\tau} = \frac{\ln 2}{T_{1/2}}$. Normally, a certain level can be depopulated by $i$ number of $\gamma_i$. Thus, the total transition rate for this level is the sum from all the transition rates for each $\gamma_i$.

$$\Gamma = \sum_i \Gamma_{\gamma_i}(1 + \alpha_{IC_i}) \tag{2.48}$$

$\Gamma_{\gamma_i}$ is the inverse of the partial mean life $\Gamma_{\gamma_i} = \frac{1}{\tau_{\gamma_i}}$. The partial mean life $\tau_{\gamma_i}$ is necessary to determinate the reduced transition probability $B(X\lambda; J_i \to J_f)$ (Eq. 2.43). $\tau_{\gamma_i}$ can be experimentally computed employing the branching ratio ($BR_i$) for this specific $\gamma_i$-ray. If the de-excitation pattern is known, $BR_i$ it is determined using the intensity of the $\gamma_i$-ray ($I_{\gamma_i}(1+\alpha_{IC_i})$) that de-excites the level and the whole set of $\sum_j \gamma_j$ intensities that de-excite the given level ($\sum_j I_{\gamma_j}(1 + \alpha_{IC_j})$). It provides information about the likelihood of a particular $\gamma_i$-ray emission occurring relative to other possible $\gamma$-ray emissions during the decay of the nucleus. The $BR_i$ of a transition is given by the following formula:

$$BR_i = \frac{\Gamma_{\gamma_i}}{\Gamma} = \frac{I_{\gamma_i}(1 + \alpha_{IC_i})}{\sum_j I_{\gamma_j}(1 + \alpha_{IC_j})} \tag{2.49}$$

Applying 2.48 and 2.49 the partial mean life $\tau_{\gamma_i}$ can be determined as:

$$\Gamma_{\gamma_i} = \Gamma BR_i = \frac{1}{\tau_{\gamma_i}} \tag{2.50}$$

thus:

$$\tau_{\gamma_i} = \frac{\tau}{BR_i} \tag{2.51}$$

so by knowing $E_\gamma$ and $\tau_{\gamma_i}$ we can calculate the reduced transition probability $B(X\lambda; J_i \to J_f)$.

### 2.4.4 Weisskopf estimates

If the single-particle approximation is assumed and taking the assumption of constant radial wave function with the radius approximation of $R = 1.2A^{1/3}$ fm for the nucleus, the reduced transition probabilities (Eq. 2.44) can be expressed as follow:

$$B_{We}(E\lambda) = \frac{1}{4\pi}\left(\frac{3}{\lambda+3}\right)^2 (1.2)^{2\lambda} A^{2\lambda/3} e^2 \mathrm{fm}^{2\lambda} \tag{2.52}$$

$$B_{We}(M\lambda) = \frac{10}{\pi}\left(\frac{3}{\lambda+3}\right)^2 (1.2)^{2\lambda-2} A^{(2\lambda-2)/3} \mu_N^2 \mathrm{fm}^{2\lambda-2} \tag{2.53}$$

Eqs. 2.52 and 2.53 are the *Weisskopf estimates*. This estimation can be interpreted as the transition to a single nucleon de-excitation moving from one orbit to another,

with no interaction from the remaining nucleons. It is quite useful to express the reduced transition probabilities in *Weisskopf units W.u.*. It is obtained by dividing the value of the experimentally reduced probability transition $B_{exp}(X\lambda)$ obtained and the value of the corresponding *Weisskopf estimates* for that nucleus $B_W(X\lambda)$:

$$Weisskopf = \frac{B_{exp}(X\lambda)}{B_W(X\lambda)} \tag{2.54}$$

If the *Weisskopf estimates* (W.u.) is significantly lower than the measured value, it could be attributed to the difference between nuclear wave functions slowing down the process. Conversely, the measured value might be much higher if there were multiple protons contributing to the transition (collective effects).

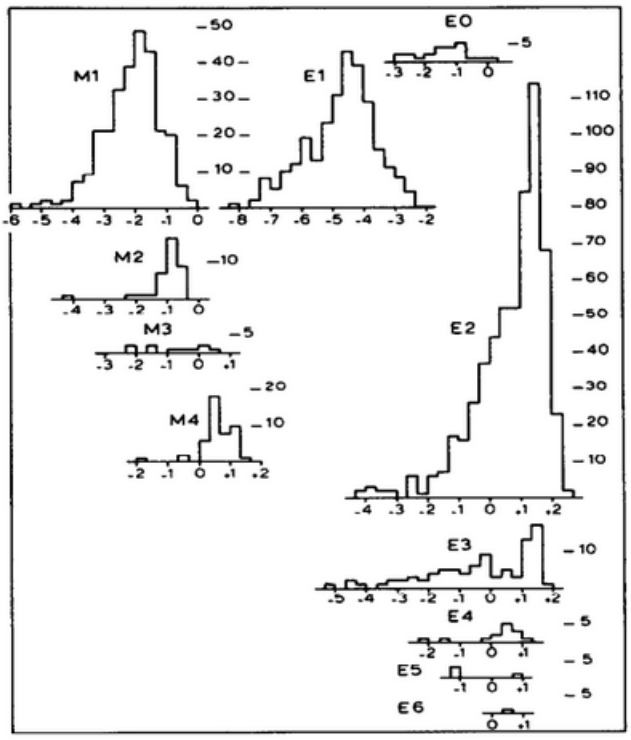


**Figure 2.5.** Gamma-ray strength distributions in the $A = 91 - 150$ region for transitions of different character ($E0 - E6$, $M1 - M4$). The logarithmic abscissa scale indicates the strength in Weisskopf units, except for $E0$ transitions which are in Wilkinson units. Image taken from Ref. [End81]

The reduced transition probabilities $B(X\lambda)$ may exhibit enhancement or quenching relative to empirical systematics or theoretical predictions. A comprehensive compilation of electromagnetic transition strengths in nuclei with mass numbers $A = 91$–$150$ was published by P. M. Endt in 1981 [End81]. This dataset provides reduced transition probabilities in Weisskopf units (W.u.) for both electric and magnetic multipole transitions and remains a valuable reference, particularly for nuclei in the vicinity of the doubly magic nucleus $^{132}$Sn.

Fig. 2.5 presents a comparison of the distribution of transition strengths for the most frequently observed multipolarities ($M1$, $E1$, and $E2$) across various mass regions. The Recommended Upper Limits (RUL) serve as empirical benchmarks; a measured transition strength significantly exceeding the RUL may suggest an incorrect multipolarity assignment.

Electric quadrupole ($E2$) transitions are generally indicative of collective nuclear excitations, such as quadrupole vibrations or rotational motion in deformed nuclei. Electric octupole ($E3$) transitions similarly reflect collective behavior associated with octupole vibrations. In contrast, magnetic dipole ($M1$) transitions are typically non-collective and exhibit comparatively low transition probabilities, seldom exceeding 1 W.u.

## 2.5 The astrophysical $r$-process

Nuclei in the $^{132}$Sn region are also known to play an important role in the astrophysical rapid neutron capture $r$-process, which impacts elemental abundances in the solar system. The heavy elements beyond $^{56}$Fe ($Z = 26$, $N = 30$) cannot be produced via fusion reactions, but are instead produced via neutron-capture reactions: the rapid neutron capture $r$-process and the slow neutron capture $s$-process.

The $s$-process proceeds close to the valley of stability in the nuclear chart [BBFH57]. It takes place in environments with relatively weak neutron fluxes and is responsible for the production of approximately half of the heavy elements. The timescale for a nucleus to capture a neutron is comparatively long, typically exceeding the mean lifetime for $\beta$ decay, so that the produced isotopes generally undergo $\beta$ decay before capturing an additional neutron.

The second neutron-capture process is the $r$-process, which accounts for roughly half of the abundances of the heavy elements. About half of the nuclei heavier than iron are produced through the $r$-process [AGT07]. This process occurs in astrophysical environments with extremely high neutron densities, where neutron-capture reactions proceed on timescales much shorter than those of $\beta$ decays.

The path of the $r$-process across the nuclide chart is determined by *waiting-point* nuclei, which are defined under two distinct conditions. Within an isotopic chain away from a neutron shell closure, the maximum of the abundance distribution occurs at one neutron number, which is considered a waiting-point nucleus. This local maximum exists in a high density $\gamma$-ray flux, so that the isotopes continue capturing neutrons until they achieve equilibrium with photo-disintegration reactions $(\mathrm{n}, \gamma) \rightleftharpoons (\gamma, \mathrm{n})$. Once $\beta$-decay occurs and the $r$-process material is transferred to the $Z + 1$ isotopic chain, multiple neutron captures and photo-disintegrations happen until a new equilibrium distribution is established.

The key astrophysical parameters governing the equilibrium of photo-disintegration

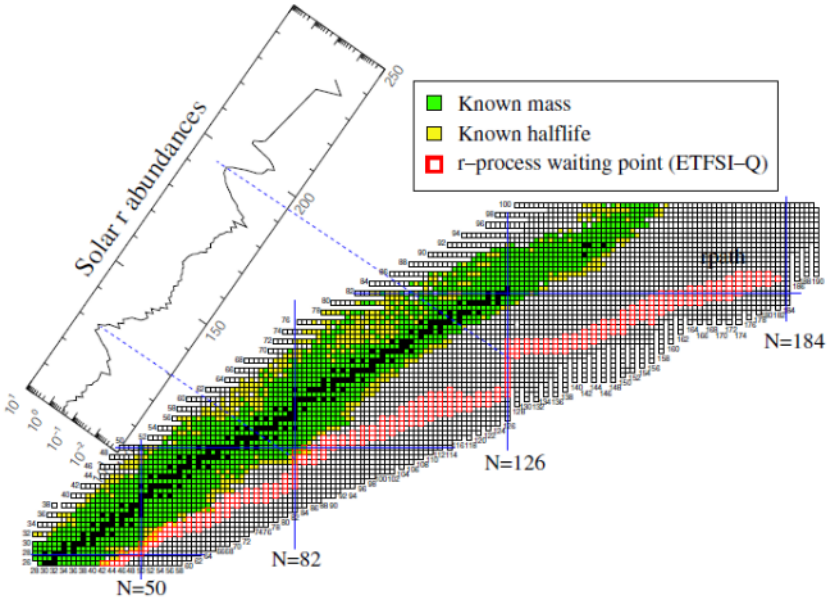


**Figure 2.6.** Nuclide chart illustrating a possible rapid neutron capture ($r$-process) path and the corresponding solar $r$-process abundances. The potential $r$-process trajectory, identified through the respective waiting-point nuclei, is indicated by red boxes. Figure adapted from Ref. [GLMP07].

reactions for each element are the neutron separation energy, $S_n$, the temperature, $T$, and the neutron density, $n_n$. Consequently, the $r$-process path is defined by the ensemble of waiting-point nuclei along an isotopic chain, for given $T$ and $n_n$, provided that the values of $S_n$ are comparable. The relative $r$-process abundances of nuclei with proton number $Z$ and mass numbers $A$ and $A+1$ at nuclear statistical equilibrium are determined by the nuclear Saha equation for neutron capture [AGT07], which can be written as:

$$\frac{n(A+1,Z)}{n(A,Z)} = n_n \cdot \left(\frac{A+1}{A} \cdot \frac{2\pi\hbar^2}{k_B T \cdot m_u}\right)^{3/2} \cdot \exp\left(-\frac{S_n(A+1,Z)}{k_B T}\right), \tag{2.55}$$

where $k_B$ is Boltzmann constant, and $m_u$ is the atomic mass unit.

The second type corresponds to the *waiting-point* nuclei, which arise from neutron shell closures and are the most relevant for the Cd isotopes studied in this work. Fig. 2.6 shows the $r$-process path of waiting point isotopes in the nuclide chart, along with the solar abundance of the elements produced by the $r$-process, including the $N = 82$ nuclei $^{128}$Pd, $^{129}$Ag, $^{130}$Cd and $^{131}$In that cluster around the doubly magic $^{132}$Sn [MSMA16]. At neutron shell closures, the energy required to capture an additional neutron above the magic number increases, halting the neutron-capture process. This effect arises from the reduced neutron separation energies of nuclei with one neutron beyond a closed shell. To proceed toward higher neutron numbers, these nuclei must first undergo a series of $\beta$ decays. Nuclei located at magic numbers exhibit longer half-lives relative to neighboring isotopes, exerting a dominant influence on the overall $r$-process timescale. Regions near shell closures act as bottlenecks

where material accumulates, producing the abundance peaks observed in $r$-process distributions. These bottlenecks provide the necessary time for $\beta$ decay to occur with appreciable probability, enabling the system to overcome the waiting point. However, following a $\beta$ decay and a subsequent neutron capture, the system is again trapped at the shell closure, establishing another *waiting point*.

Experimental information on several nuclear properties is essential for abundance calculations [MSMA16, MCP+14]. For waiting-point nuclei, the key nuclear-structure properties include the decay half-life, the $Q_\beta$ value, the $S_n$ value, the nuclear masses, and $\beta$-decay rates. In addition, neutrons from $\beta$-delayed neutron emission ($\beta$n), which provide a delayed neutron flux and temperature cease in the stellar environment [MW85], also affect the abundance distribution. In Ref. [SMA15] it was concluded that the $P_n$ values and $\beta$-decay rates of Cd and In isotopes on the neutron-rich side of $^{132}$Sn have a significant impact on the final abundances. The experimental results obtained for the $\beta$ decay of $^{133}$In [PKF+19, XMG+23a] and $^{134,135}$In [PSKB+21], located southeast of $^{132}$Sn, provide a benchmark for theoretical developments aimed at describing the key $\beta$ decays in the $r$-process. In this work, $\beta$-decay half-lives and neutron emission probabilities have been measured for isotopes in the Cd $\beta$-decay chain.

## 2.6 Shell structure around $^{132}$Sn

Experimental studies of the isotopes located in the region surrounding doubly-magic nuclei such as $^{132}$Sn provide key information to test shell-model calculations. Fig. 2.7 depicts the segment of the nuclear chart studied during the IS685 and IS685_II experimental campaigns at ISOLDE.

The shell-model interpretation explains the double-shell closure at $^{132}$Sn ($N = 82$, $Z = 50$), as a result of the spin-orbit force shifting down the $\pi g_{9/2}$ $\nu h_{11/2}$ from their respective upper harmonic oscillator shells. Fig. 2.8 shows the experimental single-particle energies in the doubly magic nucleus $^{132}$Sn. The energies, are derived from binding energies [WHK+21] and the excitation energies for the single-particle states in $^{131}$Sn [OPA+18, BFK+24], $^{131}$In [TJG+14], $^{133}$Sb [SVFM+99] and $^{133}$Sn [JAB+10]. The single-particle energies are the main ingredients for the interpretation os the excited levels in the region. The structures of the low-lying states in the single-particle/hole nuclei $^{131}$Sn, $^{131}$In, $^{133}$Sb and $^{133}$Sn, can be assumed to be mostly pure single-particle configurations. Stringent tests for this interpretation are provided by lifetime measurements of these states. Lifetime measurements for $^{129}$Sn and $^{131}$Sn indicated a highly enhanced $l$-forbidden $B(M1)$ strength for the $\nu s_{1/2} \rightarrow \nu d_{3/2}$ [LMF+16, BFK+24], indicates a departure from the single-particle picture due to the core polarization. The low excitation energy of the $5/2^+_1$ state in $^{135}$Sb and an exceptionally low $B(M1; 5/2^+_1 \rightarrow 7/2^+_1)$ value reported in Ref. [KMB+05] suggested a relative shift of the proton $d_{5/2}$ and $g_{7/2}$ orbits due to the neutron excess. Furthermore, the $1/2^+$ state in $^{135}$Sb, measured in Ref. [MFA+07], yields a highly collective $B(E2; 1/2^+ \rightarrow 5/2^+)$ value. This collectivity is significantly larger than that of the $B(E2)$ value for the $2^+ \rightarrow 0^+$ transition in the core nucleus $^{134}$Sn, and is interpreted as arising mainly

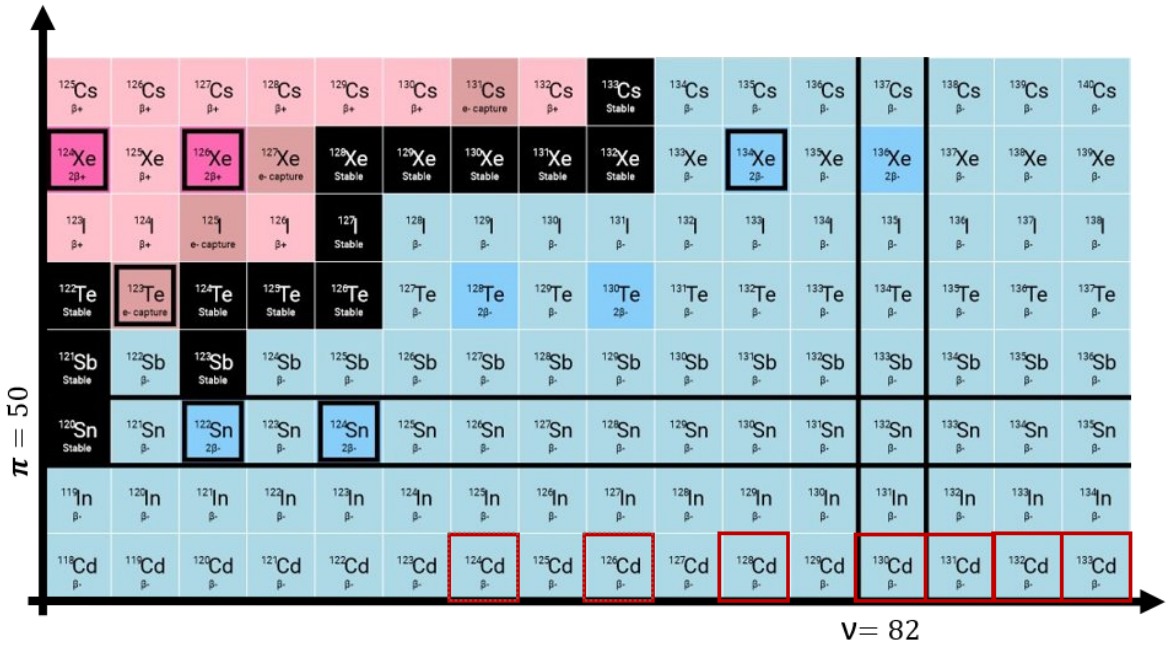


**Figure 2.7.** Segment of the nuclear chart in the vicinity of the doubly magic nucleus $^{132}$Sn. The red boxes indicate cadmium isotopes populated in the IS685 and IS685_II experimental campaigns. The black lines delimit the region defined by the neutron number $N = 82$ and proton number $Z = 50$. The figure was adapted from Ref. [Int25].

from the coupling of the $\pi d_{5/2}$ state to the collective core. Measurements of nuclear magnetic moments in the indium isotopic chain proved the quick departure from single-particle picture outside $N = 82$ [VGRM$^+$22].

The low lying structures of isotopes with an odd number of protons and neutrons neighboring $^{132}$Sn can be interpreted as multiplets arising from the coupling of unpaired protons and neutrons $^{132}$Sb ($\pi\nu^{-1}$) [KHCM72, SFW89], $^{134}$Sb ($\pi\nu$) [SWW$^+$05], $^{130}$In ($\pi^{-1}\nu^{-1}$) [JGN$^+$16] and $^{132}$In ($\pi^{-1}\nu$) [JGG$^+$16]. The identification of the states provides information on the two-body proton-neutron matrix elements. Due to the complex nature of the level-scheme in odd-odd nuclei, identification of the different multiplets is quite complex. Detailed experimental information such as lifetimes of excited states through measurement of $\gamma\gamma$ coincidences, provide valuable information to constrain the model interpretation. The experimental information is specially scarce for the more exotic indium isotopes (see Fig. 2.9). In particular for $^{132}$In where only tentative interpretations for its level-scheme has been provided [JGG$^+$16, Par23].

The excited states in even-even isotopes are dominated by the interaction of neutron and proton pairs. Determination of the $B(E2; J \to J-2)$ strengths along the yrast bands of these nuclei provide insight on the pairing and quadrupole interaction of neutrons and protons. The unexpected enhancement in the $B(E2; 6^+ \to 4^+)$ in $^{136}$Sn contradicted the expected reduction in the Seniority scheme [DTMW63]. This was interpreted as a hint of a reduced neutron pairing strength [SAG$^+$07]. Other theoretical studies, suggested that this result could be explained within a generalized multi-$j$ Seniority scheme [JM17] without the need of reducing the pairing strength.

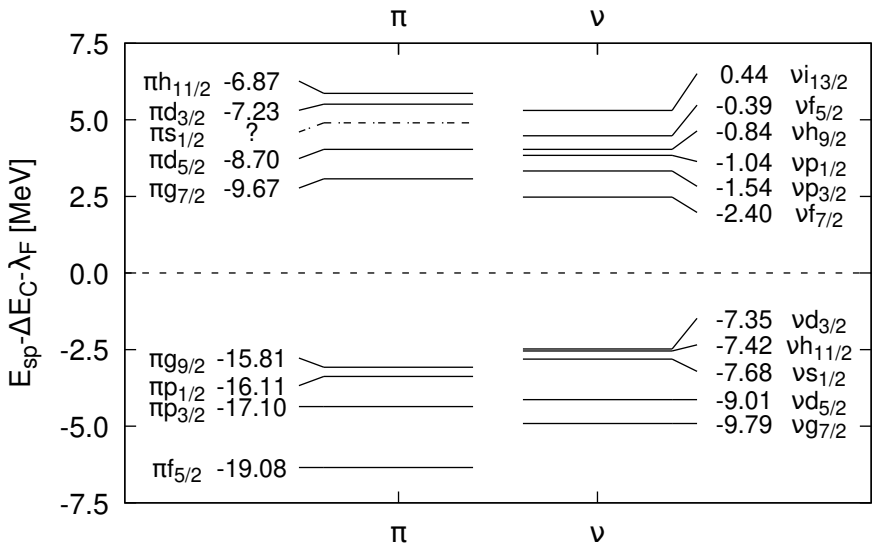


**Figure 2.8.** Experimental single-particle and single-hole energies for neutrons ($\nu$) and protons ($\pi$) in the doubly magic nucleus $^{132}$Sn. Following the prescription of Ref. [GLMP07], the energy scale is centered at the Fermi level ($\lambda_F$), effectively removing Coulomb energy shifts $\Delta E_C$ to enable a direct comparison between neutron and proton states. All energies are expressed in MeV. The energy level of the $\nu i_{13/2}$ orbital has been recently measured (2.83 MeV), as reported in Ref. [DGX+25].

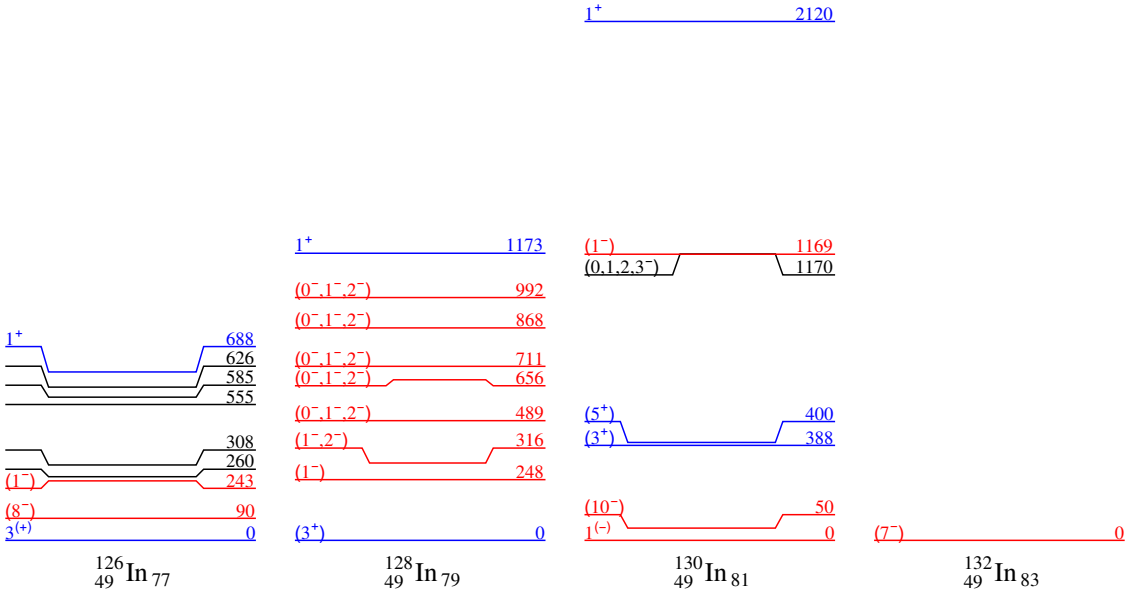


**Figure 2.9.** Energies of excited states in the odd-odd In isotopes. Positive-parity states are shown in blue and negative-parity states in red. States with unknown spin and parity are represented in black. Only states above the first $1^+$ excited state are shown. Data are taken from Ref. [NND25] and from Ref. [Ber18] for $^{128}$In.

However, these calculations failed to reproduce the enhanced $B(E2; 4^+ \rightarrow 2^+)$ in $^{134}$Sn [PS21]. Isospin dependency of protons and neutron charges was deduced from $B(E2)$ information in $^{134}$Sn and $^{130}$Cd [JGM+24]. Experimental $B(E2)$ values in $^{130,132}$Te hinted to the the influence of core-excitations [KBA+22]. Beyond $N = 82$,

a sudden enhancement in $B(E2; 2^+ \rightarrow 0^+)$ suggest a sudden onset of collectivity [VJD+19, AJA+25], while the $B(E2)$ determined for higher spin states indicate that the collective behavior is decreased [HLN+21]. Experimental information on the $B(E2)$ strengths for tin isotopes bellow $^{132}$Sn are still scarce.

At higher excitation energies, $\approx 4$ MeV, it becomes possible to excite the $^{132}$Sn core by means of cross-shell excitations [BDGE+80, BDZ+01, FHJ+94, BFK+20, WAG+20]. These excitations of the core can be well understood in terms of particle-hole (p-h) excitation of either neutrons or protons. High-energy core-excited levels can be found in all the surrounding single-particle/hole neighbors which can be interpreted as the coupling of that single-particle with the particle-hole excitations [SVFM+99, TJG+16, PKF+19, BFK+24]. These levels govern the high-energy excitation of these nuclei, playing a major role in the $\beta$-decay of isotopes, especially in the region south-east of $^{132}$Sn, where the strong GT $\nu g_{7/2} \rightarrow \pi g_{9/2}$ transitions dominate the spectra populating high-energy core-excited states. Theoretical description of these nuclei by means of shell model calculations is still challenging. Calculations involving large valence spaces for both neutrons and protons are starting to become feasible [DS21]. Experimental information on the energy of these p-h multiplets as well as information on lifetimes of excited states are crucial to test these calculations.

Information on $\beta$-decay patterns provide also stringent tests for nuclear shell models. In particular, precise half-life values along with $\beta$-decay feeding patterns derived from high-resolution $\gamma$-ray experiments, allow the determination of $\log ft$ values, which are especially sensitive to the wave functions of the involved states. Precise determination of single particle GT and (first-forbidden) FF transitions provide benchmarks for $\beta$-decay shell model calculations [XMG+23a, XMG+23b, BFK+24, PKF+19]. The presence of high-$l$ orbitals at low energy leads to multiple $\beta$-decaying states within the same isotope in the $^{132}$Sn region. High-resolution $\beta$-decay experiments with sufficient capability are essential to disentangle the $\beta$-decay patterns of the different $\beta$-decaying states.

To summarize, detailed data on excitation energies, lifetimes of excited levels as well as $\beta$-decay feeding patterns are essential to provide a comprehensive description of the nuclear structure. Experimental information is rather scarce bellow the $Z = 50$ line. The main objective of this work is to expand the experimental information in the region close to $^{132}$Sn. A systematic study of $\beta$-decay of Cd isotopes has been performed up to $^{133}$Cd at the ISOLDE facility. Expanded level-schemes are provided, along with new sub-nanosecond lifetimes measurements derived by means of fast-timing methods.

# Chapter 3

# Production of exotic Cd isotopes at ISOLDE

This chapter presents an overview of the role of the ISOLDE facility in producing high-purity Cd beams, which were essential for the nuclear structure study reported in this work, carried out during the IS685 and IS685_II experimental campaigns. The production process involves advanced techniques such as the resonance ionization laser ion source (RILIS) and a temperature-controlled quartz transfer line to ensure isotopic purity by selectively Cd isotopes and separating them from contaminants. These methods allow for the production of high-purity Cd beams. Specifically the most exotic Cd isotopes.

Chap. 3 is structured as follows. Sec. 3.1 provides an overview of the ISOLDE facility, detailing the production of high-purity Cd beams. Sec. 3.2 summarizes the yield measurements for Cd isotopes and their isobaric contaminants, highlighting the improvements observed between the IS685 and IS685_II campaigns. Finally, the main conclusions of Chap. 3 are summarized in Sec. 3.3.

## 3.1 ISOLDE facility: Production and transport to the experimental station

The high-purity cadmium (Cd) beams were produced at the ISOLDE facility, one of the most historic and scientifically productive facility within the European Organization for Nuclear Research (CERN) complex. Established in the 1960s, ISOLDE has played a pivotal role in nuclear physics research. The production process begins by removing electrons from hydrogen atoms using an electric field, generating proton beams. These proton beams are then injected into a linear accelerator Linac-4, where they are accelerated to 50 MeV. The are injected into the Proton Synchrotron Booster (PSB), reaching energies of 1.4 GeV. The protons are send in pulses of 2.4 $\mu$s length which are emitted every 1.2 s with a high intensity up to $3.6 \times 10^{13}$ protons/pulse. These pulses are grouped in supercycles, which contain a variable number of pulses between 30 and 50. The accelerated proton beam is subsequently directed to the ISOLDE facility, where it is utilized for producing the high-purity Cd beams. The ac-

celerators used in the IS685 and IS685_II experimental campaigns are shown in Fig. 3.1.

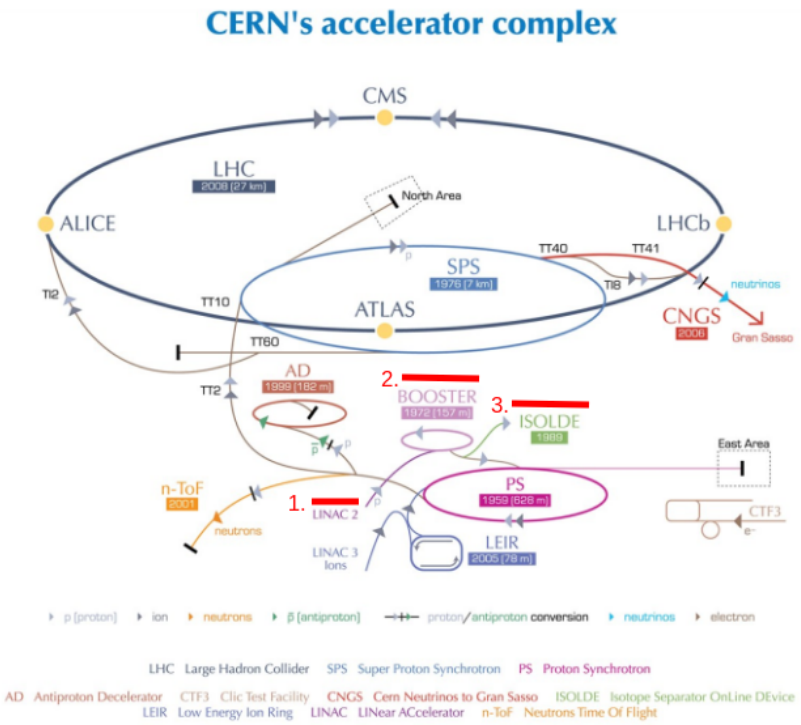


**Figure 3.1.** Schematic representation of CERN accelerator complex. Proton beam acceleration steps through the accelerators are indicated in red. The schematic was adapted from Ref. [CER25a].

A fundamental key for the success of the present experimental campaign was the availability of high-intensity and high-purity radioactive cadmium (Cd) beams. The first essential component was the use of a composite uranium-carbide/graphite ($UC_x$) target, installed in a dedicated target unit equipped with a neutron converter. In the IS685 and IS685_II experimental campaigns, ISOLDE target units #756 and #759, respectively. The high-energy proton pulses hit onto the neutron converter material. The neutron converter acts as a source of spallation neutrons when bombarded by the proton beam. This method offers a significant advantage over direct proton-induced reactions on the $UC_x$ target, as the neutron-induced fission pathway leads to a more favorable isotope yield distribution for neutron-rich nuclei and simultaneously suppresses the production of neutron-deficient isobaric contaminants, such as Cs isotopes [KTG+05]. This approach is particularly important when studying neutron rich exotic isotopes like Cd, where the isobaric separation from nearby Cs isotopes would otherwise be a major experimental challenge. The target is heated to temperatures up to T $\approx$ 2000 °C, which allows the isotopes to be thermally diffused into the temperature-controlled transfer line, which operates at T $\approx$ 2040 °C. To mitigate the risk of voltage breakdown, the voltage supply is switched off approximately 35 $\mu$s before the proton pulse arrival and is turned back on about 5 ms later.

The second key element in the beam purification chain is the implementation of a

temperature-controlled transfer line between the target and the ion source, operating at a temperature of T ≈ 520 °C (see Fig. 3.2). This component plays the role of a chemical filter, exploiting differences in volatility among the elements produced in the target. The system consists of a quartz tube that is maintained at specific temperatures such that elements with lower volatility, including many of the alkali metals, are retained or delayed in their transport, while more volatile species, such as Zn, Hg, and most importantly Cd, are allowed to pass through to the ion source. This differential transport behavior is critical for enhancing the chemical selectivity of the system. In particular, the suppression of alkali elements like Cs is of central importance, as these elements are otherwise produced in large quantities during the fission process and can lead to significant background. The quartz line thus acts as a passive yet highly effective method of purification, as demonstrated in several previous studies on neutron-rich isotope production [KGM+91, BCE+07, KTG+05].

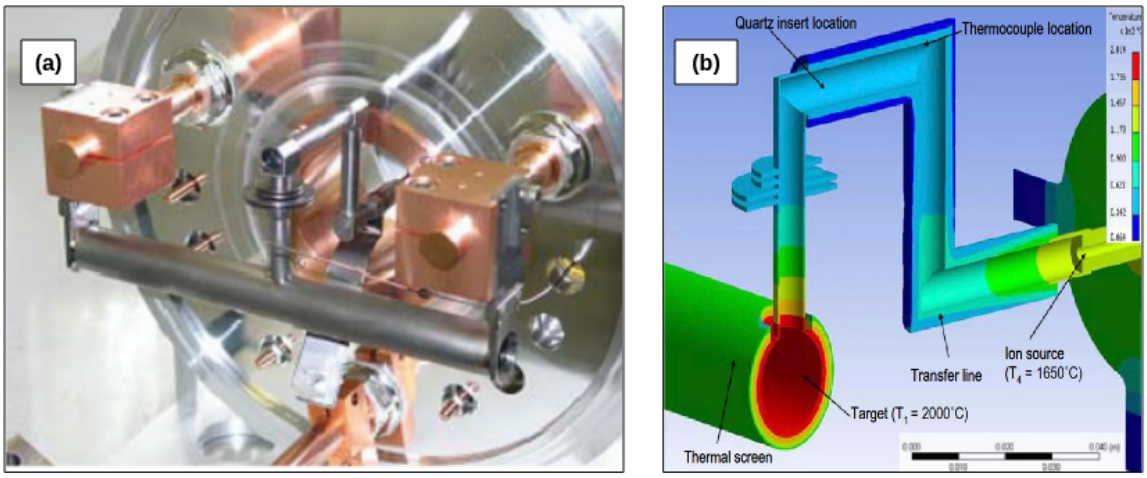


**Figure 3.2.** **(a)** Quartz transfer line linking to the tantalum oven, the ISOLDE target and the ion source. **(b)** Temperature profile through the transfer line. Images taken of Ref. [BCE+07].

The third pillar of the purification strategy is the use of the RILIS system, a laser-based ionization system that provides element-selective and, under certain conditions, even isomer-selective ionization. In the case of Cd, RILIS is configured to tune the laser wavelengths to the resonant atomic transitions of cadmium atoms, resulting in highly efficient ionization of Cd while leaving non-resonant elements largely unaffected [FCG+17]. RILIS provides fast and selective ionization of many metallic elements with high efficiency, offering both isotopic and isomeric selectivity by exploiting the distinct hyperfine splitting of nuclear states with different angular momenta. Three adjustable dye lasers and three tunable Ti:Sa(Titanium:Sapphire) lasers, all of which are Nd:YAG pumped, make up the entire setup, which also includes optical components for laser beam focussing. RILIS operates in the 210–950 nm wavelength range. The ionization scheme for Cd consisted of three steps (see Fig. 3.3). The wavelength of each laser is set to match the energy required for sequential electron transitions necessary to ionize the atom. The electrons generated from the hot metallic surface of the cavity create a negative potential that confines the atoms

for the necessary duration to allow ionization. Additionally, on the heated surface, thermal ionization can occur for atoms with low ionization potentials, due to the high temperatures.

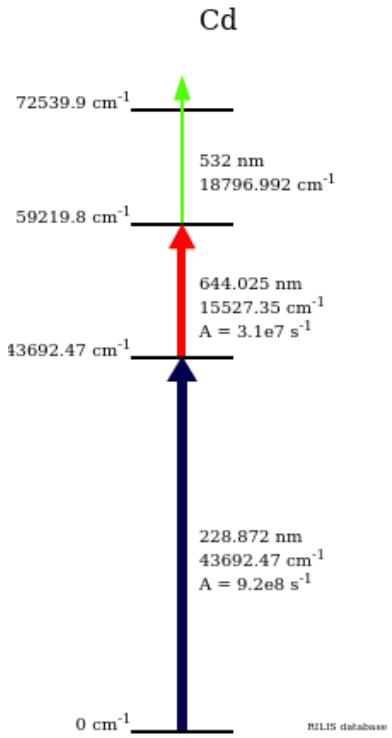


**Figure 3.3.** Diagram showing RILIS ionization process for Cd. Image taken of Ref. [CER25b].

A 60 kV acceleration gap extracts the ionized isotopes from the ion source into the beam line (see Fig. 3.5). Dry air is constantly circulating into the acceleration gap to stop sparks and nitric acid from forming. An electrostatic deflector of 4.5 kV, which acts as the beam gate, controls the transmission of ions to the beam line. When the pulses of protons arrive, the beam gate is closed in order to prevent the experimental area being saturated by background nuclei immediately ejected from the target material. This delay can be adjusted. After that, the beam gate is open according to the target release curve of the Cd isotope produced (more details in Sec. 3.2).

The extracted ion beam was accelerated to the ISOLDE mass separators. The Cd isotopes were separated according to the mass-to-charge (A/q) ratio. There are two mass separators, the High Resolution Separator (HRS) and the General Purpose Separator (GPS). In both experimental campaigns, the GPS was employed to select Cd beams (see Fig. 3.4). GPS features a $70^o$ double focus magnet with a mean radius curvature of 1.5 meters, which enables the simultaneous selection of three ion beams within a mass range of 15% from the center mass and their simultaneous channeling to three distinct experimental sites. Separator settings for a specific A/Q ratio are sometimes referred to as the settings for the given mass (A). This is because most ions are singly charged. More details about GPS and HRS in Ref. [Kug00].

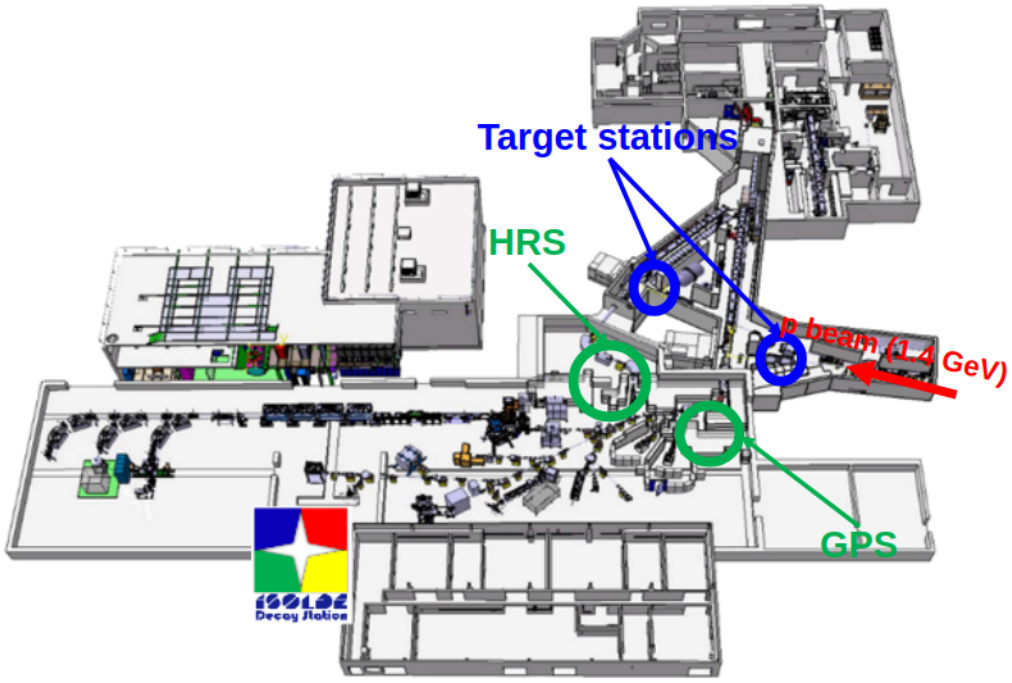


**Figure 3.4.** Layout of the ISOLDE facility. The schematic was adapted from Ref. [ISO25].

The final step is transporting the beam to the experimental station. Along every beam line, there is a set of diagnostic elements composed of wire grids, moving wire scanners, and several Faraday cups to monitor and control the beam characteristics. The user may adjust and fine-tune the beam intensity for their particular experiment in this way. Magnetic quadrupoles are used to focus the beam, while electric dipoles are used to deflect the beam towards the different beam lines. The aim is to have 100% transmission up to the area where the IDS is located (see Fig. 3.4). The transmission efficiency was 94% during the IS685 experimental campaign and 96% during the IS685_II campaign.

The combined effect of neutron-induced fission, chemically selective transport, and laser-based ionization results in a beam of exceptional purity and isotopic selectivity, ideally suited for precision decay spectroscopy and nuclear structure studies of exotic Cd and In isotopes.

## 3.2 High-purity beams of neutron-rich Cd isotopes at ISOLDE

The yields of the individual isotopes were determined from the measured $\gamma$-ray spectra by identifying characteristic transitions associated with the decay of Cd isotopes. The measurements were carried out using the high-sensitivity IDS setup, employing six Clover HPGe detectors during the IS685 experimental campaign and four Clover HPGe detectors during the IS685_II experimental campaign (more details in Sec. 4.1).

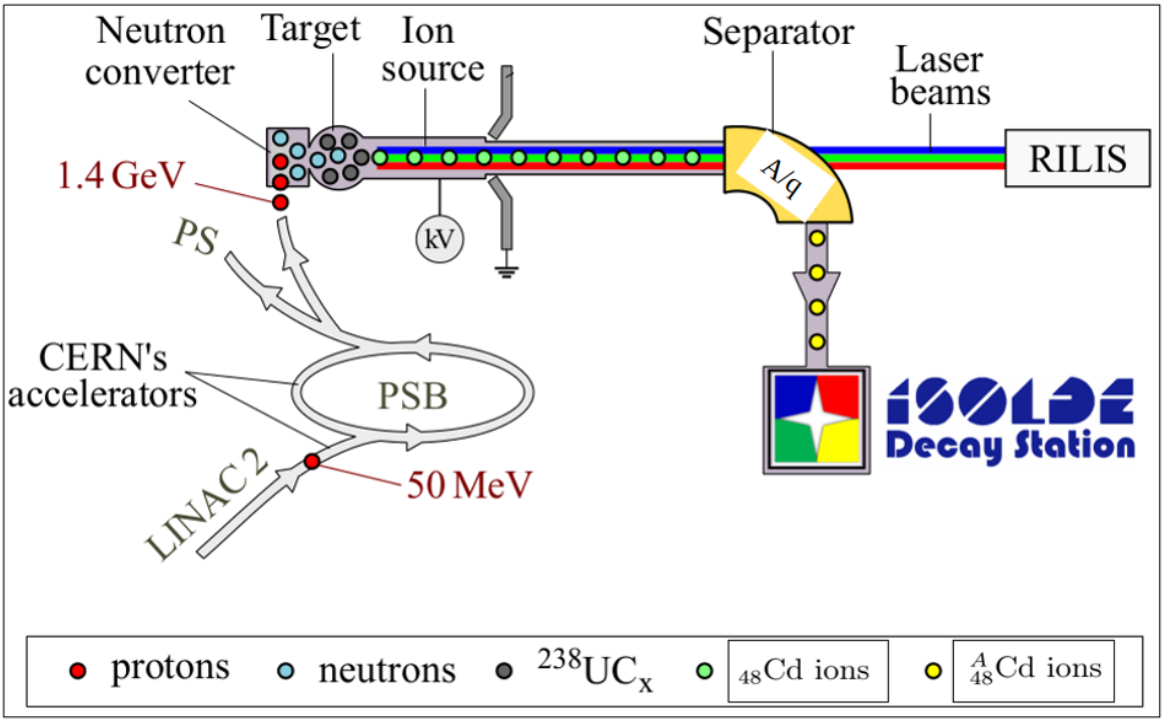


**Figure 3.5.** Diagram showing the mass separation, resonant ionization process, and target ion-source system at ISOLDE. The drawing was prepared following Ref. [PS21].

These yields were extracted using the corresponding $\gamma$-ray branching ratios reported in previous experimental studies [Ber18, BFK$^+$24, BBG$^+$16, GH78, JGN$^+$16]. The decays of $^{128,132,133}$Cd were specifically investigated in the present work.

A correction for the transmission efficiency from the ISOLDE target station to the IDS focal point was applied. Additionally, a correction due to the release fraction from the target was also taken into account, based on data from previous yield evaluation measurements [ISO21]. The release curve is the time-dependent ion-beam intensity after a proton impact on the target, reflecting the diffusion processes that govern the fraction of produced isotopes extracted from the target–ion source system. The ion-beam intensity as a function of time since the last proton impact on the target is represented in Fig. 3.6. It can vary significantly depending on the chemical properties of the target composition and the operational temperature of the target-ion source system. This curve plays a crucial role in the development and characterization of the targets employed at ISOLDE. In general, it is challenging to derive an analytical expression that accurately describes the diffusion of isotopes produced within the target material. This difficulty arises from the presence of numerous boundary conditions, the inherently complex nature of the diffusion processes—often occurring under varying thermal gradients—and the limited knowledge of the relevant diffusion coefficients and potential energy barriers.

Fig. 3.7 shows the $\gamma$-ray spectra for mass number $A = 128$ from the IS685 experimental campaign, while Fig. 3.8 presents the $\beta$-gated $\gamma$-ray energy spectrum

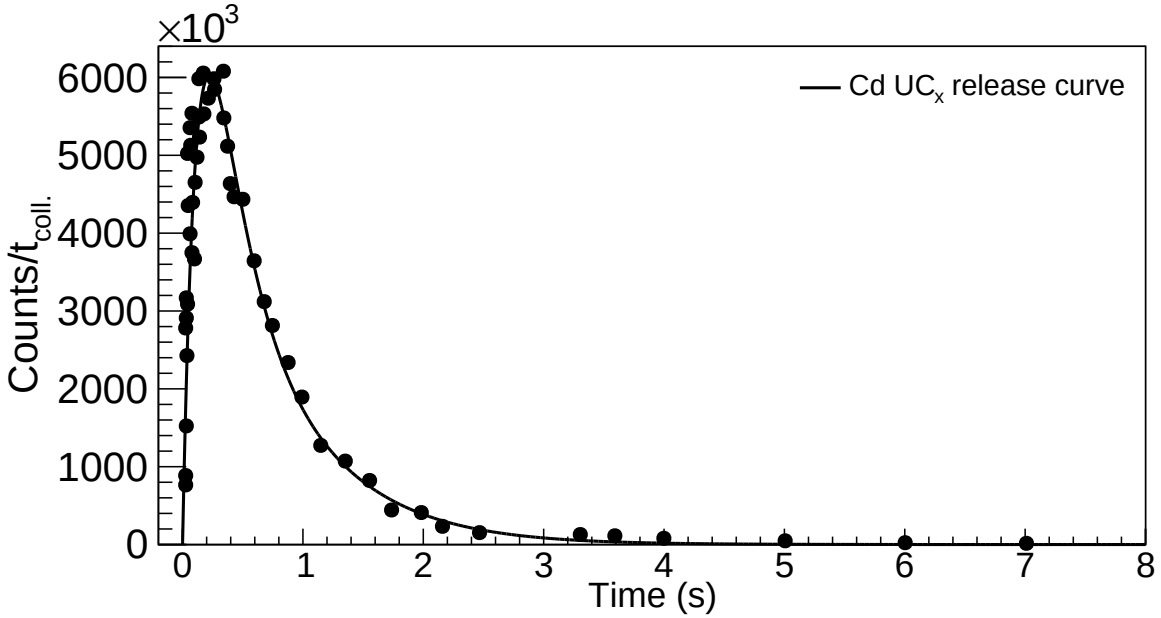


**Figure 3.6.** Release curve of $^{124}$Cd fitted to the experimental data using the equation proposed in Ref. [LCD$^+$97]. The fit parameters were taken from Ref. [ISO21] and corrected for the half-life of $^{124}$Cd [NND25].

for mass numbers $A = 130$ and $A = 131$ from the IS685_II experimental campaign. These spectra were obtained, both with and without RILIS ionization, for both experimental campaigns. Although Cd isotopes are selectively ionized via RILIS, surface-ionized contaminants may still be present if they are not significantly delayed by the quartz transfer line. To assess the yields of Cs and In at these mass numbers, measurements were also conducted with the RILIS system blocked. The resulting yields are summarized in Tab. 3.1. Detection limits are reported at the $1\sigma$ level, based on the background observed at the relevant $\gamma$-ray energies. In measurements where RILIS was active, the observed In activity is consistent with the $\beta$-decay of the corresponding Cd isotopes. As can be observed in the tables, the yields for mass $A = 130$ show a significant improvement of the production rate in the second experimental campaign (IS685_II) compared to the first.

Fig. 3.9 displays the production yields of cadmium isotopes with mass numbers $A = 124$ to $A = 133$, as measured for both experimental campaign. The results for $A = 124$ to $A = 130$ are compared with previously reported yields in Ref. [ISO21], while those for $A = 131$ to $A = 133$ are compared with the estimations given in Ref. [FBL$^+$20]. Although the total production yield is generally lower, the resulting isotopic purity is significantly enhanced, allowing for cleaner spectroscopic studies and reduced background from contaminant isotopes. These findings provide a solid foundation for subsequent spectroscopic analysis. A detailed discussion of the data analysis and the physics results extracted from these measurements is presented in the following chapters.

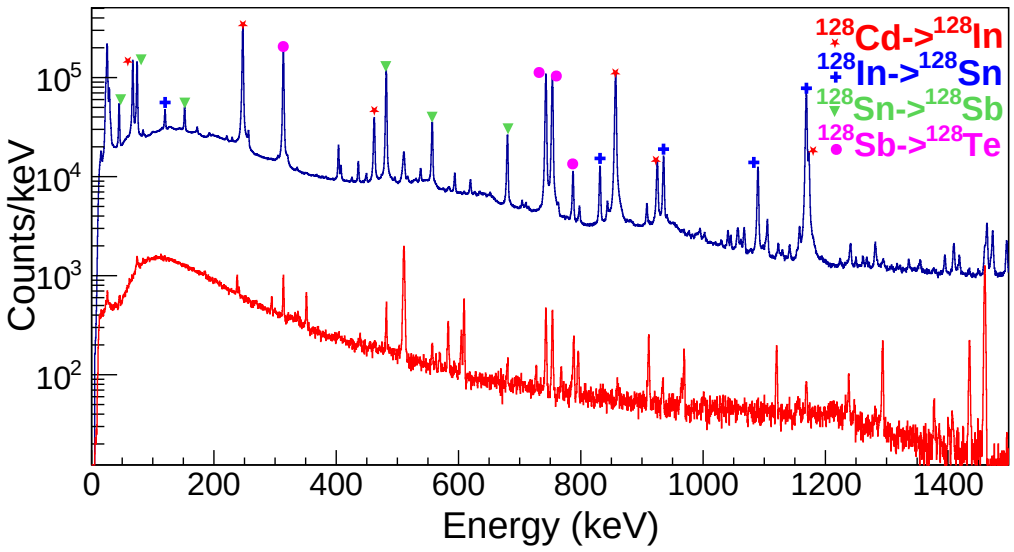


**Figure 3.7.** $\gamma$-ray spectra obtained in a saturation mode for mass $A = 128$ with (blue) and without (red) laser ionization in the IS685 experimental campaign. Data sets were collected for the same amount of time. The strongest peaks associated with the $\beta$ decay of $^{128}$Cd are identified and labeled.

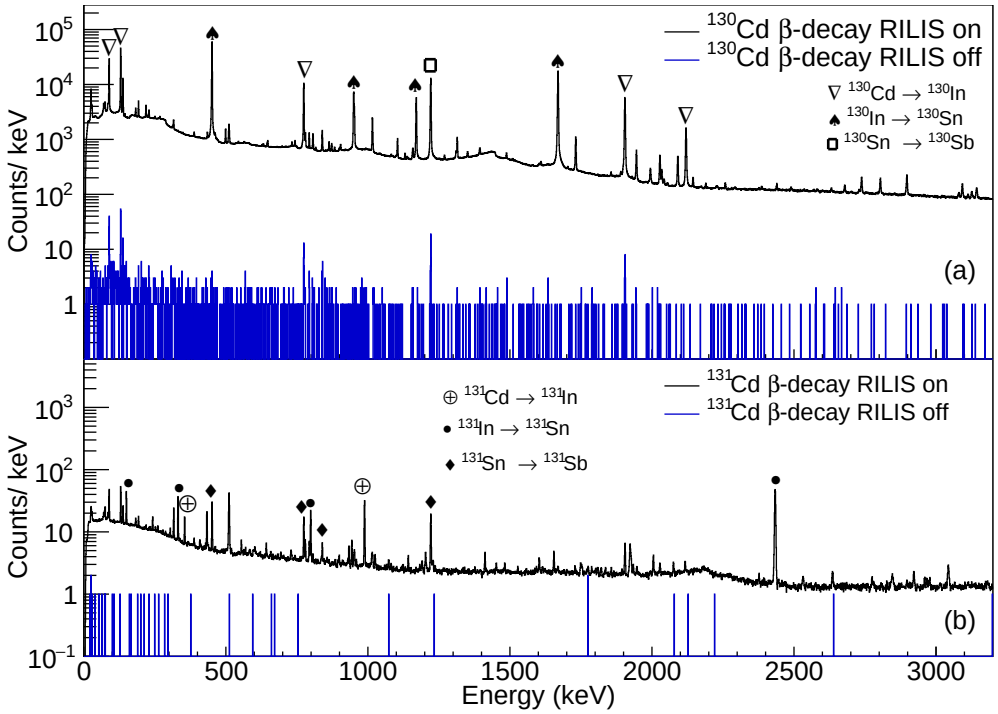


**Figure 3.8.** **(a)** Beta-gated $\gamma$-ray energy spectrum recorded following the decay of $^{130}$Cd limited to 400 ms after the proton impact to reduce $\beta$ decay activity. The black spectrum corresponds to RILIS ionization of Cd, while the blue spectrum was obtained without RILIS. The RILIS-on spectrum has been downscaled to match the proton intensity and running time of the RILIS-off one. **(b)** Beta-gated $\gamma$-ray energy spectrum recorded following the decay of $^{131}$Cd using the same procedures. The strongest peaks associated with the $\beta$ decay of $^{130}$Cd and $^{131}$Cd are identified and labeled. (Data are taken of IS685_II experimental campaign.)

**Table 3.1.** Measured yields for Cd isotopes and possible isobaric contaminants released from the $UC_x$ target with a quartz transfer line, for both IS685 and IS685_II experimental campaigns, with and without resonant ionization (RILIS). Energies and intensities are taken from Ref. [NND25].

| Isotope | Energy (keV) | $I_\gamma$ (%) | Yield (RILIS on) [ions/$\mu$C] | Yield (RILIS off) [ions/$\mu$C] | Campaign |
|---|---|---|---|---|---|
| $^{124}$Cd | 143 | 18(3) | $1.39(11)\times10^5$ | $\leq 1.1\times10^2$ | IS685 |
| | 180 | 70(11) | | | |
| $^{124}$In | 1132 | 100(14) | — | $\leq 2.3\times10^2\times10^2$ | IS685 |
| $^{124}$Cs | 354 | 47(6) | $\leq 9$ | $\leq 1.2\times10^2$ | IS685 |
| $^{126}$Cd | 260 | 87(5) | $3.0(2)\times10^4$ | $\leq 3$ | IS685 |
| | 428 | 73(3) | | | |
| $^{126}$In | 1141 | 100(7) | — | $\leq 20$ | IS685 |
| $^{126}$Cs | 818 | 99.70(10) | $\leq 6$ | $\leq 5$ | IS685 |
| $^{128}$Cd | 857[a] | 71(5)[a] | $1.59(13)\times10^4$ | $\leq 0.4$ | IS685 |
| | 925[a] | 8(1)[a] | | | |
| $^{128}$In | 832[b] | 6(1)[b] | — | $\leq 38$ | IS685 |
| | 935[b] | 9(1)[b] | | | |
| $^{128}$Cs | 443 | 27(1) | $\leq 5$ | $\leq 1$ | IS685 |
| $^{130}$Cd | 451 | 53(4) | $7.3(5)\times10^2$ / $3.6(2)\times10^3$ | $\leq 0.7$ / — | IS685 / IS685_II |
| | 1170 | 11(1) | | | |
| | 1669 | 53(3) | | | |
| $^{130}$In | 89 | 40(8) | — / — | $\leq 3$ / 0.92(7) | IS685 / IS685_II |
| | 130 | 65(5) | | | |
| | 138 | 20(3) | | | |
| | 774 | 54(6) | | | |
| | 1221 | 64(7) | | | |
| | 1905 | 79(9) | | | |
| $^{130}$Cs | 1121 | 40(8) | $\leq 7$ / $\leq 7$ | $\leq 9$ / — | IS685 / IS685_II |
| $^{131}$Cd | 987 | 9(2) | $1.06(3)\times10^2$ | — | IS685_II |
| | 2004 | 2.0(5) | | | |
| | 3555 | 9(1) | | | |
| $^{131}$In | | | — | — | IS685_II |
| $^{131}$Cs | 364 | 40(8) | $\leq 0.1$ | — | IS685_II |
| $^{132}$Cd | 331 | 42(12) | 4.7(4) | — | IS685_II |
| | 2434 | 65(11) | | | |
| | 374 | 54(44) | | | |
| | 299 | 44(6) | | | |
| | 478 | 23(6) | | | |
| $^{133}$Cd | 50[a] | 86(7)[a,c] | 0.16(2) | — | IS685_II |

[a] Value adopted in this work.
[b] Value taken from Ref. [Ber18]. See text for details.
[c] Value derived from the $P_{2n}(\%)$ reported in Ref. [PNL+22].

## 3.3 Conclusions of the chapter

The production yields of neutron-rich cadmium isotopes with mass numbers $A$ = 124–133 have been determined from $\gamma$-ray spectroscopy following their $\beta$ decay, using established branching ratios for the relevant transitions. Corrections were applied for the IDS transmission efficiency and for the release fraction of the isotopes from the target. Measurements from the IS685 and IS685_II campaigns demonstrate that the use of a neutron converter, a quartz transfer line, and selective laser ionization with the RILIS technique effectively suppresses isobaric contaminants and improves isotopic selectivity. A significant enhancement of the $^{130}$Cd production rate was achieved in the second campaign, enabling the observation of very low-yield isotopes, including $^{131,132,133}$Cd. Although the yields are in some isotopes lower than previous ISOLDE data, the enhanced purity obtained in this work provides conditions for high-resolution $\gamma$ spectroscopic studies of neutron-rich Cd isotopes. Under the present experimental conditions, no Cs contamination was detected, and In was suppressed by more than

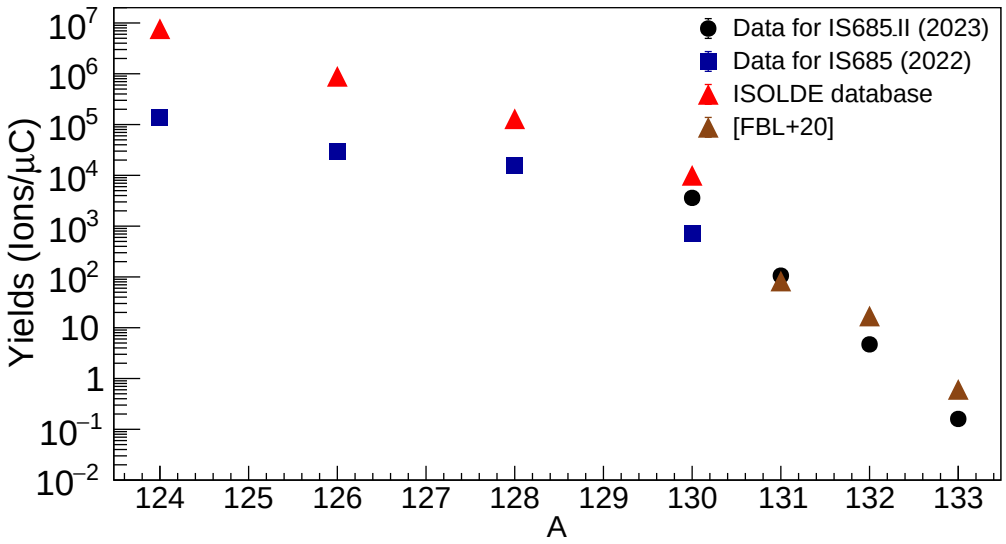


**Figure 3.9.** Comparison of the measured cadmium isotope yields from the IS685 and IS685_II experimental campaigns with previously reported data. Reference values taken from Ref. [ISO21, FBL$^+$20].

three orders of magnitude relative to cadmium.

# Chapter 4

# Experimental set-up and analysis methodologies

The study of neutron-rich nuclei populated via $\beta$ decay benefits from the combined use of high-resolution $\gamma$-ray spectroscopy and ultra-fast timing techniques to obtain detailed information on nuclear structure. HPGe detectors provide precise determination of $\gamma$-ray energies and intensities, enabling the investigation of level schemes and the estimation of $\beta$-decay feeding patterns. Coincidence techniques, such as $\gamma\gamma$ and $\beta\gamma$ spectroscopy, enhance the selectivity of the measurement, allowing the identification of cascade transitions, placement of states, and discrimination against background. Accurate energy and efficiency calibrations are required to convert measured spectra into physical observables such as absolute intensities or transition probabilities.

The chapter details the experimental setup at the IDS, which includes a combination of high-resolution detectors and fast-timing systems optimized for studying the decay properties of cadmium isotopes. The setup combines HPGe clover detectors for gamma-ray spectroscopy, $LaBr_3$(Ce) detectors and $\beta$-detectors for fast-timing measurements.

Ultra-fast timing methods provide access to the mean lifetimes of excited states, which are necessary to extract reduced transition probabilities and characterize electromagnetic transition rates. In particular, the Advanced Time-Delayed $\beta\gamma\gamma$(t) method (ATD), based on time-coincidence measurements between fast scintillators and $\beta$ detectors, allows for the extraction of lifetimes in the 10 picoseconds to nanosecond range. This chapter also presents the methodology used during the IS685 and IS685_II experiments, including the treatment of detector response, energy-dependent time-walk effects, calibration procedures, and the analysis strategies employed for both $\beta\gamma$(t) and $\gamma\gamma$(t) time spectra.

Chap. 4 is structured as follows. The experimental setup is described in Sec. 4.1, including the high-resolution detectors and fast-timing systems employed for studying the decay properties of cadmium isotopes. The data acquisition system and electronic setup are detailed in Sec. 4.2, outlining how the timing and energy signals are processed. Sec. 4.3 explains the methods used for data analysis, focusing on gamma-ray

spectroscopy and lifetime measurements. Secs. 4.4 and 4.5 present the procedures for energy and efficiency calibrations of HPGe and $LaBr_3$(Ce) detectors. The methodologies of $\beta\gamma$(t) and $\gamma\gamma$(t) analysis and background subtraction is presented in Sec. 4.6. The calibration and correction procedures required for accurate timing measurements, including TAC calibration, $\beta$-walk, and FEP-walk curves, are discussed in Sec. 4.7. Finally, a summary of the main points of this chapter is provided in Sec. 4.8.

# 4.1 The ISOLDE decay station (IDS)

The IDS primarily consists of a core featuring HPGe detectors for high-resolution $\gamma$-ray spectroscopy. Depending on the specific experiment, a range of additional detectors can be integrated into the set-up. This work focuses specifically on the fast-timing configuration for lifetime measurements. The experimental set-up will be explained in detail in the following sections. This setup includes the addition of $LaBr_3$(Ce) and fast temporal response $\beta$-detectors [Fra17, LMF$^+$16].

## 4.1.1 Detectors details

An array of 6 HPGe clover detectors was employed at the IDS for the IS685 experimental campaign, while 4 HPGe clover detectors for IS685_II experimental campaign. Additionally, three $\beta$ detectors were positioned around the implantation point in the tape. The setup included two SiPM $\beta$ detectors, a 3-mm-thick NE111A plastic scintillator for ultrafast measurements, and two $LaBr_3$(Ce) crystals shaped as truncated cones, coupled to fast PMTs, arranged in a compact geometry for fast-timing measurements. The experimental setup, indicating the position of the detectors, is shown in Fig. 4.1.

The IDS has **6 HPGe clover Canberra EUROGAM CLOVER** type detectors [DBT$^+$99]. Two of the HPGe clovers have a carbon composite window at the entrance providing transmission to below 10 keV. The remaining four detectors have an aluminum window designed to block low-energy $\beta$ particles, although this configuration results in reduced detection capabilities for energies below 30 keV. The 4 HPGe crystals in each clover detector are allocated in a cryostat that is automatically cooled by a Liquid Nitrogen ($LN_2$) cooling system every 12 hours, ensuring the optimum operating temperature for each crystal. The size of the detector are $\sim$ 70 mm long and $\sim$ 50 mm of the diameter. These detectors also show excellent energy resolution, having a 2.01(2) keV of FWHM for the 1332-keV peak of $^{60}$Co.

The **$LaBr_3$(Ce) scintillators detectors** employed in this work exhibit an energy resolution of $\approx$ 3% at 662 keV and a time resolution of 254 ps at $\approx$ 1 MeV, with $\gamma$ detection efficiency of $\approx$ 0.7% at 1 MeV. The crystals have the shape of truncated cones, with a height of 1 inch, and base diameters of 1.5 inches and 1 inch. The crystal is hermetically sealed within an aluminum housing featuring a thin entrance window and a glass light guide on the coupling side. Inside the housing, multiple layers of reflective and shock-absorbing materials are included to ensure mechan-

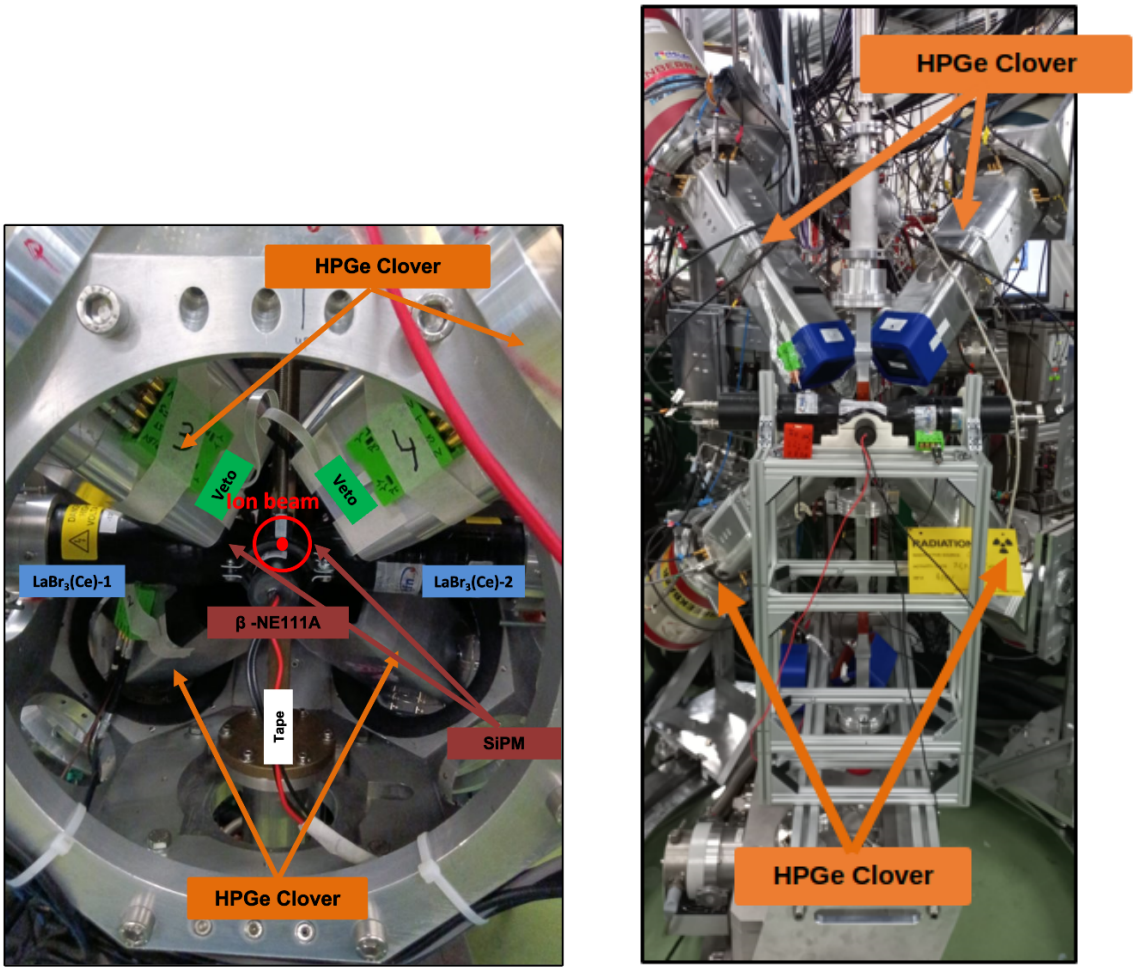


**Figure 4.1.** IDS set-up used in the IS685 experimental campaign (left) and IDS set-up used in the IS685_II experimental (right).

ical stability and minimize photon losses. The scintillators are coupled to 2-inch Hamamatsu R9779 photomultiplier tubes (PMTs) with 8 dynode stages [FMV+13]. This configuration was selected based on extensive optimization studies reported in Refs. [VMF+15, VCGF+17, VMF+15]. In the experimental setup, the two $LaBr_3(Ce)$ detectors were placed at an angle of 80° with respect to the beam axis, avoiding direct face-to-face alignment in order to reduce $\gamma$-ray backscattering.

The **three** $\beta$ **detectors** were positioned around the implantation point on the tape, achieving a combined $\beta$ detection efficiency of 44(2)%. Two of the detectors were EJ-232Q plastic scintillators with dimensions of $6 \times 6 \times 3$ mm$^3$, each coupled to a MICROFJ-SMA-30035-GEVB silicon photomultiplier from Onsemi (formerly SensL). The third detector consisted of an ultrafast EJ-232 cylindrical plastic scintillator, 3 mm thick and 25 mm in diameter, coupled to a fast Hamamatsu H6610 (R5320) photomultiplier tube.

In some cases, plastic detectors were also placed in front of the HPGe detectors to veto high-energy $\beta$ particles. These detectors are strategically placed in front

of the HPGe clover detectors to identify and reject events in which high-energy $\beta$ particles escape the main detection volume and could lead to spurious coincidences or background contributions. Each veto detector employs a SiPM array based on the MicroFJ-60035-TSV-TR1, J-Type series, manufactured by ONSEMI (formerly SensL). The SiPMs are configured into custom $3 \times 3$ arrays, with each individual cell measuring $6 \times 6, \mathrm{mm}^2$. The plastic scintillator utilized in conjunction with the SiPM array is the ELJEN EJ-200, chosen for its favorable scintillation characteristics and vacuum compatibility. The scintillator dimensions are $87 \times 87 \times 3$ mm$^3$. The selected scintillator thickness minimizes sensitivity to incident $\gamma$-rays while preserving high detection efficiency for $\beta$ particles within the high energy range. Further technical specifications of the VETO system and its integration can be found in Ref. [NLP+22].

## 4.2 Electronics

The signal treatment is independent and different for each detector on the experimental set-up. The electronic chain is divided into two branches: one for energy processing and another for timing extraction from the scintillators.

For the **energy branch** the positive dynode (DY) signal of the PMTs was pre-processed by an integrated preamplifier and sent to the XIA Pixie16 data acquisition system (DAQ) to digitize all the detector signals. The same procedure was performed for the 24 or 16 HPGe-clover detectors signals depending on the experimental campaign.

For the **timing branch**, fast-timing signals were extracted from the negative anode outputs (SIG) of the PMTs for pre-processing using analog modules. These fast signals cannot be directly digitized by the data acquisition system (DAQ) due to the limited sampling rate. The primary objective of the timing branch is to measure the time differences between pairs of scintillator detectors. All timing signals were processed using ORTEC 935 Quad Constant Fraction Discriminators (CFDs), with appropriate delay adjustments applied for both the $LaBr_3$(Ce) and $\beta$ detectors. The CFD parameters including the zero-crossing (Z), threshold (T), and external delay values were optimized in order to have an optimal time response at the expense of a long time walk. These parameters are summarized in Fig. 4.2. From each detector, two signals were extracted from the CFD output. Time differences between signals were converted into amplitude signals using three ORTEC 567 Time-to-Amplitude Converter (TAC) modules, each operating at 200 MHz. When a pair of signals arrives within the defined coincidence window, the TAC produces a voltage pulse with amplitude proportional to the time interval between the START and STOP signals. The voltage begins to rise upon arrival of the START signal and stops once the STOP signal is received. In the IS685_II experimental campaign, three TACs were used: two to measure the time difference between the $\beta$ PMT detector and each of the $LaBr_3$(Ce) detectors, and one to measure coincidences between the two $LaBr_3$(Ce) detectors. Delays for both input and output connections to the TACs were adjusted to position the prompt timing peak optimally within the TAC output range.

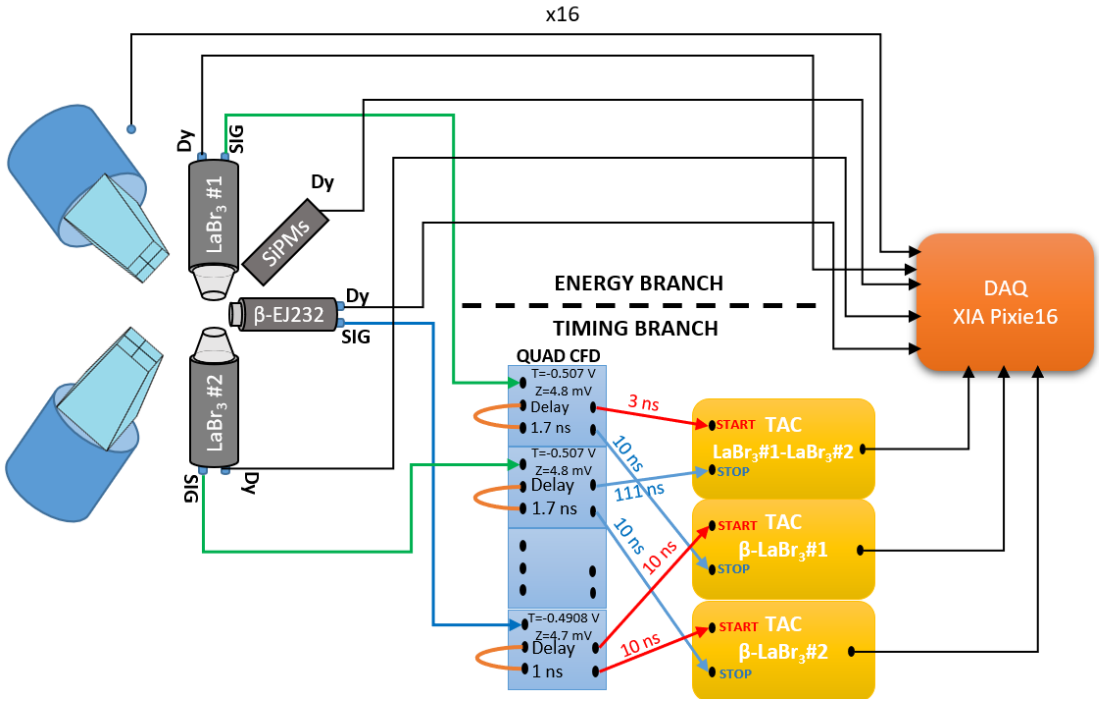


**Figure 4.2.** Schematic diagram of the electronic setup employed in the IS685_II experimental campaign.

In the IS685 experimental campaign, the two SiPM $\beta$ detectors were used as timing detectors, thus requiring two additional CFD modules. The SiPM $\beta$ signals were pre-processed using ZX60-3018G Mini-Circuits amplifiers before being connected to the CFD modules. A Fan-in Fan-Out (Fi/Fo) module was used to replicate the $LaBr_3$(Ce) signals for further distribution. A total of four TACs were employed in the IS685 experimental campaign. Three TACs were dedicated to measuring the time differences between each of the three $\beta$ detectors and the $LaBr_3$(Ce) signal from the Fi/Fo module, while the fourth TAC was used to measure coincidences between the two $LaBr_3$(Ce) detectors.

Due to the limited timing resolution of the two SiPM $\beta$ detectors, $FWHM_{\beta\text{-SiPM}_1}$ = 2861(14) ps and $FWHM_{\beta\text{-SiPM}_2}$ = 2712(14) ps (See Fig. 4.3), in comparison with the superior timing resolution of the $\beta$ PMT detector ($FWHM_{\beta\text{-PMT}}$ = 254.5(6) ps), the two SiPM $\beta$ detectors in the timing configuration was not employed during the IS685_II experimental campaign.

## 4.3 Data acquisition and online data analysis

The detector signals were digitized using a data acquisition (DAQ) system based on the XIA Pixie-16 digitizer. This data acquisition system consists of ten 16 bit digitizer cards with 16 channels each with a sampling rate of 100 MHz. Digitized data is

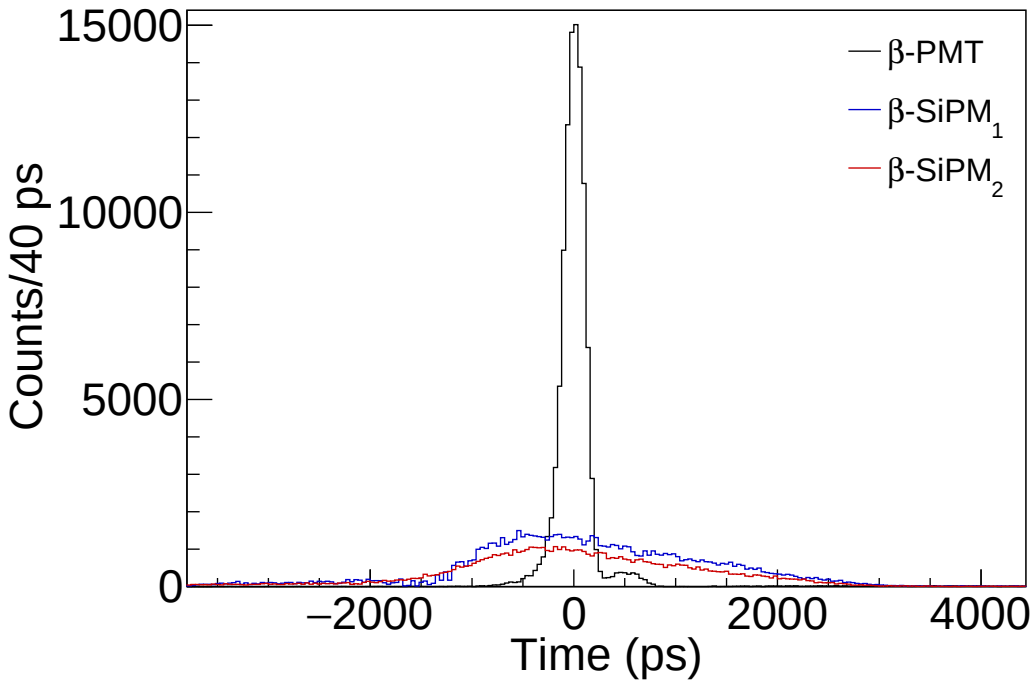


**Figure 4.3.** Time-delayed $\beta\gamma$(t) coincidence spectra measured using the TACs $\beta$–PMT, $\beta$–SiPM$_1$, and $\beta$–SiPM$_2$, obtained by placing energy gates on the 925- and 936-keV $\gamma$-ray transitions in the LaBr$_3$(Ce)-2 detector from the $^{128}$Cd $\beta$ decay.

processed by a trapezoidal filter, whose parameters are independently adjusted for every signal. The distribution of each signal is displayed in Tab. 4.1. The T1 signal from the PSB, which is sent every time that a proton is sent to the target and provides valuable timing information, is entered in the first channel in Module 4. Other signals were recorded for the beam gate closure and the start and stop of the tape movement.

Information related to the pulse amplitude, timestamp, and detection channel is transmitted and organized into files with a maximum size of 2 GB. These RAW data files are generated on an event-by-event basis by the event builder *xia4ids* [LPC+23], which produces output files in list-mode format. Events are constructed according to predefined coincidence conditions and are time-correlated with the arrival of the proton beam. The resulting list files contain all the essential parameters required to analyze the decay processes under investigation and can be produced in either ROOT [ROO25] or GASPware [Tay17] formats.

Subsequent data analysis relies on a set of dedicated programs capable of sorting the multiparametric events based on user-defined selection criteria and generating spectra appropriate for physical interpretation. The analysis proceeds along two main lines: **$\gamma$-ray spectroscopy** and **lifetime measurements**.

The data analysis of the $\gamma$-ray spectra emitted in the decay under study is primarily based on the data recorded by the HPGe detectors. This part of the analysis was performed using list-mode files in the GASPware format. Three complementary

**Table 4.1.** Distribution of the the IDS signals in the XIA Pixie16 cards for IS685_II experimental campaign.

| Channel | Mod 0 | Mod 1 | Mod 2 | Mod 3 |
|---|---|---|---|---|
| 0 | Clover 1 | Clover 5 | Veto (Clover 1) | TAC $\beta$-$LaBr_3$(Ce)-1 |
| 1 | Clover 1 | Clover 5 | Veto (Clover 2) | TAC $\beta$-$LaBr_3$(Ce)-2 |
| 2 | Clover 1 | Clover 5 | $\beta$-$SiPM_L$ | TAC $LaBr_3$(Ce)-$LaBr_3$(Ce) |
| 3 | Clover 1 | Clover 5 | $\beta$-$SiPM_R$ | - |
| 4 | Clover 2 | - | - | - |
| 5 | Clover 2 | - | Proton | - |
| 6 | Clover 2 | - | Supercycle | - |
| 7 | Clover 2 | - | BG On | - |
| 8 | Clover 3 | $LaBr_3$(Ce)-1 | BG Off | - |
| 9 | Clover 3 | $LaBr_3$(Ce)-2 | Tape START | - |
| 10 | Clover 3 | Collimator | Tape STOP | - |
| 11 | Clover 3 | - | - | - |
| 12 | Clover 4 | - | $\beta$-PMT Energy | - |
| 13 | Clover 4 | - | - | - |
| 14 | Clover 4 | - | - | - |
| 15 | Clover 4 | - | - | - |

methods are employed to identify the $\gamma$ rays in the spectra. First, the time distribution of the $\gamma$ rays with respect to the arrival time of the proton pulse is characteristic of the half-life of the decaying isotope, and thus can be used to assign $\gamma$ rays to a specific decay sequence. In particular, the short-lived parent isotopes such as $^{133}$Cd and $^{132}$Cd produce $\gamma$ rays predominantly within the first second after the proton pulse, while longer-lived daughter isotopes of the $\beta$-decay chain result in more delayed time distributions. Second, requiring a coincidence with the $\beta$-detectors provides an effective method to suppress background contributions from isobaric contaminants and other no $\beta$-decay processes, enhancing the selectivity for true $\beta$-decay events. Third, the use of $\gamma\gamma$ coincidences between HPGe detectors, especially when correlated with known transitions, allows the unambiguous placement of $\gamma$ rays within the level scheme of the daughter nucleus.

The analysis of excited-state lifetime measurements was performed using a suite of fast-timing analysis tools originally based on the framework developed in Ref. [Ben20], which have been further developed, extended, and optimized in the present work. The process was divided into two steps: a presorting stage, performed by the *FTGlobalTree* program and after presorting, the analysis proceeds through two parallel paths depending on whether $\beta\gamma$(t) or $\gamma\gamma$(t).

The *FTGlobalTree* program filters and calibrates the relevant timing events from the raw data. The output includes all calibrated timing and energy information for $LaBr_3$(Ce), $\beta$, and HPGe detectors, as well as the reference timing with respect to the proton pulse. After presorting, for $\beta\gamma$(t) data analysis, 2D histograms of TAC values

versus energy are constructed, gated by HPGe clover detectors, and corrected for $\beta$ time-walk. The program *BG_Time_distribution* is then used to extract and correct the time spectra, including the separation of full-energy peak (FEP) and Compton background contributions. For $\gamma\gamma$(t) events, the *GG_Time_distribution* program performs the complete extraction in a single step, using energy gates in the START and STOP detectors and applying Compton background corrections. More details of the analysis methods are explain in Sec. 4.6.

A schematic overview of the data acquisition and online data analysis workflow for the IS685 and IS685_II experimental campaigns is presented in Fig. 4.4.

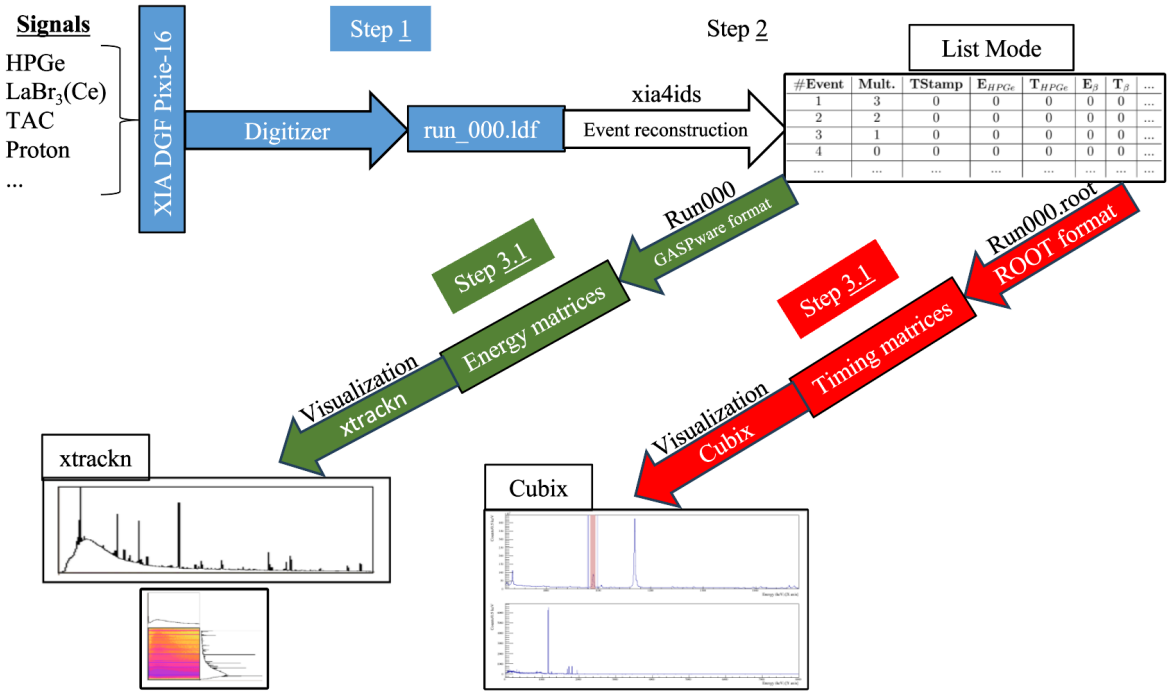


**Figure 4.4.** Successive processing steps scheme of data acquisition.

## 4.4 Energy calibrations

Energy calibrations of the $\gamma$-ray detectors were performed using $^{140}$Ba, $^{152}$Eu, $^{138}$Cs, $^{88}$Rb sources (see Tab. 4.2) and internal $\gamma$-rays in the decay chain. Using these sources, it is possible to reach up to 2.7 MeV. Neutron-rich Cd isotopes have a large $Q_{\beta^-}$ value, thus for higher energies (5-7.2 MeV) neutron capture $\gamma$-rays were employed and also their single and double escape respectively.

When protons arrive to the neutron converter, a flash of fast neutrons is produced that can be captured by the materials composing the surrounding areas (e.g., Al, Fe) and specifically the IDS experimental setup (e.g., Ge). The isotopes with the higher masses produced in each experimental campaign are used for high energy calibrations. The production of the neutrons is produced in the first 3-40 ms after the interaction of

the proton and the target. In order to detected the high-energy $\gamma$-rays a 20 ms time gate in the initial proton reference spectrum is used (Fig. 4.5). The strongest $\gamma$-rays are from Fe neutron capture, but neutron capture from Al and Ge (from HPGe-clover detectors itself) are also observed.

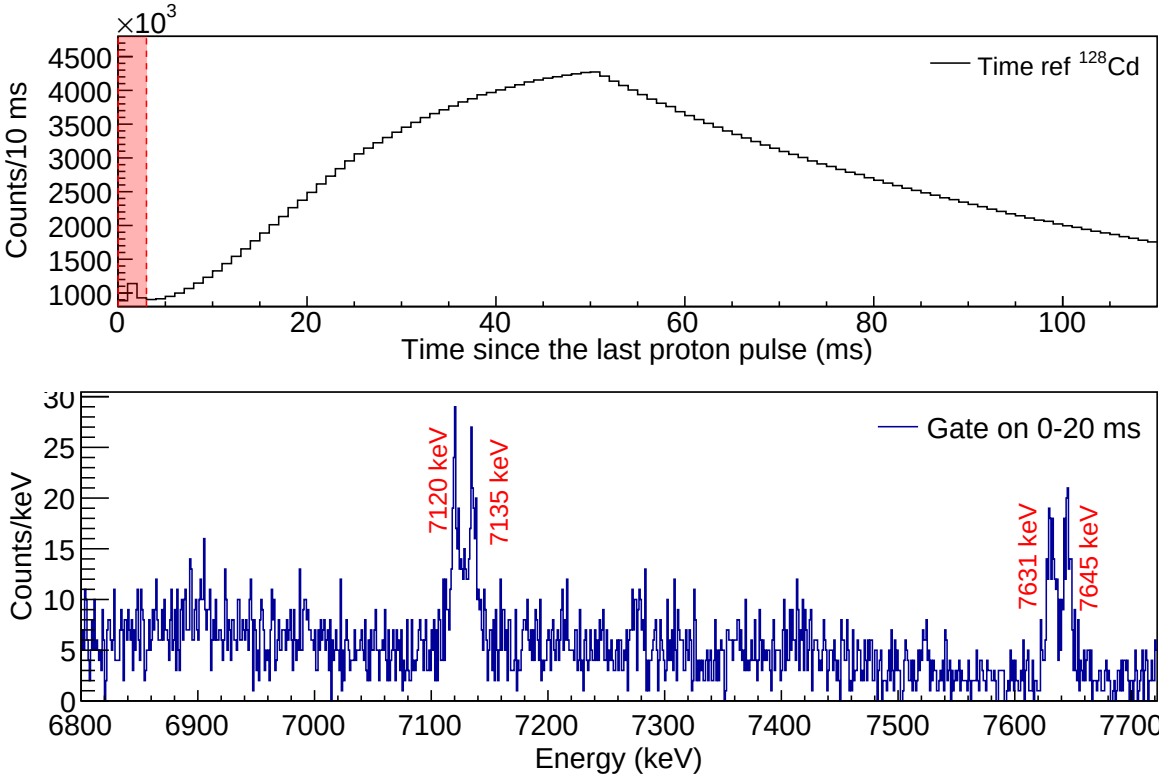


**Figure 4.5.** Time distribution relative to the proton impact analysis of the $^{128g}$Cd (upper panel). High energy $\gamma$-rays corresponding to $^{56}$Fe(n,$\gamma$)$^{57}$Fe (lower panel).

### 4.4.1 HPGe-Clover energy calibrations

HPGe detectors are characterized by their linear energy response within the energy range that is focus this thesis. Therefore, the energy calibration coefficients can be obtained by fitting a linear function for each of the 24 crystals. In the IS685 experimental campaign, non-linearity effects required adjusting the calibration equation for different energy ranges. The resulting residuals exhibited a sawtooth pattern, a clear indication of fluctuations in the calibration caused by the specific acquisition channels to which certain HPGe detector signal were connected (see Fig. 4.6). Notably, this linearity problem was observed only in two of the HPGe-clover detectors. To address this linearity problem, the HPGe detectors were calibrated in different energy ranges.

In the IS685_II experimental campaign, a comprehensive study of all the digitizer channels was conducted to identify those affected by these linearity issues. Channels exhibiting the sawtooth-pattern residuals were avoided, thereby preventing the recurrence of the linearity issues observed in the IS685 experimental campaign.

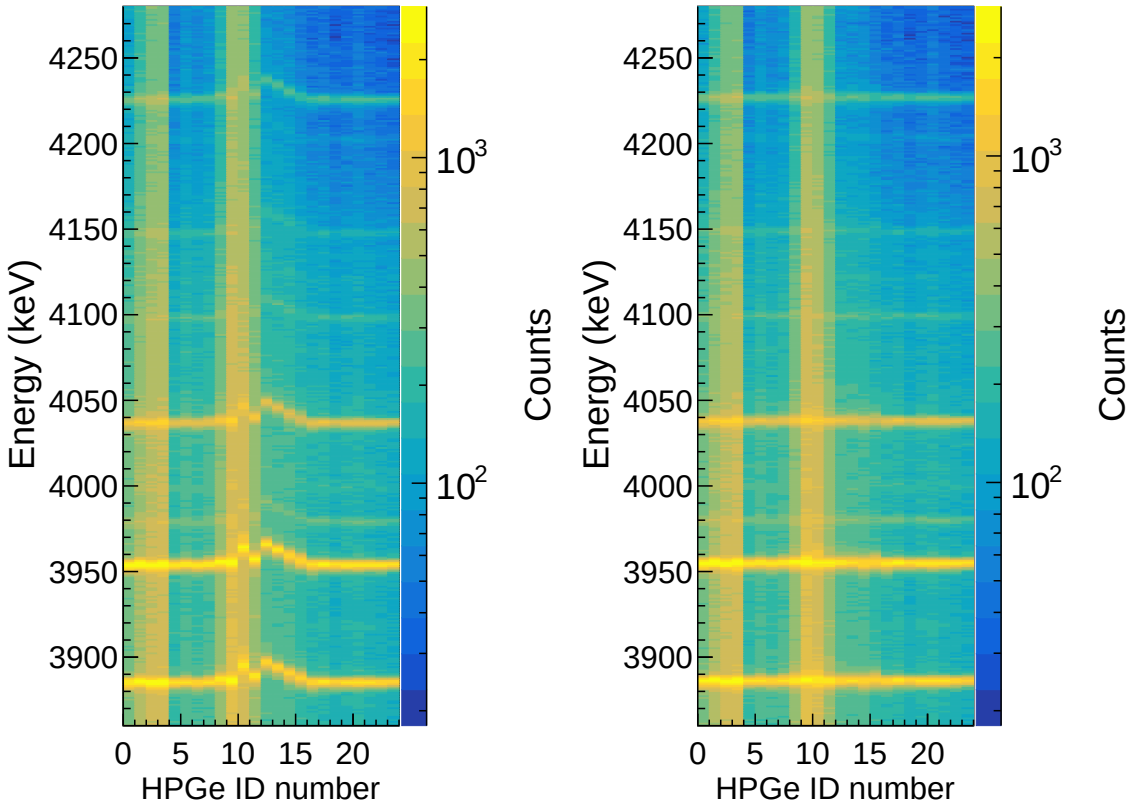


**Figure 4.6.** Comparison of the HPGe detector energy spectra before and after energy calibration. Each panel shows the two-dimensional histogram of energy (keV) versus detector ID for all clover crystals. The left panel shows the spectrum calibrated using a single global energy range for all crystals, while the right panel presents the corrected spectrum obtained after applying the full calibration procedure. Improved peak alignment across detector channels is clearly visible post-calibration, particularly near the reference energy region around 4 MeV.

After calibrating each individual crystal, the data from all crystals were combined into a single spectrum, with the *add-back correction* applied. In this context, the add-back correction combines coincident energy deposits occurring in different crystals of the same HPGe clover detector that originate from a single $\gamma$-ray interaction. By summing these correlated signals, the procedure recovers the full deposited energy and increases the detector efficiency. The residual is calculated to test the quality of the fit. The IS685_II campaign focused on low-energy calibrations, since the data used from this experiment did not require high-energy $\gamma$ rays. The final results obtained from the IS685 and IS685_II experimental campaigns are presented in Fig. 4.7.

### 4.4.2 $LaBr_3(Ce)$ energy calibrations

$LaBr_3(Ce)$ detectors are used for $\gamma$ lines peak selection in timing measurements. Combination of the $LaBr_3(Ce)$+PMT are characterized by their non-linear energy response. Detailed studies in Ref. [VMF+15] have shown that the degree of linearity is primarily influenced by the voltage applied to the PMT, given that the intrinsic scintillation yield of $LaBr_3(Ce)$ is approximately linear. Specifically, energy responses

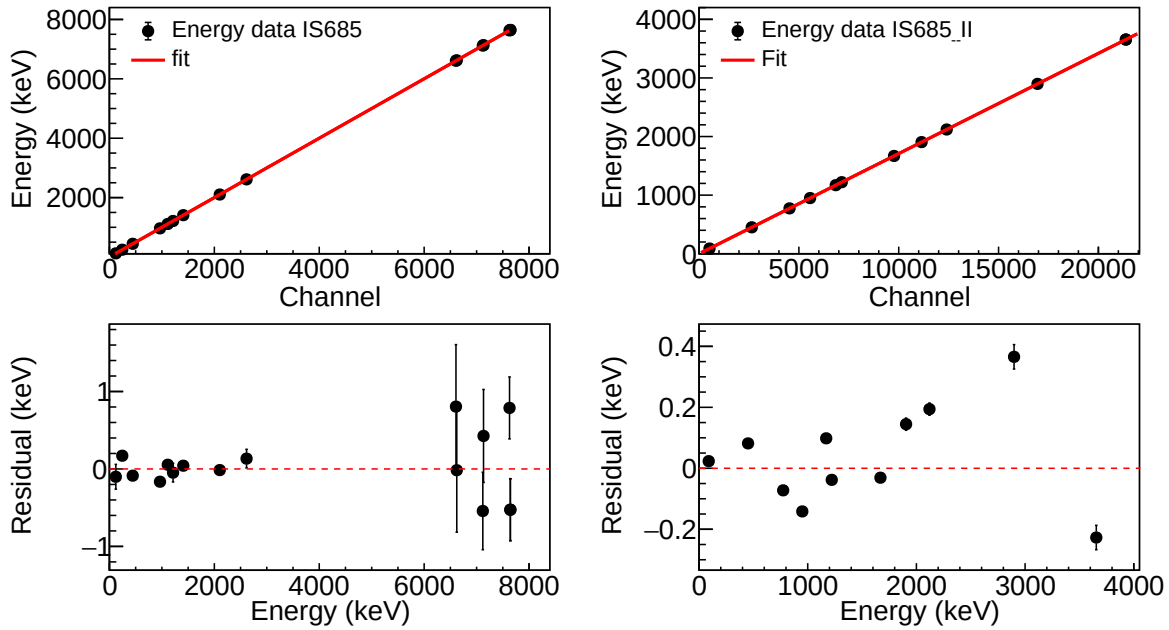


**Figure 4.7.** Energy calibration of the HPGe detectors performed during the IS685 (left plot) and IS685_II (right plot) experimental campaigns. The residuals displayed in the lower panel provide a quantitative assessment of the calibration accuracy.

remain linear when the operating voltage is maintained below −1300 V [VMF+15]. This non-linear energy response required a 4 degree polynomial function for both detectors.

The more intense transitions of the standard energy calibrations sources at IDS (see Tab. 4.2) were considered. A gate with the HPGe detectors was employed to enhance selectivity. $LaBr_3(Ce)$ detectors are also characterized by their poor stability over the time scales that encompass the measurement periods of the IS685 experiment. For these reasons, not only is the calibration with the energy calibration sources necessary, but also a slight correction using the most intense, well-tabulated, strongest $\gamma$-rays from the nucleus under study (Fig. 4.8). The first calibration was sufficient to identify the strongest $\gamma$-rays from the $\beta$-decay of Cd, which had been previously identified using HPGe detectors. The LaBr3(Ce) detectors were not utilized in the data analysis presented in this work from the IS685_II experimental campaign.

## 4.5 Efficiency calibrations

In order to estimate the intensities of the $\gamma$ transitions $I_\gamma$ it is necessary to perform an efficiency calibration. The efficiency depends on the nature of the radiation being measured, the type of detector used and the geometrical arrangement of the source-detector system. Once the intensity of each transition is determined, they are normalized to the most intense one in the nucleus. In this way, the relative intensities of the studied transitions is computed.

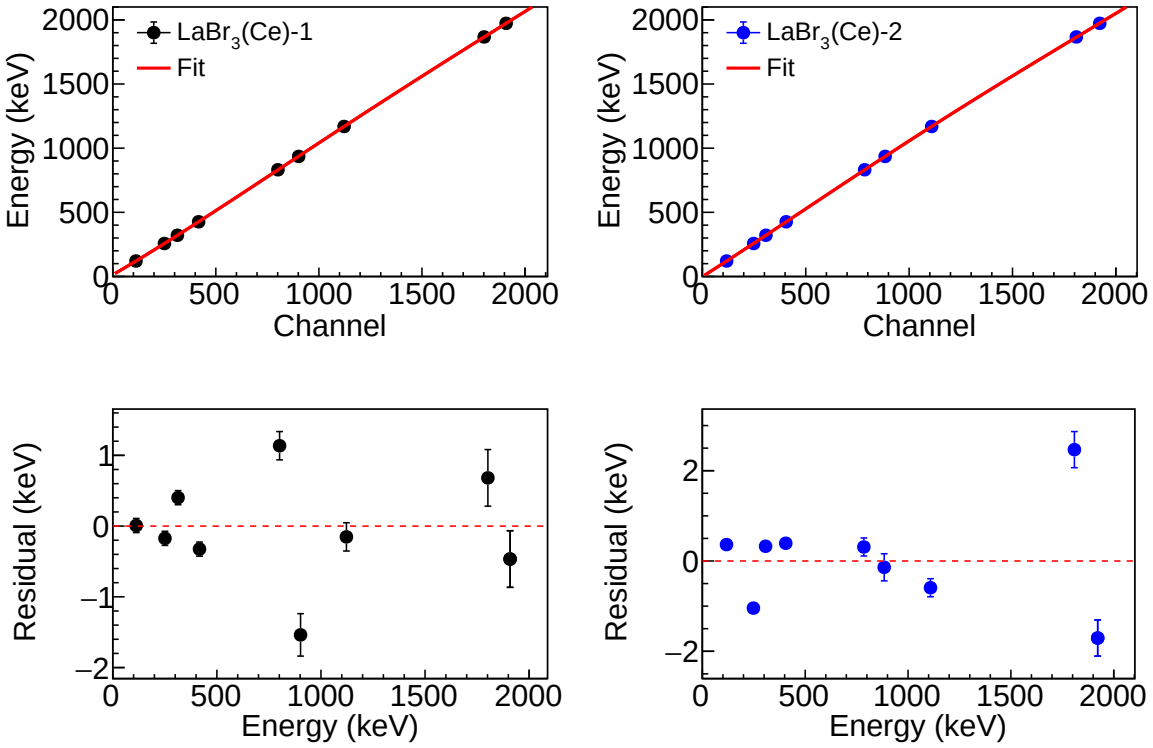


**Figure 4.8.** Energy calibration for the $LaBr_3(Ce)$ detectors during the IS685 experimental campaign. After the gain shift, the $\gamma$-rays of the $^{128}$Cd $\beta$-decay were used for the fit to ensure correct stability. The residuals for each detector are displayed in the low graphs.

A standard $^{152}$Eu calibration source is used to estimate the efficiency calibration curve that will act as a normalization to the efficiency for the energy range between 40 keV to 1500 keV. In the experiment the $^{152}$Eu source was placed at the implantation point inside the chamber to obtain efficiency calibrations. The area of the photopeak in the spectrum obtained by the HPGe detectors is analyzed and divided by the intensity percentage tabulated in the literature (see Tab. 4.2) and the measurement time. For the analysis, the HPGe singles spectra built after add-back correction was employed.

The data obtained are fitted to the empirical curve expressed in equation:

$$\epsilon(E_\gamma) = \frac{1}{E_\gamma} \sum_{i=1}^{N} b_i (\log E_\gamma)^{i-1} \tag{4.1}$$

The choice $N = 4$ yields a statistically acceptable fit to the full-energy peak efficiency data, according to the $\chi^2$ test. To cover a wider energy range, several complementary calibration sources are employed (see Tab. 4.2). The detection relative efficiency curve obtained for the calibration sources ($\varepsilon_{rel}^{source}$) will be proportional to the $^{152}$Eu absolute efficiency ($\varepsilon_{abs}^{Eu}$) curve computed using Eq. 4.1. This multiplicative factor can be expressed as described in Eq. 4.2. The factor $f^{source}$ has a negligible energy dependence in the energy range of 0.04-4.7 MeV.

$$f^{source} = \frac{\varepsilon_{abs}^{Eu}(E_\gamma)}{\varepsilon_{rel}^{source}(E_\gamma)} \tag{4.2}$$

Each efficiency data set for each source must be normalized to the maximum value so that the offset term $b_0$ in Eq. 4.1 coincides for the different curves. For each source, the same parameter is determined. The uncertainty is propagated quadratically. The factors have been estimated to maximize the fit between the efficiency curves of each source with the $^{152}$Eu data points within their common energy range. This is because $\varepsilon_{abs}^{Eu}(E_\gamma^{source})$ is derived from the coefficient resulting from fitting Eq. 4.1 for $^{152}$Eu at a given energy $E_\gamma^{source}$. The relative efficiency $\varepsilon_{rel}^{source}(E_\gamma^{source})$ is calculated by dividing the area of the photopeak by the intensity percentage of the other calibration source. Once $f^{source}$ is calculated, all the data of the calibration source curve is renormalized by multiplying by this factor. After this procedure for all the rest of calibration sources, the global calibration curve is obtained and this data is fitted to Eq. 4.1 covering the energy range between 0.04 and 4.7 MeV. The final result for both experimental campaigns is shown in Fig. 4.9. For the IS685 campaign with 6 HPGe-clover detectors, the efficiency at 1 MeV is 5%, whereas for the IS685 campaign with only 4 HPGe-clovers detectors, the efficiency is 4%. The detection efficiency is provided with a relative uncertainty of approximately 5% for energies less than 1.7 MeV. However, for the energy range below 100 keV, this uncertainty has been raised to 15%.

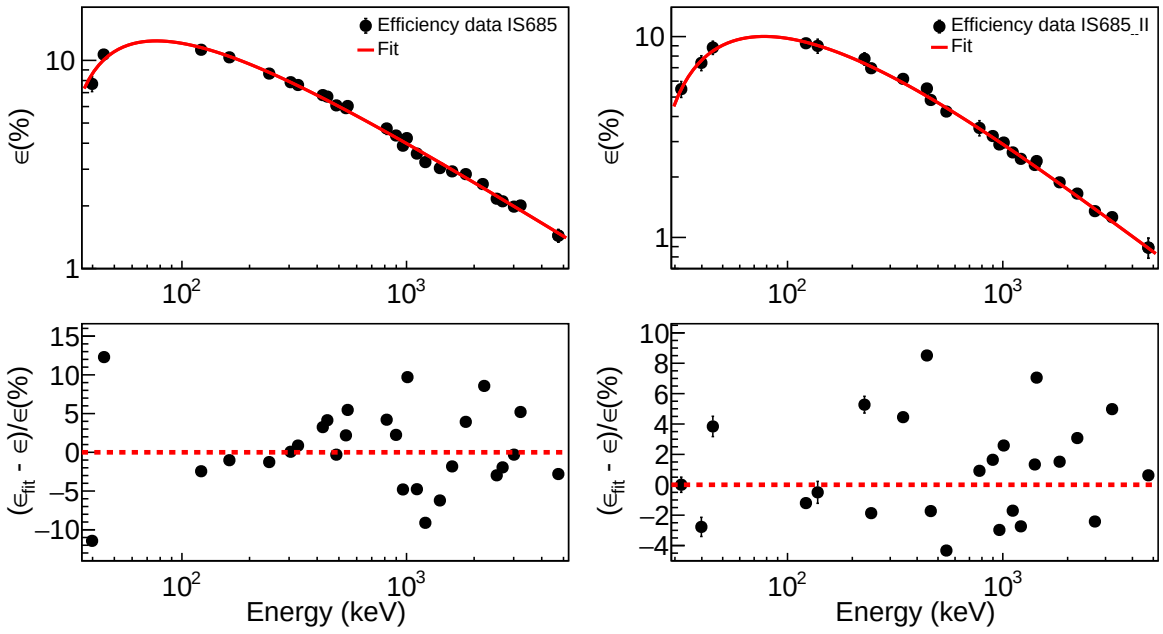


**Figure 4.9.** Efficiency calibration of HPGe-Clovers detectors performed during the IS685 (left) and IS685_II (right) experimental campaigns. Calibration points were determined for the energy range spanning from 0.04 to 4.7 MeV.

**Table 4.2.** Gamma ray used for HPGe detectors efficiency calibration. Data taken from NNDC Decay radiation information database [NND25].

| Isotope | $E_\gamma$ (keV) | Intensity (%) |
|---|---|---|
| $^{152}$Eu | 39.89(29) | 58.7(9) |
| $^{152}$Eu | 45.58(47) | 13.41(19) |
| $^{152}$Eu | 121.7817(3) | 28.53(16) |
| $^{152}$Eu | 244.6974(8) | 7.55(4) |
| $^{152}$Eu | 443.9606(16) | 2.827(14) |
| $^{152}$Eu | 964.057(5) | 14.51(7) |
| $^{152}$Eu | 1112.076(3) | 13.67(8) |
| $^{152}$Eu | 1212.948(11) | 1.415(8) |
| $^{152}$Eu | 1408.013(3) | 20.87(9) |
| $^{140}$Ba | 162.66(1) | 6.22(9) |
| $^{140}$Ba | 304.849(3) | 4.29(6) |
| $^{140}$Ba | 423.722(1) | 3.1(4) |
| $^{140}$Ba | 537.261(9) | 24.39(22) |
| $^{140}$La | 328.762(8) | 20.3(3) |
| $^{140}$La | 487.021(12) | 45.5(6) |
| $^{140}$La | 815.772(19) | 23.28(19) |
| $^{140}$La | 1596.2(4) | 95.4(8) |
| $^{140}$La | 2521.4(5) | 3.46(4) |
| $^{138}$Cs | 546.99(15) | 10.8(3) |
| $^{138}$Cs | 1009.78(7) | 29.8(6) |
| $^{138}$Cs | 2218.00(10) | 15.2(4) |
| $^{88}$Rb | 898.03(4) | 14.40(24) |
| $^{88}$Rb | 1836.0(7) | 22.81(11) |
| $^{88}$Rb | 2677.9(10) | 2.13(21) |
| $^{24}$Na | 1368.625(5) | 99.994(2) |
| $^{24}$Na | 2754.008(11) | 99.867(10) |

## 4.6 Advanced Time-Delayed $\beta\gamma\gamma$(t) method

The Advanced Time-Delayed (ATD) method provide a versatile tool to measure lifetimes of excited states populated in $\beta$-decay. It relies on the use of delayed coincidences between an ultra-fast plastic-scintillators as $\beta$ detectors and $LaBr_3$(Ce) crystals as $\gamma$-detectors [MM89]. It makes use of the coincidences using the Time-to-Amplitude Converter (TAC) modules using the START signal from the particle detected by the $\beta$-plastic and the $LaBr_3$(Ce) crystal when the $\gamma$ ray is detected as STOP. An additional coincidence condition is used with a specific $\gamma$ ray detected in HPGe-clover detectors. The third coincidence is employed to improve selectivity, but also for decay branch selection. By performing an accurate calibration of the time response of the system, it is possible to measure lifetimes down to $\approx 10$ ps with these methods.

To minimize the time walk, CFD modules are employed prior to the TAC, which

provide the timing signal for each event (see Sec. 4.2).

The TAC spectrum output yields a time distribution $F(t_i)$, which corresponds to the time difference distribution $f(t)$ between the emission of the $\beta$ particles and $\gamma$ rays. The physical time distribution can be described as a sum of exponential decay components:

$$f(t) = \sum_i a_i e^{-t/\tau_i} \quad (t > 0), \tag{4.3}$$

where each term corresponds to the lifetimes of the excited levels $\tau_i$ of an intermediate excited state populated after $\beta$ decay and de-excited by emission of the $\gamma$ ray detected in the $LaBr_3$(Ce) scintillator. In Eq. 4.3, $a_i$ denotes the relative amplitude of each exponential component, reflecting the population probability of the corresponding excited state with lifetime $\tau_i$. In the simplest scenario, the level of interest is fed directly by the $\beta$ decay, in which case the distribution reduces to a single exponential $f(t) = e^{-t/\tau}$.

However, the measured time spectrum is not simply $f(t)$ due to the finite time resolution of the system and the energy-dependent time response of the detectors. The observed delayed time distribution $F(t_i)$ results from the convolution of $f(t)$ with the system response function $P(t_i)$, which accounts for the intrinsic prompt timing characteristics of the system:

$$F(t_i) = N \int_{t_0}^{+\infty} P(t_i - t) f(t - t_0)\, dt, \tag{4.4}$$

where $N$ is a normalization factor and $t_0$ is the start time reference.

The response function $P(t_i)$ encapsulates the combined time resolution contributions from the scintillator, PMTs, CFD, and TAC modules. This function is typically approximated by a quasi-Gaussian shape characterized by a centroid $C$ and standard deviation $\sigma$, both of which depend on the energy of the $\beta$ or $\gamma$ ray. The energy dependence of the centroid, referred to as the detector time walk, must be carefully calibrated to perform precise lifetime measurements using the centroid shift method. The parameter $\sigma$ reflects the overall timing resolution, which also varies with energy.

Half-lives of excited states can be determined from the analysis of the corresponding time distributions. Depending on the lifetime range, two main methodologies can be distinguished: the **deconvolution** method and the **centroid-shift** method.

### De-convolution method

For excited states with lifetimes longer than the timing resolution of the detection system, the decay manifests as an exponential tail on the right-hand side of the time spectrum, referred to as the delayed region. In the case, where only one level contributes to the time distribution, and assuming a Gaussian instrumental response function $P(t_i)$, the time spectrum $F(t_i)$ (Eq. 4.4) can be expressed as the convolution of the Gaussian response with an exponential decay:

$$F(t_i) = N \int_{t_0}^{\infty} \frac{1}{\sqrt{2\pi}\sigma} \exp\left(-\frac{(t_i - t_0)^2}{2\sigma^2}\right) \cdot \frac{1}{\tau} \exp\left(-\frac{t - t_0}{\tau}\right) dt \tag{4.5}$$

where $N$ is the total number of events in the time distribution, $t_0$ represents the centroid of the prompt time distribution for the energy of the $\gamma$ ray, $\sigma$ is the standard deviation of the Gaussian response, and $\tau$ is the mean lifetime of the excited level.

Eq. 4.5 can be expressed in closed form, as the convolution yields an analytical solution involving the error function, $\mathrm{erf}(x)$, which characterizes the Gaussian temporal response of the system. The resulting expression is given by:

$$F(t_i) = \frac{N}{2\tau} \exp\left(\frac{t_i - t_0}{\tau} + \frac{\sigma^2}{2\tau^2}\right) \left[1 + \mathrm{erf}\left(\frac{t_i - t_0}{\sqrt{2}\sigma} - \frac{\sigma}{\sqrt{2}\tau}\right)\right] \tag{4.6}$$

In the asymptotic regime where $\tau \gg \sigma$ and $(t_i - t_0) \gg \sigma$, the error function approaches unity, and Eq. 4.6 reduces to a simple exponential:

$$F(t_i) \approx \frac{N}{\tau} \exp\left(-\frac{t_i - t_0}{\tau}\right). \tag{4.7}$$

An illustrative example is shown in Fig. 4.10

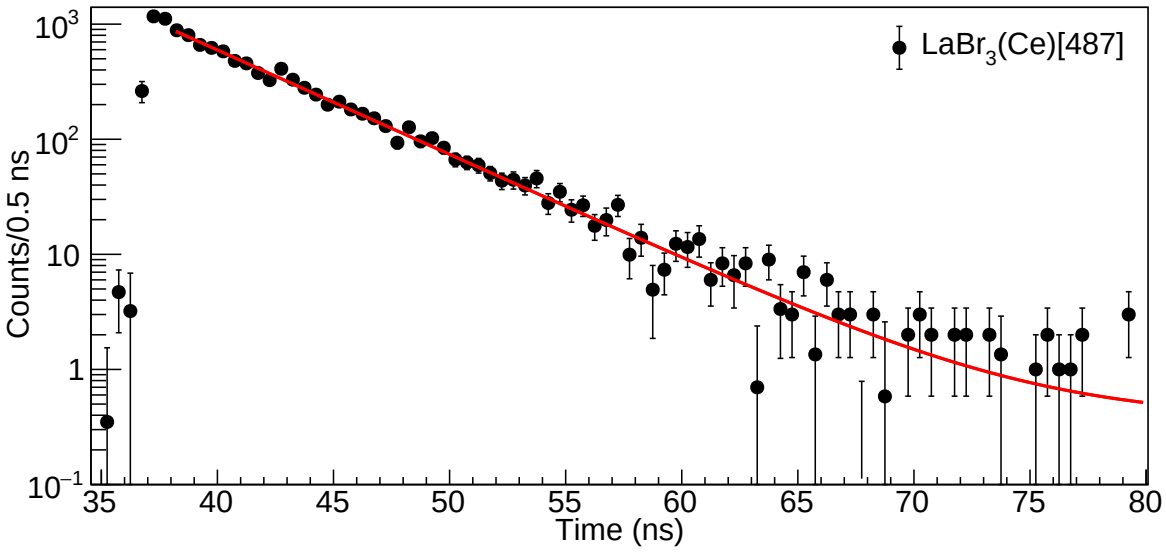


**Figure 4.10.** Half-life of the 2083-keV state in $^{140}$Ce. The analysis was performed using $\beta\gamma$(t) events.This plots shows the de-convolution technique, where the lifetime is measured from the slope of the time distribution. The lifetime was extracted by fitting an exponential decay, along with a constant background, to the tail of the spectra.

### Centroid shift method

In the case of nuclear lifetimes in the range of $10 \lesssim \tau \lesssim 100$ ps or longer, the centroid shift method is employed. Under these conditions, determining the lifetime via direct exponential decay fitting becomes impractical, as the exponential decay tail

is significantly masked by the intrinsic timing resolution of the detection system.

The centroid shift method is illustrated in Fig. 4.11. The blue distribution represents the timing spectrum associated with gamma rays de-exciting a short-lived nuclear state. In the limit of $\tau \rightarrow 0$, this time spectrum defines the *prompt time distribution* (blue time distribution). Assuming that the prompt time experimental distribution for monoenergetic $\gamma$ events is Gaussian the centroid position of this distribution depends on the $\gamma$-ray energy.

In the simplest scenario, involving only a single lifetime component, the lifetime of the excited state is derived directly from the difference between the centroid positions of the convoluted time distribution $F(t)$ and the prompt distribution $P(t)$:

$$\tau = \int_{-\infty}^{+\infty} tF(t)dt - \int_{-\infty}^{+\infty} tP(t)dt = C(F) - C(P). \tag{4.8}$$

However, measuring the prompt centroid position directly poses practical challenges. To overcome this, a reference $\gamma$-ray ($\gamma_{\text{ref}}$) is typically used to establish the centroid position. Nonetheless, due to energy-dependent time-walk effects, the centroid position of this reference $\gamma_{\text{ref}}$ is also subject to shifts. Thus, accurate determination of the lifetime necessitates employing the FEP-walk correction.

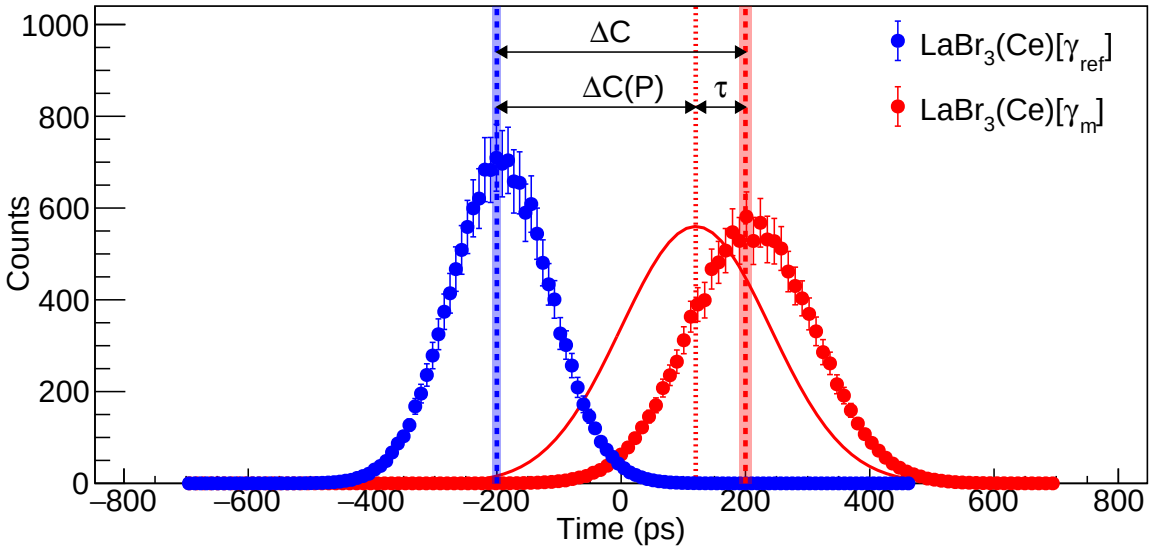


**Figure 4.11.** Example of the $\beta\gamma(t)$ centroid shift analysis, obtained through a simulation. The blue spectrum represents the time distribution corresponding to the delayed $\gamma$ ray that de-excites the level of interest ($\gamma_m$), while the red distribution corresponds to the prompt-reference $\gamma$ ray ($\gamma_{ref}$). The centroid is shown with a dashed line, while the shaded area represents its uncertainty. The red Gaussian distribution corresponds to the expected prompt position of the delayed $\gamma$ ray, which is obtained from the shift in the FEP walk curve. See text for details.

Depending on the level scheme, one of the following analyses is performed in the centroid shift technique: **sequential transitions** (Fig. 4.12 (a)), **parallel transitions**

(Fig. 4.12 (b)) and **absolute transitions** (Fig. 4.12 (c)).

A schematic representation of the level scheme corresponding to the **sequential transitions** method is shown in Fig. 4.12 (a). In this configuration, the measured lifetime corresponds to the intermediate level characterized by the mean life $\tau_1$. This level is populated by an intense $\gamma_1$ transition and subsequently depopulated by an intense $\gamma_2$ transition. Both $\gamma$ rays exhibit sufficient statistical significance in the $LaBr_3$(Ce) detectors, enabling a reliable extraction of the lifetime. No contribution from higher-lying long-lived states is present in this configuration, ensuring that the observed time distribution is solely associated with the lifetime of the intermediate level.

When $\gamma_1$ is selected in the HPGe detector (HPGe[$\gamma_1$]), the coincident $\gamma_2$ is detected in the $LaBr_3$(Ce) detector ($LaBr_3$(Ce)[$\gamma_2$]), which serves as the STOP signal for the $\beta$–$LaBr_3$(Ce) TAC $\beta$-$LaBr_3$(Ce). In this configuration, the $\beta$ feeding into the first excited state does not influence the measurement. Only the $\beta$ feeding to the second level is registered in coincidence in the $\beta$ detector, which provides the START signal for the TAC $\beta$-$LaBr_3$(Ce).

The resulting time distribution recorded by the TAC $\beta$-$LaBr_3$(Ce) corresponds to the convolution of two Gaussian functions: one associated with the mean lifetime $\tau_2$ of the final level, and the other representing the prompt response function $\tau_0(E_{\gamma_2})$ of the $LaBr_3$(Ce) detector at the energy of $\gamma_2$. Thus, the total observed time delay in this configuration is given by:

$$\text{HPGe}[\gamma_1] - \text{LaBr}_3(\text{Ce})[\gamma_2] \rightarrow t_2 = \tau_0(E_{\gamma_2}) + \tau_2 \tag{4.9}$$

Here, $\tau_0(E_{\gamma_2})$ accounts for the energy-dependent instrumental delay between the detectors. The mean lifetime $\tau_1$ does not contribute to this delay, as the detection of $\gamma_1$ in the HPGe detector occurs significantly later due to its comparatively slower response.

If the selection order is reversed, HPGe[$\gamma_2$] and $LaBr_3$(Ce)[$\gamma_1$], the TAC $\beta$-$LaBr_3$(Ce) will display a time delay including contributions from both $\tau_1$ and $\tau_2$, as well as the prompt response at $E_{\gamma_1}$:

$$\text{HPGe}[\gamma_2] - \text{LaBr}_3(\text{Ce})[\gamma_1] \rightarrow t_1 = \tau_0(E_{\gamma_1}) + \tau_1 + \tau_2 \tag{4.10}$$

The difference between the two measured centroids, $\Delta t = t_1 - t_2$, isolates the mean life of the intermediate level $\tau_1$ and yields:

$$t_1 - t_2 = [\tau_0(E_{\gamma_1}) + \tau_1 + \tau_2] - [\tau_0(E_{\gamma_2}) + \tau_2] = \tau_1 + \Delta\tau_0$$

where $\Delta\tau_0 = \tau_0(E_{\gamma_1}) - \tau_0(E_{\gamma_2})$ is the differential prompt response time, which is determined from the FEP-walk calibration curve.

A schematic representation of the level scheme corresponding to the **parallel transitions** method is shown in Fig. 4.12 (b). In this configuration, the measured lifetime corresponds to the lifetime $\tau_3$ of an intermediate level populated and depopulated by

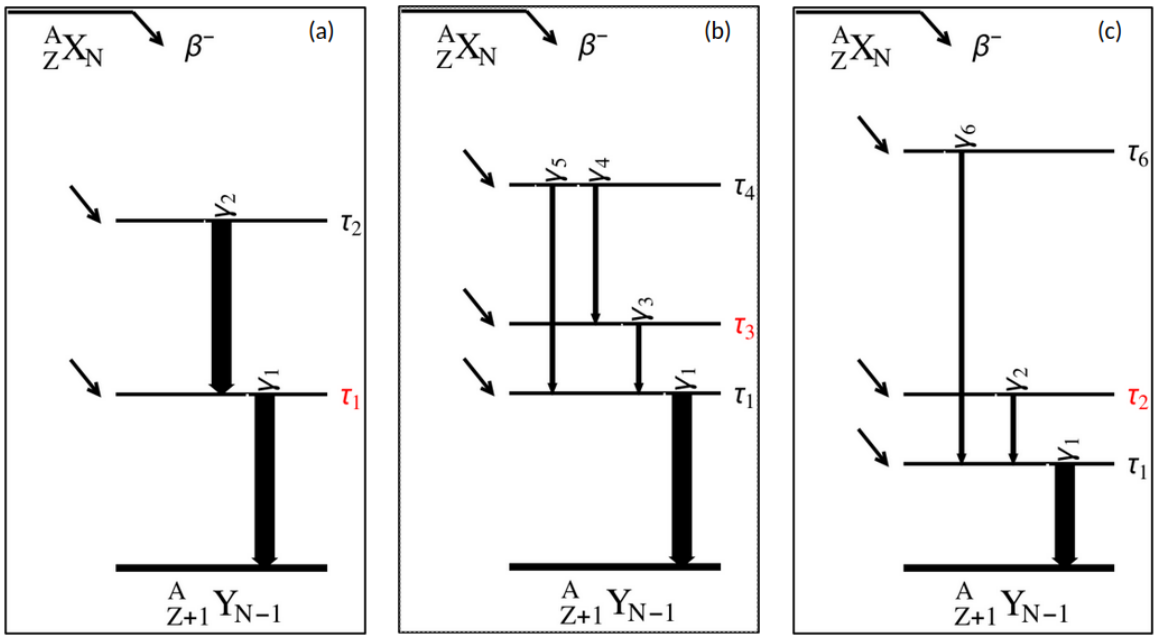


**Figure 4.12.** Level scheme illustrating the $\beta^-$ decay of ${}^{A}_{Z}X_N$ isotope populating excited states in ${}^{A}_{Z+1}Y$ isotope. The lifetime $\tau$ (shown in red) is determined using the sequential method (panel (a)), the parallel method (panel (b)), and the absolute method (panel (c)), respectively.

transitions that are parallel in the decay scheme. Typically, only the $\gamma_1$ transition is detected with sufficient statistical significance in the $LaBr_3(Ce)$ detectors, although this is not strictly required for the method to be applicable.

The key advantage of the parallel configuration is that it allows the elimination of energy-dependent timing corrections associated with the prompt response $\tau_0(E_\gamma)$, since the same $\gamma_1$ line is detected in the $LaBr_3(Ce)$ detector for both configurations. For instance, by selecting the transitions $\gamma_4$ and $\gamma_5$ in the HPGe detectors and $\gamma_1$ in $LaBr_3(Ce)$, the $LaBr_3(Ce)$ detector records the same $\gamma$ ray, and thus the timing response contribution $\tau_0(E_1)$ remains constant.

$$\mathrm{HPGe}[\gamma_4] - \mathrm{LaBr_3(Ce)}[\gamma_1] \rightarrow t_4 = \tau_0(E_{\gamma_1}) + \tau_1 + \tau_3 + \tau_4 \tag{4.11}$$

$$\mathrm{HPGe}[\gamma_5] - \mathrm{LaBr_3(Ce)}[\gamma_1] \rightarrow t_5 = \tau_0(E_{\gamma_1}) + \tau_1 + \tau_4 \tag{4.12}$$

The lifetime $\tau_3$ can then be directly obtained from the difference in time delays associated with the two coincidence conditions:

$$t_4 - t_5 = [\tau_0(E_{\gamma_1}) + \tau_1 + \tau_3 + \tau_4] - [\tau_0(E_{\gamma_1}) + \tau_1 + \tau_4] = \tau_3 \tag{4.13}$$

A schematic representation of the level scheme corresponding to the **absolute transitions** method is shown in Fig. 4.12 (c). High-energy states, typically located above 2 MeV (excluding isomeric states), are characterized by very short mean lives, generally in the femtosecond range. This property enables the determination of $\tau_2$, as illustrated in Fig. 4.12 (c). If the $\gamma_6$ transition is assumed to depopulate excited states above

2 MeV, then $\tau_6 \approx 0$. The corresponding time distribution $t_6$ is obtained by gating $\gamma_6$ in the HPGe detector and $\gamma_1$ in the $LaBr_3$(Ce) detector, resulting in:

$$\text{HPGe}[\gamma_6] - \text{LaBr}_3(\text{Ce})[\gamma_1] \rightarrow t_6 = \tau_0(E_{\gamma_1}) \tag{4.14}$$

The time distribution in the delayed configuration is given by:

$$\text{HPGe}[\gamma_2] - \text{LaBr}_3(\text{Ce})[\gamma_1] \rightarrow t_6 = \tau_0(E_{\gamma_1}) + \tau_1 + \tau_2 \tag{4.15}$$

By subtracting both time responses, the lifetime of the intermediate level is extracted as:

$$t_2 - t_6 = \tau_1 + \tau_2 \tag{4.16}$$

where $\tau_1$ has been previously measured using sequential transitions.

More complex level schemes can be addressed using sequential, parallel, or absolute transition methods. However, the examples discussed above represent simplified cases and may not be applicable to more intricate configurations. A common limitation occurs when the TAC $\beta$–$LaBr_3$(Ce) time spectra lack sufficient statistics to extract a reliable centroid.

### 4.6.1 Analysis of $\gamma\gamma$(t) time delayed events

The fast-timing $\gamma\gamma$(t) method extends the principles of $\beta\gamma$(t) time spectroscopy to the analysis of delayed coincidences between two $\gamma$ rays, enabling the extraction of nuclear level lifetimes. In this approach, one $\gamma$ ray that feeds the level of interest ($\gamma_f$) and another that de-excites it ($\gamma_d$) are selected in coincidence in two $LaBr_3$(Ce) detectors acting as START and STOP. Because both signals originate from $\gamma$ rays, the time distributions are influenced solely by the lifetimes of the intermediate levels. This method is particularly advantageous when investigating levels below long-lived isomers.

For a given $\gamma\gamma$ pair, two time distributions can be formed depending on which detector registers the feeding or de-exciting $\gamma$ ray: the delayed and anti-delayed spectra (See Fig. 4.13). In the delayed configuration, the exponential decay tail appears on the right-hand side of the distribution, whereas in the anti-delayed case it is mirrored to the left. This symmetry enables two independent measurements of the lifetime for long-lived states by fitting the exponential tails of both distributions. For shorter lifetimes, where the decay component is embedded within the prompt peak, the centroid-shift method is employed.

This method can be generalized to an array of $LaBr_3$(Ce) detectors, giving place to the Mirror Symmetric Centroid Difference technique [RSSR$^+$16], adapted to the configuration of the IS685 experiment, is employed to extract mean lifetimes from the difference in centroid positions between the delayed and anti-delayed spectra. The centroid shift $\Delta C$ is related to the mean life $\tau$ via the equation:

$$\Delta C = C(F_{\text{Delayed}}) - C(F_{\text{Anti-Delayed}}) = \Delta P + 2\tau, \tag{4.17}$$

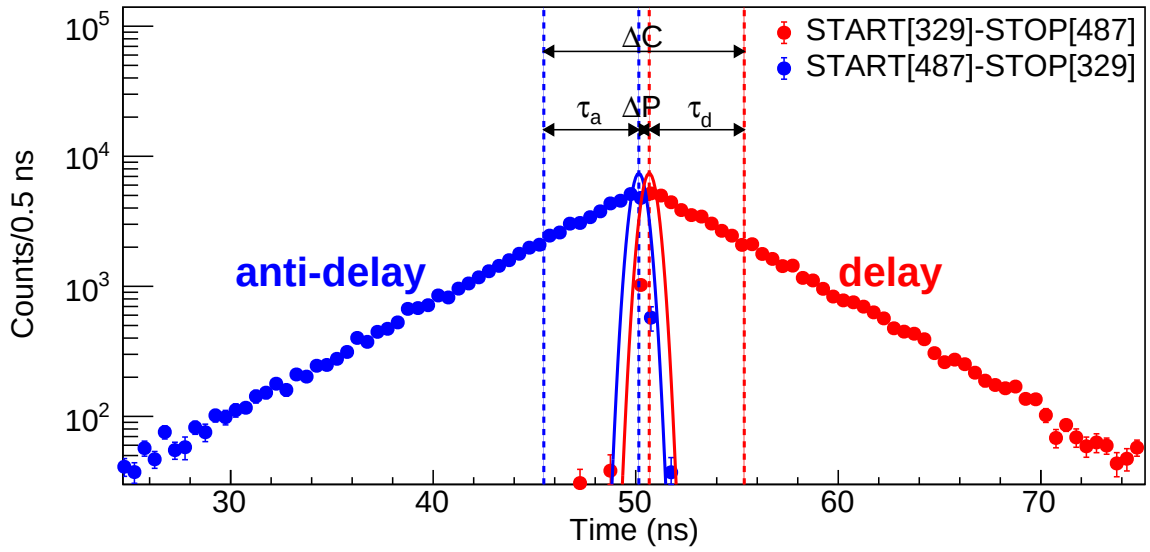


**Figure 4.13.** Lifetime analysis using the $\gamma\gamma$(t) method for the 2083-keV level in $^{140}$Ce. To extract the lifetime, a pair of coincident $\gamma$-rays is selected in the two $LaBr_3$(Ce) detectors: one feeding the 329-keV transition and the other de-exciting it via the 487-keV transition. Two time distributions can be constructed depending on the assignment of the feeding and de-exciting $\gamma$-rays to the detectors, referred to as the delayed (red) and anti-delayed (blue) spectra. For longer lifetimes, exponential decay tails can be fitted in both distributions. For shorter lifetimes, the mean lifetime is obtained from the centroid shift between the delayed and anti-delayed spectra. The centroid shift method requires correcting for time-walk effects, quantified by the $\Delta P$ parameter, which accounts for the time-walk between the two selected energies in both $LaBr_3$(Ce) detectors.

where $\Delta P$ accounts for the energy-dependent time-walk differences between the detectors from a prompt response. In this work the $\gamma\gamma$(t) prompt distribution is obtained from the walk curves of both $LaBr_3$(Ce) detectors, measured using $\beta\gamma$(t) coincidences for known transitions (See Subsec. 4.7.3). It is defined as:

$$P(E_{\text{start}}, E_{\text{stop}}) = -FEP^{\text{START}}_{\text{walk}}(E_{\text{start}}) + FEP^{\text{STOP}}_{\text{walk}}(E_{\text{stop}}), \tag{4.18}$$

and the difference between detector combinations is given by:

$$\begin{aligned} \Delta P &= P(E_{\gamma_f}, E_{\gamma_d}) - P(E_{\gamma_d}, E_{\gamma_f}) \\ &= -FEP^{\text{START}}_{\text{walk}}(E_{\gamma_f}) + FEP^{\text{START}}_{\text{walk}}(E_{\gamma_d}) \\ &\quad + FEP^{\text{STOP}}_{\text{walk}}(E_{\gamma_f}) - FEP^{\text{STOP}}_{\text{walk}}(E_{\gamma_d}). \end{aligned} \tag{4.19}$$

### 4.6.2 Correction methods for $\beta\gamma\gamma$(t) delayed coincidences

The dependence of the timing signal on energy differs between full-energy and Compton events. This behavior originates from the distinct interaction mechanisms. Full-energy events, particularly at high $\gamma$-ray energies, predominantly result from a sequence of multiple interactions, typically initiated by Compton scattering and terminated by photoelectric absorption. The corresponding interaction cross sections govern the likelihood of each process and introduce a dependence on the depth of interaction within the $LaBr_3$(Ce) crystals.

To mitigate these effects, apart from the full-energy walk correction a time walk correction for Compton is also employed [MGM89]. Whereas in in normal $\gamma$-$\gamma$ coincidence high-resolution spectroscopy with HPGe clover detectors subtracting the Compton background from the full-energy peaks is typically done to eliminate true or accidental coincidences unrelated to the selected gamma transition, in fast timing experiments, the background beneath a peak in the $LaBr_3$(Ce) spectrum carries a time dependence that needs to be taken into account.

Background under full-energy peaks in the $LaBr_3$(Ce) spectra mainly originates from Compton events of higher-energy transitions, which can be either in true coincidence or, to a lesser extent, random events. Merely setting a gate on the Compton continuum close to the FEP as a background gate for subtraction does not simply reduce the number of counts in the spectrum but also shifts the centroid of the background spectrum. The magnitude of this correction varies depending on the average lifetime of the transitions contributing to the Compton background and the relative number of background events compared to the peak of interest, ranging from negligible to several picoseconds.

The Compton-correction procedure for $\beta\gamma(t)$ events is illustrated in Fig. 4.14. As an example, the 1009-keV $\gamma$ ray de-exciting the 2446-keV level in $^{138}$Cs from the calibration source is considered. If an energy gate is placed on the 1009-keV peak, the resulting time distribution, defined in Eq. 4.20, where $F(t_i)$ denotes the number of events recorded within the selected energy gates at time $t_i$, will contain both full-energy-peak (FEP) and Compton components (blue time distribution in Fig. 4.14).

$$F(t_i) = F_{\mathrm{FEP}}(t_i) + F_{\mathrm{Compton}}(t_i) \tag{4.20}$$

For each TAC bin, the $LaBr_3$(Ce) energy spectrum is projected to evaluate the relative contributions of FEP and Compton events. A statistical separation is performed by estimating the Compton background through linear interpolation of adjacent energy regions where two selected regions from the background at both sides, left and right, of the peak were used as a reference. The total number of Compton events within the FEP window is estimated from each projection, separately for each time bin (red time distribution in Fig. 4.14). The FEP time distribution (black time distribution in Fig. 4.14) is obtained by subtracting the Compton component $F_{\mathrm{Compton}}(t_i)$ from the total spectrum $F(t_i)$. This approach inherently corrects the intrinsic time-shifts due to the Compton-walk. Uncertainty propagation is performed analytically by combining the statistical uncertainties of the individual spectra. However, caution should be exercised when the FEP to Compton ratio is too low, as the errors would become excessively large, rendering it impossible to obtain a reliable result.

To further suppress the Compton contribution, a third coincidence condition is applied using HPGe detectors. Although the HPGe signal does not contribute to the timing, it improves the selectivity of the $\gamma$ transition of interest. Most of the Compton background in the $LaBr_3$(Ce) spectrum is due to the germanium background. This contribution is estimated by performing the time-distribution analysis separately for the

events gated on the HPGe peak and the Compton background, and subtracting them bin-by-bin. The analysis to derive the $F(t_i)$ and $F_{\mathrm{Comp}}(t_i)$ time spectra, is performed independently for the events in coincidence with the HPGe peak gate and those in the HPGe Compton gate.

$$F(t_i) = F_{\mathrm{HPGe–Peak}}(t_i) - F_{\mathrm{HPGe–Comp}}(t_i) \tag{4.21}$$

$$F_{\mathrm{Comp}}(t_i) = F_{\mathrm{HPGe–Comp}}(t_i) - F_{\mathrm{HPGe–Comp}}(t_i) \tag{4.22}$$

The combined correction based on $LaBr_3(Ce)$ energy spectra and gated HPGe coincidences allows for a robust extraction of Compton-free FEP time distributions, even in complex decay schemes. However, the use of triple $\beta\gamma\gamma(t)$ events comes at a significant cost in statistics due to the low absolute efficiency of the HPGe detectors. This methodology is employed throughout the analysis to ensure accurate half-life determinations from $\beta\gamma\gamma(t)$ time spectra. For a detailed account of the background subtraction technique and its application to $\beta\gamma(t)$ timing, the reader is referred to Ref. [Ben20].

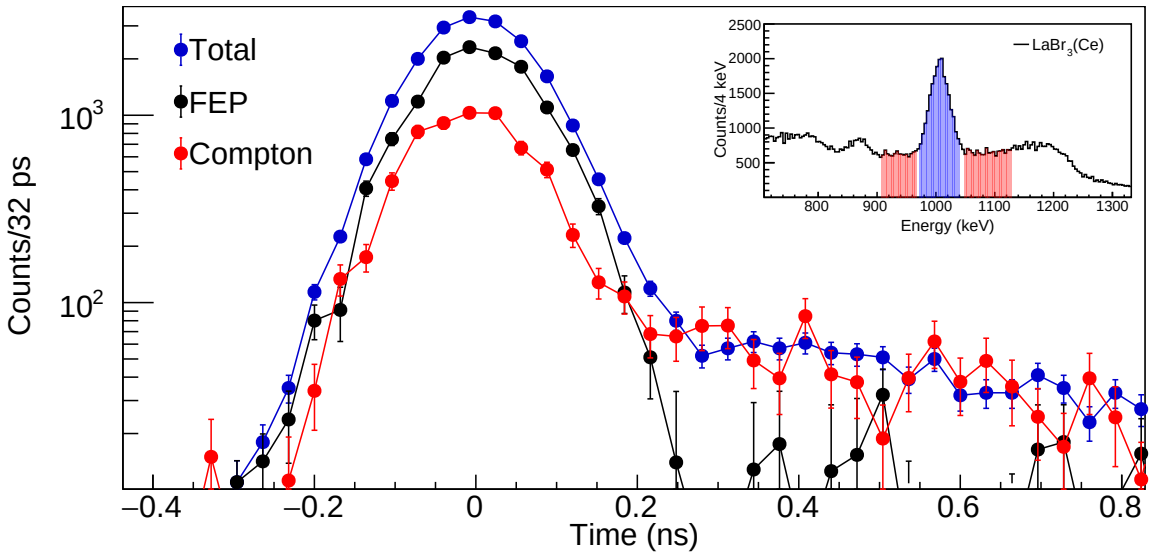


**Figure 4.14.** Compton correction procedure for $\beta\gamma(t)$ events for de $^{138}$Cs $\beta$-decay. The main panel shows TAC timing spectrum projection of $\beta$-$LaBr_3(Ce)(t)$ events. $LaBr_3(Ce)$ energy projections for the colored bins from the TAC spectrum. Time distributions for the Peak (blue), Compton (red), and FEP (black) events. The inset plot shows the $LaBr_3(Ce)$ energy spectrum. The chosen energy gates to select the 1009-keV peak (blue) and to estimate the Compton background (red) are also plotted. See text for details.

### 4.6.3 Correction methods for $\gamma\gamma(t)$ delayed coincidences

In the case of $\gamma\gamma(t)$ between two $LaBr_3(Ce)$, the corrections of the Compton background beneath the peak is a two-dimensional problem since one needs to account for the Compton background in both START and STOP detectors. Fig. 4.15 shows the typical $\gamma\gamma(t)$ coincidence matrix obtained for the two $LaBr_3(Ce)$ detectors in the $\beta$-decay of the $^{140}$La source. The region depicted in the figure, shows the 329-

487 coincidence corresponding to the [2412- keV $3^+$]→[2083-keV $4^+$]→[1596-keV $2^+$] cascade. By analyzing the time distribution of this coincidence, one can extract the half-life of the 2083-keV, which is known to be 3.474(10) ns in Ref. [MF95]. Within this region we can identify both the delayed START[329]-STOP[487] and anti-delayed START[487]-STOP[329] combinations.

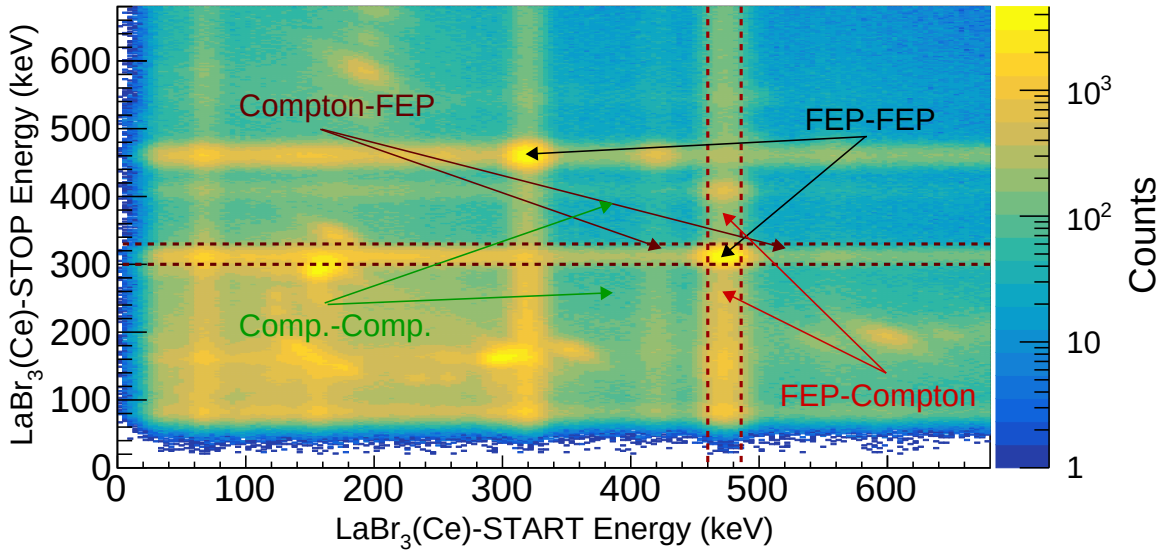


**Figure 4.15.** Gamma-gamma coincidence matrix measured for the $^{140}$Ba $\beta$ decay between two $LaBr_3$(Ce) detectors. The darker red dashed lines indicate the gates on the 329-keV transition in the $LaBr_3$(Ce)-STOP detector, while the dark red dashed lines indicate the gates on the 487-keV transition in the $LaBr_3$(Ce)-START detector.

When selecting the coincidence peak of interest by means of a double energy gate in both $LaBr_3$(Ce) detectors, it is not possible to avoid the contribution of Compton events. We can distinguish 4 components in the selected region depending on the type of event that ocurred in each detector, either full absorption or Compton (see Eq.4.6.3). The total distribution obtained by simply gating in both detectors correspond to the sum of the 4 components. The FEP–FEP, which contains the information of interest, built by the events where both $\gamma$-rays where fully absorbed within the detectors. The FEP–Compton and Compton–FEP distributions are built by the events where only one of the scintillators absorbed completely the $\gamma$-ray of interest, while the other detected a Compton event from a higher energy transition which deposited the same energy than the one of interest. Depending on which $LaBr_3$(Ce) detected the FEP and Compton, they will contribute to the FEP-Compton or Compton-FEP respectively. The last contribution arise from events where two Compton scattering events are detected, with energies matching the ones of interest.

$$F_{Peak-Peak}(t_i) = F_{FEP-FEP}(t_i) + F_{FEP-Comp}(t_i) + F_{Comp-FEP}(t_i) + F_{Comp-Comp}(t_i) \tag{4.23}$$

Separation of the contributions in an event by event basis is not posible. However, they can be extrapolated statistically from the analysis of the time distribution from

the Compton background near to the peak. In order to do so, three energy gates are defined for each START and STOP detector. One for the Peak of interest, and another for the Compton background at the left and the right of the peak. Analogously to the $\beta\gamma$(t) case, a bin by bin analysis of the TAC is perform, analyzing the $\gamma\gamma$ energy matrix obtained after selecting the events corresponding only to a specific bin of the TAC. The combination of the Compton background gates in each detector gives rise to 4 Compton-Compton reference regions. These regions contain only Compton-Compton events. The contribution of Compton-Compton events for each TAC bin is estimated by estimating the number of counts present in each Compton-Compton region. This information is used to build a plane in the 2D energy matrix containing the amount of Compton-Compton events per keV$^2$. The total contribution of these Compton-Compton events is then estimated by integrating this surface over the area defined by the two energy gates defined for the Peaks.

The FEP-Compton and Compton-FEP components can be derived from the energy regions defined by combining the gate at the peak in one detector, with the gates corresponding with the Compton-background at the other. For example, the FEP-Compton distribution can be extracted by selecting the events with an energies within the peak gate in the START detector and then projecting the energy spectra for each TAC bin in the stop detector. The contribution of Compton events below the peak can thus be extracted by an analogous way than in the $\beta\gamma$(t) case. Nonetheless, the extracted time-distribution, does not correspond with the one containing only FEP-Compton events. This is because, the energy gate in the START detector contain also Compton events, hence, this distribution is the Peak-Compton which correspond to the sum of FEP-Compton plus Compton-Compton. The FEP-Compton can be derived by subtracting the Compton-Compton time distribution previously derived from the Peak-Compton obtained by this method.

$$F_{FEP-Comp}(t_i) = F_{Peak-Comp}(t_i) - F_{Comp-Comp}(t_i) \tag{4.24}$$

In an analogous manner, the Compton-FEP time distribution can be also derived by following the same procedure but swapping the detectors:

$$F_{Comp-FEP}(t_i) = F_{Comp-Peak}(t_i) - F_{Comp-Comp}(t_i) \tag{4.25}$$

Finally the FEP-FEP time distribution can be obtained bysubtracting the different time distributions derived for the three Compton background components.

$$F_{FEP-FEP}(t_i) = F_{Peak-Peak}(t_i) - F_{Peak-Comp}(t_i) - F_{Comp-Peak}(t_i) + F_{Comp-Comp}(t_i) \tag{4.26}$$

Uncertainty propagation is performed analytically by combining the statistical uncertainties of the individual spectra, ensuring correct estimation of the uncertainty in the derived FEP–FEP contribution. Fig. 4.16 shows all the distributions derived for the 329-487 delayed-coincidence peak in $^{140}$Ce. A pure exponential decay with no prompt component should be observed due to the $T_{1/2}$.=3.470(10) ns half-life. However a prompt gaussian component can be observed at the beginning of the spectra in the Peak-Peak distribution, which contains all the background. After

the background subtraction procedure, the derived FEP-FEP time spectrum is derived, showing only the exponential decay behavior that is expected for this coincidence.

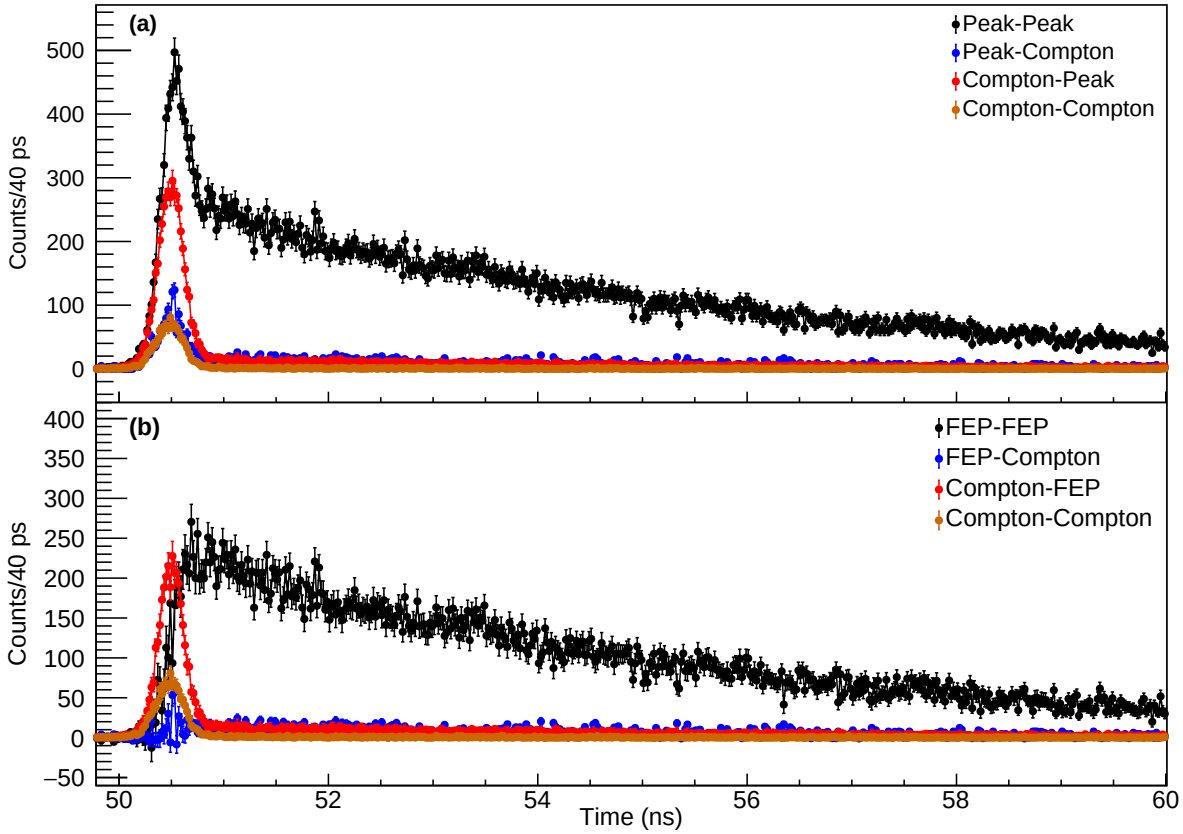


**Figure 4.16.** Analysis of Compton background contributions in $\gamma\gamma$(t) coincidence events for the lifetime measurement of the 2083-keV level in $^{140}$Ce. (a) Time distributions obtained directly from the energy gates. (b) *Decoupled* time distributions corresponding to the four individual components.

To further enhance selectivity and suppress background, additional coincidence requirements—such as gating on the proton arrival, $\beta$ detection, or coincident $\gamma$-rays in HPGe detectors—may be applied. However, such constraints drastically reduce the available statistics. As a result, triple-coincidence $\gamma\gamma\gamma$(t) analyses are only viable for large statistic data sets. For a detailed account of the background subtraction technique and its application to $\gamma\gamma$(t) timing, the reader is referred to Ref. [Ben20].

## 4.7 Time calibrations

The fast-timing method requires precise timing calibrations. In particular, it is necessary to calibrate the dependence of the time response on the deposited energy. These time-response characteristics are commonly referred to as time-walk curves. These shifts in time response are on the order of nanoseconds or even picoseconds, making them particularly relevant for the measurement of half-lives below 100 ps. In this section, a detailed examination will be carried out of the time response of the $\beta$ detectors,

and particularly that of the $LaBr_3$(Ce) detectors, because they are the most significant correction in lifetime measurements in fast-timing method.

### 4.7.1 TAC calibration

In order to obtain the channel-to-ps equivalence in the TAC modules, an ORTEC 462 Time Calibrator was used. This module generates two consecutive signals, a START and a STOP, with an adjustable period and range, and a highly precise frequency. The spectrum generated in the TAC $\beta$PMT-$LaBr_3$(Ce) is shown in Fig. 4.17. The pulses produced are gaussian-shaped, separated by a distance of 10 ns in the IS685 experiment. A linear calibration is performed to obtain the channel-to-ps conversion (see Fig. 4.18).

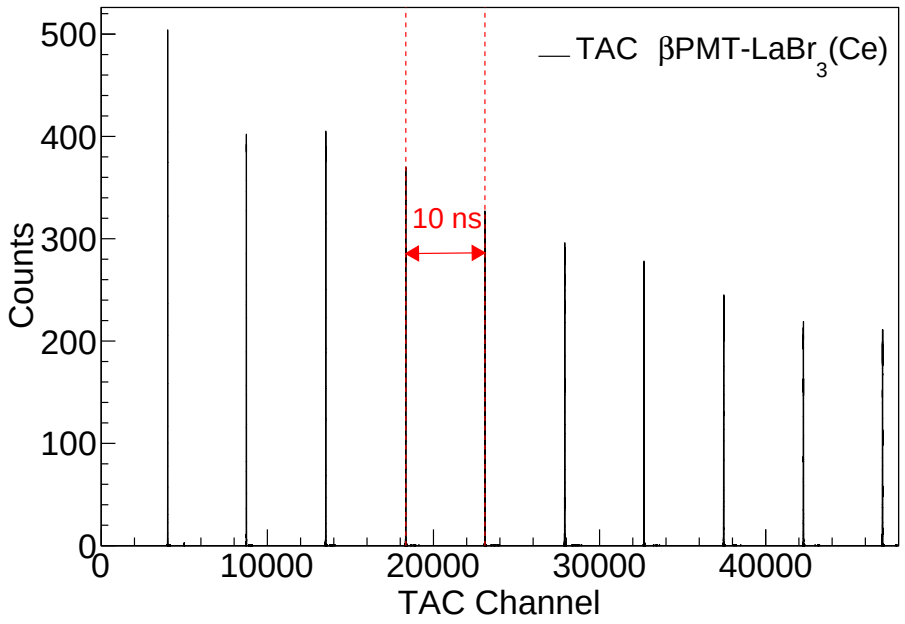


**Figure 4.17.** Time distribution of the TAC $\beta$PMT-$LaBr_3$(Ce) using ORTEC 462 Time Calibrator. All the TACs employed have the same time distribution structure. Each pulse had 10 ns period.

To validate the values obtained from the linear fits, well-known half-lives of calibration sources were employed. In particular, the 2083-keV level in the $\beta$-decay of $^{140}$La, with a half-life of 3.474(10) ns as reported in Ref. [MF95], was used as a reference. This measurement was applied to the three TAC $\beta$–$LaBr_3$(Ce) detector modules. The time-delayed $\beta\gamma\gamma$(t) spectra between the $\beta$ and $LaBr_3$(Ce) detectors, gated by the 487-keV transition, are shown in Fig. 4.19. The lifetime was obtained by a $\chi^2$ fit of the time distribution to a exponential decay plus a constant background to account for the random background.

In the case of the TAC LaBr3(Ce)–LaBr3(Ce) module, the time-delay distributions between the two $LaBr_3$(Ce) detectors are obtained for $\gamma\gamma$(t) events. The spectra are constructed by selecting the 329-keV $\gamma$ ray that feeds the level in one detector, and the 487-keV peak in the other one. Depending on the selected $\gamma$ line in the START

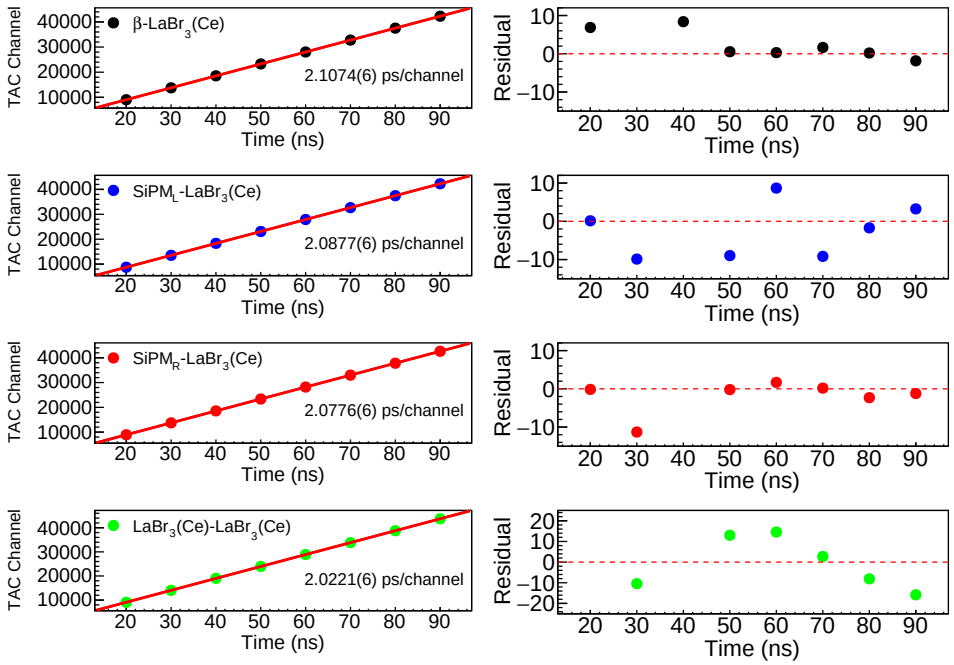


**Figure 4.18.** Linear time calibration of the TAC modules (left). The corresponding TAC channel-to-time conversion factors are indicated. The residuals for each TAC module are shown on the right.

and STOP detectors, either the delayed or the anti-delayed distributions are derived. The lifetime was obtained by a $\chi^2$ fit of the time distribution to a exponential decay plus a constant background to account for the random background. All the results were in accordance with the previously reported. This evidence suggests that the time calibrations obtained using the Time Calibrator are robust and reliable.

### 4.7.2 $\beta$-walk

The thin $\beta$ plastics allowed only a fraction of the $\beta$ particles energy to be deposited, resulting in a more uniform time response. Nevertheless, a residual dependence on the $\beta$ particle energy remains and requires correction. Additionally, $\gamma$-rays and fast neutrons, can deposit minimal energy contributing to irregularities in the low-energy range of the $\beta$-decay spectrum. All of these effects result in a time response that is not completely uniform, leading to what is known as the $\beta$-walk curve. This curve, is obtained by dividing the $\beta$ energy spectrum into small intervals and projecting each one onto the TAC spectrum using $\beta\gamma$(t) coincidences. As an example, the $\beta$-walk curve corresponding to the decay of $^{128}$Cd was obtained by applying a gate on the 1169-keV $\gamma$-ray, attributed to the $(2^+) \rightarrow (0^+)$ transition in $^{128}$Sn [FC79, FHS81], detected with the $LaBr_3$(Ce) detector (as shown in Fig. 4.21). The correction is achieved by shifting the TAC value by a specific number of channels, depending on the energy of the $\beta$ particle. The $\beta$-walk curve shows a variation of more than 350 ps along the $\beta$ energy range. The $\beta$-walk correction is necessary for the lifetime analysis and must be applied individually to each isotope of the decay chain, as the $\beta$-walk is sensitive to the $Q_\beta$ value.

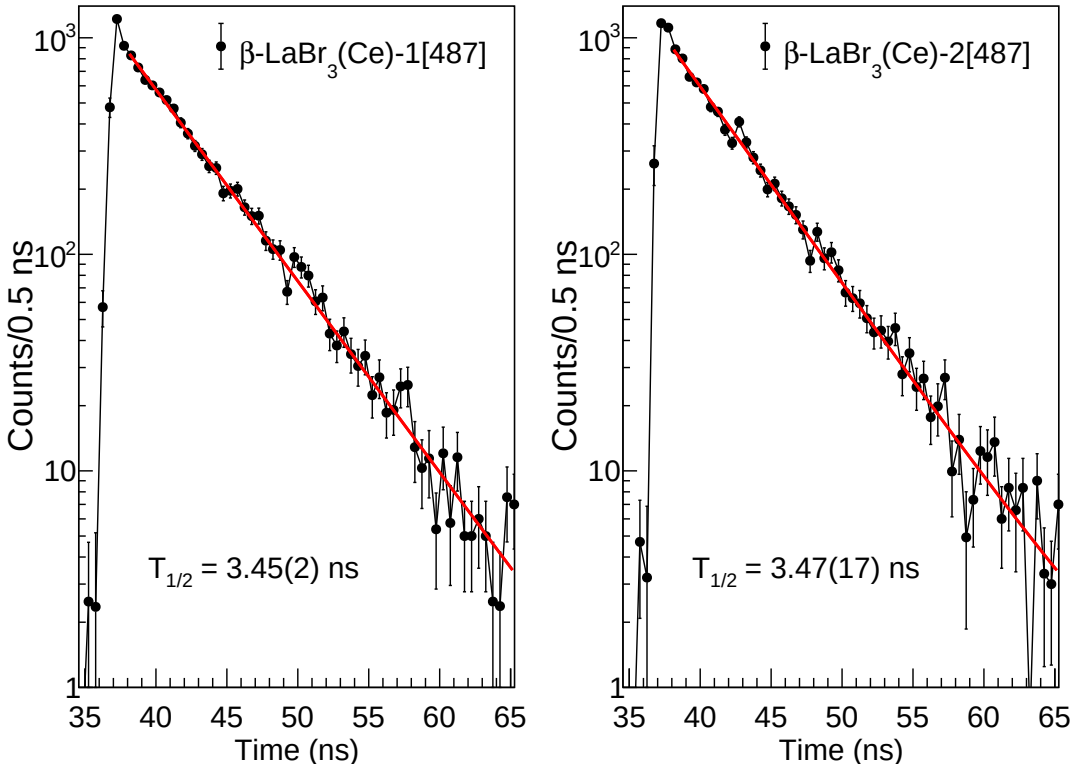


**Figure 4.19.** Half-life of 2083-keV state in $^{140}$Ce. The analysis was performed using $\beta\gamma$(t) events. The lifetime was extracted by fitting an exponential decay, along with a constant background, to the tail of the spectra. The 2083-keV level is populated in the $\beta$ decay of $^{140}$La, and its half-life was measured to be 3.474(10) ns in Ref. [MF95].

### 4.7.3 $LaBr_3$(Ce) FEP-walk

It is well known that the $LaBr_3$(Ce) detectors exhibit a time response dependence based on the $\gamma$-rays energy deposited. This time dependence as a function of energy is called the FEP walk. To characterize the FEP walk in both $LaBr_3$(Ce) detectors, the centroid position of well-known and tabulated prompt or quasi-prompt $\gamma$-rays at different energies is analyzed. Any transition that de-excites a level with a well-known lifetimes in the range below 10 ps can also be used, correcting the centroid position for that lifetime. The $LaBr_3$(Ce) FEP-walk for each detector depends on many factors, such as the shape of the crystal, PMT electronics, CFD pulses, among others. The range of energies, from 100 keV to 2600 keV, was covered by the use of an entire set of calibration sources. Firstly the transitions of the $^{140}$Ba $\rightarrow$ $^{140}$La $\rightarrow$ $^{140}$Ce were analyzed. Additionally, $^{138}$Cs, $^{88}$Rb and $^{24}$Na were applied. The list of $\gamma$ lines employed to measured the FEP-walk curves are shown in Tab. 4.3

The results are fitted to Eq. 4.27

$$FEP_{walk}[E_\gamma] = a_0 + \frac{a_1}{\sqrt{E_\gamma + a_2}} + a_3 \cdot E_\gamma + a_4 \cdot E_\gamma^2 \tag{4.27}$$

The FEP walk for each isotope present the same shape but shifted by an offset (term $a_0$ in Eq. 4.27). This constant is obtained by taking the $^{140}$Ba $\beta$-decay data reference.

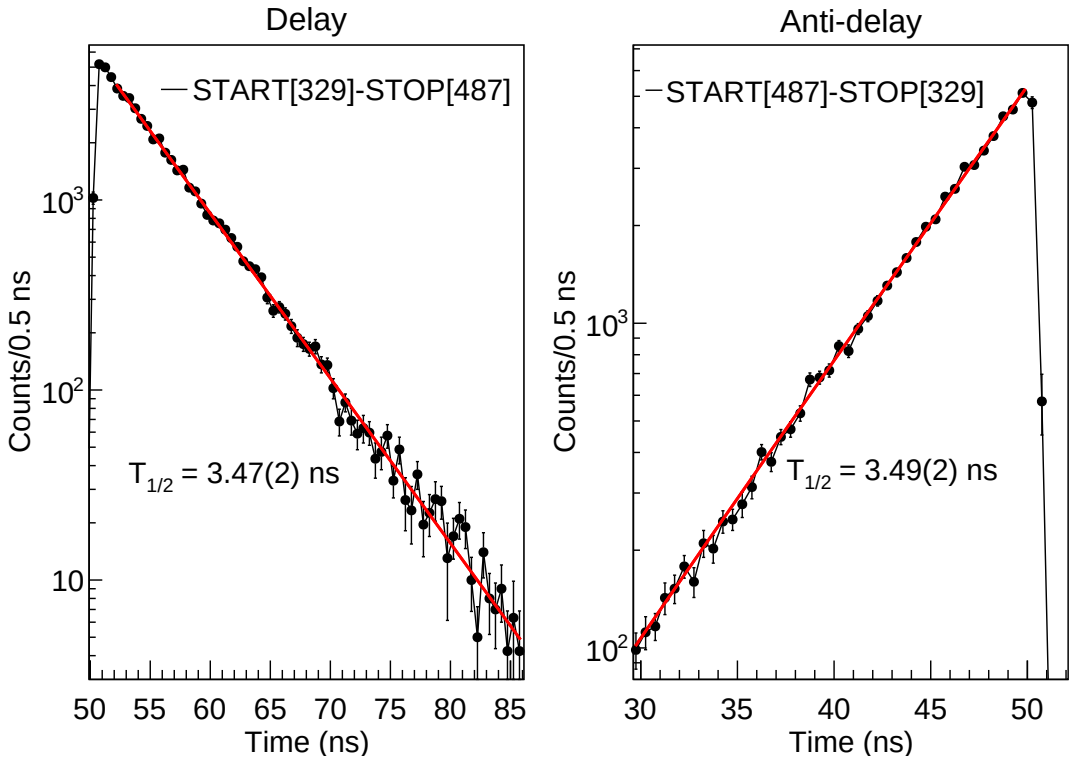


**Figure 4.20.** Half-life of 2083-keV state in $^{140}$Ce. The analysis was performed using triple $\gamma\gamma$(t) events. The lifetime was extracted by fitting an exponential decay, along with a constant background, to the tail of the spectra for the delay and anti-delay time distributions. The 2083-keV level is populated in the $\beta$ decay of $^{140}$La, and its half-life was measured to be 3.474(10) ns in Ref. [MF95].

It is important to emphasize that the FEP-walk exclusively measures relative timing differences. The FEP-walk curves that were calculated for both detectors in the IS685 experimental campaign are displayed in Fig. 4.22

## 4.8 Summary of the chapter

This chapter has described the experimental setup at the IDS included a range of 11 detectors, such as HPGe clover detectors for $\gamma$-ray spectroscopy and $LaBr_3$(Ce) detectors and $\beta$ detectors for fast-timing measurements, as well as the electronic setup, which processes the signals produced in the detectors. The energy and efficiency calibrations carried out for the IDS detectors are described. A complete set of calibration sources was employed.

Additionally, this chapter presents the analytical techniques employed to study the nuclear structure of neutron-rich isotopes. The ATD $\beta\gamma\gamma$(t) method was implemented to determine level lifetimes in the sub-nanosecond regime. Two analysis strategies—deconvolution and centroid-shift—were applied depending on the lifetime scale. Accurate timing required dedicated calibrations of TAC modules, energy-dependent time-walk corrections for both $\beta$ and $LaBr_3$(Ce) detectors, and detailed treatment of Compton background. Additionally, the $\gamma\gamma$(t) timing method was employed when $\beta$-

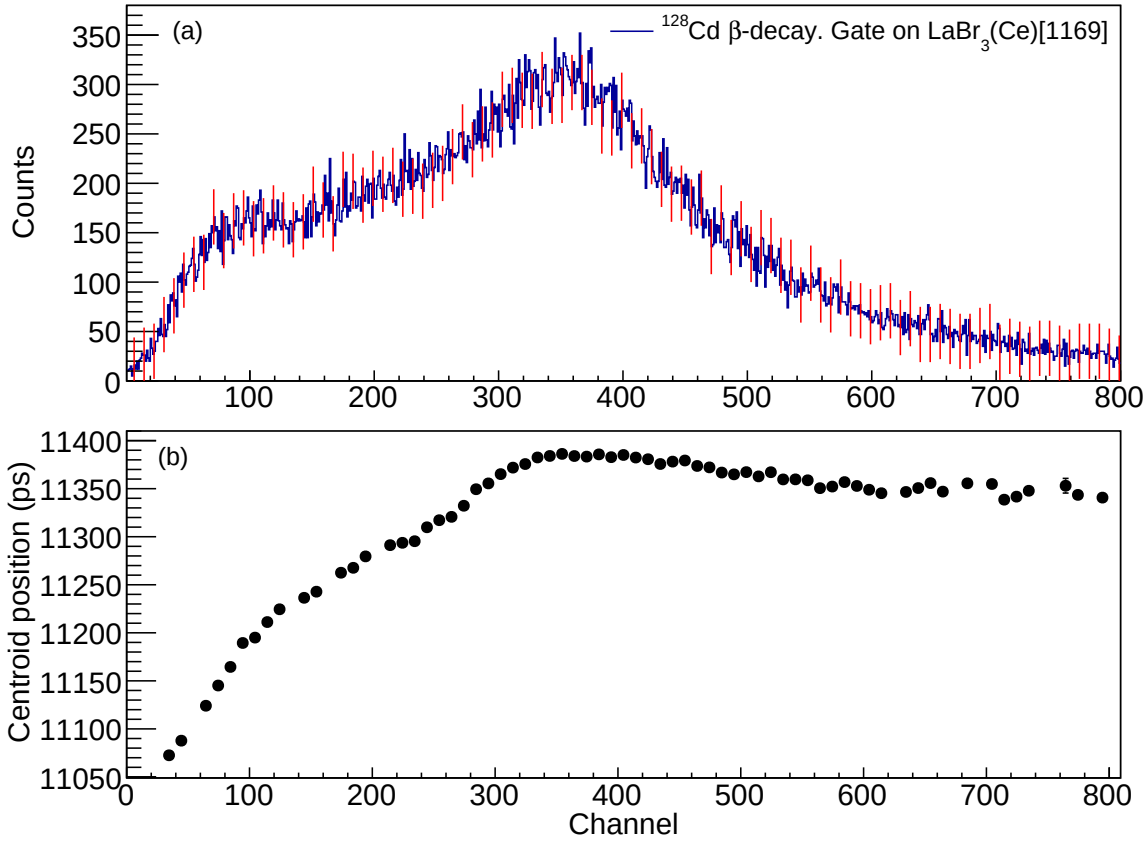


**Figure 4.21.** (a) $\beta$-energy spectrum obtained by projecting 1169-keV strongest $\gamma$ line from $^{128}$In $\beta$ decay. (b) $\beta$-walk curve. A variation exceeding 300 ps across the $\beta$ energy spectrum is observed. See the text for more details.

feeding was not selective or insufficient. The combination of these techniques provides a robust experimental framework for extracting level lifetimes.

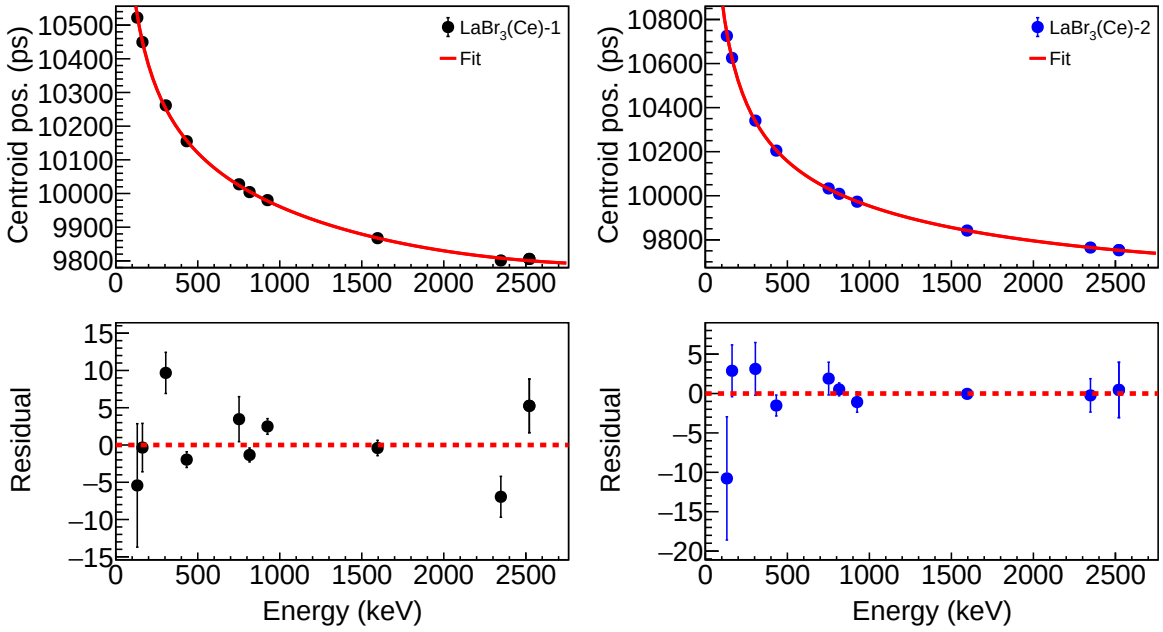


**Figure 4.22.** FEP walk curves for the $LaBr_3(Ce)$ detectors as a function of prompt $\gamma$-ray energy from the IS685 experimental campaign. The residuals are displayed in the bottom graph.

**Table 4.3.** List of $\gamma$ transitions employed to measured the FEP-walk curves. The energy gate of the HPGe detectors is also indicated. Data taken from NNDC Decay radiation information database [NND25].

| **Isotope** | **$E_{level}$ (keV)** | **$T_{1/2}$ (ps)** | **$LaBr_3(Ce)$ (keV)** | **HPGe (keV)** | **Method** |
|---|---|---|---|---|---|
| $^{140}$Ba | 2521.43(3) | $\leq$2.4 | 109.422(11) | 815.772(19) | $\beta\gamma\gamma$(t) |
| | | | 925.189(21) | 1596.21(4) | $\beta\gamma\gamma$(t) |
| | | | 2521.40(5) | | $\beta\gamma$(t) |
| $^{140}$Ba | 2525.77(3) | $\leq$ 2.5 | 919.550(23) | 1596.21(4) | $\beta\gamma\gamma$(t) |
| | | | 432.493(12) | 487.021(12) | $\beta\gamma\gamma$(t) |
| $^{140}$Ba | 2464.09(4) | *Prompt* | 867.846(20) | 1596.21(4) | $\beta\gamma\gamma$(t) |
| $^{140}$Ba | 2412.02(3) | 1.3(4) | 815.772(19) | 1596.21(4) | $\beta\gamma\gamma$(t) |
| $^{140}$Ba | 2347.89(3) | 0.15(10) | 751.637(18) | 1596.21(4) | $\beta\gamma\gamma$(t) |
| $^{140}$Ba | 1596.24(3) | 0.123(14) | 1596.21(4) | 815.772(19) | $\beta\gamma\gamma$(t) |
| $^{138}$Cs | 2639.53(7) | *Prompt* | 2639.59(19) | | $\beta\gamma$(t) |
| $^{138}$Cs | 2445.64(6) | 5(4) | 138.08(6) | 871.72(7) | $\beta\gamma\gamma$(t) |
| | | | 227.76(6) | 2218.00(10) | $\beta\gamma\gamma$(t) |
| | | | 546.990(15) | 462.785(5) | $\beta\gamma$(t) |
| | | | 1009.78(7) | 1435.77(7) | $\beta\gamma$(t) |
| $^{138}$Cs | 2307.59(6) | 7(3) | 408.98(6) | 462.785(5) | $\beta\gamma\gamma$(t) |
| $^{138}$Cs | 2217.92(6) | 15.2(3) | 2218.00(10) | 227.76(6) | $\beta\gamma\gamma$(t) |
| $^{138}$Cs | 1435.86(5) | 0.202(8) | 1435.77(7) | 1009.78(7) | $\beta\gamma\gamma$(t) |
| $^{88}$Rb | 2734.128(12) | 0.70(5) | 898.03(4) | 1836.00(5) | $\beta\gamma\gamma$(t) |
| $^{88}$Rb | 1836.077(21) | 0.154(8) | 1836.00(5) | 898.03(4) | $\beta\gamma\gamma$(t) |
| $^{24}$Na | 4122.844(12) | *Prompt* | 2754.088(11) | 1368.625(5) | $\beta\gamma\gamma$(t) |
| $^{24}$Na | 1368.667(5) | *Prompt* | 1368.625(5) | 2754.088(11) | $\beta\gamma\gamma$(t) |

# Chapter 5

# Fast-timing in the $^{128}$Cd $\beta$-decay chain

Lifetime measurements of excited states provide direct access to electromagnetic transition probabilities $B(X\lambda)$. These quantities are sensitive to the underlying configuration of nuclear states and offer a stringent test of shell-model predictions, particularly when extracted from lifetime measurements using fast-timing techniques.

The $A = 128$ isobars, including $^{128}$In and $^{128}$Te, are close to shell closures and have relatively simple level schemes. However, experimental knowledge of their excited states is limited, with sparse lifetime information available. As such, the application of fast-timing spectroscopy to the $^{128}$Cd decay chain provides valuable insights into the structure of these neutron-rich nuclei.

The $\beta$ decay of $^{128}$Cd provides access to the excited structure of $^{128}$In and $^{128}$Te, directly from $^{128}$Cd $0^+$ ground state and from the $^{128}$Sb $5^+$ isomer, respectively (see Fig. 5.1). The difference in half-lives between $^{128}$Cd ($T_{1/2} = 256(5)$ ms) and $^{128}$Sb ($T_{1/2} = 10.4(2)$ min [Eva21]) facilitates a clear separation of their respective decay activities based on the time distribution relative to the implantation cycle. This chapter presents the results of lifetime measurements of excited states in the $^{128}$Cd $\beta$-decay using fast-timing techniques, see Chap. 4.

Chap. 5 is structured as follows: The fast-timing results for $^{128}$In, obtained via the $\beta$ decay of $^{128}$Cd are presented in Sec. 5.1. Sec. 5.2 focuses on the fast-timing analysis of $^{128}$Te following the $\beta$ decay of the $5^+$ isomer in $^{128}$Sb. The comparison of the extracted $B(E2)$ values with shell-model predictions are discussed in Subsec. 5.2.4. Finally, the main conclusions of Chap. 5 are summarized in Sec. 5.3.

## 5.1 Fast-timing investigation of $^{128}$In

No lifetime measurements in the sub-nanosecond range have previously been reported for the excited states of $^{128}$In. The available experimental data on the $\beta$ decay of $^{128}$In originate primarily from a study conducted at the OSIRIS ISOL facility in Studsvik, Sweden, by Fogelberg *et al.* [Fog88], and more recently from measurements performed with the GRIFFIN spectrometer at the TRIUMF facility in Vancouver, Canada, by

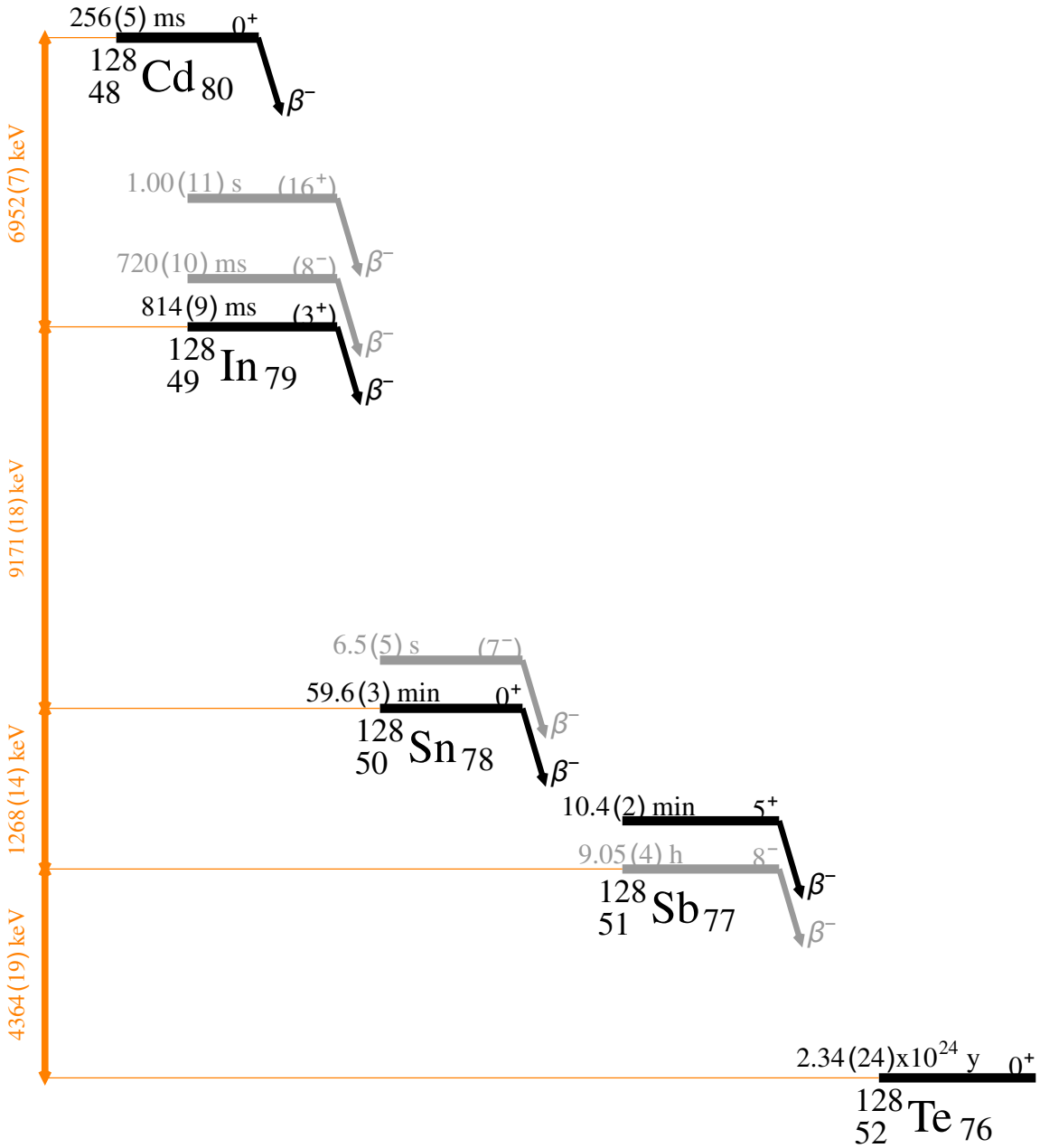


**Figure 5.1.** Decay scheme of $^{128}$Cd. $Q_{\beta^-}$ values are indicated in orange. Data are taken from Ref. [NND25], except for the half-lives of $^{128g}$Cd and $^{128g}$In, which have been extracted in the present work. Isomers that are not populated in the $\beta^-$ decay of the $0^+$ ground state of $^{128}$Cd are shown in grey. The isomers in the scheme are not drawn to scale.

Bernier *et al.* [Ber18] (see Fig. 5.3). Both the spin and parity of the ground-state remain unmeasured experimentally, and the proposed $(3^+)$ assignment is based on systematics and shell-model proton–neutron coupling considerations [Ber18, SGP$^+$04]. Two $\beta$-decaying isomeric states are known in $^{128}$In: a low-spin $(8^-)$ isomer and a high-spin $(16^+)$ isomer. The $(8^-)$ isomer, denoted $^{128m1}$In, was first identified at an excitation energy of 321 keV with a measured half-life of $T_{1/2} = 0.72(10)$ s, as reported in Ref. [GELF86]. Subsequent measurements yielded excitation energies of

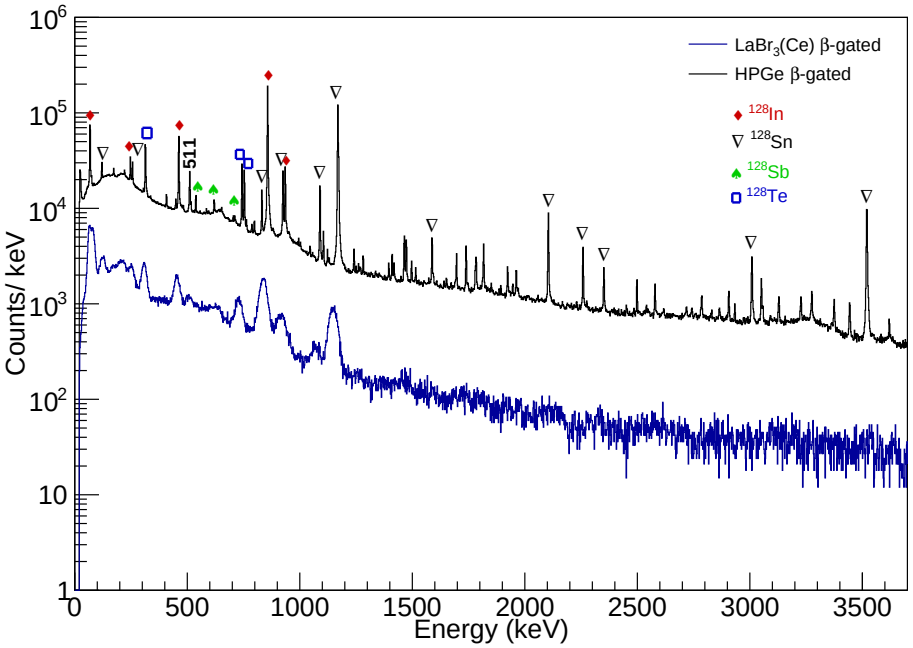


**Figure 5.2.** Beta-gated $LaBr_3$(Ce) and HPGe energy spectra observed in the $\beta$ decay of $^{128}$Cd. A large number of $\gamma$-ray transitions are observed in the HPGe $\beta$-gated spectrum (black), reflecting the high detection efficiency and energy resolution of the detector. To achieve the level of selectivity required for precise lifetime measurements with $LaBr_3$(Ce) detectors, triple-coincidence events of the type $\beta\gamma\gamma$(t) are employed. The strongest peaks associated with the $\beta$ decay chain of $^{128}$Cd are identified and labeled.

340(60) keV [SBLW90], 262(13) keV [BKL$^+$18], and 285.1(25) keV, as determined at the IGISOL facility using the JYFLTRAP Penning trap [NKK$^+$20]. The most recent measurement reports an excitation energy of 259(28) keV, obtained with the TITAN multiple-reflection time-of-flight mass spectrometer (MR-TOF-MS) [IBD$^+$21]. The high-spin ($16^+$) isomer, labeled $^{128m2}$In, was first observed in Ref. [NKK$^+$20] with an excitation energy of 1797.6(20) keV. A lower limit of $T_{1/2} > 3$ s was established for this state. Its existence was subsequently confirmed in Ref. [IBD$^+$21], which also reported an excitation energy of 1813(17) keV. Neither of the isomeric states were observed in the present experiment, as they are not populated via the $\beta$ decay of the $^{128}$Cd $0^+$ ground state.

In Ref. [Fog88], the 248-keV transition was assigned as a mixed $M2/E3$ multipolarity, and the 68-keV transition was identified as $M1$, both deduced from internal conversion electron spectroscopy. It is important to note that the decay scheme was based on an unpublished study, and consequently, detailed experimental and analytical information is limited. The decay scheme initially proposed in 1988 was later re-evaluated by the Evaluated Nuclear Structure Data File (ENSDF) evaluators in 2015 [ET15]. Notably, the tentative spin and parity assignment of the 316-keV level was revised from ($2^-$) to ($1^-$) [ET15]. The half-life of the 248-keV transition was measured to be 23(2) $\mu$s, as reported in Ref. [SGP$^+$04]. In Ref. [Ber18], decay spectroscopy of $^{128}$Cd led to the identification of 32 previously unreported $\gamma$ transitions and the construction of 11 new excited states in the daughter nucleus. A total of

eight allowed Gamow–Teller $\beta$ decays were observed populating tentative $(1^+)$ levels, supporting their spin-parity assignments. Additionally, first-forbidden $\beta$ decays were found to populate seven states. Tentative spin assignments of $(0^-, 1^-, 2^-)$ remain for these levels (see Fig. 5.3). For three of these states, located at 248, 316, and 711 keV, were further constrained through $\gamma\gamma$ angular correlation measurements, which excluded the $0^-$ assignment. The half-life of the isomeric state at 247 keV was measured in Ref. [Ber18], yielding a value of 245.4(30) ms.

The following sections detail the investigation of the lifetime of a low-lying excited state in $^{128}$In populated via the $\beta$ decay of the $0^+$ ground state of $^{128}$Cd using $\beta\gamma\gamma$(t) fast-timing methods providing the first lifetime measurements in the sub-nanosecond regime for this nucleus.

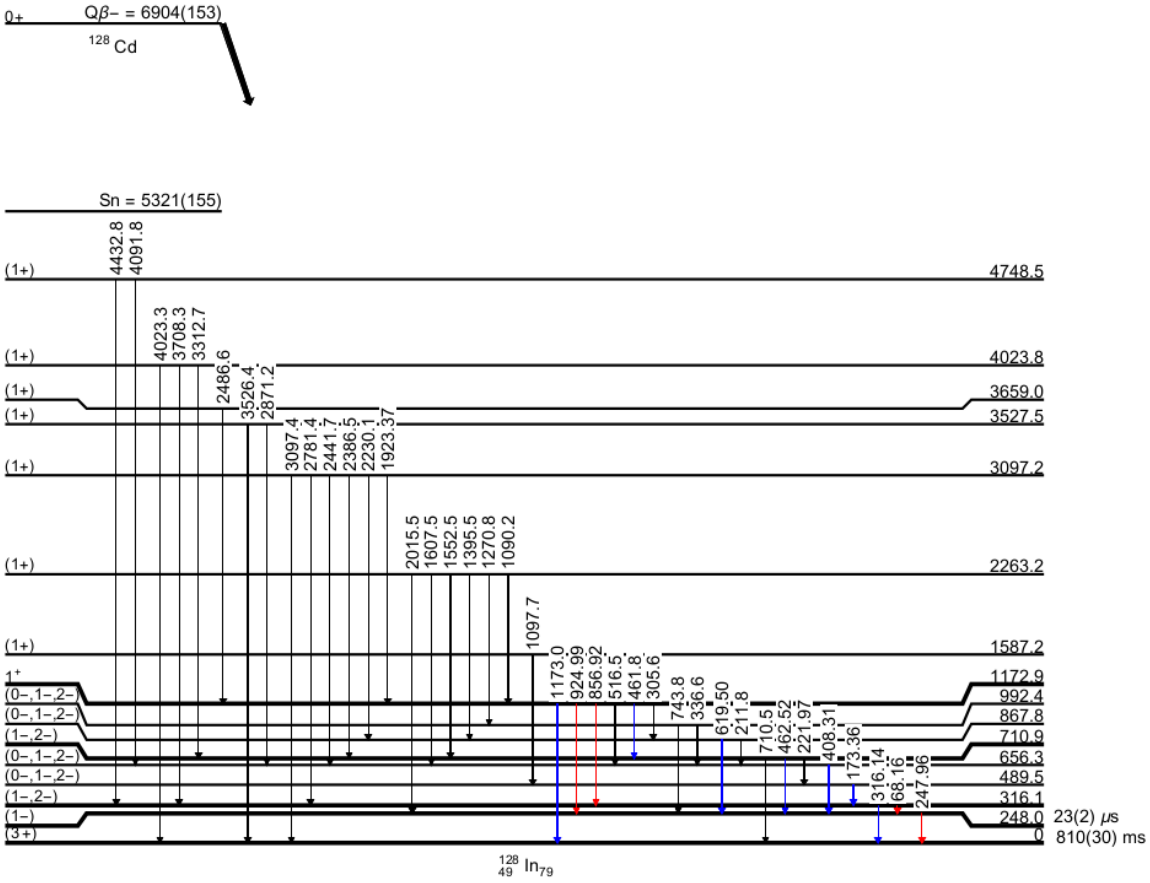


**Figure 5.3.** Proposed level scheme of $^{128}$In observed following the $\beta$ decay of the $^{128g}$In $0^+$ ground state in Ref. [Ber18]. The colour of the transitions represents the intensity of the $\gamma$-ray relative to the 248-keV transition: $I_\gamma > 10\%$ in red, $I_\gamma < 10\%$ in blue, and $I_\gamma < 2\%$ in black.

### 5.1.1 Lifetime of the 315-keV level

The main feeding of the 315-keV level originates from $\gamma$-ray cascades following the de-excitation of higher-lying states, most prominently the 857-keV transition from the 1173-keV level (see Fig. 5.3). The time spectra used for the lifetime analysis were

constructed from triple $\beta\gamma\gamma$(t) coincidence events, selecting the 315-keV $\gamma$-ray in the $LaBr_3$(Ce) detectors. The $LaBr_3$(Ce) detectors exhibit a nonlinear time response below 100 keV, thus the 68-keV $\gamma$-ray transition was excluded. The 857-keV $\gamma$-ray transition was used as a timing reference, gating on the 68- and 315-keV $\gamma$-rays detected in HPGe detectors. A time window of 0–800 ms relative to the proton impact was used to enhance the selectivity for $\gamma$ rays associated with the decay of $^{128}$Cd $\beta$ decay (see Fig. 5.4). The statistics from both combinations were summed to obtain the final time distribution used in the analysis (see Fig. 5.5). Fig. 5.5 (b) illustrates the centroid-shift method employed to determine the level lifetime. A lifetime of $\tau = 27(15)$ ps was obtained using the $LaBr_3$(Ce)-1 detector, while the measurement with the $LaBr_3$(Ce)-2 detector yielded $\tau = 21(12)$ ps. From the weighted average of both measurements, a final value of $\tau = 23(9)$ ps was determined, corresponding to a half-life of $T_{1/2} = 16(6)$ ps.

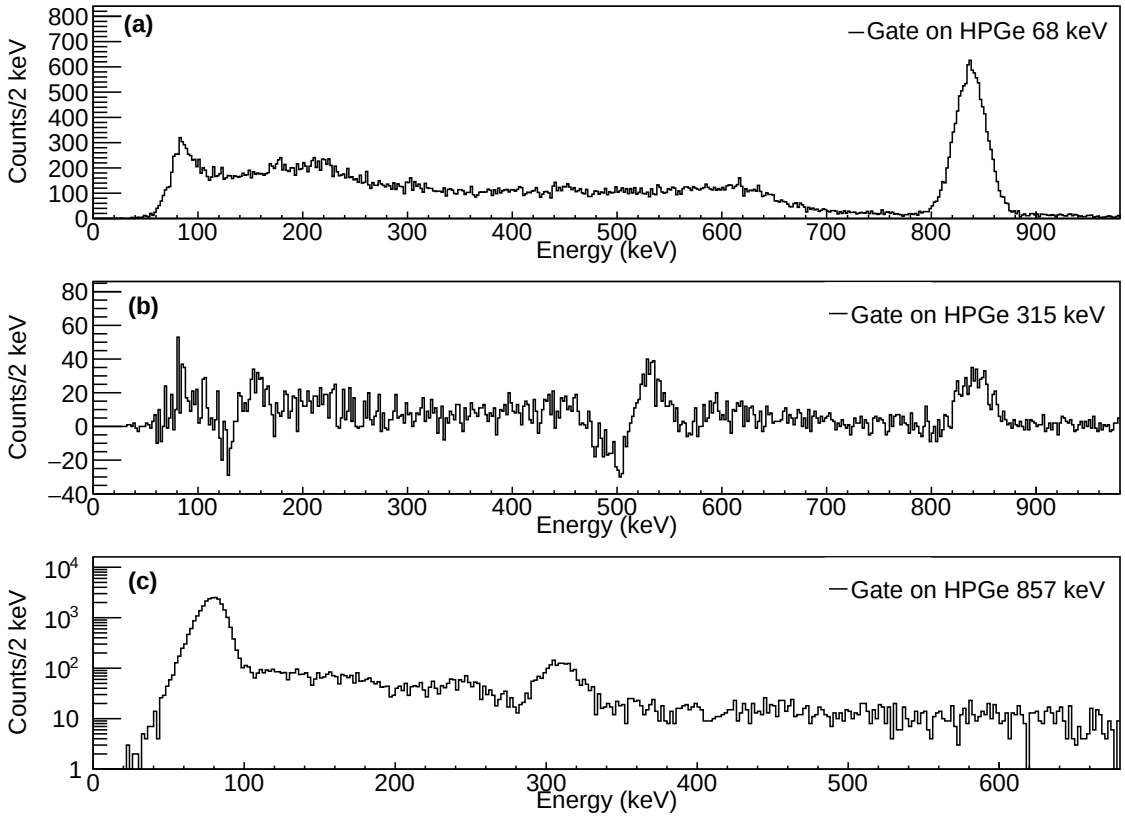


**Figure 5.4.** $LaBr_3$(Ce) energy spectra. Panels (a), (b) and (c) show $\gamma$-ray coincidence spectra gated on the 68-, 315- and 857-keV transitions detected in the HPGe detectors. A time window of 0–800 ms relative to the proton impact was applied to enhance the selectivity for $\gamma$ rays associated with the decay of $^{128}$Cd $\beta$ decay. The negative peaks in the spectrum arise from background subtraction, due to Compton scattering between the $LaBr_3$(Ce) and HPGe clover detectors.

### 5.1.2 Lifetime of the 488-keV level

The lifetime of the 488-keV level has been measured by the analysis of the $\beta\gamma\gamma$(t) time difference distributions of the 173-keV $\gamma$-ray measured in both $LaBr_3$(Ce) detectors. Since the 173 keV peak cannot be selected cleanly in the double coincidence

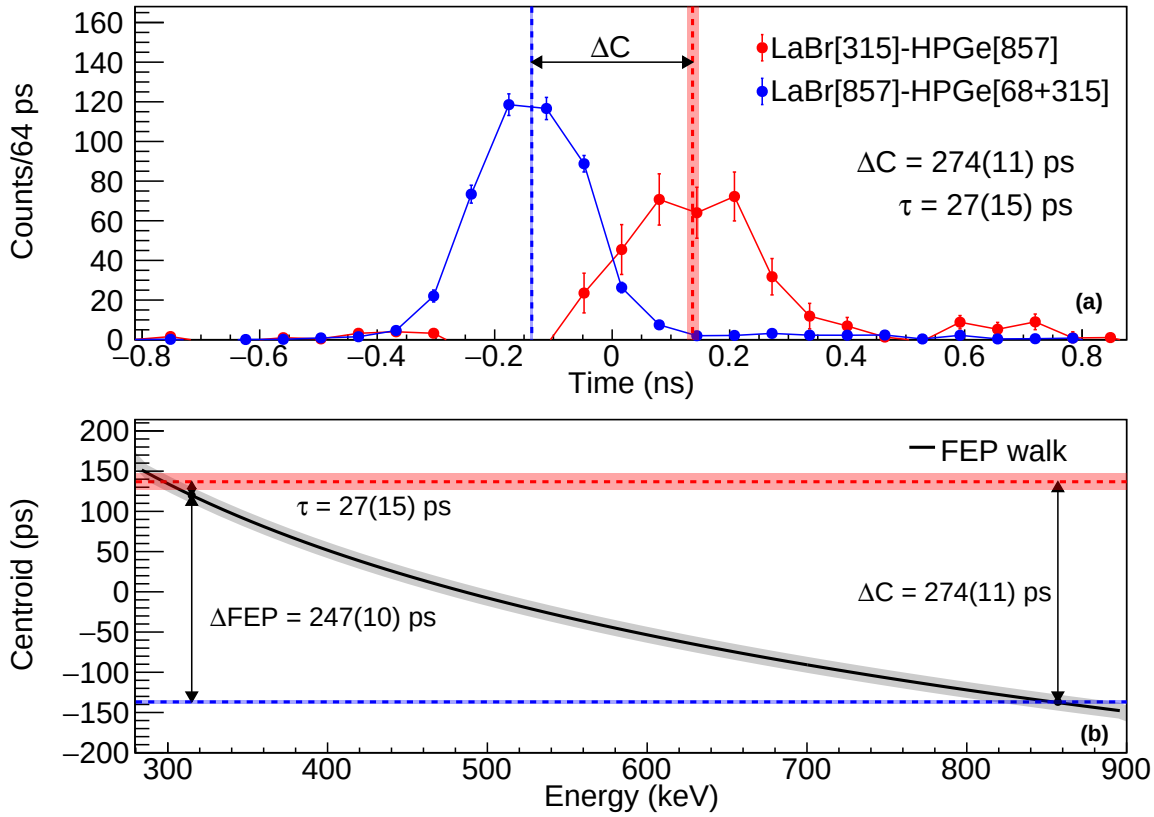


**Figure 5.5.** (a) Time-delayed $\beta\gamma\gamma$(t) coincidence spectra used to determine the lifetime of the 315-keV excited state in $^{128}$In. The blue spectrum corresponds to the prompt time distribution, obtained by placing energy gates on the 315- and 68-keV transitions in the HPGe detector and the 857-keV transition in the $LaBr_3$(Ce) detector. The red spectrum is obtained by the 857-keV transition selected in the HPGe and the 314-keV in the $LaBr_3$(Ce). The centroid is shown with a dashed line, while the shaded area represents its uncertainty. (b) Calibrated FEP prompt curve, the black shaded band represents the uncertainty associated to the FEP prompt curve. The blue spectrum has been scaled down by a factor of 0.1.

$\beta$-$LaBr_3$(Ce) spectra, a third coincidence in the HPGe clover detectors has been required The 1098-keV $\gamma$-ray transitions have not been considered due to the insufficient amount of statistics. The 222-keV $\gamma$ transition as a time reference was selected for the application of the centroid-shift method to sequential transitions. Fig. 5.6 shows the spectra in one of the $LaBr_3$(Ce) detectors after gating on the 173- and 222-keV $\gamma$-rays in the HPGe detectors. A time window of 0–800 ms relative to the proton impact was applied to enhance the selectivity for $\gamma$ rays associated with the decay of $^{128}$Cd $\beta$ decay. The centroid shift time distributions analysis is depicted in Fig. 5.7. In this case, the observed shift is compatible with the $\Delta$FEP. An upper limit on the lifetime was established. The final value was adopted as the weighted average of the two $LaBr_3$(Ce) measurements, which yielded a $\tau \leq 29$ ps value for the 488-keV level at the $2\sigma$ confidence level.

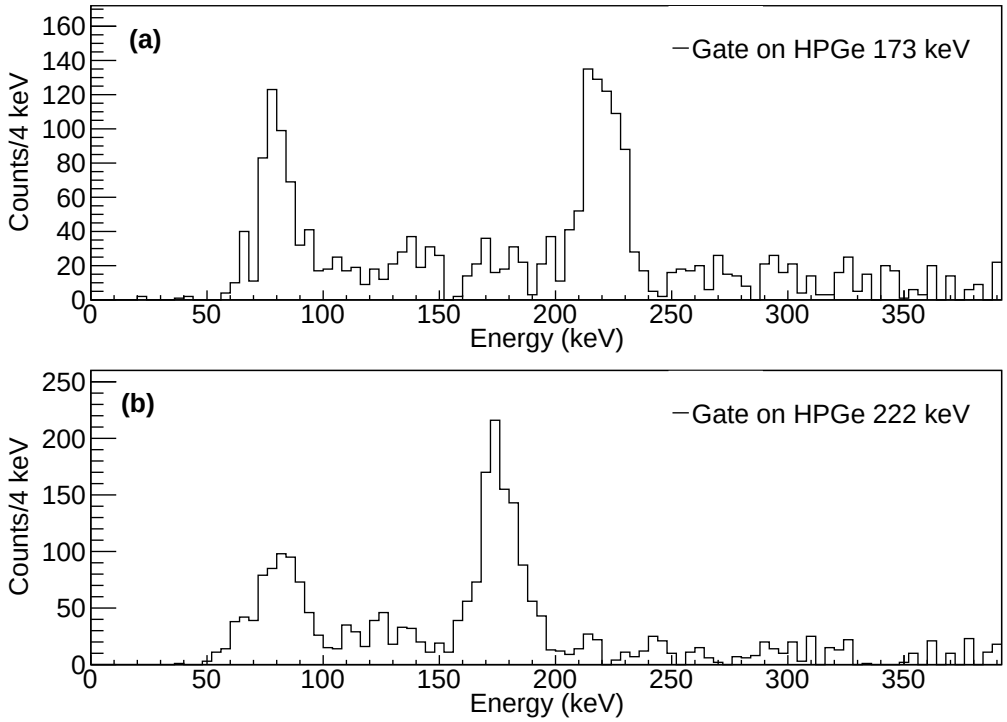


**Figure 5.6.** $LaBr_3$(Ce) energy spectra. Panels (a) and (b) show $\gamma$-ray coincidence spectra gated on the 173- and 222-keV transitions detected in the HPGe detectors. A time window of 0–800 ms relative to the proton impact was applied to enhance the selectivity for $\gamma$ rays associated with the decay of $^{128}$Cd $\beta$ decay.

### 5.1.3 Lifetime of the 710-keV level

The 710-keV level is populated through the 461.8-keV $\gamma$ transition and depopulated via the 462.5-keV $\gamma$ transition, whose energies are very close. This overlap complicates the unambiguous identification of these transitions in the $LaBr_3$(Ce) detectors.

Under these circumstances, the 222-keV $\gamma$ ray can be selected in the $LaBr_3$(Ce) spectrum by applying an energy gate on the HPGe clover detectors, since the 222 keV transitions overlaps with other transitions with similar energies in the $\beta$ decay chain in the $LaBr_3$(Ce) $\gamma$-ray energy spectra (see Fig. 5.2). The 710-keV $\gamma$ transition lacks sufficient statistics. However, when applying a coincidence gate on the 173- and 462-keV $\gamma$ rays detected with the HPGe clover detectors, the statistics for the 222-keV $\gamma$ transition observed in the $LaBr_3$(Ce) detectors were insufficient to perform a reliable timing analysis. Consequently, the centroid-shift method could not be applied. In addition, $\gamma\gamma$(t) fast-timing analysis involving the 222-keV $\gamma$ transition was not feasible due to insufficient statistics in the $LaBr_3$(Ce) energy spectra gated on the 462-keV $\gamma$ transition.

The time distribution was built using $\gamma\gamma$(t) coincidence selecting the 462-keV energy in both start and stop detectors. Since both transitions involved have identical energies, it is not possible to separate the delayed and anti-delayed contributions. Consequently, the $LaBr_3$(Ce)–$LaBr_3$(Ce) TAC spectrum was fitted with the sum of two exponential decay functions convoluted with a Gaussian functions (see Fig. 5.8). A scan over a

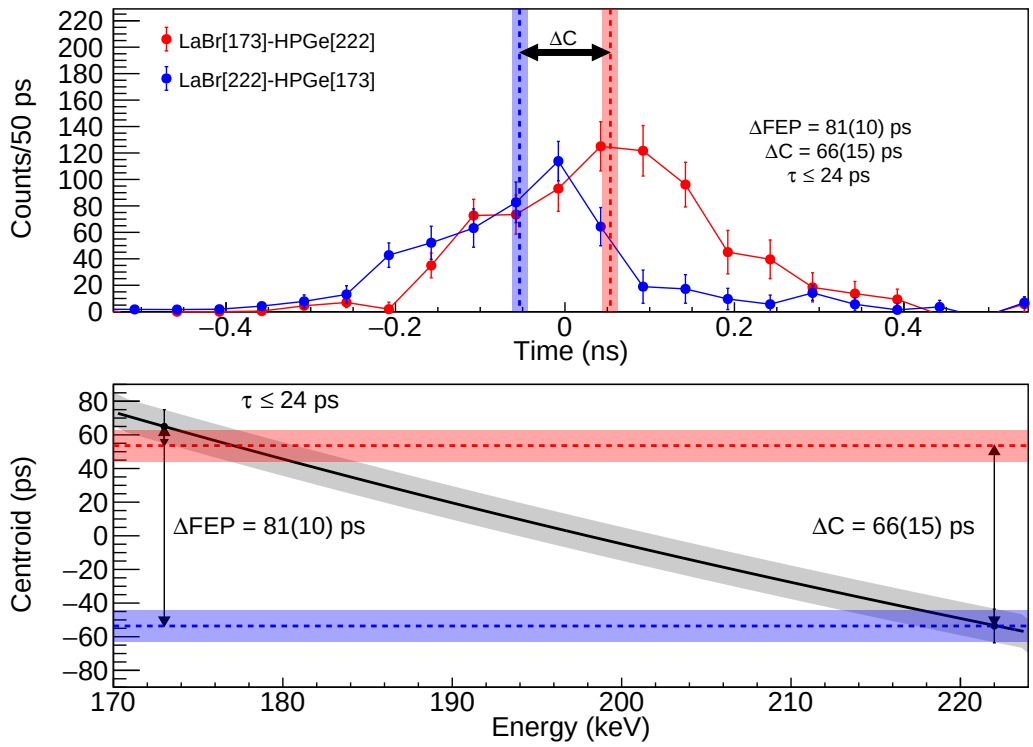


**Figure 5.7.** (a) Time-delayed $\beta\gamma\gamma$(t) coincidence spectra used to determine the lifetime of the 488-keV excited state in $^{128}$In. The blue spectrum corresponds to the prompt time distribution, obtained by placing energy gates on the 173-keV transition in the HPGe detector and the 222-keV transition in the $LaBr_3$(Ce) detector. The red spectrum is obtained by the 222-keV transition selected in the HPGe and the 173-keV in the $LaBr_3$(Ce). (b) Calibrated FEP prompt curve, the black shaded band represents the uncertainty associated to the FEP prompt curve.

range of trial half-lives was performed, and the resulting fits were evaluated using the $\chi^2$/NDF test statistic. An upper limit of $T_{1/2} \leq 17$ ps was extracted using the criterion $\chi^2 = (\chi^2_{min} + 1)/\text{NDF}$.

### 5.1.4 Lifetime of the 1173-keV level

The 1173-keV level is depopulated via the 1173-, 925-, 857-, 516-, 462-, and 306-keV $\gamma$-ray transitions. In this analysis, delayed $\beta\gamma\gamma$(t) events were employed to investigate the time-difference distributions of the intense $\gamma$ ray at 857 keV observed in the $LaBr_3$(Ce) detectors. When a coincidence gate was applied on the high-energy $\gamma$ rays detected with the HPGe detectors feeding the 1173-keV level, the statistics for the 1173-keV $\gamma$ transition observed with the $LaBr_3$(Ce) detectors were insufficient to carry out a reliable timing analysis. Additionally, the coincidence gate on the 248-keV $\gamma$ transition with the HPGe detectors was excluded, since it is strongly influenced by the feeding from the 245.4(30) ms ($1^-$) level at 248 keV [Ber18], affecting the 925 keV $\gamma$-ray intensity measured in the $LaBr_3$(Ce) detectors. Only the 857 keV transition was used, since the 1173 and 925 keV transitions overlap with other transitions of similar energies in the $\beta$ decay chain in the $LaBr_3$(Ce) $\gamma$-ray energy spectra (see Fig. 5.2).

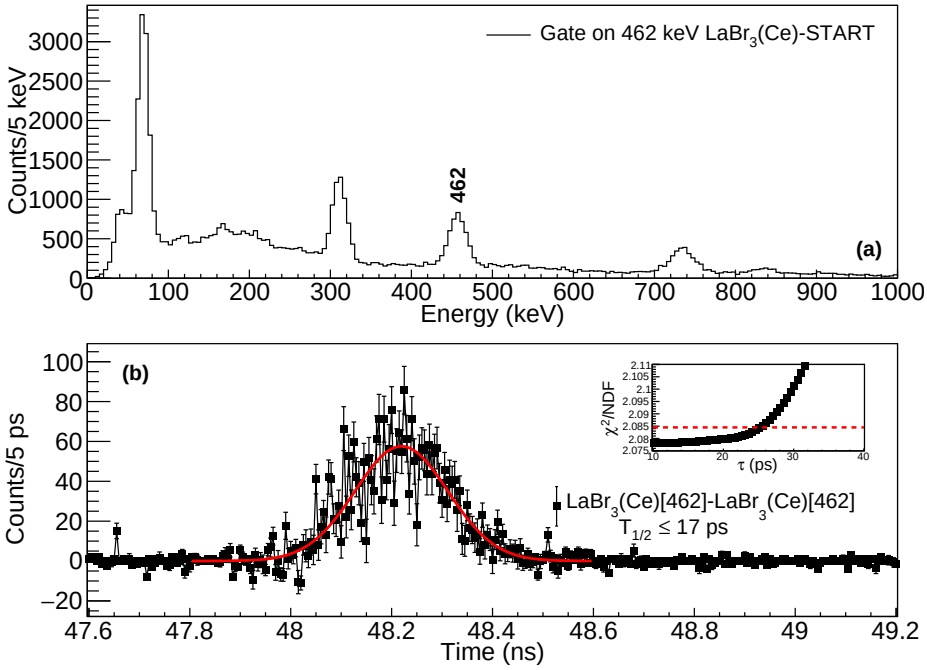


**Figure 5.8.** Energy spectrum recorded in the $LaBr_3$(Ce) start detector after gating in the 462-keV on the stop $LaBr_3$(Ce) detector (a). Time-delayed $\gamma\gamma$(t) spectra used to measure the lifetime of the 710-keV excited level (b). The spectrum was constructed by setting coincident gates on the 462-keV $\gamma$ transition in both the start and stop detectors. Both the delayed and anti-delayed time distributions were summed into the same time spectrum. The lifetime was obtained from a $\chi^2$ minimization of the distribution to a summing Gaussian convoluted with exponential functions. The inset plot shows the $\chi^2$/NDF vs half-life dependence.

The 857-keV transition was employed for the timing distribution analysis in coincidence with the 68- and 315-keV transitions detected by the HPGe detectors, as described in Subsec. 5.1.1 (see Fig.5.9). The time distribution exhibited no evidence of a delayed component, indicating a short lifetime for the 1173-keV level. Due to the lack of an independent prompt time reference, the centroid shift method could not be applied. The lifetime was extracted by fitting the time spectra with a model consisting of an exponential decay function convoluted with a Gaussian function. A range of half-lives was scanned and the corresponding $\chi^2$/NDF test was evaluated. An upper limit of $T_{1/2} \leq 16$ ps was determined using the condition $(\chi^2_{min} + 4)$/NDF.

### 5.1.5 Discussion of fast-timing results for $^{128}$In

Reduced transition probabilities $B(X\lambda)$ for transitions in $^{128}$In were calculated from the measured lifetimes of the 315-, 488-, 711-, and 1173-keV levels, the corresponding $\gamma$-ray intensities, and the tabulated internal conversion coefficients [KBT$^+$08], assuming pure multipolarities. The results are summarized in Tab. 5.1.

For the 315-keV level, The 68-keV transition connects this state with the 248-keV $(1^-)$ isomeric state. Taking into account the short lifetime, and assuming pure $M1$ or $E2$ multipolarity, a value of $B(M1) = 1.4^{+1.7}_{-0.5}$ W.u. and $B(E2) = 7.2^{+8.6}_{-2.5} \times 10^4$ W.u.

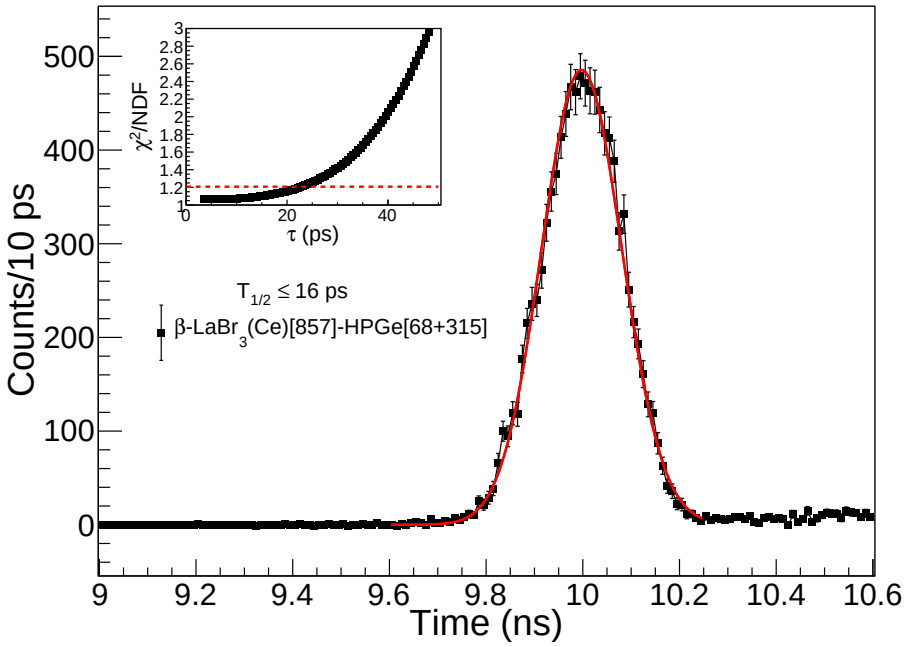


**Figure 5.9.** Time-delayed $\beta\gamma\gamma$(t) spectrum between the $\beta$ and the $LaBr_3$(Ce) detectors selected by the 857-keV transition. An extra condition was required on the the 315- and 68-keV $\gamma$ transitions in the HPGe detectors. The lifetime was obtained from a $\chi^2$ minimization of the distribution to a Gaussian convoluted with exponential function. The inset plot shows the $\chi^2$/NDF vs half-life dependence.

**Table 5.1.** Level lifetimes and reduced transition probabilities for transitions in $^{128}$In. The $B(X\lambda)$ were deduced from the lifetimes and branching ratios obtained in this work, using conversion coefficients taken from Ref. [KBT+08].

| $\mathbf{E_i(keV)}$ | $\mathbf{J_i^\pi}$ | $\boldsymbol{\tau}$ | $\mathbf{E_f(keV)}$ | $\mathbf{J_f^\pi}$ | $\mathbf{E_\gamma(keV)}$ | $\mathbf{X\lambda}$ | $\boldsymbol{B(X\lambda)(W.u.)}$ |
|---|---|---|---|---|---|---|---|
| 315 | $(2^-)$ | 27(15) ps | 0 | $0^+$ | 315 | $E1$ | $2.6(^{+3.1}_{-0.9}) \times 10^{-5}$ |
| | | | 248 | $(1^-)$ | 68 | $M1$ | $1.4(^{+1.7}_{-0.5})$ |
| 488 | $(1^-)$ | $\leq$ 24 ps | 315 | $(2^-)$ | 173 | $M1$ | $\geq 2 \times 10^{-1}$ |
| 711 | $(2^-)$ | $\leq$ 23 ps | 0 | $(3^+)$ | 710 | $E1$ | $\geq 4.2 \times 10^{-6}$ |
| | | | 248 | $(1^-)$ | 462 | $M1$ | $\geq 1.1 \times 10^{-2}$ |
| | | | 488 | $(1^-)$ | 222 | $M1$ | $\geq 1.9 \times 10^{-3}$ |
| 1173 | $1^+$ | $\leq$ 24 ps | 0 | $(3^+)$ | 1173 | $E2$ | $\geq 3 \times 10^{-2}$ |
| | | | 248 | $(1^-)$ | 925 | $E1$ | $\geq 1.7 \times 10^{-6}$ |
| | | | 315 | $(2^-)$ | 857 | $E1$ | $\geq 1.7 \times 10^{-5}$ |
| | | | 656 | $(0^-, 1^-, 2^-)$ | 516 | $E1$ | $\geq 7.2 \times 10^{-7}$ |
| | | | 710 | $(2^-)$ | 462 | $E1$ | $\geq 1.0 \times 10^{-5}$ |
| | | | 868 | $(0^-, 1^-, 2^-)$ | 306 | $E1$ | $\geq 1.4 \times 10^{-6}$ |

were derived. The $B(E2)$ value obtained is unrealistically high, which indicates that the transition is predominantly of $M1$ character. The $E1$ component is expected to be negligible, since a $B(E1) = 2.8^{+3.3}_{-1.0} \times 10^{-2}$ W.u. value is too large to be realistic. Additionally, for the 315-keV transition connecting this level with the $(3^+)$ g.s., $B(E1) = 2.6^{+3.1}_{-0.9} \times 10^{-5}$ W.u. and $B(M2) = 1.1(^{+1.3}_{-0.4}) \times 10^3$ W.u. values were obtained assuming pure multipolarities. Once again, the $B(M2)$ value is too high

to be realistic, thus a predominant $E1$ character is assumed for this transition. In conclusion, considering the $M1$ character of the 68-keV transition feeding the $(1^-)$ isomeric state and the $E1$ character of the transition to the $(3^+)$ g.s., a $(2^-)$ spin-parity assignment for the 315-keV state is the only one consistent with the results. This is therefore proposed as an outcome of this value.

For the 488-keV level, the 173-keV transition connects this state with the 315-keV $(2^-)$ level. Assuming a pure $M1$ the 173-keV transition yields a reduced transition probability of $B(M1) \geq 1.9 \times 10^{-1}$ W.u., whereas assuming a pure $E2$ multipolarity would require $B(E2) \geq 3.88 \times 10^{3}$ W.u., which is inconsistent with known systematics. These results exclude a $(0^-)$ spin-parity assignment, since this $\gamma$ transition would imply a predominant $E2$ multipolarity. Additionally, no $\gamma$-ray transitions depopulating the 488-keV level directly to the $(3^+)$ g.s. have been observed. This seems to indicate that an $E1$ transition is not possible to the $(3^+)$ g.s., supporting its assignment as $(1^-)$. Taking into account all this information together, the results support $(1^-)$ as the most probable spin-parity assignment for the 488-keV state.

For the 710-keV level, the upper limit on its half-life, $T_{1/2} \leq 17$ ps, indicates that the 710-keV $\gamma$ ray connecting this state to the $(3^+)$ ground state is predominantly of $E1$ character. Assuming a pure $E1$ transition, this $\gamma$ decay yields a reduced transition probability of $B(E1) \geq 4.2 \times 10^{-6}$ W.u. A pure $M2$ multipolarity, in contrast, would correspond to an unrealistic value of $B(M2) \geq 3.8 \times 10^{1}$ W.u. Furthermore, for the 462-keV transition to the 248-keV $(1^-)$ isomeric state, assuming pure multipolarities gives $B(M1) \geq 1.1 \times 10^{-2}$ W.u. and an unrealistically large $B(E2) \geq 3.6 \times 10^{1}$ W.u. Similarly, for the 222-keV transition to the 488-keV $(1^-)$ state, the measured half-life yields $B(M1) \geq 1.9 \times 10^{-3}$ W.u., while a pure $E2$ multipolarity would again imply an unrealistic value of $B(E2) \geq 2.6 \times 10^{1}$ W.u. Since these are lower limits, the $M1/E2$ mixing ratios for the 462- and 222-keV transitions are unknown, and given that the $B(E2)$ values are too large to be realistic, the $E2$ component is expected to be negligible. Overall, the experimental evidence supports a $(2^-)$ spin-parity assignment for the 710-keV level.

For the 1173-keV $1^+$ state, the 1173-keV $\gamma$ ray connecting this level to the $(3^+)$ ground state is predominantly of $E2$ character. For the 857- and 462-keV transitions connecting the 315-keV $(2^-)$ level and the 710-keV $(2^-)$ level, with spin–parity assignments discussed previously, the observed $\gamma$ decays are consistent with pure $E1$ character. These yield reduced transition probabilities of $B(E1) \geq 1.7 \times 10^{-5}$ W.u. and $B(E1) \geq 1.0 \times 10^{-5}$ W.u., respectively. Similarly, the 516- and 306-keV transitions connecting the 656-keV $(0^-, 1^-, 2^-)$ level and the 868-keV $(0^-, 1^-, 2^-)$ level are also consistent with pure $E1$ character, yielding reduced transition probabilities of $B(E1) \geq 7.2 \times 10^{-7}$ W.u. and $B(E1) \geq 1.4 \times 10^{-6}$ W.u., respectively. Finally, for the 925-keV transition to the 248-keV $(1^-)$ isomeric state, the measured upper limit half-life yields $B(E1) \geq 1.7 \times 10^{-6}$ W.u. All quoted $B(X\lambda)$ values correspond to the most likely multipolarities. The experimental results support the previously reported $1^+$ spin–parity assignment for the 1173-keV level given in Refs. [Fog88, Ber18].

The measured half-life of the 315-, 488-, 711-, and 1173-keV levels are presented in Fig. 5.10. The half-life of the isomeric state at 247 keV was taken form Ref. [Ber18].

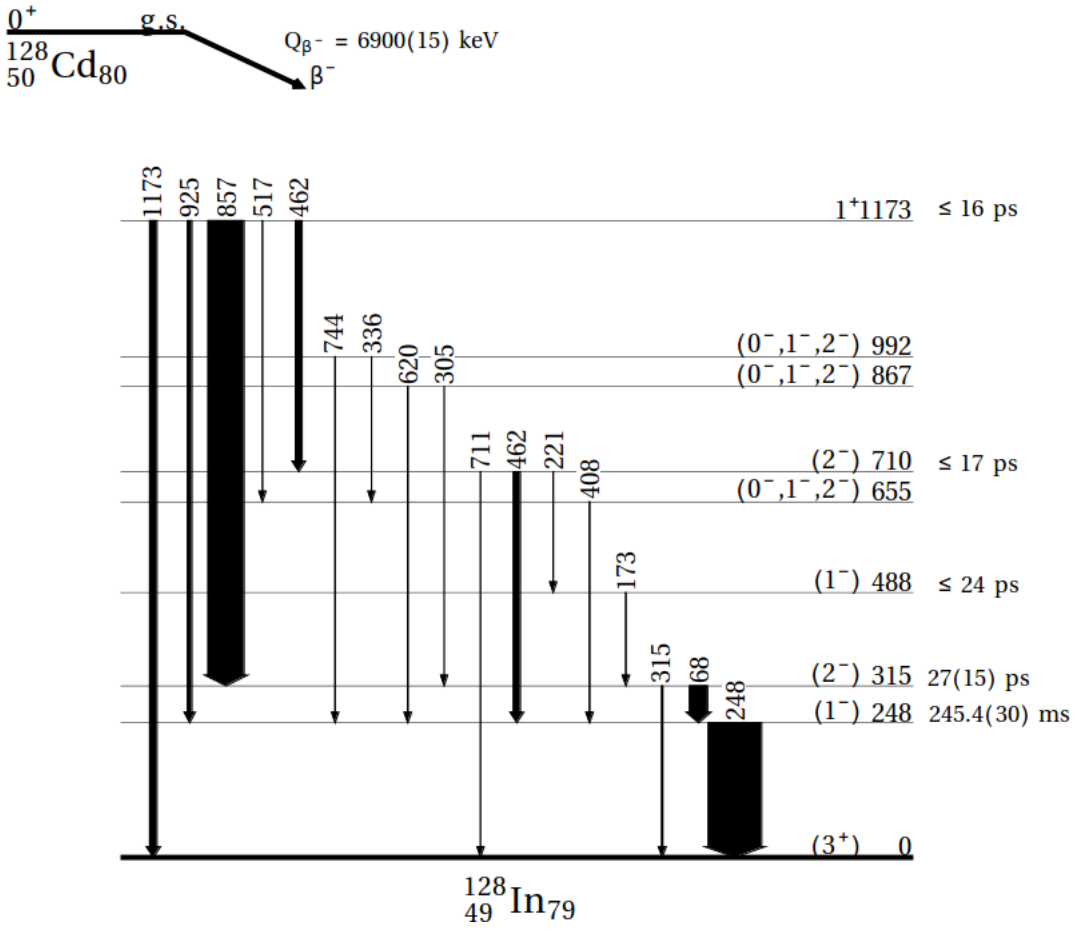


**Figure 5.10.** Partial level scheme of $^{128}$In observed following the $\beta$ decay of the $^{128g}$In $0^+$ ground state. Line widths are proportional to their relative intensities. The $Q_{\beta^-}$ value is taken of Ref. [NND25]. The measured half-life of the 315-, 488-, 711-, and 1173-keV levels are presented. The half-life of the isomeric state at 247 keV was taken form Ref. [Ber18].

## 5.2 Fast-timing spectroscopy of $^{128}$Te

This section focuses on the fast-timing investigation of the excited structure of $^{128}$Te populated in the $\beta$ decay of the $5^+$ isomeric state in $^{128}$Sb [MM71]. The $8^-$ ground state of $^{128}$Sb [Ker72] is not populated in the decay of the $^{128}$Sn $0^+$ ground state. The decay path from the $6^+$ state constitutes an excellent case for investigating the lifetimes of the yrast band in this nucleus. This results in the population of the yrast $6^+ \rightarrow 4^+ \rightarrow 2^+ \rightarrow 0^+$ states in $^{128}$Te through a cascade of intense E2 $\gamma$-ray transitions, with energies of 314, 754, and 743 keV [MM71] (see Fig. 5.11). In this context, lifetime measurements of the yrast $2^+$, $4^+$ and $6^+$ states in $^{128}$Te have been measured using $\beta\gamma\gamma$(t), and $\gamma\gamma\gamma$(t) fast-timing methods.

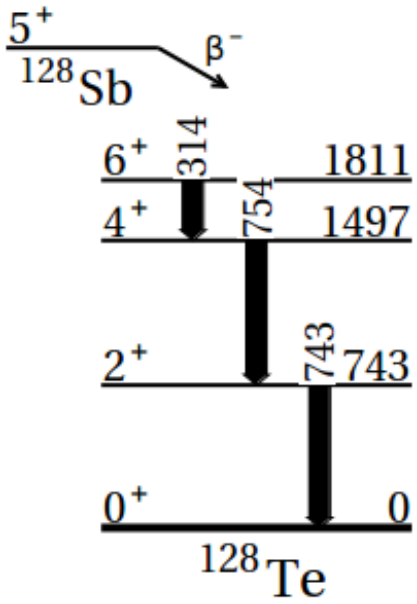


**Figure 5.11.** Partial $\beta$-decay scheme of the $5^+$ isomer in $^{128}$Sb. Only the yrast levels $6^+$, $4^+$, and the ground state in $^{128}$Te are shown. Data taken from Ref. [MM71].

### 5.2.1 Lifetime of the 1811-keV $6^+$ state

The half-life of the $6^+$ state was determined from the time distributions measured between the $\beta$ detectors and the $LaBr_3$(Ce) detectors. The 1811-keV state lifetime is free from the influence of other long-lived states and appears as an exponential tail that can be fitted to measure the half-life. Since the lifetimes of the intermediate states are much shorter, the lifetime of the $6^+$ level has been obtained by summing the 314-, 754-, and 743-keV full-energy peaks in the two $LaBr_3$(Ce) detectors. A beam gate condition in the time reference of the protons was imposed after 2 s to have a better selectivity in the identification of $\gamma$ rays. No extra selectivity in the HPGe detectors was needed since the 3 $\gamma$-rays are clearly resolved (see Fig. 5.12). The energy difference between the 754-keV and 743-keV transitions is only 11 keV, which is not resolved in the $LaBr_3$(Ce) $\gamma$-ray spectrum without applying an additional gating condition on the HPGe detectors. However, since the half-lives of the $4^+$ and $2^+$ states are of the order of a few picoseconds, this $\gamma$-ray transition can be selected, without affecting the slope of the delayed component.

The half-life was extracted by a $\chi^2$ minimization of the time-delayed slope of the coincidence spectra to an exponential decay function with a constant background component, after correcting for the contribution of Compton-scattered events underlying the peaks. The analysis is shown in Fig. 5.13. A half-life of $T_{1/2} = 461(2)$ ps was adopted. This result is consistent with previously reported values of $T_{1/2} = 420(30)$ ps [MM71] and $T_{1/2} = 480(30)$ ps [SHH+75], but provides significantly improved precision.

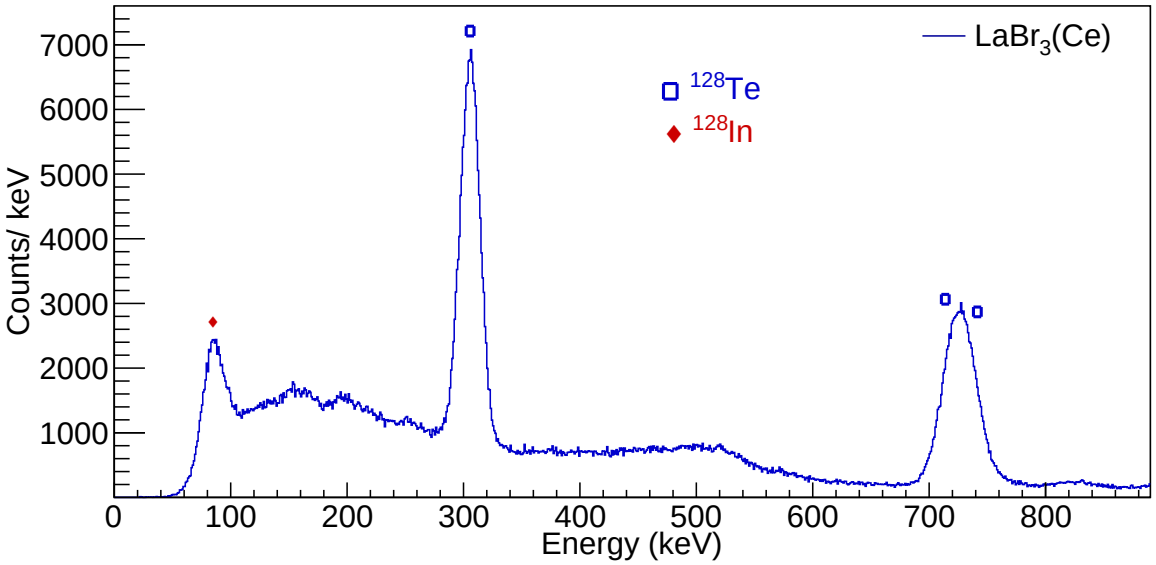


**Figure 5.12.** $LaBr_3(Ce)$ $\gamma$-ray energy spectra. A beam gate condition in the time reference of the protons was imposed after 2000 ms to have a better selectivity in the identification of $\gamma$ rays associated to the $^{128}$Te.

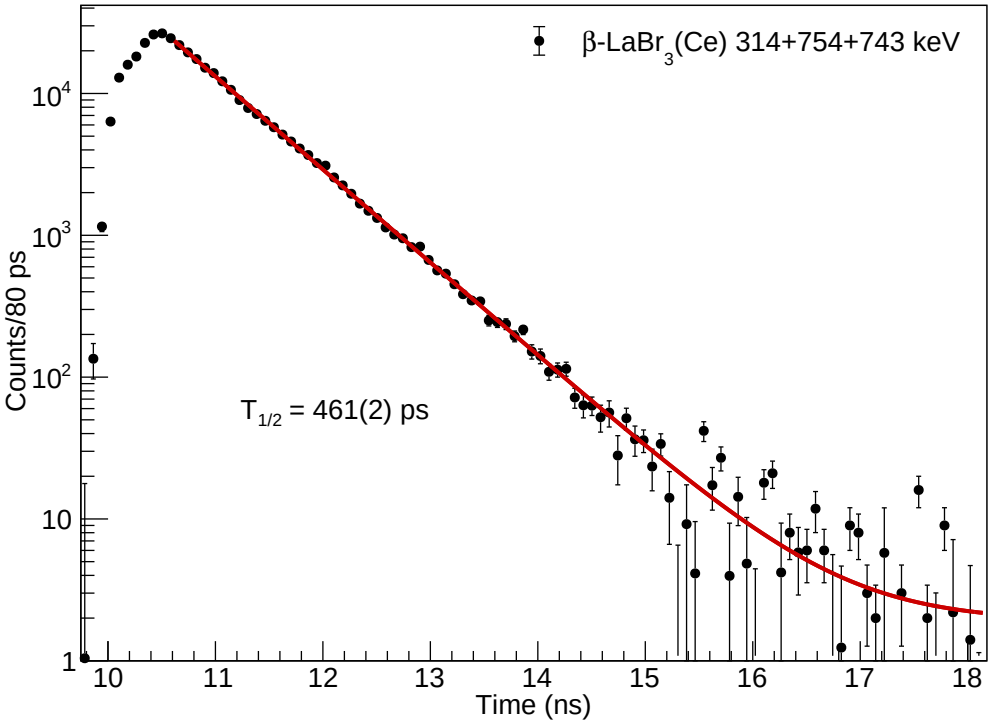


**Figure 5.13.** Time-delayed spectrum between the $\beta$ detector and either of the two $LaBr_3(Ce)$ detectors for $\beta\gamma$(t) events. This distribution is built by adding up the 314-, 743-, and 754-keV transitions in the $LaBr_3(Ce)$ detectors. A time window after 2000 ms relative to the proton impact was applied to have a better selectivity in the identification of $\gamma$ rays associated to the $^{128}$Te. The lifetime was obtained by a $\chi^2$ minimization of the time distribution to an exponential decay with a constant background component.

### 5.2.2 Lifetime of the 1497-keV $4^+$ state

The lifetime of the $4^+$ state was determined using time-delayed $\gamma\gamma$(t) coincidence measurements between the 314- and 754-keV transitions detected in the $LaBr_3(Ce)$ scintil-

lators. This level is mostly fed by $\gamma$-ray transitions. An additional coincidence with the 743-keV transition detected in the HPGe detector was required to suppress the contribution from the nearby 754-keV $\gamma$ ray in the $LaBr_3$(Ce) energy spectra (see Fig. 5.2). The resulting lifetime analysis of the 1497-keV state is presented in Fig. 5.14. A mean lifetime of $\tau = 11(7)$ ps, corresponding to a $T_{1/2} = 8(5)$ ps, was obtained from the centroid shift difference between the delayed and anti-delayed time distributions. This result is inconsistent, within experimental uncertainties, with the latest value, $\tau = 0.741^{+1.072}_{-0.280}$ ps, reported in Ref. [PBE+22], which was measured using the doppler-shift attenuation method (DSAM) in p–$\gamma$ coincidences.

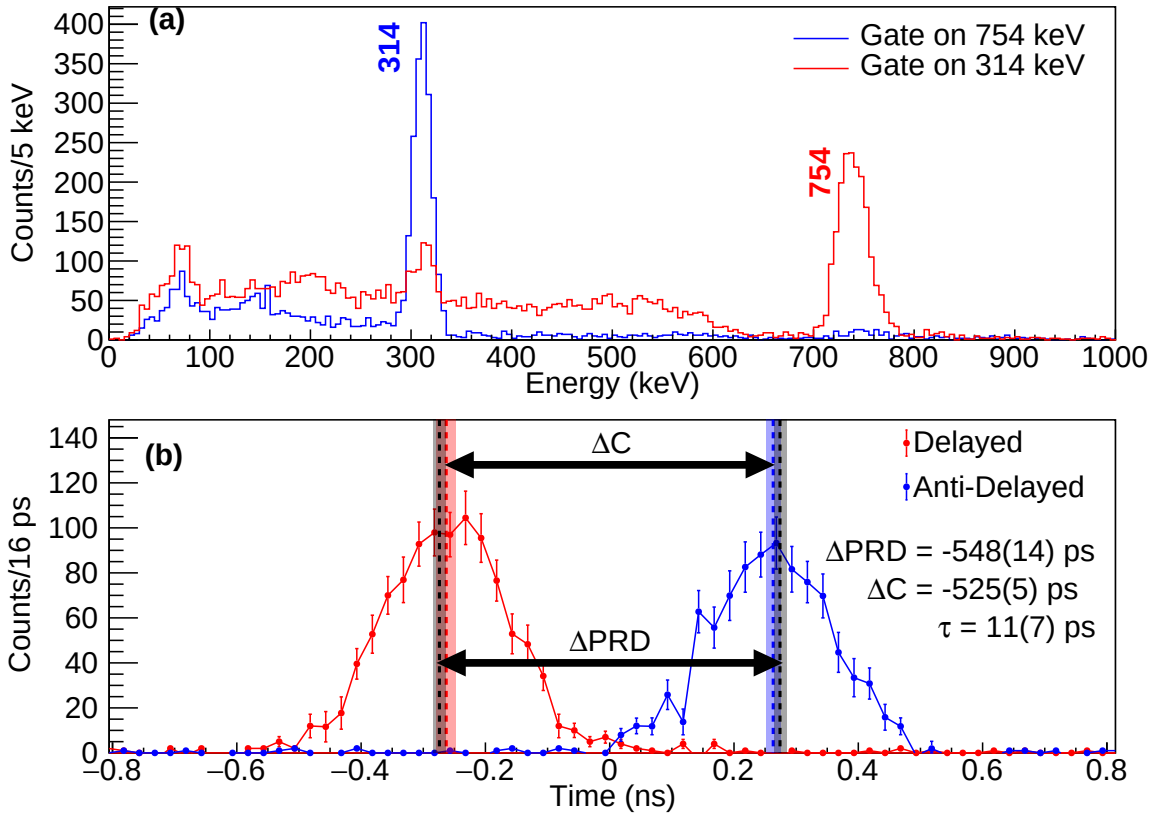


**Figure 5.14.** Energy spectra recorded in the $LaBr_3$(Ce) start detector after gating in the 314- and 743-keV on the stop $LaBr_3$(Ce) detector respectively. An extra condition was required in the 743-keV $\gamma$ transition in the HPGe clover detectors (a). Time-delayed $\gamma\gamma\gamma$(t) spectra used to measure the lifetime of the 1497-keV $4^-$ excited level. (b). Depending on the selected $\gamma$ transition in the start and stop detectors, either the delayed or the anti-delayed distributions are derived. The centroid is shown with a dashed line, while the shaded area represents its uncertainty. The centroid shift measured between the delayed and anti-delayed time spectra ($\Delta$C), is caused by the lifetime of the level and the shift in the Prompt Response Difference ($\Delta$PRD)

### 5.2.3 Lifetime of the 743-keV $2^+$ state

The measurement of the half-life of the 743-keV $2^+$ level could not be extracted from triple $\beta\gamma\gamma$(t) coincidence events due to unavoidable contributions from the delay component due to the half life of the $6^+$ state. Additionally, the 754-keV $\gamma$-ray feeding

the $2^+$ level has an energy very close to the 743-keV $\gamma$-ray de-exciting it, complicating the clean identification of these transitions in the $LaBr_3$(Ce) detectors. The energy spectrum obtained with one of the $LaBr_3$(Ce) detectors, in coincidence with the 754- and 743-keV peaks detected in the HPGe detectors, is shown in Fig. 5.15 (a), where a slight overlap between the two peaks is evident. The lifetime of the $2^+$ level was measured using triple $\gamma\gamma\gamma$(t) coincidence measurements involving the 314- and 743-keV transitions detected in the $LaBr_3$(Ce) detectors, along with an additional 754-keV coincidence in the HPGe detector (see Fig. 5.15). In this case, the centroid shift between the delayed and anti-delayed time distributions corresponds to the sum of the lifetimes of the $4^+$ and $2^+$ states, $\tau_{4^+} + \tau_{2^+}$, once the PRD has been accounted for. Therefore, the lifetime of the $2^+$ state, $\tau_{2^+}$, can be obtained by subtracting the contribution of $\tau_{4^+}$. The extracted lifetime distribution for the $2^+$ state yields an average value of $\tau = 9(8)$ ps, indicating a large statistical uncertainty. This large uncertainty arises from the fact that the measurement approaches the sensitivity limit of the fast-timing techniques. Nevertheless, the result remains compatible with the more precise value of $\tau = 3.30(3)$ ps reported in Ref. [BDSS78].

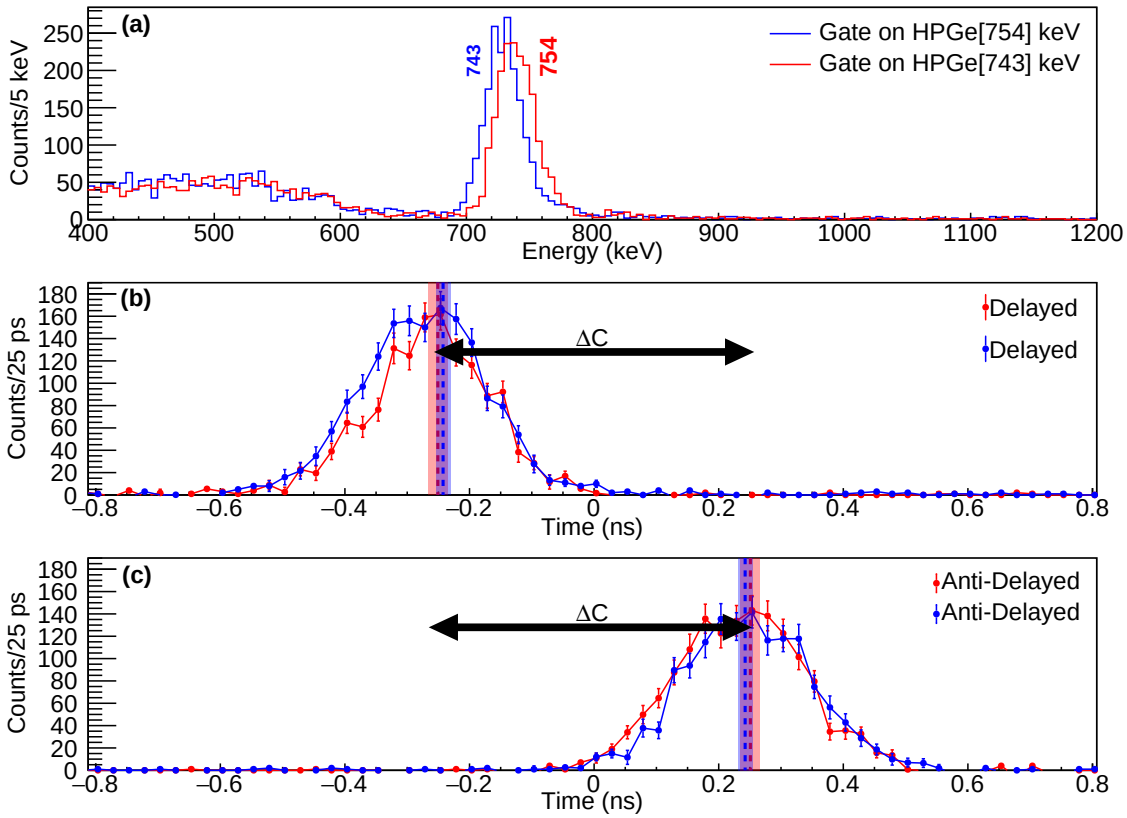


**Figure 5.15.** Energy spectra recorded in the $LaBr_3$(Ce) start detector after gating in the 314- and 743-keV on the stop $LaBr_3$(Ce) detector respectively (a). An extra condition was required in the 743-keV $\gamma$ transition in the HPGe clover detectors. Time-delayed $\gamma\gamma\gamma$(t) spectra used to measure the lifetime of the 1497-keV $4^+$ excited level (b) and (c). Depending on the selected $\gamma$ transition in the start and stop detectors, either the delayed or the anti-delayed distributions are derived. The centroid is shown with a dashed line, while the shaded area represents its uncertainty.

### 5.2.4 Discussion of fast-timing results for $^{128}$Te

The experimental $B(E2;\ 6^+ \rightarrow 4^+)$, $B(E2;\ 4^+ \rightarrow 2^+)$ and $B(E2;\ 2^+ \rightarrow 0^+)$ reduced transition probabilities have been deduced using the $\gamma$-ray intensities, the tabulated internal conversion coefficients from Ref. [KBT$^+$08] and the lifetime measurements for the $6^+$ state at 1811 keV and the $4^+$ state at 1497 keV. The results are summarized in Tab. 6.2. These values are compared with the experimental $B(E2;\ 6^+ \rightarrow 4^+)$, $B(E2;\ 4^+ \rightarrow 2^+)$ and $B(E2;\ 2^+ \rightarrow 0^+)$ reduced transition probabilities for the even-even Te isotopes, as well as with shell model calculations reported in the literature [TYHO15, CSA$^+$20, NND25] (see Fig. 5.16).

**Table 5.2.** Level lifetimes and reduced transition probabilities for transitions in $^{128}$Te. The spin assignments for the initial and final level follow Ref. [NND25]. The $B(X\lambda)$ were calculated from the lifetimes and branching ratios obtained in this work, using conversion coefficients taken from Ref. [KBT$^+$08].

| $\mathbf{E_i(keV)}$ | $\mathbf{J_i^\pi}$ | $\boldsymbol{\tau}$ | $\mathbf{E_f(keV)}$ | $\mathbf{J_f^\pi}$ | $\mathbf{E_\gamma(keV)}$ | $\mathbf{X\lambda}$ | $\boldsymbol{B(X\lambda)(W.u.)}$ |
|---|---|---|---|---|---|---|---|
| 1811 | $6^+$ | 665(3) ps | 1497 | $4^+$ | 314 | E2 | 10.15(4) |
| 1497 | $4^+$ | 11(7) ps | 743 | $2^+$ | 754 | E2 | $8(^{+15}_{-3})$ |
| 743 | $2^+$ | 9(8) ps | 0 | $0^+$ | 743 | E2 | $10(^{+63}_{-5})$ |

Ref. [TYHO15] employs $^{132}$Sn as an inert core and considers the full set of single-particle orbitals in the $50 \leq N, Z \leq 82$ major shell, namely $2s_{1/2}$, $1d_{5/2}$, $1d_{3/2}$, $0g_{7/2}$, and $0h_{11/2}$. The interaction includes two-body terms composed of pairing and quadrupole-quadrupole components. An effective interaction is derived via perturbative many-body techniques, starting from a free nucleon-nucleon interaction. In contrast, Coombes *et al.* [CSA$^+$20] adopt a different approach based on a $^{100}$Sn inert core, with a valence space comprising the same five orbitals for both protons and neutrons. The two-body matrix elements are derived from the CD-Bonn nucleon-nucleon potential. Empirical effective charges of $e_p = 1.7e$ and $e_n = 0.9e$ are employed to account for core polarization effects.

As shown in Fig. 5.16, the experimental value of $B(E2; 4^+ \rightarrow 2^+) = 118^{+76}_{-73}$ W.u., reported in Ref. [PBE$^+$22], departs from the systematics observed in neighboring even-even Te isotopes and is inconsistent with shell-model predictions in Refs. [TYHO15, CSA$^+$20]. Comparisons with recent theoretical calculations for $^{124–130}$Te reported in Ref. [CSA$^+$20] show agreement within the bounds of the experimental uncertainty, suggesting that these models capture, at least qualitatively, the collective behavior associated with the $4^+$ to $2^+$ $E2$ transition in this mass region. However, shell model predictions from Ref. [TYHO15] exhibit significant discrepancies, underestimating the measured transition strength and failing to reproduce the new experimental $B(E2;\ 4^+ \rightarrow 2^+)$ value. These differences underscore the sensitivity of $E2$ transition rates to the choice of effective interactions, model space, and treatment of configuration mixing. The trend observed in the $B(E2)$ strengths as a function of neutron number appears to vary considerably depending on the specific theoretical approach employed. In this context, additional experimental data are crucial.

The experimental value of $B(E2;\ 6^+ \rightarrow 4^+) = 10.15(4)$ W.u., extracted from the lifetime of the $6^+$ state at 1811 keV, is consistent within uncertainties with shell-model predictions reported in Refs. [TYHO15, CSA$^+$20], as well as with the systematics observed in neighboring even-even Te isotopes. The value of $B(E2;\ 2^+ \rightarrow 0^+) = 10^{+63}_{-5}$ W.u., deduced from the lifetime of the $2^+$ state at 473 keV, carries a large uncertainty, rendering it compatible with both theoretical predictions [TYHO15, CSA$^+$20] and the experimental trend observed in the region. Once again, the observed trend depends significantly on the type of calculation and the theoretical model employed.

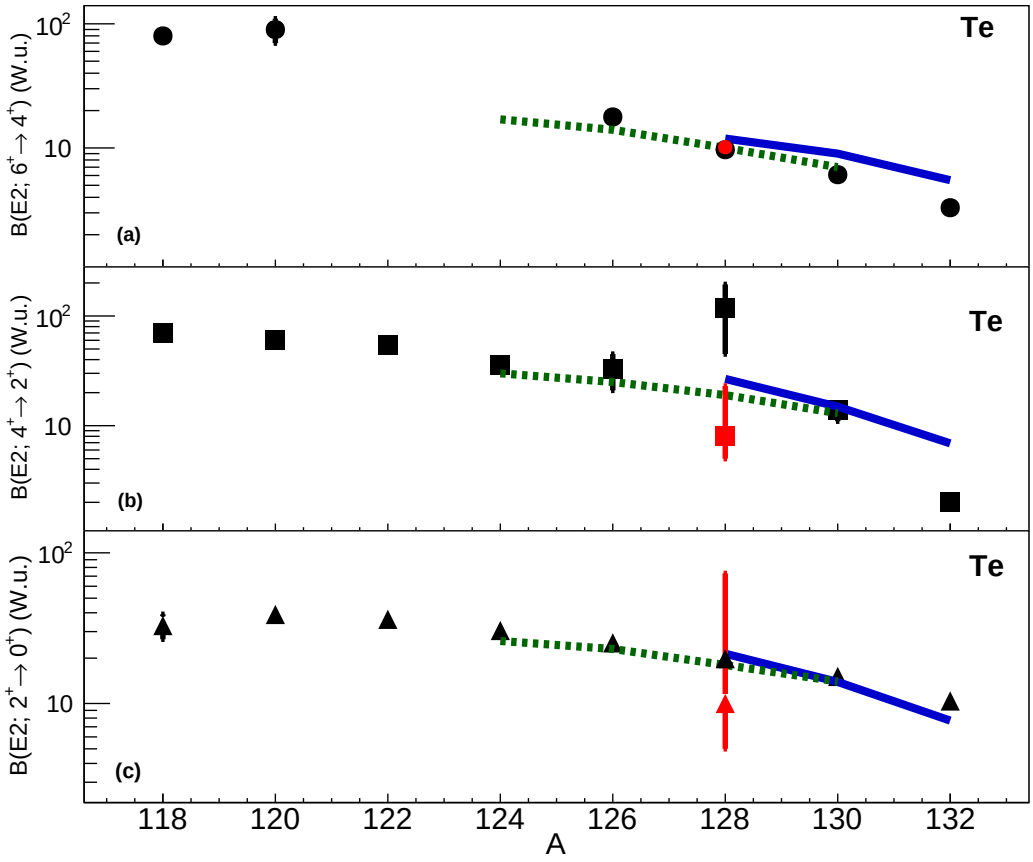


**Figure 5.16.** Experimental reduced transition probabilities in W.u. for the $6^+ \rightarrow 4^+$ (a), $4^+ \rightarrow 2^+$ (b) and $2^+ \rightarrow 0^+$ (b) transitions in the even Te isotopes taken from Ref. [NND25]. For $^{128}$Te $B(E2;\ 4^+ \rightarrow 2^+)$ the value was taken from Ref. [PBE$^+$22]. The $B(E2;\ 6^+ \rightarrow 4^+)$, $B(E2;\ 4^+ \rightarrow 2^+)$ and $B(E2;\ 2^+ \rightarrow 0^+)$ values for $^{128}$Te that have been measured in this work are plotted in red. Theoretical calculations are shown with lines, Teruya *et al.* solid (blue) [TYHO15] and Coombes *et al.* dashed (dark green) [CSA$^+$20].

## 5.3 Conclusions of the chapter

The fast-timing spectroscopy study of the $^{128}$Cd $\beta$-decay chain has yielded the first sub-nanosecond lifetime measurements in $^{128}$In, along with improved lifetime

determinations for excited states in $^{128}$Te.

In $^{128}$In, no sub-nanosecond lifetime data were available prior to the present work. The lifetimes of the 315- and 488-keV levels were measured using the centroid-shift method applied to $\beta\gamma\gamma$(t) coincidence data. For the 710- and 1173-keV excited states, the limited statistics and the absence of independent prompt timing references prevented a reliable determination of their lifetimes. The lifetimes were extracted by fitting the time spectra of the 462- and 857-keV $\gamma$ transitions corresponding to each level with a model consisting of a Gaussian function convoluted with an exponential decay. These measurements enabled, for the first time, the determination of $B(X\lambda)$ values for several $\gamma$ transitions. The experimental results support spin–parity assignments of $(2^-)$ for the 315- and 710-keV states, $(1^-)$ for the 488-keV state, and confirm the previous $1^+$ assignment for the 1173-keV level.

In $^{128}$Te, populated via the $\beta$ decay of the $5^+$ isomer in $^{128}$Sb, the half-lives of the yrast $6^+$, $4^+$, and $2^+$ states were measured using both $\beta\gamma$(t) and $\gamma\gamma$(t) timing techniques. The $6^+$ state at 1811 keV was found to have a half-life of $T_{1/2} = 461(2)$ ps, determined from a fit to the time-delayed slope of the decay curve. This result is in good agreement with prior measurements but with significantly improved precision. The $4^+$ state at 1497 keV was measured, yielding a mean lifetime of $\tau = 11(7)$ ps, and the $2^+$ state at 743 keV was found to have a lifetime of $\tau = 9(8)$ ps, albeit with large uncertainty. These measurements enabled the extraction of $B(E2)$ transition strengths along the yrast cascade.

Comparison with shell-model predictions reveals varying levels of agreement. The measured $B(E2;\ 6^+ \rightarrow 4^+) = 10.15(4)$ W.u. aligns with shell-model calculations in Ref. [TYHO15, CSA$^+$20]. The newly obtained $B(E2;\ 4^+ \rightarrow 2^+) = 8^{+15}_{-3}$ W.u. supports the trend observed in neighboring even-even Te isotopes and is broadly consistent with the shell-model calculations in Ref. [CSA$^+$20], while the shell-model calculations in Ref. [TYHO15] model underpredicts this transition strength. The $B(E2;\ 2^+ \rightarrow 0^+) = 10^{+63}_{-5}$ W.u. value, owing to its large uncertainty, remains compatible with both the systematics observed in neighboring even-even Te isotopes and with theoretical predictions.

# Chapter 6

# The nuclear structure of $^{128}$Sn

Early relevant publications on $^{128}$Sn are based on $\beta$-decay experiments at the OSIRIS ISOL facility in Studsvik (Sweden) by Fogelberg *et al.* [FC79, FHS81], using a mass-separated A = 128 beam containing Cd, In, Sn, Sb and Ag isobars. Several $\gamma$-rays following the $\beta$ decay of both the $(3^+)$ $^{128g}$In g.s. and $(8^-)$ $^{128m1}$In isomer are reported, populating levels up to 4510 and 4898 keV, respectively. It should be noted that the $Q_{\beta^-}$ value is 9171(18) keV, while the neutron separation energy is 7963(20) keV [WCS$^+$20]. A strongly fed $(7^-)$ state at 2091 keV with $T_{1/2}$ = 6.5(5) s was identified in the $\beta^-$ decay of the $(8^-)$ state. The population of the $(5^-)$ and $(7^-)$ negative-parity states in Ref. [FC79] was somewhat uncertain due to the difficulty in obtaining sources where $^{128}$In and $^{128}$Sn were in equilibrium. Their placement in the decay scheme is doubtful, indicating the need for a re-evaluation of the $^{128}$In $\rightarrow$ $^{128}$Sn decay. Multipolarities of low-lying transitions were obtained from internal conversion electron measurements [FC79, FHS81]. Furthermore, lifetime measurements using plastic and NaI(Tl) scintillators are also provided in Ref. [FC79] for the 2121-keV state, yielding $T_{1/2}$ = 8.6(8) ns. In addition, the 2492-keV level half-life was measured, giving a value of $T_{1/2}$ = 2.91(14) $\mu$s [NND25].

A more recent measurements of the high-spin $(16^+)$ isomeric state in $^{128m2}$In, performed at the IGISOL facility with JYFLTRAP purification, identified a $(15^+)$ state in $^{128}$Sn at $\approx$ 5.8 MeV [NKK$^+$20, IBD$^+$21]. This state decays via a 1779-keV $\gamma$-ray to the known $(15^-)$ isomer at 4099.5 keV ($T_{1/2}$ = 220(30) ns), already reported in fragmentation [PJG$^+$11] and heavy-ion fusion-fission reactions [IBJ$^+$14], and interpreted as a seniority-four $\nu h_{11/2}^{-3} d_{3/2}^{-1}$ configuration.

In spite of being just four neutrons lighter than $^{132}$Sn, the structure of $^{128}$Sn has not been experimentally explored in sufficient detail. In particular, reduced transition probabilities remain largely unmeasured, despite their importance for testing nuclear wave functions. This work presents the study of $^{128}$Sn levels populated in the $\beta$-decay chain $^{128}$Cd $\rightarrow^{128}$ In $\rightarrow^{128}$ Sn $\gamma$ and fast-timing investigation of the excited structure. Out of the three known $\beta$-decaying states in $^{128}$In, the $(3^+)$ g.s., the low-lying $(8^-)$ isomer, and the $(16^+)$ isomer at 1.8 MeV, this measurement benefits from the selective population of the low-spin ground state of $^{128}$In in the $\beta$ decay of the $^{128}$Cd $0^+$ state. The analysis is focused on two fundamental aspects: the potential misplacement

of transitions in the $^{128}$In decay scheme and the limited knowledge of lifetimes and transition probabilities in $^{128}$Sn. To this end, a detailed study of the $\beta$ decay of the $^{128}$In ($3^+$) g.s. has been performed. Furthermore, the difference in half-lives between $^{128}$Cd and $^{128}$In facilitates a clear separation of their respective decay activities. The results provide new insights into the nuclear structure of $^{128}$Sn and enable a re-evaluation of the $^{128}$In decay scheme.

Chap. 6 is structured as follows: Sec. 6.1 details the measurement of the $\beta$-decay half-lives of $^{128}$Cd and $^{128}$In. Sec. 6.2 presents the level scheme of $^{128}$Sn populated in the $\beta$ decay of the $^{128}$In ($3^+$) ground state, including the identification of 81 new $\gamma$ transitions and 30 new excited states based on $\gamma\gamma$ coincidences and intensity balance. Sec. 6.3 discusses the lifetimes of excited states in $^{128}$Sn measured via fast-timing techniques. Sec. 6.4 discusses the level structure in terms of $\beta$-decay selection rules, reduced transition probabilities, and comparisons with shell-model predictions. Finally, the main conclusions of Chap. 6 are presented in Sec. 6.5.

## 6.1 Half-life of $^{128g}$In ($3^+$)

The $^{128g}$Cd and $^{128g}$In $\beta$-decay half-lives were measured by fitting the time distributions relative to the proton pulse impact (Fig. 6.1). Due to the high instantaneous decay rate, dead time effects are present just after the implantation. Therefore, the starting point of the time window for the fit has been optimized employing a $\chi^2$ test, leading to an optimal value of 800 ms. The end of the fit range is defined by the 3600 ms minimum time between implantation, which corresponds to 14 half-lives of $^{128}$Cd and 4 half-lives of $^{128}$In.

The $\beta$-decay half-life of $^{128g}$Cd was determined by fitting an exponential decay function with a constant background, selecting the full-energy peaks of the most intense 315-, 857-, and 935-keV $\gamma$-rays, Compton background subtracted. For each of the transitions, a probability distribution was created by sampling both the fit range and data binning, and the uncertainty was calculated as its standard deviation. The final value was obtained by a weighted mean of the three individual values with a coverage factor of $2\sigma$, yielding a half-life of $T_{1/2} = 256(5)$ ms. The result is in agreement with the recently measured 243(11) ms $^{128g}$Cd half-life [HDE$^+$21] and within $2\sigma$ from the $T_{1/2} = 246(2)$ ms value reported in the latest evaluation [KWH$^+$21].

In the case of $^{128g}$In, a function corresponding to the solution of the Bateman equations [Bat10] for a two-step decay chain was employed. The lifetime of $^{128g}$Cd was fixed to the measured value discussed above, taking into account its uncertainty. The procedure was applied to the 1169-, 936-, 1090-, and 2105-keV $\gamma$-rays, using the same procedure as above. The final value was obtained from the weighted average, giving $T_{1/2} = 814(9)$ ms. The result is in agreement, but more precise, with $T_{1/2} = 816(27)$ ms from the latest evaluation [KWH$^+$21].

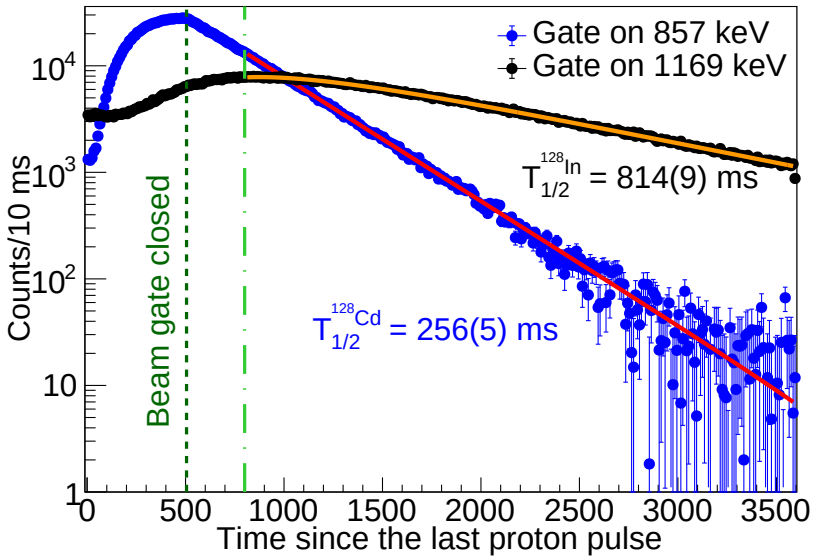


**Figure 6.1.** Time distribution analysis of the $^{128g}$Cd $0^+$ (blue curve) and $^{128g}$In $(3^+)$ (black curve) $\beta$-decay half-lives and decay fit curves. The dark green vertical dashed line represents the end of the implantation. The start of the region considered for the fit is indicated with a light green dot-dashed line. Time distributions gated on 1169- and 857-keV transitions are shown. The final values adopted for $^{128g}$Cd and $^{128g}$In $\beta$-decay half-lives obtained from the weighted average of several transitions are shown in the plot (see text for more details).

## 6.2 Level scheme of $^{128}$Sn

The implantation tape was moved every 38.4 s to avoid the buildup of long-lived activities. Since the $\beta$-decay half-life of $^{128}$Sn is 59.07(14) min [KWH$^+$21], the analyzed data mostly contains the decays of $^{128}$Cd and $^{128}$In. By turning the RILIS ionization off, the release of surface-ionized $^{128}$In was cross-checked, and it was found to be well below 1% of the total beam [LEFB$^+$24].

The $\beta$-delayed neutron emission from the $^{128}$In g.s. is very small, with $P_n = 3.84(36)\times10^{-2}$% [RWE$^+$85, RAS93], so the vast majority of the $\beta$-decay feeds $^{128}$Sn. No $\gamma$ transitions have been observed from the $\beta$n-decay branch in this work.

The time distribution of the two most intense $\gamma$-ray transitions observed is plotted in Fig. 6.1, reflecting the different $\beta$-decay lifetimes convoluted with the implantation profile and the characteristic release time structure arising from the pulsed proton beam at ISOLDE. Owing to the large difference in the half-lives of 246(2) and 816(27) ms, respectively [KWH$^+$21], it is possible to unambiguously identify most of the $\gamma$ rays from the $^{128}$Cd and $^{128}$In decays. In addition, the identification of the $\gamma$ transitions in $^{128}$Sn is based on $\gamma\gamma$ coincidences with previously known transitions.

A $\beta$-gated $\gamma$-ray spectrum is presented in Fig. 6.2. The spectrum was constructed to ensure that only $\gamma$-rays belonging to $^{128g}$In decay are shown by selecting a time window of 130 to 740 ms relative to the proton impact (see Fig. 6.1) and subtracting

contributions of $\gamma$-rays associated with $^{128}$Cd decay using a 30 to 51 ms range. In this way, $\gamma$ transitions in $^{128}$Sn can be identified up to 6.4 MeV. The list of $\gamma$ rays observed in $^{128}$Sn, together with their corresponding intensities, is given in Table 6.1.

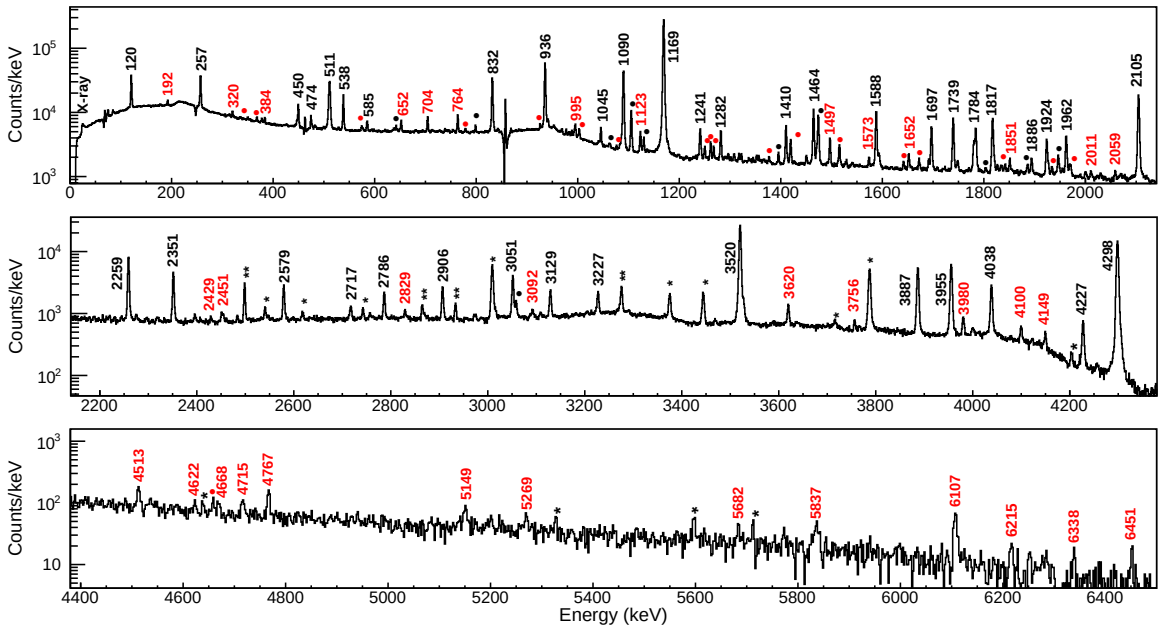


**Figure 6.2.** Beta-gated $\gamma$-ray energy spectrum recorded following the decay of $^{128}$Cd. The spectrum is constructed with a time window since proton impact and subtraction of long-lived isotopes to observe only $\gamma$ rays from the $\beta$ decay of $^{128g}$In $\rightarrow$ $^{128g}$Sn. The negative counts at 857 keV arise from oversubtraction of the most intense $^{128}$Cd full-energy peak. The previously known $\gamma$ rays are labeled in black when the label size allows it; otherwise, only black solid circles are shown. The new transitions identified in this work are labeled in red or marked with red solid circles. Single- and double-escape peaks are labeled with $*$ and $**$, respectively.

The $^{128g}$In decay scheme to $^{128}$Sn has been built based on $\gamma\gamma$ coincidences and intensity balance. As an example, the $\gamma$-ray spectrum in coincidence with the intense 1169-keV $2^+ \rightarrow 0^+$ transition is shown in Fig. 6.3 above 2500 keV, illustrating previously unobserved peaks at high energies. The observed coincidences with the 1357-keV $\gamma$-ray, assigned to the $(2^+) \rightarrow (0_2^+)$ transition (see Sec. 6.4) are presented in Fig. 6.4. The level scheme includes previously known levels and $\gamma$ transitions [FC79, FHS81] with the addition of 81 new $\gamma$ transitions and 30 new states. The expanded level scheme is shown in Figs. 6.5 and 6.6. In Tab. 6.1, the initial (de-exciting) and final (populated) states corresponding to each observed $\gamma$ ray are also listed.

**Table 6.1.** List of $\gamma$ rays observed following the $\beta$ decay of $^{128g}$In to $^{128}$Sn, including transition energies and intensities. The initial and final levels for each connecting transition are also given. Relative $\gamma$ intensities are normalized to 1000 units for the 1169-keV $2^+ \rightarrow 0^+$ transition. For intensity per 100 decays of the parent $^{128}$In multiply by 0.0539(12). Gamma-ray energies listed in the table already include the recoil correction.

| $E_\gamma$ (keV) | $I_\gamma$ | $E_i$ (keV) | $E_f$ (keV) |
|---|---|---|---|
| 120.5(5) | 76(12) | 2121.2(7) | 2000.8(5) |
| 177.4(4) | 2.1(3) | 2756.8(3) | 2579.1(3) |
| 192.1(4) | 2.7(4) | 2825.4(5) | 2633.4(5) |
| 256.9(4) | 68(5) | 2378.2(8) | 2121.2(7) |
| 310.1(4) | 0.5(2) | 2953.0(4) | 2642.8(3) |
| 320.5(4) | 13(2) | 2579.1(3) | 2258.9(4) |
| 351.0(4) | 3.0(6) | 3092.8(3) | 2742.4(5) |
| 368.1(4) | 1.67(14) | 2642.8(3) | 2274.5(4) |
| 377.7(4) | 2.2(2) | 2378.2(8) | 2000.8(5) |
| 384.1(4) | 2.3(3) | 2642.8(3) | 2258.9(4) |
| 447.1(4) | 2.8(7) | 2825.4(5) | 2378.2(8) |
| 449.6(4) | 12(2) | 3092.8(3) | 2642.8(3) |
| 474.5(4) | 10(2) | 2579.1(3) | 2104.6(4) |
| 538.4(3) | 25(2) | 2642.8(3) | 2104.6(4) |
| 574.6(3) | 2.1(4) | 2953.0(4) | 2378.2(8) |
| 584.9(3) | 6.7(7) | 3227.5(3) | 2642.8(3) |
| 638.1(3) | 0.85(7) | 3955.5(4) | 3317.4(5) |
| 642.1(3) | 1.90(14) | 2642.8(3) | 2000.8(5) |
| 652.4(3) | 6.2(8) | 2756.8(3) | 2104.6(4) |
| 704.2(3) | 8.2(9) | 2825.4(5) | 2121.2(7) |
| 763.6(3) | 8.6(8) | 3520.1(5) | 2756.8(3) |
| 778.9(3) | 2.0(4) | 3421.9(3) | 2642.8(3) |
| 831.7(3) | 104(10) | 2000.8(5) | 1169.1(3) |
| 935.6(3) | 172(20) | 2104.6(4) | 1169.1(3) |
| 941.0(3) | 24(3) | 3520.1(5) | 2579.1(3) |
| 966.3(3) | 8(2) | 2967.1(6) | 2000.8(5) |
| 969.0(3) | 4.9(13) | 3227.5(3) | 2258.9(4) |
| 977.3(3) | 2.4(2) | 3619.8(3) | 2642.8(3) |
| 983.0(3) | 1.6(3) | 4075.8(4) | 3092.8(3) |
| 988.4(3) | 3.1(5) | 3092.8(3) | 2104.6(4) |
| 994.8(3) | 11(2) | 2163.9(5) | 1169.1(3) |
| 1002.8(3) | 4.7(6) | 3955.5(4) | 2953.0(4) |
| 1045.5(3) | 8.0(10) | 3998.3(3) | 2953.0(4) |
| 1089.9(3) | 153(20) | 2258.9(4) | 1169.1(3) |
| 1105.4(3) | 29(3) | 2274.5(4) | 1169.1(3) |
| 1123.2(3) | 11(2) | 3227.5(3) | 2104.6(4) |
| 1130.0(3) | 5.5(8) | 3886.7(5) | 2756.8(3) |
| 1136.7(3) | 0.42(11) | 3241.3(5) | 2104.6(4) |
| 1169.1(3) | 1000 | 1169.1(3) | 0.0 |
| 1241.3(3) | 16(2) | 3998.3(3) | 2756.8(3) |

| $E_\gamma$ (keV) | $I_\gamma$ | $E_i$ (keV) | $E_f$ (keV) |
|---|---|---|---|
| 1250.2(3) | 3.2(3) | 4075.8(4) | 2825.4(5) |
| 1261.7(3) | 5.3(5) | 3520.1(5) | 2258.9(4) |
| 1267.8(3) | 4.2(5) | 4093.2(6) | 2825.4(5) |
| 1281.8(3) | 15.0(10) | 4038.5(5) | 2756.8(3) |
| 1307.4(3) | 2.2(3) | 3886.7(5) | 2579.1(3) |
| 1317.5(3) | 2.4(2) | 3421.9(3) | 2104.6(4) |
| 1322.3(3) | 1.6(3) | 3955.5(4) | 2633.4(5) |
| 1357.1(3) | 1.2(3) | 3520.1(5) | 2163.9(5) |
| 1377.1(3) | 2.5(3) | 3955.5(4) | 2579.1(3) |
| 1395.6(3) | 10.3(10) | 4220.7(3) | 2825.4(5) |
| 1410.1(3) | 20(2) | 2579.1(3) | 1169.1(3) |
| 1419.2(3) | 10.0(12) | 3998.3(3) | 2579.1(3) |
| 1464.4(3) | 41(4) | 2633.4(5) | 1169.1(3) |
| 1473.6(3) | 37(6) | 2642.8(3) | 1169.1(3) |
| 1496.7(3) | 9.9(9) | 4075.8(4) | 2579.1(3) |
| 1515.2(3) | 7.4(7) | 3619.8(3) | 2104.6(4) |
| 1573.3(3) | 3.2(3) | 2742.4(5) | 1169.1(3) |
| 1587.7(3) | 44(4) | 2756.8(3) | 1169.1(3) |
| 1641.4(3) | 2.7(3) | 4220.7(3) | 2579.1(3) |
| 1651.9(3) | 5.1(6) | 3756.5(4) | 2104.6(4) |
| 1672.4(3) | 2.9(4) | 3931.2(4) | 2258.9(4) |
| 1696.8(3) | 23(2) | 3955.5(4) | 2258.9(4) |
| 1739.4(3) | 35(3) | 3998.3(3) | 2258.9(4) |
| 1783.9(3) | 22(2) | 2953.0(4) | 1169.1(3) |
| 1817.1(4) | 37(4) | 4075.8(4) | 2258.9(4) |
| 1826.3(4) | 2.0(3) | 3931.2(4) | 2104.6(4) |
| 1834.4(4) | 1.3(2) | 3998.3(3) | 2163.9(5) |
| 1841.2(4) | 1.45(13) | 3962.5(8) | 2121.2(7) |
| 1851.1(4) | 3.7(4) | 3955.5(4) | 2104.6(4) |
| 1885.6(4) | 2.1(2) | 3886.7(5) | 2000.8(5) |
| 1893.8(4) | 4.6(4) | 3998.3(3) | 2104.6(4) |
| 1924.0(4) | 18(2) | 3092.8(3) | 1169.1(3) |
| 1934.2(4) | 1.9(4) | 4038.5(5) | 2104.6(4) |
| 1946.6(4) | 7.6(8) | 4220.7(3) | 2274.5(4) |
| 1954.7(4) | 2.4(4) | 3955.5(4) | 2000.8(5) |
| 1962.0(4) | 20(2) | 4220.7(3) | 2258.9(4) |
| 1969.7(4) | 7.1(9) | 4228.2(4) | 2258.9(4) |
| 2010.9(4) | 1.6(3) | 3180.0(5) | 1169.1(3) |
| 2058.7(4) | 1.9(2) | 3227.5(3) | 1169.1(3) |
| 2074.8(4) | 1.1(4) | 4075.8(4) | 2000.8(5) |
| 2104.6(4) | 111(11) | 2104.6(4) | 0.0 |
| 2148.3(4) | 0.95(12) | 3317.4(5) | 1169.1(3) |
| 2219.3(4) | 1.2(3) | 4220.7(3) | 2000.8(5) |
| 2258.8(4) | 50(5) | 2258.9(4) | 0.0 |
| 2275.1(4) | 3.0(3) | 2274.5(4) | 0.0 |

| $E_\gamma$ (keV) | $I_\gamma$ | $E_i$ (keV) | $E_f$ (keV) |
|---|---|---|---|
| 2351.3(4) | 27(3) | 3520.1(5) | 1169.1(3) |
| 2429.1(4) | 1.2(2) | 4533.5(4) | 2104.6(4) |
| 2450.9(4) | 2.6(3) | 3619.8(3) | 1169.1(3) |
| 2532.4(5) | 0.8(3) | 4533.5(4) | 2000.8(5) |
| 2578.9(5) | 16.0(14) | 2579.1(3) | 0.0 |
| 2717.1(5) | 3.0(7) | 3886.7(5) | 1169.1(3) |
| 2786.4(5) | 10.7(3) | 3955.5(4) | 1169.1(3) |
| 2829.3(5) | 2.9(3) | 3998.3(3) | 1169.1(3) |
| 2906.4(5) | 17(2) | 4075.8(4) | 1169.1(3) |
| 3051.3(5) | 28(3) | 4220.7(3) | 1169.1(3) |
| 3059.7(5) | 5.78(10) | 4228.2(4) | 1169.1(3) |
| 3059.7(5) | 0.52(7) | 5181.0(9) | 2121.2(7) |
| 3091.7(5) | 3.4(4) | 3092.8(3) | 0.0 |
| 3128.5(5) | 15.0(14) | 4298.1(6) | 1169.1(3) |
| 3226.9(5) | 12.9(13) | 3227.5(3) | 0.0 |
| 3520.0(6) | 278(30) | 3520.1(5) | 0.0 |
| 3619.6(6) | 8.3(9) | 3619.8(3) | 0.0 |
| 3756.2(6) | 2.0(2) | 3756.5(4) | 0.0 |
| 3886.6(6) | 60(6) | 3886.7(5) | 0.0 |
| 3955.4(6) | 70(7) | 3955.5(4) | 0.0 |
| 3980.4(6) | 5.4(6) | 5149.5(7) | 1169.1(3) |
| 4038.4(6) | 31(3) | 4038.5(5) | 0.0 |
| 4099.7(6) | 3.4(3) | 5268.8(7) | 1169.1(3) |
| 4149.4(6) | 2.5(3) | 5318.5(7) | 1169.1(3) |
| 4227.2(6) | 8.4(9) | 4228.2(4) | 0.0 |
| 4298.1(6) | 198(20) | 4298.1(6) | 0.0 |
| 4309.8(6) | 1.3(2) | 5478.9(7) | 1169.1(3) |
| 4512.8(6) | 0.77(12) | 5681.9(6) | 1169.1(3) |
| 4621.7(6) | 0.24(6) | 4621.8(6) | 0.0 |
| 4658.3(6) | 0.4(2) | 4658.4(6) | 0.0 |
| 4668.2(6) | 0.4(1) | 4668.3(6) | 0.0 |
| 4715.4(5) | 0.59(13) | 4715.5(5) | 0.0 |
| 4766.7(5) | 0.94(11) | 4766.8(5) | 0.0 |
| 5148.8(5) | 0.42(6) | 5149.5(7) | 0.0 |
| 5269.1(5) | 0.17(10) | 5268.8(7) | 0.0 |
| 5681.6(5) | 0.19(4) | 5681.9(6) | 0.0 |
| 5836.8(4) | 0.39(7) | 5836.9(4) | 0.0 |
| 6107.3(4) | 0.95(9) | 6107.4(4) | 0.0 |
| 6215.0(4) | 0.12(2) | 6215.2(4) | 0.0 |
| 6337.7(4) | 0.017(7) | 6337.8(4) | 0.0 |
| 6451.3(3) | 0.08(2) | 6451.5(3) | 0.0 |

The $\beta$-decay feeding has been determined from the intensity balance between feeding and de-populating $\gamma$ rays for each level. Since the $\beta$ decay of the $^{128}$In ($3^+$) g.s. to the $^{128}$Sn $0^+$ g.s. would be via a second-forbidden transition, direct $\beta$ feeding

to the g.s. has been taken to be zero. Apparent $\log ft$ values are derived assuming allowed transitions [TMSZ23] from $\gamma$-ray intensities corrected for internal conversion [KBT+08], the $Q_{\beta^-}$ and the measured $\beta$-decay half-life.

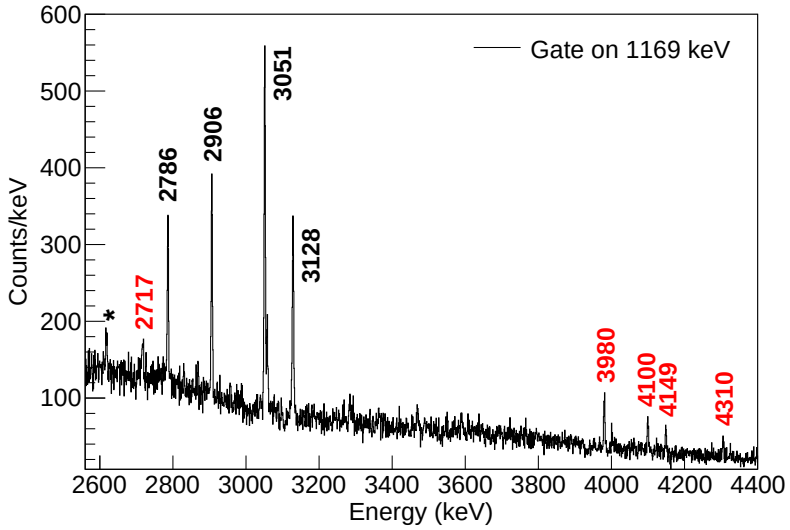


**Figure 6.3.** Compton-subtracted $\gamma$-$\gamma$ energy projection spectrum gated on the 1169-keV $2^+ \rightarrow 0^+$ transition in $^{128}$Sn in the 2600-4400 keV high energy range. The previously known $\gamma$-rays are labeled with their energies in black, while new ones are marked in red. The 3128-keV single-escape peak is labeled with an asterisk.

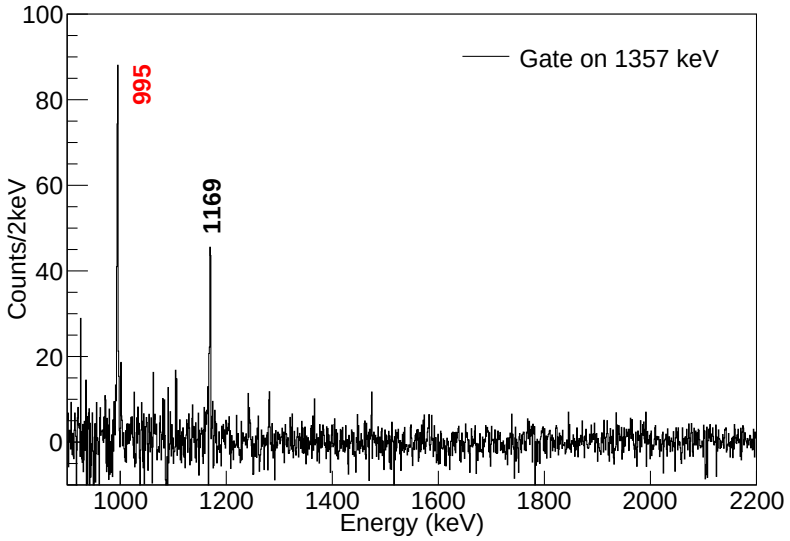


**Figure 6.4.** Compton-subtracted $\gamma$-$\gamma$ energy projection spectrum gated on the 1357-keV $(2^+) \rightarrow (0_2^+)$ transition in $^{128}$Sn in the 940-2200 keV energy range. The new coincident 995-keV $\gamma$-ray is labeled in red.

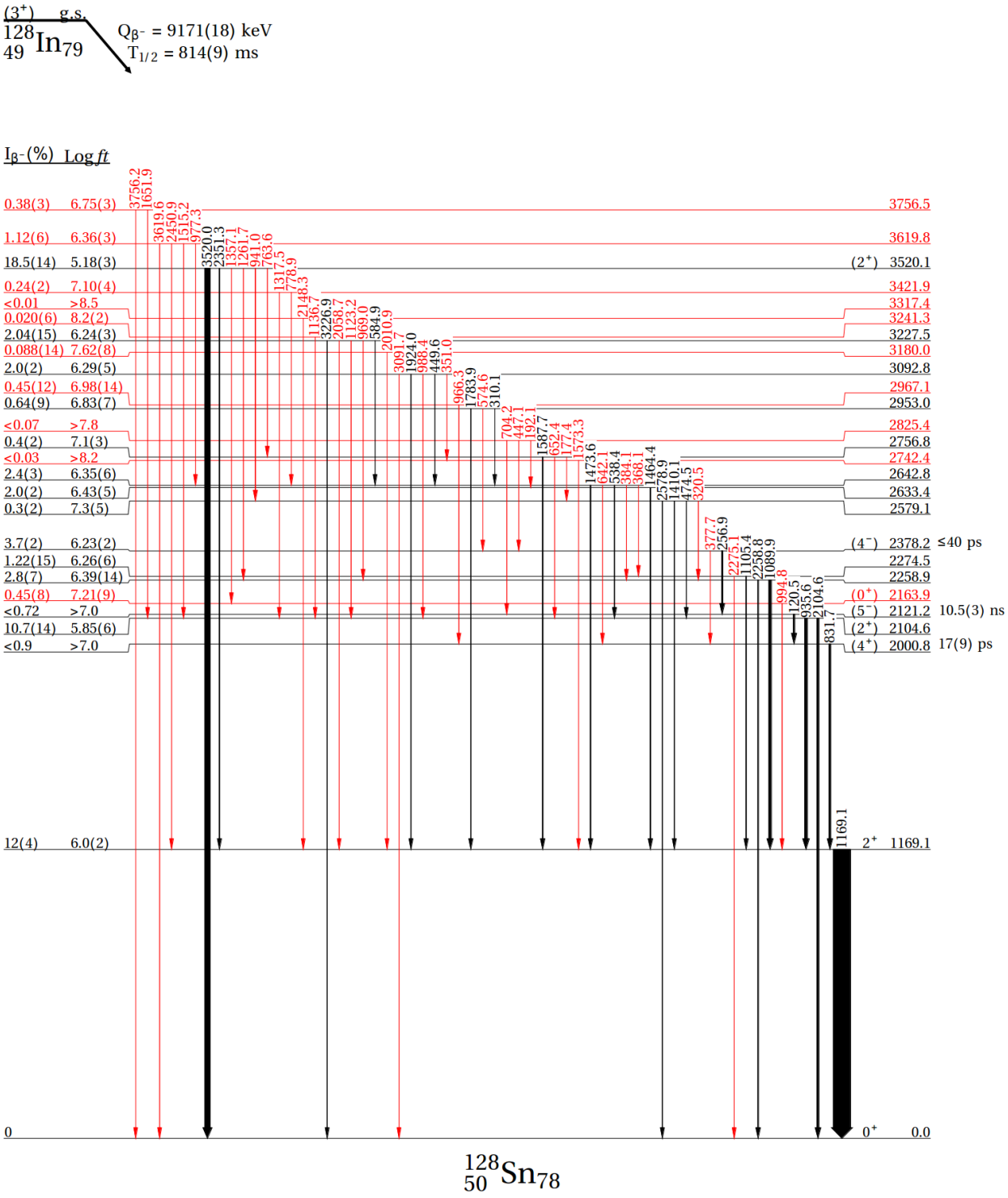


**Figure 6.5.** Level scheme of $^{128}$Sn observed following the $\beta$ decay of the $^{128g}$In $(3^+)$ state. Levels and transitions previously identified are colored in black, while those newly identified in this work are highlighted in red. Line widths are proportional to their relative intensities.

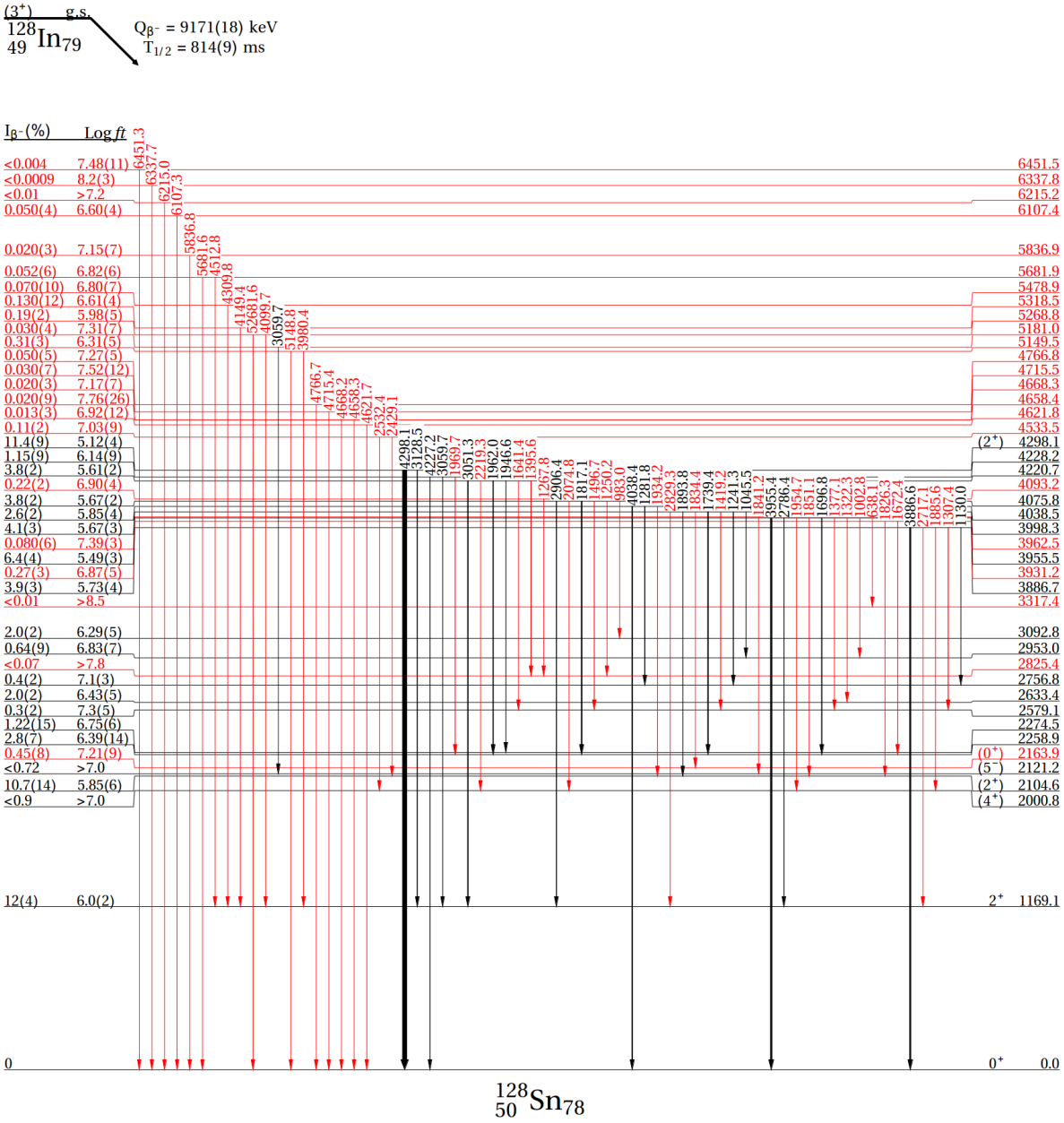


**Figure 6.6.** Level scheme of $^{128}$Sn observed following the $\beta$ decay of the $^{128g}$In $(3^+)$ state. Levels and transitions previously identified are colored in black, while those newly identified in this work are highlighted in red. Line widths are proportional to their relative intensities.

## 6.3 Lifetimes of excited states in $^{128}$Sn

Lifetimes of excited states in $^{128}$Sn in the nanosecond and sub-nanosecond ranges have been investigated via $\beta\gamma\gamma$(t), $\beta\gamma$(t), and $\gamma\gamma$(t) fast-timing methods (see Chap. 4). The half-lives of the 2378-keV state, 2121-keV ($5^-$) state, and 2001-keV ($4^+$) state are discussed.

The time-delayed spectrum for the analysis of the lifetime of the 2121-keV state, with a proposed ($5^-$) spin-parity (see Sec. 6.4) is displayed in Fig. 6.7. The half-life has been obtained from $\beta\gamma$(t) events time-selected for the $^{128}$In decay, and measured by summing the 120-, 832-, and 1169-keV full-energy peaks in the two $LaBr_3$(Ce) detectors. The half-life was measured by fitting the delayed slope of the combined spectra once the influence of Compton events under the peaks were subtracted. Neither the population of known isomeric states, nor evidence of an unknown isomeric state that may feed the ($5^-$) level has been observed. An exponential decay plus a constant background fit results in $T_{1/2}$ = 10.5(3) ns. The resulting half-life is larger than the previously measured, $T_{1/2}$ = 8.6(8) ns, using NaI(Tl) detectors [FC79].

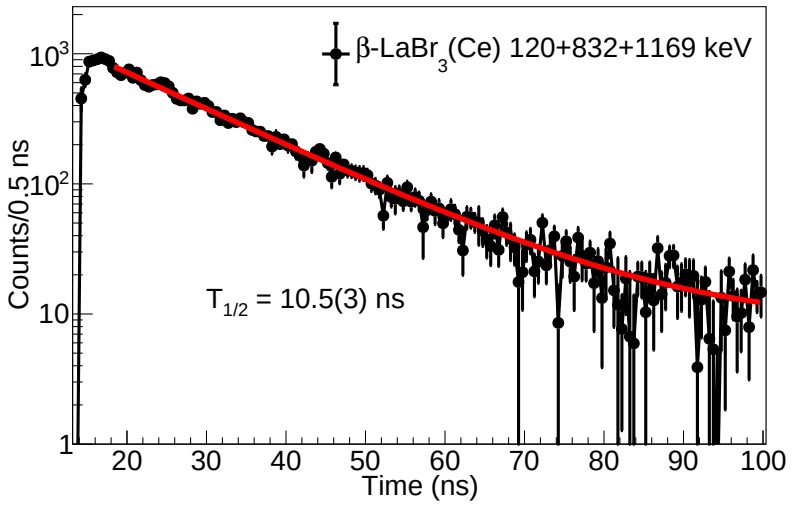


**Figure 6.7.** Time-delayed spectrum between the $\beta$ detector and either of the two $LaBr_3$(Ce) detectors for $\beta\gamma$(t) events. This distribution is built by adding up the 120-, 832-, and 1169-keV transitions in the $LaBr_3$(Ce) detectors. A time window gate corresponding to the $^{128}$In half-life was imposed to reduce the background. The lifetime was obtained by a $\chi^2$ minimization of the time distribution to an exponential decay with a constant background component. See text for details.

The lifetime of the 2001-keV ($4^+$) state was obtained from the time-delayed coincidences between the two $LaBr_3$(Ce). No prior lifetime measurement was reported in the literature. This level is almost entirely fed by $\gamma$ transitions ($I_\beta < 0.9$ %). Besides, almost all the feeding is provided by the 120-keV transition from the long-lived ($5^-$) state with $T_{1/2}$ = 10.5(3) ns. Thus, the analysis was performed using time difference information between the two $LaBr_3$(Ce) detectors. In this manner, the ($5^-$) level half-life does not affect the measurement. An extra condition in the $\beta$-$LaBr_3$(Ce) TAC was required by including only $\beta$-delayed events by more than 2 ns relative to the $\beta\gamma$

prompt ($\leq$ 200 ps) (see Fig. 6.8). This suppresses most of the $\gamma$-rays, leaving only the 120-832-1169 cascade peaks below the $(5^-)$ state in the spectra. The lifetime analysis of the 2001-keV state is shown in Fig. 6.9. A mean lifetime of $\tau$ = 25(13) ps, which translates to $T_{1/2}$ = 17(9) ps, was obtained from the centroid shift method.

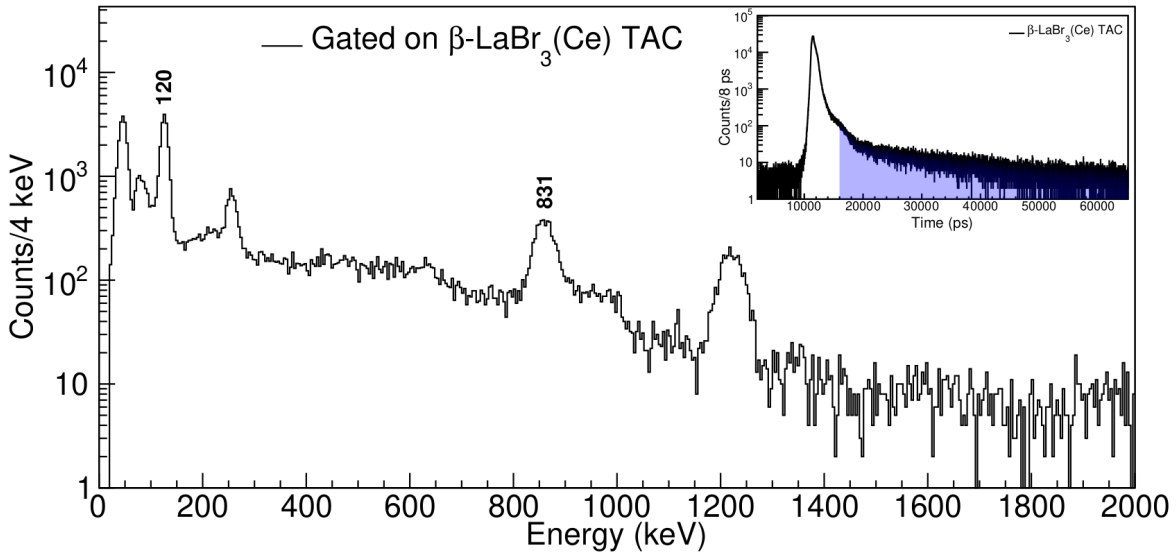


**Figure 6.8.** $LaBr_3$(Ce) $\gamma$-ray energy spectra obtained with an additional timing condition applied to the $\beta$-$LaBr_3$(Ce) TAC. Only $\beta$-delayed events occurring more than 2 ns after the $\beta\gamma$ prompt coincidence were included. The inset plot shows the $\beta$-$LaBr_3$(Ce) TAC spectrum. The shaded area represents the gate that was selected.

The lifetime of the 2378-keV level has been measured by the analysis of the $\beta\gamma\gamma$(t) time difference distributions of the 257-keV $\gamma$-ray in the $LaBr_3$(Ce) detectors vs. the $\beta$ events, with an extra coincidence condition on the 120-keV transition in the HPGe detectors (See Fig. 6.10).

The lifetime analysis of the 2378-keV level is depicted in Fig. 6.11. The time distribution does not have a delayed component, which is characteristic of a short lifetime. Unfortunately, the centroid shift method could not be employed because no independent time reference was found. Instead, the half-life was measured from a fit to a Gaussian convoluted with an exponential function, by probing different half-life values while evaluating the $\chi^2$/NDF. An upper limit of $T_{1/2} \leq 40$ ps was adopted from the $T_{1/2}$ value given by $(\chi^2_{min} + 1)$/NDF.

Reduced transition probabilities $B(X\lambda)$ for transitions in $^{128}$Sn were calculated from the measured lifetimes of the $(4^-)$, $(5^-)$, and $(4^+)$ levels, the $\gamma$-ray intensities, and the tabulated internal conversion coefficients [KBT+08] assuming pure multipolarities. The results are summarized in Table 6.2.

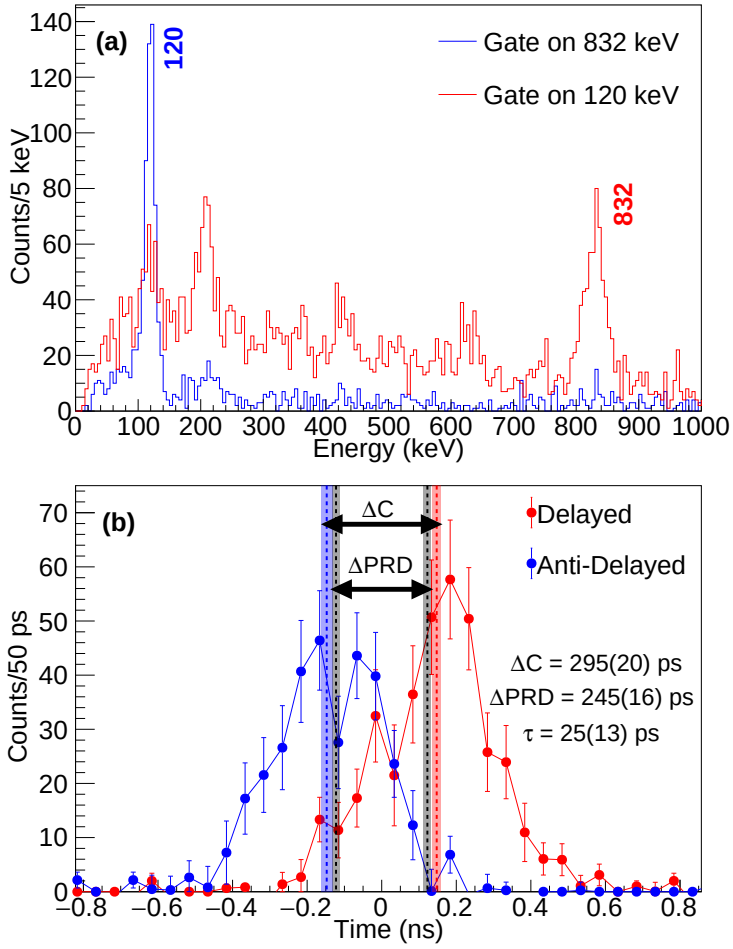


**Figure 6.9.** Energy spectra recorded in the $LaBr_3$(Ce) start detector after gating in the 120 and 832-kev on the stop $LaBr_3$(Ce) detector respectively (a). Time delay distributions between the two $LaBr_3$(Ce) detectors for $\gamma\gamma$(t) events (b). Depending on the selected $\gamma$ transition in the start and stop detectors, either the delayed or the anti-delayed distributions are derived. The centroid is shown with a dashed line, while the shaded area represents its uncertainty. The centroid shift measured between the delayed and anti-delayed time spectra ($\Delta$C), is caused by the lifetime of the level and the shift in the Prompt Response Difference ($\Delta$PRD)

## 6.4 Discussion

Tentative spin-parity assignments for the populated states in $^{128}$Sn are based on the $\beta$-decay selection rules, the observed $\gamma$-ray transitions between levels, and the transition probabilities provided by the lifetime measurements. The starting point is the proposed $(3^+)$ g.s. for the $^{128}$In, interpreted as a member of the $\pi g_{9/2}^{-1}\nu d_{3/2}^{-1}$ multiplet [Ber18, SGP+04], and the previous information about $^{128}$Sn [FC79].

The systematics of excited states in even-even Sn isotopes is shown in Fig. 6.12, including the $2^+$, $4^+$, and $6^+$ yrast states, the second $0^+$ and $2^+$ states, and the low-lying $4^-$, $5^-$, $6^-$ and $7^-$ levels.

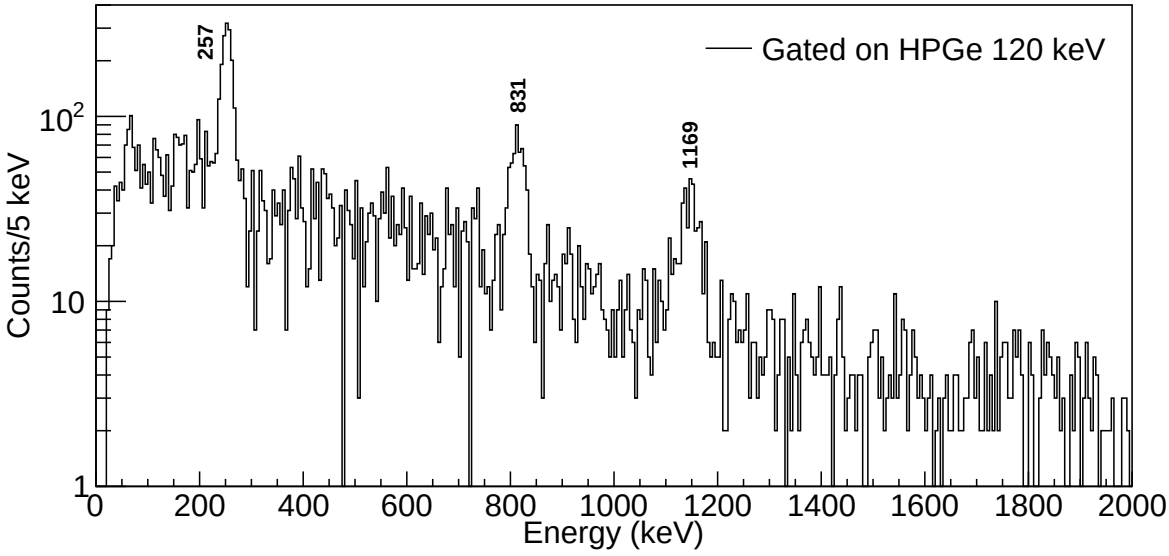


**Figure 6.10.** $LaBr_3(Ce)$ $\gamma$-ray energy spectra gated on the 120-keV transitions detected in the HPGe detectors.

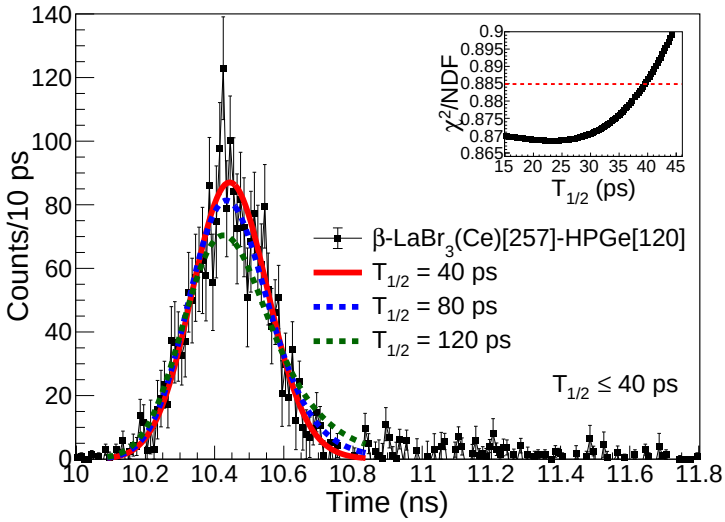


**Figure 6.11.** Time-delayed $\beta\gamma\gamma$(t) spectrum between the $\beta$ and the $LaBr_3(Ce)$ detectors selected by the 257-keV transition. An extra condition was required in the 120-keV $\gamma$ transition in the HPGe detectors. The lifetime was obtained from a $\chi^2$ minimization of the distribution to a Gaussian convoluted with exponential function. The inset plot shows the $\chi^2$/NDF vs half-life dependence. To show the robustness of the fitting method half-lives of 80 and 120 ps with a Gaussian prompt with fixed width are shown by the blue and green dotted lines, respectively.

Shell-model calculations for states for $^{128}$Sn are discussed in Refs. [HEHJO98, TYHO15, PSC+19, WLWJ22]. Ref. [HEHJO98] uses $^{132}$Sn as a core and employs the $2s_{1/2}$, $1d_{5/2}$, $1d_{3/2}$, $0g_{7/2}$, and $0h_{11/2}$ orbits, as valence space, where neutrons are holes and protons are particles. An effective interaction is derived employing perturbative many-body techniques starting from a free nucleon-nucleon interaction. Teruya *et al.* [TYHO15] adopt the same model space with all five single-particle orbitals in the 50−82 major shell, with a phenomenological interaction with two-body terms

**Table 6.2.** Level lifetimes and reduced transition probabilities for transitions in $^{128}$Sn. The spin assignments for the initial and final level follow Ref. [NND25], except for the $(4^-)$ level, which is proposed in this work. The $B(X\lambda)$ were calculated from the lifetimes and branching ratios obtained in this work, using conversion coefficients taken from Ref. [KBT+08] and assuming pure multipolarities as indicated.

| $E_i$(keV) | $J_i^\Pi$ | $\tau$ | $E_f$(keV) | $J_f^\Pi$ | $E_\gamma$(keV) | X$\lambda$ | $B$(X$\lambda$)(W.u.) |
|---|---|---|---|---|---|---|---|
| 2121 | $(5^-)$ | 15.2(4) ns | 2001 | $(4^+)$ | 120 | $E1$ | $1.31(4)\times10^{-5}$ |
| 2378 | $(4^-)$ | $\leq$57 ps | 2121 | $(5^-)$ | 257 | $M1$ | $\geq3\times10^{-2}$ |
| | | | 2001 | $(4^+)$ | 378 | $E1$ | $\geq4\times10^{-6}$ |
| 2001 | $(4^+)$ | 25(13) ps | 1169 | $(2^+)$ | 832 | $E2$ | $2.1(^{+2.3}_{-0.7})$ |

consisting of pairing and quadrupole-quadrupole interactions. The same model space and a similar approach is adopted in Ref. [PSC+19] by using the jj55 interaction.

The shell-model calculations in Ref. [WLWJ22] employ an extended pairing plus multipole-multipole (EPQQM) model with a frozen $^{78}$Ni core and all orbitals in the 28−50 major shell plus $0g_{7/2}$ and $1d_{5/2}$ for protons, and those in the 50−82 major shell plus $1f_{7/2}$ and $2p_{3/2}$ for neutrons.

Finally, Cheng *et al.* [CQZA16] take a different approach by performing three sets of calculations in the so-called nucleon-pair approximation, a pair-truncation scheme of the shell model based on the generalized seniority scheme. The calculations use the full 50−82 major shell-model space, a truncated nucleon-pair approximation space and an optimized pair basis where no mixing is considered, respectively.

### 6.4.1 Positive parity states

Assuming the dominant $\pi g_{9/2}^{-1}\nu d_{3/2}^{-1}h_{11/2}^{-2}$ configuration of the parent g.s. [WLWJ22], the most favorable $\beta$-decay route is an allowed GT $\nu g_{7/2} \rightarrow \pi g_{9/2}$ transition [BFK+24], which populates positive parity states with a dominant component of the $\nu g_{7/2}^{-1}d_{3/2}^{-1}h_{11/2}^{-2}$ configuration. Since $g_{7/2}$ is the most bound orbit in the neutron shell (2.44 MeV more compared to $d_{3/2}$, see Chap. 2), a high excitation energy can be expected for this configuration. The strong $\beta$ population observed to high-energy levels above 3 MeV, such as the 3520- and 4298-keV states with log$ft$ values equal to 5.18(3) and 5.12(4), respectively, is likely due to this GT transition. These states are tentatively assigned $(2^+)$ spin-parity. In fact, the $2^+$ states above 3.2 MeV may contain admixtures of other neutron-hole wave functions from the $s_{1/2}$, $d_{5/2}$ and $g_{7/2}$ orbitals. For example, the shell-model calculations in Ref. [WLWJ22] obtain that the $2^+$ state at 4298 keV has a 57% contribution from the $\nu h_{11/2}^{-2}d_{3/2}^{-1}g_{7/2}^{-1}$ and 14% from the $\nu h_{11/2}^{-2}d_{3/2}^{-1}s_{1/2}^{-1}$ configurations.This indicates that, while the primary configuration is still $\nu h_{11/2}^{-2}d_{3/2}^{-1}g_{7/2}^{-1}$, there is significant mixing, which contributes to increasing the energy of the state.

Turning now to the $2^+$ states below 3.2 MeV, they are dominated by the $\nu h_{11/2}^{-2}d_{3/2}^{-2}$

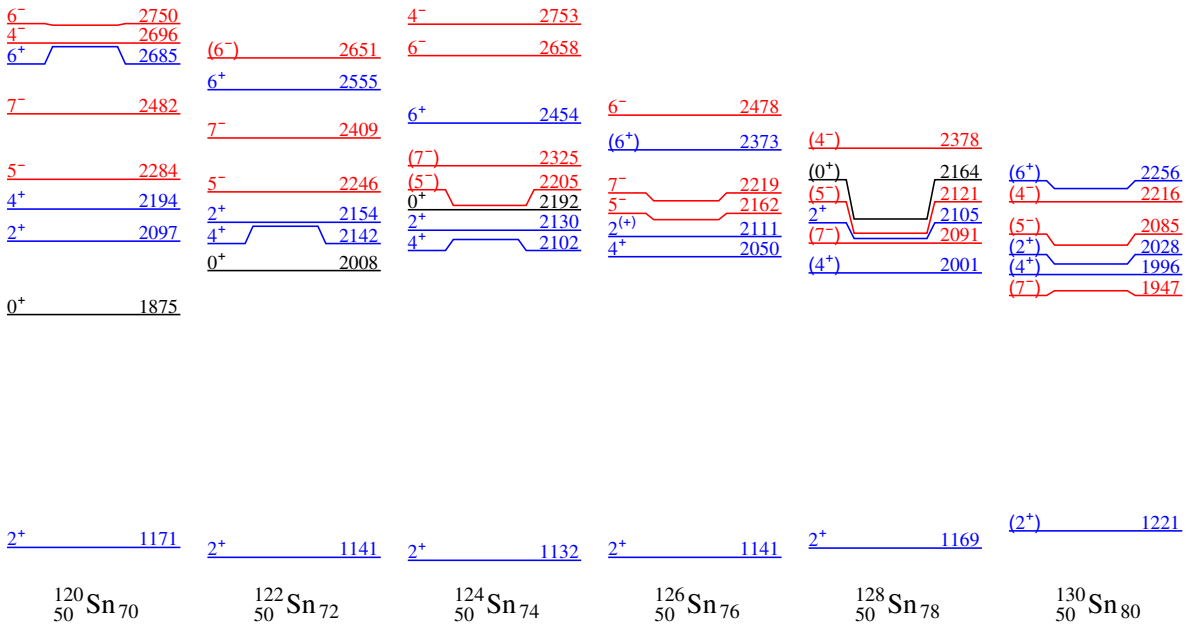


**Figure 6.12.** Energies of excited states in the even-even Sn isotopes. Positive- and negative-parity states are shown in blue and red, respectively. The $0^+_1$ ground states are not plotted for the sake of clarity. Data are taken from Ref. [NND25] and from the present work for $^{128}$Sn.

configuration according to the shell-model calculations [WLWJ22]. In this energy range, the neutron orbitals $h_{11/2}$ and $d_{3/2}$ are close in energy, which facilitates their coupling to $2^+$ states. The direct $\beta$-decay feeding to these $2^+$ states is much more suppressed in comparison to those located above, their $\log ft$ values being consistently higher than 5.8, which does not support a GT character [TMSZ23]. The hindrance is even more pronounced for the first $4^+$ state, with $\log ft > 7$. The origin of this strong suppression can be the small overlap between the initial and final state configurations, which in the single-particle picture, would require a second-forbidden $\nu d_{3/2} \rightarrow \pi g_{9/2}$ transition to connect them. However, the 1.5 MeV gap between the highest observed level and the neutron separation energy suggests the possibility of unobserved feeding into higher-lying states. These states could feed the $2^+$ levels through high-energy $\gamma$-ray cascades that remain undetected due to experimental limitations [HCJH77].

In this work the first lifetime measurement for the $(4^+)$ state at 2001 keV has been provided, from which an experimental $B(E2;\ 4^+ \rightarrow\ 2^+) = 2.1(^{+2.3}_{-0.7})$ W.u. has been deduced. Fig. 6.13 shows experimental $B(E2;\ 2^+ \rightarrow 0^+)$ and $B(E2;\ 4^+ \rightarrow 2^+)$ reduced transition probabilities for the even-even Sn isotopes compared to calculations available in the literature. Shell model calculations in Ref. [HEHJO98] are in agreement with the experimental values. More recent calculations for $^{126-130}$Sn [TYHO15, CQZA16] are also consistent with the experimental results and seem to reproduce the new $B(E2;\ 4^+ \rightarrow 2^+)$ within the large experimental uncertainty. The observed trend varies significantly depending on the type of calculation and the model employed. Data about the yet to be experimentally measured $B(E2;\ 4^+ \rightarrow 2^+)$ values in the neighboring $^{126}$Sn and $^{130}$Sn will help to understand the systematics of E2 transition strengths approaching $^{132}$Sn.

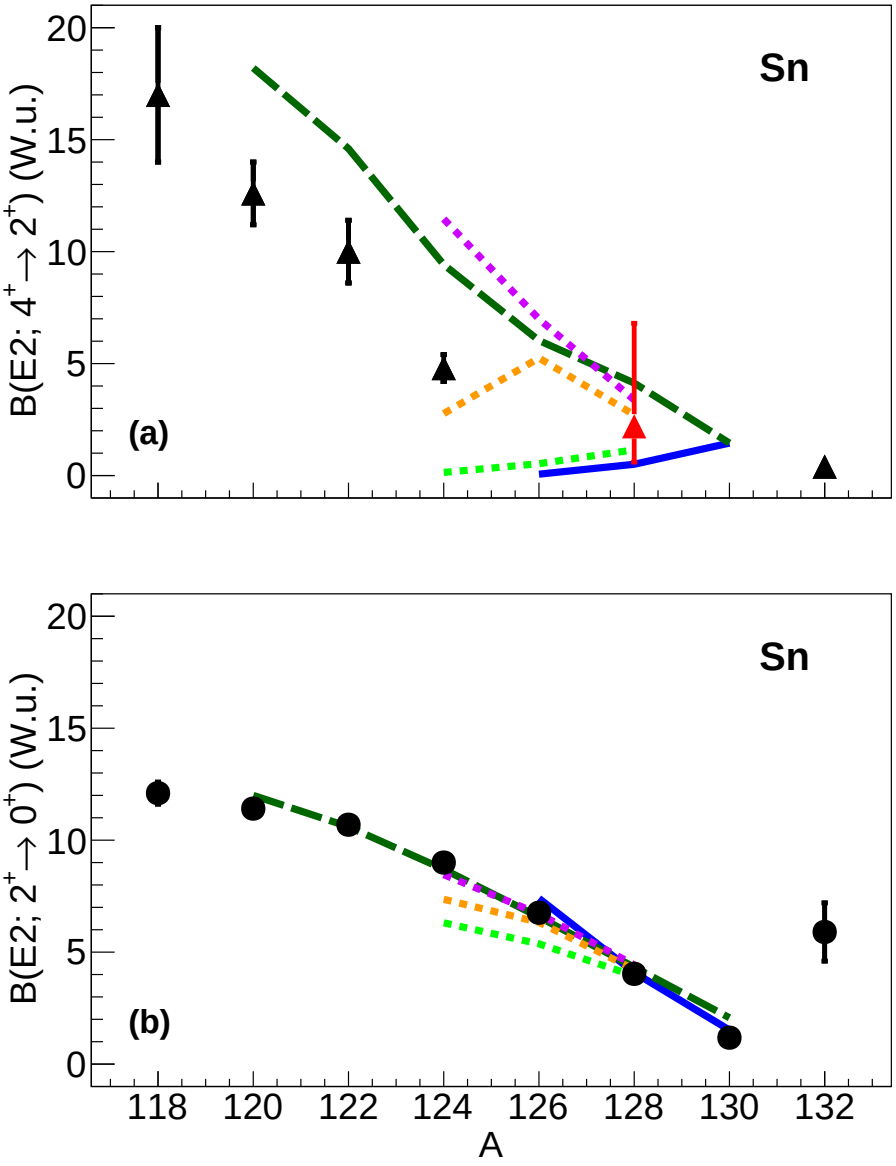


**Figure 6.13.** Experimental reduced transition probabilities in W.u. for the $4^+ \rightarrow 2^+$ (a) and $2^+ \rightarrow 0^+$ (b) transitions in the even Sn isotopes taken from Ref. [NND25]. The $B(E2;\ 4^+ \rightarrow 2^+)$ value for $^{128}$Sn that has been measured in this work is plotted in red. Theoretical calculations are shown with lines, Holt *et al.* solid (blue) [HEHJO98], Teruya *et al.* dashed (dark green) [TYHO15] and Cheng *et al.* dotted (light green, orange and violet) [CQZA16].

The new level established at 2164 keV (see Fig. 6.4) has been tentatively assigned spin-parity $(0^+)$, based on its de-exciting pattern and in agreement with the systematics of the $0_2^+$ states in even Sn nuclei, see Fig. 6.12. This is consistent with the shell model calculations presented in Ref. [PSC+19], which predict an energy of 2159 keV for the $0_2^+$ level with the main $\nu h_{11/2}^{-4}$ configuration having an amplitude of 47%.

### 6.4.2 Negative parity states

The close-lying levels of $\nu h_{11/2}$ and $\nu d_{3/2}$ orbitals lead to the existence of low-lying negative parity states based on the $\nu h^{-1}_{11/2} d^{-1}_{3/2}$ coupling, leading to a $J^\pi$=(4,5,6,7)$^-$ multiplet. One expects a sizable direct feeding to members of the multiplet in the $\beta$-decay transition from the (3$^+$) ground state in $^{128}$In. More particularly, the population of the 4$^-$ state should be observed due to the predominance of the first-forbidden $\nu h_{11/2} \rightarrow \pi g_{9/2}$ transition [BFK$^+$24]. The 5$^-$ and 7$^-$ members are assigned to the 2121-keV and 2091-keV experimental states, respectively, while the 4$^-$ and 6$^-$ states remain unidentified. The systematics of even-even tin isotopes in Fig. 6.12 and the shell-model calculations [CQZA16] indicate their positions in the 2-3 MeV range.

An interesting result emerges from the observed direct feeding to the 2378-keV level in the $\beta$ decay of $^{128}$In (3$^+$) g.s., with an I$_\beta$ = 3.7(2)% and log$ft$ = 6.23(2). This state was formerly assigned spin-parity (7$^-$) [FC79], which would imply a third-forbidden unique $\beta$ transition. This is difficult to reconcile with the experimental observation, even if populating high-energy $\gamma$ transitions are missed. Moreover, the upper limit of 40-ps half-life indicates that the 257-keV $\gamma$ ray that connects this state to the 2121-keV (5$^-$) level is predominantly of $M1$ character. A pure $E2$ multipolarity required by a potential (7$^-$) $\rightarrow$ (5$^-$) transition would yield an unrealistic $B(E2) \geq 304$ W.u. Additionally, a small branching ratio for a 378-keV transition connecting to the 2001-keV (4$^+$) state has been found. Considering the half-life upper limit and the branching ratio, a lower limit of $B(E1) \geq 4{\times}10^{-6}$ W.u. is obtained, which is compatible with the $B(E1) = 1.31(4){\times}10^{-5}$ W.u. measured for the (5$^-$) $\rightarrow$ (4$^+$) transition. The evidence supports the interpretation of the 2378-keV state as the missing 4$^-$ member of the $\nu d^{-1}_{3/2} h^{-1}_{11/2}$ multiplet, see Fig. 6.12.

## 6.5 Conclusions of the chapter

A detailed investigation of the excited state structure of $^{128}$Sn, populated exclusively through the $\beta$-decay of $^{128g}$In, was conducted. Utilizing high-resolution $\gamma$-ray spectroscopy and advanced fast-timing techniques the previously known $\beta$ decay scheme from $^{128g}$In (3$^+$) to $^{128}$Sn was disentangled and significantly expanded. A total of 81 new $\gamma$ transitions and 30 new levels were identified providing a comprehensive update to the $^{128}$Sn level scheme.

The new level at 2164 keV has been established and is tentatively assigned (0$^+$) based on its de-exciting pattern and shell-model calculations, consistent with the systematics of the $0^+_2$ states in even-mass Sn isotopes.

New values for the half-life of the $^{128g}$Cd 0$^+$ g.s. T$_{1/2}$ = 256(5) ms and $^{128g}$In (3$^+$) g.s. T$_{1/2}$ = 814(9) ms, have been measured. This measurement was obtained by analyzing the time distribution of the ten strongest $\gamma$-rays emitted in the $^{128}$Cd $\beta$-decay.

Using fast-timing techniques, the lifetime of the (4$^+$) state at 2001 keV was

measured for the first time. The experimental $B(E2;\ 4^+ \rightarrow 2^+) = 2.1(^{+2.3}_{-0.7})$ W.u. is consistent within the large experimental uncertainty with the shell-model predictions and with the systematics of the neighboring even-even Sn isotopes.

The reassessment of the half-life of the $(5^-)$ state at 2121 keV yielded $T_{1/2} = 10.5(3)$ ns, more than two standard deviations away from the adopted value. Additionally, the lifetime of the 2378 keV level was measured, establishing an upper limit for the half-life of 40 ps. This level de-excites via a 257-keV $\gamma$ ray to the $(5^-)$ level at 2121 keV and via a 378-keV $\gamma$ ray to the 2001-keV $(4^+)$ level. The derived reduced transition probabilities, $B(M1) \geq 3 \times 10^{-2}$ W.u. for the 257-keV transition and $B(E1) \geq 4 \times 10^{-6}$ W.u. for the 378-keV transition, support a tentative spin-parity assignment of $(4^-)$ for the 2378-keV state.

# Chapter 7

# Investigation of the structure of $^{132}$In

This chapter describes the investigation of the nuclear structure of the exotic nucleus $^{132}$In carried out in the framework of this PhD thesis. The nucleus $^{132}$In is characterized by proton number $Z = 49$ and neutron number $N = 83$. Having one extra neutron and a missing proton with respect to the $^{132}$Sn closed core, it is expected that its low-lying states could be interpreted in terms of the coupling between the neutron particle and the proton hole. The main orbitals involved are $f_{7/2}$, $p_{3/2}$, $p_{1/2}$, $h_{9/2}$, $i_{13/2}$ for neutrons [JAB$^+$10, BFK$^+$20], and $g_{9/2}$, $p_{1/2}$, $p_{3/2}$, $f_{5/2}$, for protons [TJG$^+$14, TJG$^+$16]. Each combination of neutron and proton-hole can generate a particle-hole multiplet of states, with the $\pi g_{9/2}^{-1}\nu f_{7/2}$ being the lowest-lying one according to the experimental single-particle (and single-hole) energies for neutrons and protons around the doubly magic nucleus $^{132}$Sn [BFK$^+$20], see Chap. 2.

Despite the expected simple structure of $^{132}$In, the experimental information that may confirm this picture is still very scarce. Gamma-ray transitions in $^{132}$In were first experimentally identified following the $\beta$n-decay of $^{133}$Cd, which was produced at RIKEN, as part of the EURICA project [JGG$^+$16]. Six $\gamma$-ray lines were assigned to the $\beta$-delayed neutron emission at energies of 50, 86, 103, 227, 357, and 602 keV. A tentative ordering of these transitions was provided based on the comparison with large-scale shell-model calculations. The 25(25) keV transition was not experimentally observed but was introduced to account for the lowest unresolvable $\gamma$ decay within the multiplet, whose energy was expected to lie in the few-tens-of-keV region according to shell-model calculations. The calculations were performed using realistic interactions specifically developed for the neighboring $^{134}$Sb ($Z = 51$, $N = 83$) nucleus, where the missing TBMEs were scaled from the well-established ones in the $^{208}$Pb region. Based on the results of these calculations, the six observed $\gamma$ rays were tentatively proposed as $M1$ $\gamma$ transitions connecting a cascade of low-lying negative-parity states, ranging from $1^-$ to $6^-$, which were interpreted as members of the $\pi g_{9/2}^{-1}\nu f_{7/2}$ multiplet. The assignment relied on the expectation that the $\beta$-delayed neutron emission predominantly populates low-spin states starting from the $^{133}$Cd ($1^-$) g.s. Nevertheless, no $\gamma\gamma$ coincidences that could confirm it could be measured in Ref. [JGG$^+$16].

In a more recent experiment, $^{132}$In was produced via a one-proton-knockout reaction on $^{133}$Sn at the RIKEN facility, as reported in the PhD thesis work by Parry [Par23].

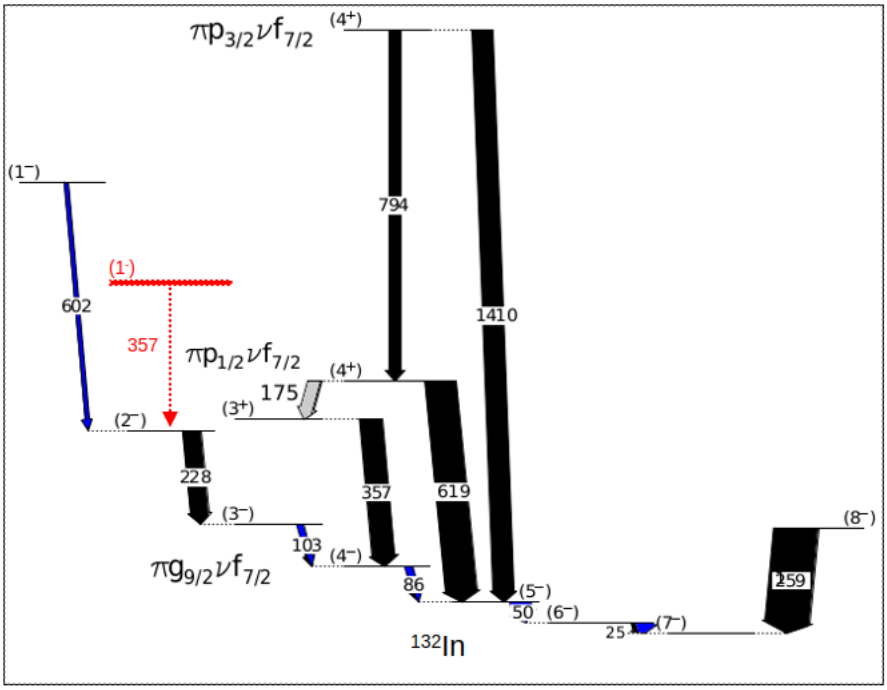


**Figure 7.1.** Proposed level scheme for $^{132}$In in Ref. [Par23]. The blue arrows represent the $\gamma$ transitions taken from Ref. [JGG$^+$16]. The main dominant configurations proposed are also indicated. The red dashed $\gamma$ transition corresponds to the assignment made in Ref. [JGG$^+$16], connecting the $(2^-)$ and $(1^-)$ states, in contrast to the scheme proposed in Ref. [Par23]. See text for further details.

In this experiment, seven new $\gamma$-ray transitions at energies of 175, 228, 259, 357, 462, 619, 798, and 1410 keV where assigned to $^{132}$In. Only the 228- and 357-keV transitions had previously been reported in Ref. [JGG$^+$16]. Half-lives for some excited states were also extracted from their Doppler broadening. In spite of the limited statistics, 619-keV and 798-keV $\gamma$ rays were observed in coincidence. A level scheme extended to higher excitation energies was proposed, guided by shell-model calculations using the jj46 interaction [YLX$^+$16] and the so-called Napoli interaction [CCG$^+$09], and invoking $\pi p^{-1}_{1/2}\nu f_{7/2}$ and $\pi p^{-1}_{3/2}\nu f_{7/2}$ couplings in addition to the $\pi g^{-1}_{9/2}\nu f_{7/2}$ multiplet. The previous tentative assignments made in the $\beta$-decay experiment referred above [JGG$^+$16] were also included in the proposed level scheme by Parry, which is reproduced in Fig. 7.1. In Fig. 7.1, the $\gamma$ transitions from Ref. [JGG$^+$16] are depicted in blue, and the newly proposed ones in black, including the already known 228-keV transition and the proposed relocation of the 351-keV $\gamma$-ray. The earlier proposal for the latter is shown in dashed red line. The proposed dominant shell-model configurations are also shown.

As illustrated, experimental data are required to verify the proposed structure of the exotic nucleus $^{132}$In, disentangle the assignment of the 357-keV transition and potentially expand the level scheme. In this work, the structure of $^{132}$In populated by $\beta$ and $\beta$-n decays is investigated, taking advantage of the Cd beam purity and the enhanced yields obtainable at the ISOLDE facility (see Chap. 3). Specifically, the selective population of excited states via the direct $\beta$ decay of $^{132}$Cd and the $\beta$-delayed neutron emission of $^{133}$Cd, provides data that is expected to help scrutinize

the previous proposals.

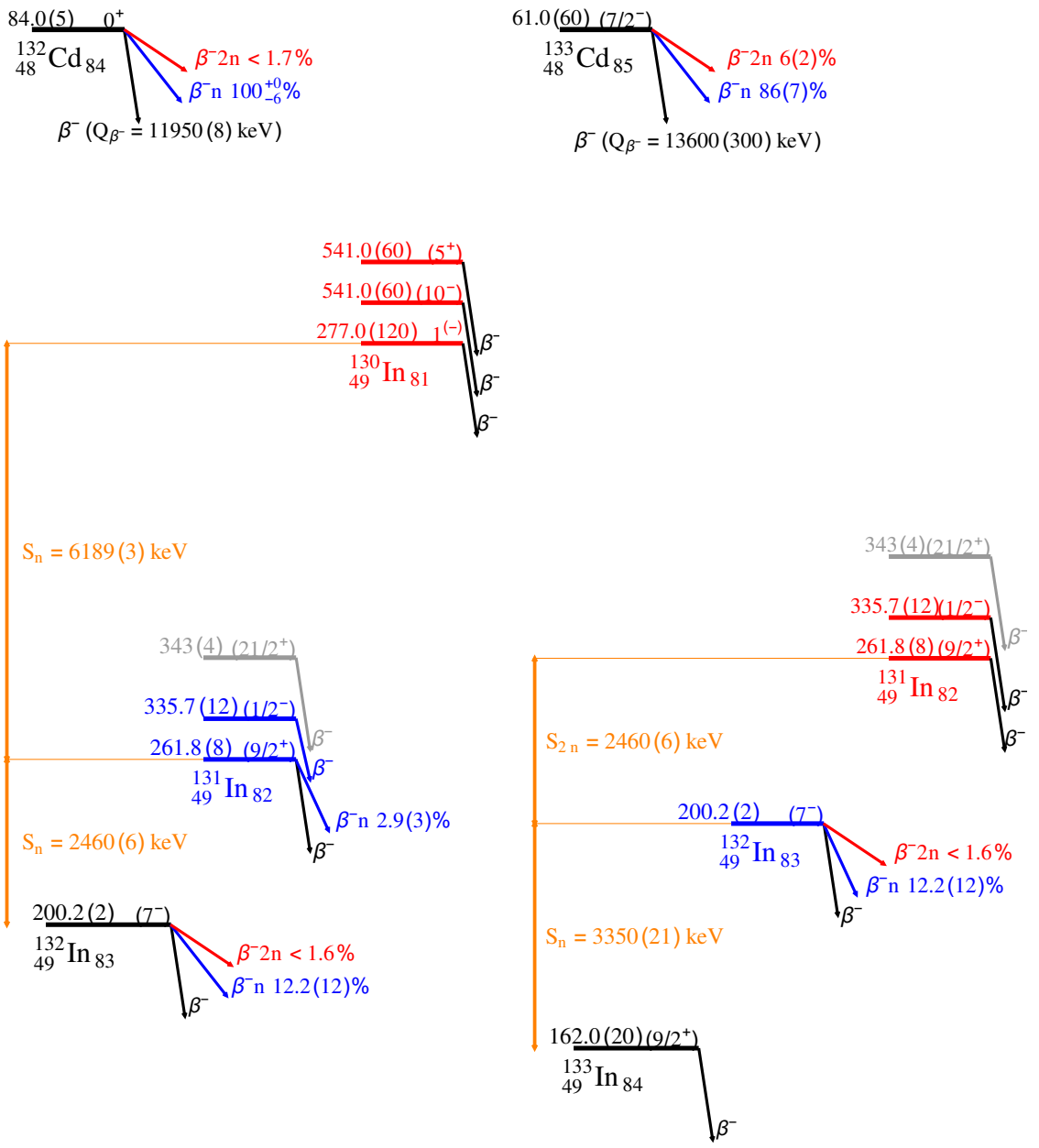


**Figure 7.2.** Decay scheme of $^{132}$Cd (left) and $^{133}$Cd (right). Level and transition data are taken from Ref. [NND25], while $P_{xn}$ branching ratios are and half-life values are taken from the more recent results [PNL+22, BFK+24, BFK+20]. Levels populated through $\beta$-delayed neutron emission are shown in blue, while those populated through $\beta$-delayed two-neutron emission are shown in red. Levels that are not populated in the $\beta^-$ decay of the $0^+$ ground state of $^{132}$Cd are indicated in gray. The energies of the isomeric states are not drawn to scale. Half-life values [BFK+20, BFK+24] are given in ms.

The discussion begins with the $\beta$-decay branches from $^{132}$Cd and $^{133}$Cd. Fig. 7.2 shows their decay schemes. While $^{132}$Cd is an even-even nucleus, leading to $J^\pi = 0^+$, no direct experimental determination of the ground-state spin and parity of $^{133}$Cd is reported in the literature. The $(7/2^-)$ assignment is based on the systematics of tin

isotopes, but other shell-model calculations [MNK97] suggest a $(3/2^-)$ assignment instead. In the figure, the level and decay information is taken from the most recent evaluation in NNDC [NND25]. As discussed in Chap. 2, a distinctive feature of the region southeast of the doubly magic nucleus $^{132}$Sn, characterized by $Z < 50$ and $N > 82$, is the relatively low neutron separation energy: $S_n = 2460(6)$ keV for $^{132}$In and $S_n = 3550(21)$ keV for $^{133}$In [Eva21]. Both nuclei are characterized by rather large $Q$-values: $Q_{\beta^-} = 11.95(8)$ MeV for $^{132}$Cd and $Q_{\beta^-} = 13.6(3)$ MeV (from systematics) for $^{133}$Cd [Eva21]. Another feature of the beta-decay in this region is the predominance of GT $\nu g_{7/2} \rightarrow \pi g_{9/2}$ transitions, which remove deeply-bound neutrons feeding core-excited levels at very high excitation energies above the neutron separation energy. This large $Q_{\beta^-}/S_n$ ratio, along with the large strength of the GT transition, leads to a high $\beta$-delayed neutron emission probabiliby, close to 100% [PNL$^+$22].

The remainder of the chapter is structured as follows: the experimental results obtained in this thesis from the decay of $^{132}$Cd and $^{133}$Cd are presented in Secs. 7.1 and 7.2, respectively; the $^{132}$In structure, including the supporting shell-model calculations and the proposed new level scheme, is discussed in Sec. 7.3. Finally, the main conclusions are summarized in Sec. 7.4.

# 7.1 Beta-decay of $^{132}$Cd

The implantation tape was moved every super-cycle in the $^{132}$Cd data taking to avoid the buildup of longer-lived daughters, see Fig. 7.2. Nonetheless, due to the low $^{132}$Cd yield, the intensity observed in singles is about three orders of magnitude lower than the typical ISOLDE hall background. Coincidence with the $\beta$ signal effectively suppresses the background, and thus $\gamma$ rays following the $\beta$ decay of $^{132}$Cd were identified through the analysis of $\beta$-gated $\gamma$-ray spectra. An example recorded with the HPGe clover detectors is shown in Fig. 7.3.

## 7.1.1 Time distribution of $\beta$-delayed $\gamma$-rays

Once the $A = 132$ isotopes are discriminated from background, the information on the time distribution of the $\gamma$ rays relative to the proton beam pulse is employed for identification of the parent nuclei. Fig. 7.4 displays several $\beta$-gated spectra constructed with different time conditions selected to enhance the contribution of each isotope in the decay chain. The spectrum in black was constructed using events within a time window of 10 to 410 ms after the proton impact, in order to enhance and isolate $\gamma$ rays originating from the $\beta$ decay of $^{132}$Cd. The upper limit of 410 ms corresponds to approximately five half-lives of $^{132}$Cd, according to $T_{1/2} = 82.5(9)$ ms [PNL$^+$22]. This time selection effectively reduces the contribution from the $\beta$-decay chain daughters, in particular from $^{132}$In and $^{131}$In, with half-lives of 200.2(2) ms and 261.8(8) ms, respectively [BFK$^+$20, BFK$^+$24]. The initial 0 to 10 ms range is excluded to minimize contributions from neutron-induced reactions in surrounding materials, due to neutrons traveling from the target area.

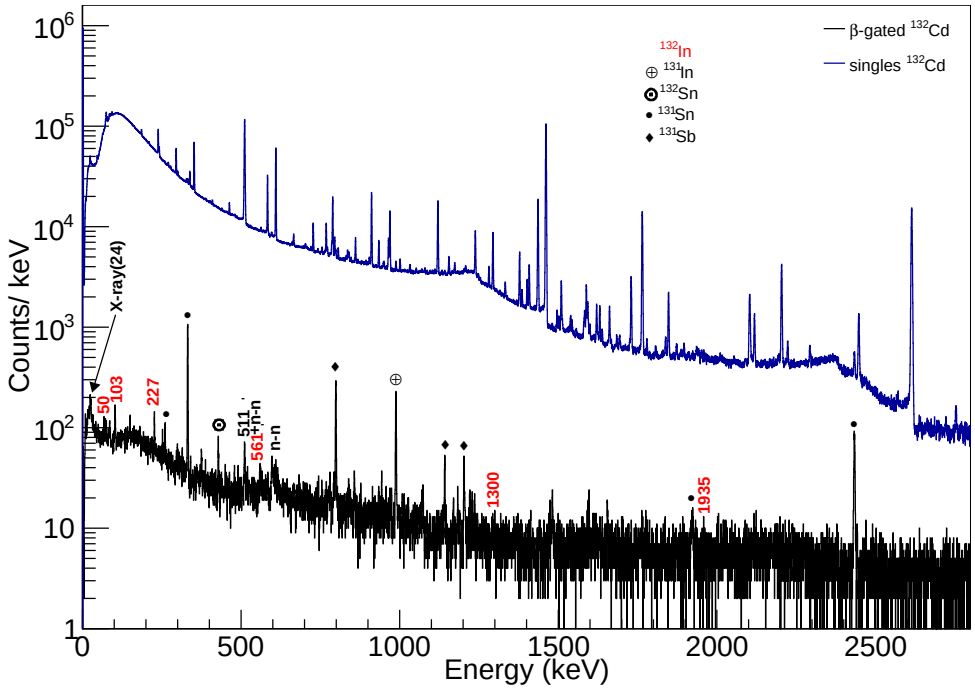


**Figure 7.3.** Beta-gated $\gamma$-ray energy spectrum following the decay of $^{132}$Cd (black) compared with the singles $\gamma$-ray energy spectrum (blue). The $\gamma$ rays from the $\beta$ decay of $^{132}$Cd $\rightarrow$ $^{132}$In identified in this work are labeled in red.

The spectrum in blue shows $\gamma$ rays in a 500 to 1000 ms interval. This time window was selected to obtain a similar contribution of the $\gamma$-rays belonging to the $\beta$ decay of $^{131}$In while ensuring that all $^{132}$Cd has already decayed. A third spectrum, shown in red, was built requesting a 1800-6000 ms time condition where both $^{132}$Cd and indium daughters had already decayed, this condition enables the identification of $\gamma$ lines arising from delayed nucleus in the chain such as $^{131}$Sn.

### 7.1.2 Identification of $\beta$-delayed $\gamma$ rays from $^{132}$Cd

The time-based identification is taken further in Fig. 7.5, where the $\beta$-gated $\gamma$-ray spectrum shown in black was constructed to feature only $\gamma$-rays belonging to the $^{132}$Cd decay, by selecting a time window of 10 to 410 ms relative to the proton impact and subtracting contributions of $\gamma$-rays associated to the decay of $^{132}$In using a 500 to 1000 ms range, as presented in Fig. 7.4. The surviving peaks in the subtracted black spectrum in Fig. 7.5 can be unambiguously assigned to the decay of $^{132}$Cd, populating $^{132}$In and $^{131}$In via direct $\beta$ decay and $\beta$-delayed neutron emission, respectively. Indeed, the strong 988-keV $\gamma$ ray [TJG+14] in $^{131}$In is clearly observed. Additionally, three of the $\gamma$ rays previously assigned to $^{132}$In in the $\beta$-n decay of $^{133}$Cd [JGG+16] are observed, namely those at 50, 103, and 227 keV. Additionally new $\gamma$ lines at 561, 1301 and 1935 keV appear in the spectrum. The 561-keV $\gamma$ line partially overlaps with the 563-keV $\gamma$ line originating from $^{76}$Ge(n,n'$\gamma$) reactions (see for instance Ref. [MCB+17]). The characteristic shape of the resulting peak arises from the recoil of the germanium

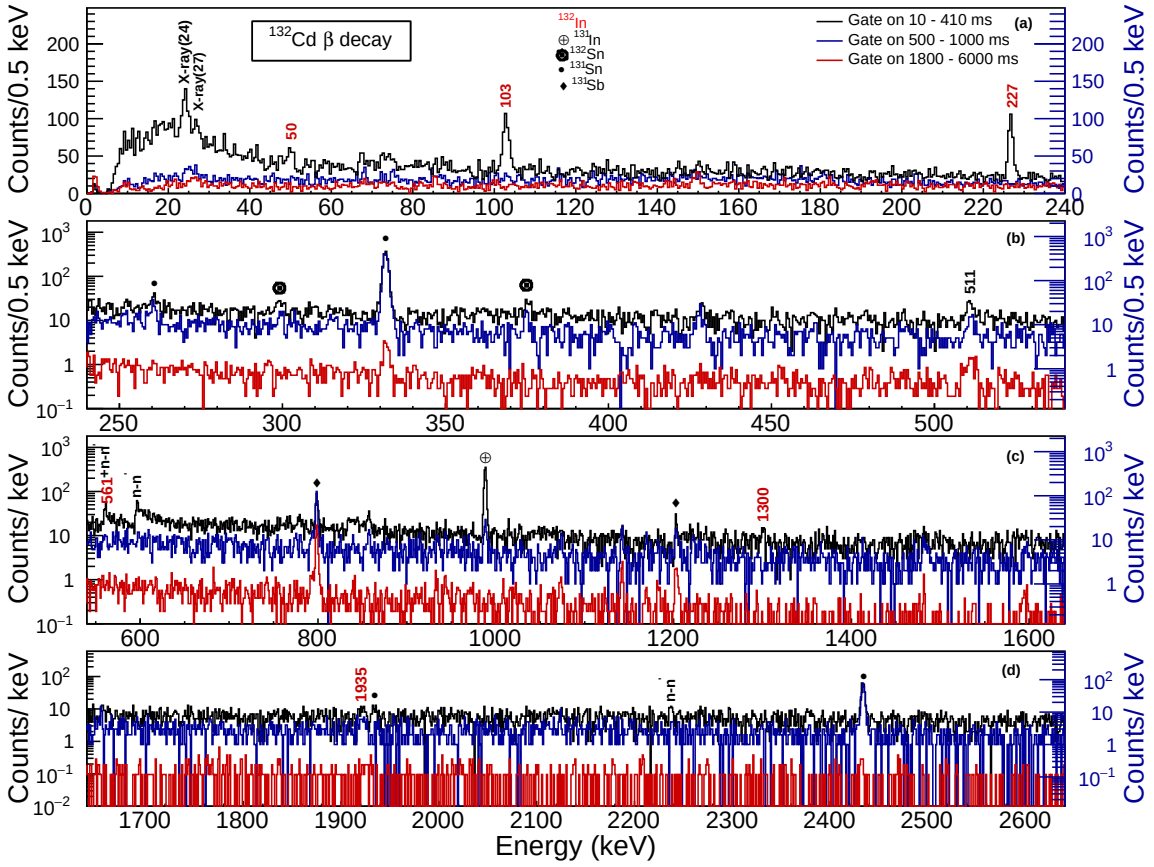


**Figure 7.4.** Beta-gated $\gamma$-ray energy spectra recorded following the decay of $^{132}$Cd. Three beam-gate conditions in the time reference of the protons was imposed to distinguish the observed $\gamma$-ray transitions of the different isotopes in the $A = 132$ $\beta$ decay chain. The $\gamma$ rays from the $\beta$ decay of $^{132}$Cd $\rightarrow$ $^{132}$In identified in this work are labeled in red. The red and blue spectra corresponding to the long-lived $\beta$-decay products of $^{132}$Cd in panels (b), (c), and (d) have been offset for clarity.

atom during the inelastic scattering process induced by neutrons, emitted following $\beta$-delayed neutron emission, which interact with the HPGe detectors via Ge(n,n'$\gamma$) reactions. The comparison with other (n,n'$\gamma$) peaks helps discriminate the excess of counts. Additionally, the $\gamma\gamma$ coincidence analysis confirms that the 561-keV $\gamma$ ray arises from the decay of $^{132}$Cd (see Subsec. 7.1.5).

The list of the identified $\gamma$ rays in $^{132}$In after the $\beta$ decay of $^{132}$Cd, along with their corresponding intensities, is provided in Tab. 7.1. The 103-keV transition is used for normalization of the $\gamma$ intensities. The 988-keV $\gamma$ ray in $^{131}$In from the $\beta$-n channel is also included.

### 7.1.3 Beta-decay $^{132}$Cd half-life

Due to the limited statistics of the $\beta$-gated $\gamma$-ray $^{132}$Cd spectra, fitting the time distribution of the strongest $\gamma$ transitions to obtain the $^{132}$Cd $\beta$-decay lifetime is particularly challenging. Nevertheless, the extracted time behaviour can be used to confirm the identification of the $\gamma$ rays associated to the decay of $^{132}$Cd $\rightarrow$ $^{132}$In.

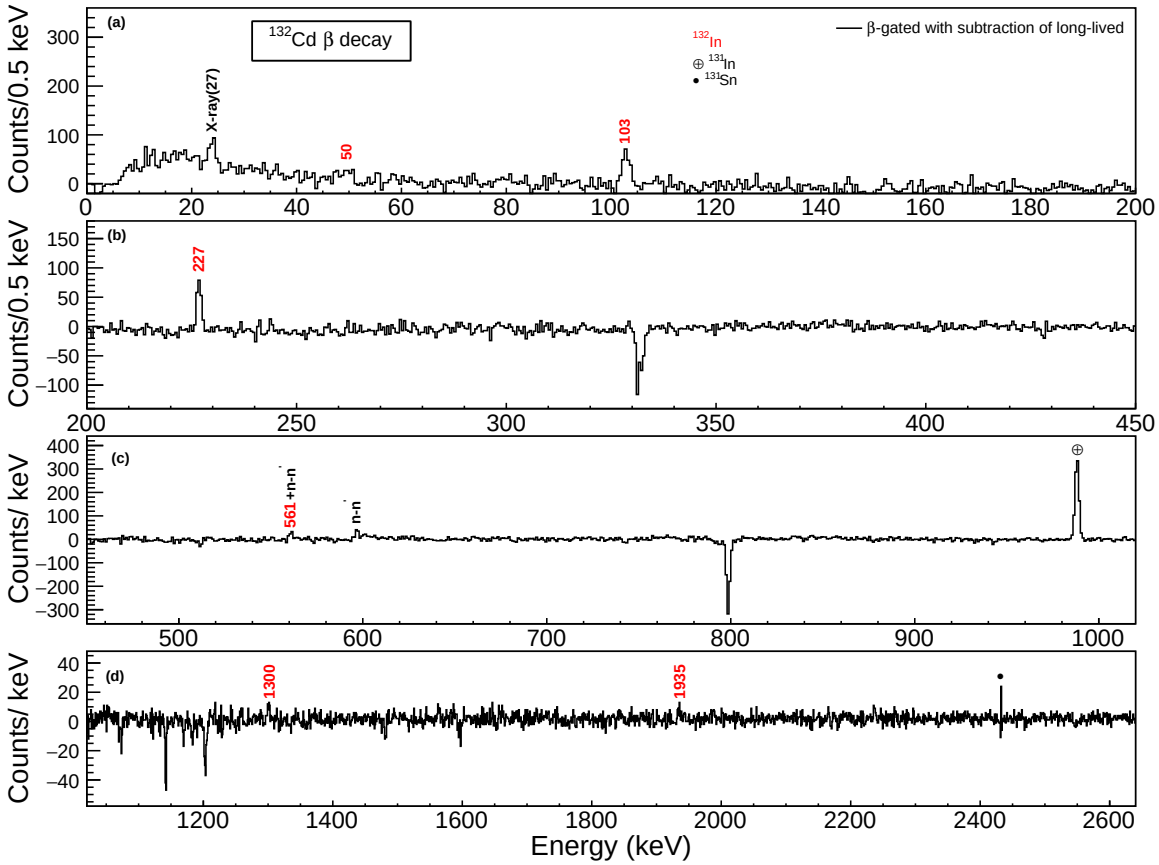


**Figure 7.5.** Beta-gated $\gamma$-ray energy spectra following the decay of $^{132}$Cd. The spectrum was constructed with a time window since proton impact and subtraction of long-lived to observe only $\gamma$ rays from the $\beta$ decay chain. The negative counts at arise from oversubstraction of the most intense $\gamma$-ray in the the $\beta$ decay chain. The $\gamma$ rays from the $\beta$ decay of $^{132}$Cd $\rightarrow$ $^{132}$In identified in this work are labeled in red.

**Table 7.1.** List of $\gamma$ rays observed following the $\beta$ decay of $^{132}$Cd, including the relative $\gamma$ intensities ($I_\gamma$) normalized to 100 units for the 103-keV $\gamma$ transition. The 988-keV $\gamma$-ray transition following the $\beta$-delayed neutron emission of $^{132}$Cd is indicated in italics.

| $E_\gamma$ (keV) | $I_\gamma$ |
|---|---|
| 49.9(3) | 30(7) |
| 102.9(3) | 100 |
| 226.7(3) | 109(14) |
| 560.7(3) | 62(11) |
| 1301.1(2) | 58(12) |
| 1934.6(2) | 72(16) |
| *988.2(2)* | *1178(123)* |

The time distribution relative to the proton pulse impact of the strongest $\gamma$ rays from the $\beta$-decay branch, specifically those at 30, 103, and 227 keV, as well as the 988-keV $\gamma$ ray from the $\beta$n-decay branch is shown in Fig. 7.6. The Compton-subtracted

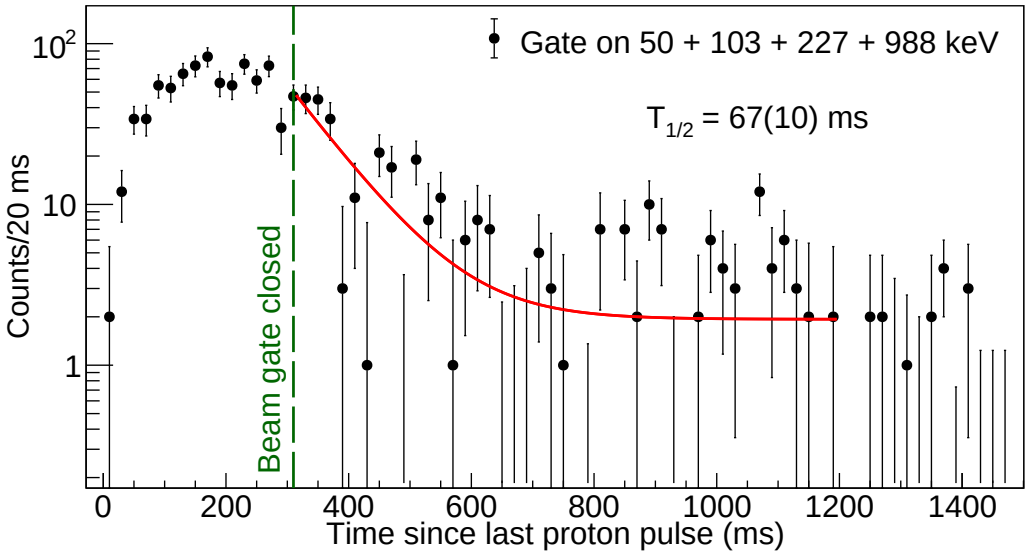


**Figure 7.6.** Time distribution analysis of the $^{132}$Cd $\beta$ decay and the fit curve. The dark green vertical dashed line represents the end of the implantation. Time distribution gated on 50-, 103- ,227- and 988-keV transitions is shown. See text for more details.

contributions of the four $\gamma$ rays are summed. The time profile is characterized by a growth in activity due to the release until the beam gate is closed, 310 ms after the proton pulse, and an exponential decay after the implantation. The half-life of $^{132}$Cd was estimated by fitting the $\beta$-gated time distribution from 310 ms up to 1200 ms, which corresponds approximately to 14 $^{132}$Cd half-lives. An exponential decay function plus a constant parameter to account for background was used. The obtained $^{132}$Cd $\beta$-decay half-life is $T_{1/2}$ = 67(10) ms, which is within $2\sigma$ of the recently reported half-life of $T_{1/2}$ = 82.5(9) ms [PNL$^+$22] and the most recent evaluated value of $T_{1/2}$ = 84.0(5) ms [NND25]. The value confirms the identification of the strongest $\gamma$-rays to the decay of $^{132}$Cd. The analysis cannot be extended to other $\gamma$-rays due to the lack of statistics.

### 7.1.4 Beta-delayed one-neutron emission probability of $^{132}$Cd

Beta-delayed neutron emission is the dominant decay branch for $^{132}$Cd. The $P_{1n}$ values reported in the literature are 60(15) [HKP$^+$00], 88(5) [TJG$^+$14] and $100^{+0}_{-6}$ [PNL$^+$22]. The upper limit of the value reported in Ref. [PNL$^+$22] is clearly not consistent with the present findings, since $\gamma$-ray transitions following the direct $\beta$ decay of $^{132}$Cd are observed in the present work.

The $P_{1n}$ value has been derived from the observed $\gamma$-ray intensities in the $\beta$-decay and $\beta$n-decay chains. Due to the short $\beta$-decay lifetimes ($T_{1/2}[^{132}\text{In}]$ = 202.2(2) ms [BFK$^+$20], $T_{1/2}[^{131g}\text{In}]$ = 261.8(8) ms and $T_{1/2}[^{131m1}\text{In}$ = 335.7(12) ms [BFK$^+$24]) compared to the tape movement sequence we can safely assume that all members of chain have decayed. A comparison of the $\gamma$-ray intensities in the $\beta$ and $\beta$-n decay branches is performed. The used $\gamma$-rays along the relative intensities and branching ratios are summarized in Tab. 7.2.

**Table 7.2.** Gamma-ray intensities for the decay of the $^{132}$In $(9/2^+)$ ground state, the $^{131}$In ground state and the $^{131m1}$In $(1/2^-)$ $\beta$-decaying isomer. The $\gamma$ intensities ($I_\gamma$(%) and $I_\gamma^{decay}$(%)) normalized to 100 units for the 103-keV $\gamma$ transition. The absolute intensity (branching) $I_\gamma^{abs}$(%) were taken from Refs. [BFK$^+$20, BFK$^+$24].

| Isotope | $E_\gamma$ (keV) | $I_\gamma^{abs}$(%) | $I_\gamma^{rel103}$(%) | $I_\beta^{rel}$(%) |
|---|---|---|---|---|
| $^{132g}$In $(7^-)$ | 478.4(3) | 23(6) | 39(13) | 170(73) |
| $^{131g}$In $(9/2^+)$ | 2433.8(2) | 65(11) | 1464(85) | 2252(403) |
| $^{131m1}$In $(1/2^-)$ | 331.1(3) | 42(12) | 2253(111) | 5365(1555) |

For the $^{132}$In $\rightarrow$ $^{132}$Sn decay branch, only the intensity of the 478-keV $4^- \rightarrow 3^-$ $\gamma$ transition was considered. The strongest 299-keV $6^+ \rightarrow 4^+$ and 375-keV $4^+ \rightarrow 2^+$ transitions were excluded because they are affected strongly by the indirect population from the 2.108(14) $\mu$s $8^+$ state [BFK$^+$20], impacting the $\gamma$-ray intensity measured in the $\beta$-gated spectra. In the $^{131}$In $\rightarrow$ $^{131}$Sn cascade, two main $\gamma$ lines can be identified in the spectra, corresponding the 2434-keV and the 332-keV transitions from the $^{131g}$In and $^{131m1}$In decays, respectively. Both observed $^{131}$In $\beta$-decaying states are summed for the analysis. A value of $P_{1n}$[$^{132}$Cd] = 97.8(10) % is obtained in this work, where the uncertainty is obtained from the error propagation of the values in Tab. 7.2. A comparison with previous values is presented in Tab. 7.3. The present result is consistent, within experimental uncertainties, with the latest $P_n$ value reported in Ref. [PNL$^+$22], but not with earlier measurements reported in Refs. [HKP$^+$00, TJG$^+$14].

**Table 7.3.** Comparison of previously reported $\beta$-delayed neutron emission probabilities ($P_{1n}$) for the $^{132}$Cd with the result obtained in this work.

| Reference | $P_{1n}$ (%) |
|---|---|
| Hannawald *et al.* (2000) [HKP$^+$00] | 60(15) |
| Taprogge *et al.* (2014) [TJG$^+$14] | 88(5) |
| Phong *et al.* (2022) [PNL$^+$22] | $100^{+0}_{-6}$ |
| This work | 97.8(10) |

Considering the two-neutron separation energy in $^{132}$In, $S_{2n}$($^{132}$In) = 8.65(6) MeV [NND25], there exists an energy window of approximately 3300 keV within the available $Q_{\beta^-}$($^{132}$Cd) that would allow for the $\beta$-delayed two-neutron decay channel to occur. Nonetheless, the $\beta$-delayed two-neutron emission probability limit from $^{132}$Cd in the literature is extremely low, $P_{2n} < 1.7\%$ [PNL$^+$22]. We have conducted a dedicated search for $\gamma$ rays associated with the $A = 130$ mass chain. However, none of the most intense 451-, 950- and 1169-keV $\gamma$ transitions reported in Ref. [RM25] for the $^{130}$In $\rightarrow$ $^{130}$Sn $\beta$-decay were observed.

### 7.1.5 $\gamma\gamma$ coincidence analysis

The analysis of $\gamma\gamma$ coincidences is now undertaken to construct the level scheme. The time gate of 10–410 ms relative to the proton impact was applied. An additional $\beta$ condition is required to reduce background contributions, and thus the analysis is peformed on $\beta\gamma\gamma$ events. The $\beta$-gated $\gamma\gamma$ total projection spectrum is shown in

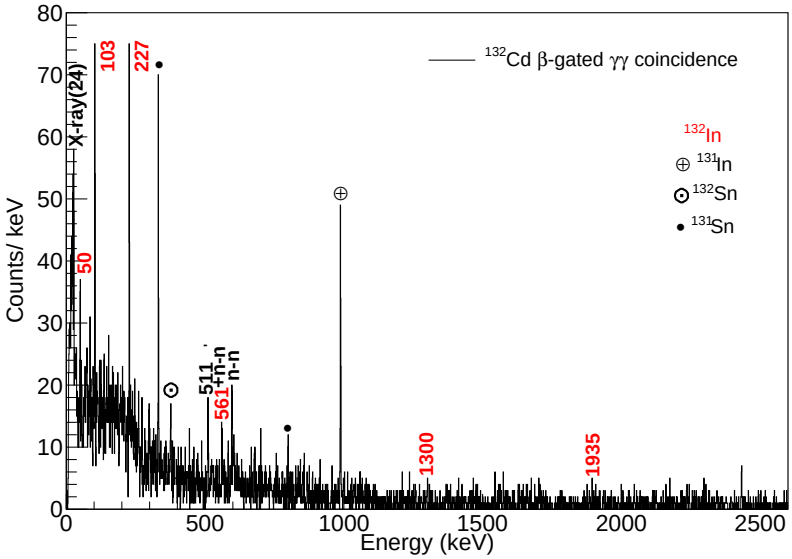


**Figure 7.7.** Beta-gated $\gamma\gamma$ total projection spectrum showing $\gamma$-ray transitions in $^{132}$In following the $\beta$ decay of $^{132}$Cd. A time gate of 10–410 ms relative to the proton impact is applied. The $\gamma$ rays from the $\beta$ decay of $^{132}$Cd identified in this work are labeled in red.

Fig. 7.7. Beta-delayed coincident $\gamma$- and X-rays from $^{132}$Cd are identified.

Fig. 7.8 displays the $\beta$-gated $\gamma$-ray spectra in coincidence with $\gamma$ rays and X-ray transitions associated with the $\beta$ decay of $^{132}$Cd. As can be observed in the coincident spectra for the 50-, 103-, and 227- keV transitions, there is clear evidence that all three are in mutual coincidence. This fact confirms their assignment as a $\gamma$-ray cascade. A weak coincidence can also be observed between the 561-keV transition and the 103 and 227-keV transitions, which suggests it may be part of the same cascade. No coincidences have been observed between the 561 keV and 50 keV transitions, though, but this may be caused by the limited statistics. X-rays are expected to be emitted as a consequence of the strongly converted 50-, 103- and, in a minor degree, 227-keV transitions. The presence of the 50-, 103-, and 227-keV $\gamma$-ray in the $\beta$-gated $\gamma\gamma$ coincidence spectrum gated on the 24-keV X-ray supports the strong coincidence of the 50- and 103-keV transitions. Coincidence spectra for the 1301- and 1934-keV $\gamma$-ray transitions are also presented. However, due to the limited data, no strong coincidences appear.

In order to identify possible new isomeric states, delayed $\beta\gamma$ coincidence measurements were performed. Using the same conditions as above, delayed coincidences were constructed using successive time windows starting at 500 ns and extending up to 2500 ns in steps of 1000 ns. The resulting spectra are depicted in Fig. 7.9, where no change in intensity is observed, and thus no evidence of isomeric transitions is found.

The discussion of the level scheme is defered to Sec. 7.3, once the $\beta$-n decay of $^{133}$Cd and SM calculations have been presented.

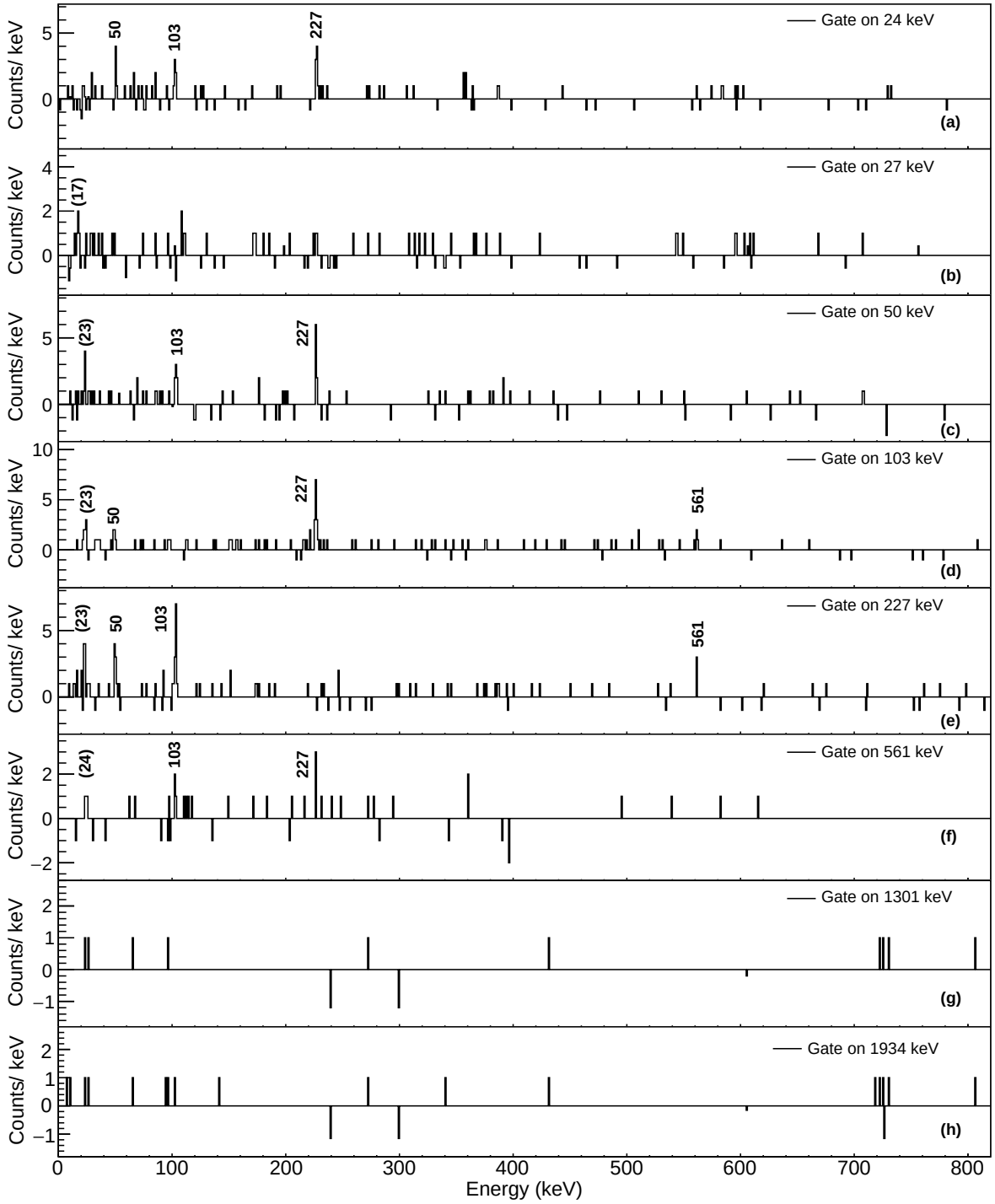


**Figure 7.8.** Beta-gated $\gamma\gamma$ coincidence spectra following the implantation of $^{132}$Cd. A time window of 10–410 ms relative to the proton impact was applied to suppress background contributions. Panels (a) and (b) show X-rays associated with indium. Panels (c), (d), (e), (f), (g) and (h) display coincidence spectra gated on the 50-, 103-, 227-, 561-, 1301- and 1934-keV $\gamma$-ray transitions respectively. Transitions labeled in brackets remain unassigned.

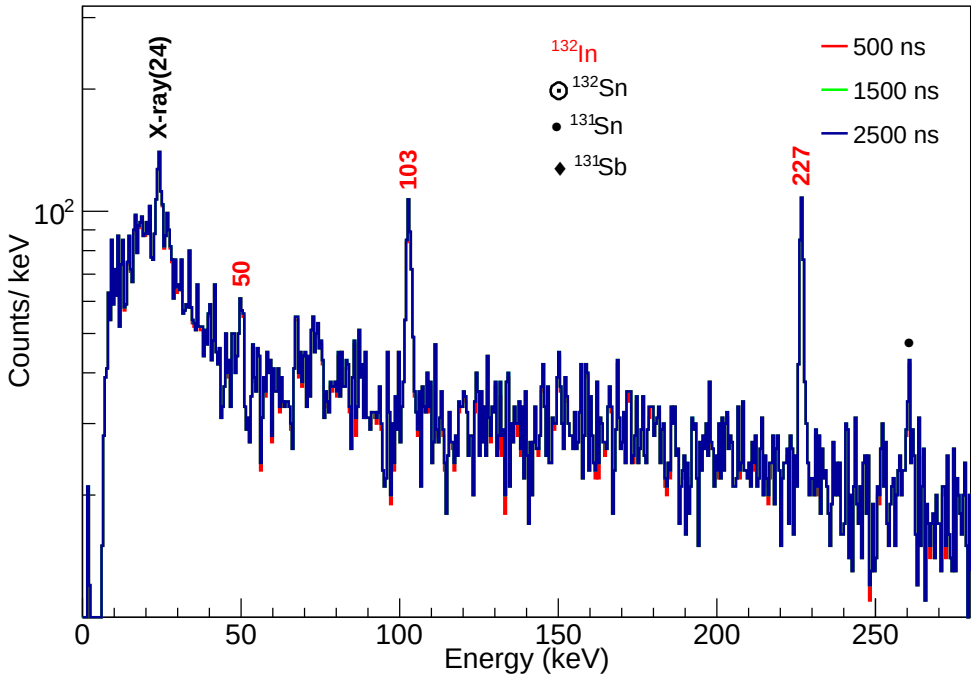


**Figure 7.9.** Beta-$\gamma$ spectra measured for the $\beta$ decay of $^{132}$Cd with different time coincidence gates, using successive time windows starting at 500 ns and extending up to 2500 ns in steps of 1000 ns. The $\gamma$ rays from the $\beta$ decay of $^{132}$Cd identified in this work are labeled in red. A beam-gate condition of 10–410 ms relative to the proton impact was applied to enhance the selectivity for $\gamma$ rays associated with the decay of $^{132}$Cd.

## 7.2 Beta decay of $^{133}$Cd

In the following section we discuss the analysis of the $^{133}$Cd $\beta$-decay data focusing on the $\beta$-delayed neutron branch. As shown in Fig. 7.10, $\gamma$-rays belonging to $^{132}$In can be identified only once the $\beta$-gated condition is requested, as it was the case for $^{132}$Cd.

### 7.2.1 Time distribution of $\beta$-delayed $\gamma$-rays

In order to discriminate the transitions from the decay of $^{133}$Cd from those of its daughters, $\gamma$-ray spectra obtained with different time conditions were built. In analogy to the $^{132}$Cd decay, three time regions were explored, seeking to enhance the relative predominance of Cd (10-310 ms), its decay products (400-600 ms) and the subsequent, more delayed, decays (800-2000 ms). The upper limit of 310 ms corresponds to approximately five half-lives of $^{133}$Cd, $T_{1/2} = 61(6)$ ms [PNL$^+$22]. In Fig. 7.11 an overview of the $\beta$-gated $\gamma$-ray spectra under these different time windows is shown.

The $\beta$-gated $\gamma$-ray spectrum presented in Fig. 7.12 was constructed to aid the identification by enhancing $\gamma$ rays from the decay of $^{133}$Cd. It is constructed by selecting events within a time window of 10 to 310 ms relative to the proton impact, and subtrating contributions from $\gamma$ rays associated with the subsequent decay of $^{132}$In using a time window from 400 to 600 ms.

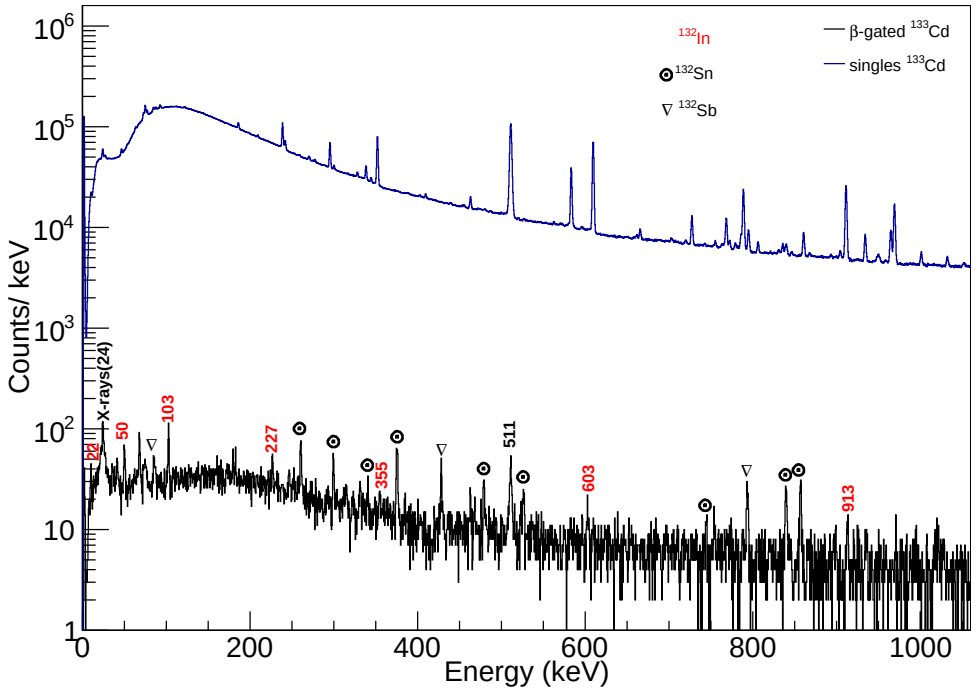


**Figure 7.10.** Beta-gated $\gamma$-ray energy spectra recorded following the $\beta$ decay of $^{133}$Cd (black) compared with the singles $\gamma$-ray energy spectrum (blue). The $\gamma$-ray transitions following the $\beta$-delayed neutron emission of $^{133}$Cd identified in this work are labeled in red.

**Table 7.4.** List of $\gamma$-ray transitions following the $\beta$-delayed neutron emission of $^{133}$Cd with the relative $\gamma$ intensities ($I_\gamma$) normalized to 100 units for the 103-keV $\gamma$ transition. X rays are included and indicated in italics. The transitions are attributed to $^{132}$In, see text for details.

| $E_\gamma$ (keV) | $I_\gamma$ |
|---|---|
| 22.0(1) | 90(47) |
| *24.3(1)* | *216(113)* |
| *27.1(1)* | *82(45)* |
| 50.1(3) | 84(13) |
| 102.7(3) | 100 |
| 226.7(3) | 45(12) |
| 355.0(3) | 29(10) |
| 602.7(2) | 40(10) |
| 913.4(2) | 39(13) |

### 7.2.2 Identification of $\beta$-delayed $\gamma$-rays from $^{133}$Cd

The comparison of the spectra under these time windows enables the unambiguous identification of seven transitions that can be attributed to the $\beta$ decay of $^{133}$Cd. These include the 50-, 103-, 227-, 355- and 603-keV transitions already observed in the previous $^{133}$Cd decay study [JGG+16] and two previously unreported $\gamma$-ray transitions at 22 and 913 keV. The 50-, 103- and 227-keV transitions were observed in the $\beta$ decay of $^{132}$Cd and assigned to $^{132}$In. It should be noted that the 86-keV transition that was previously assigned to this decay [JGG+16] is more prominent in the grand-daughter

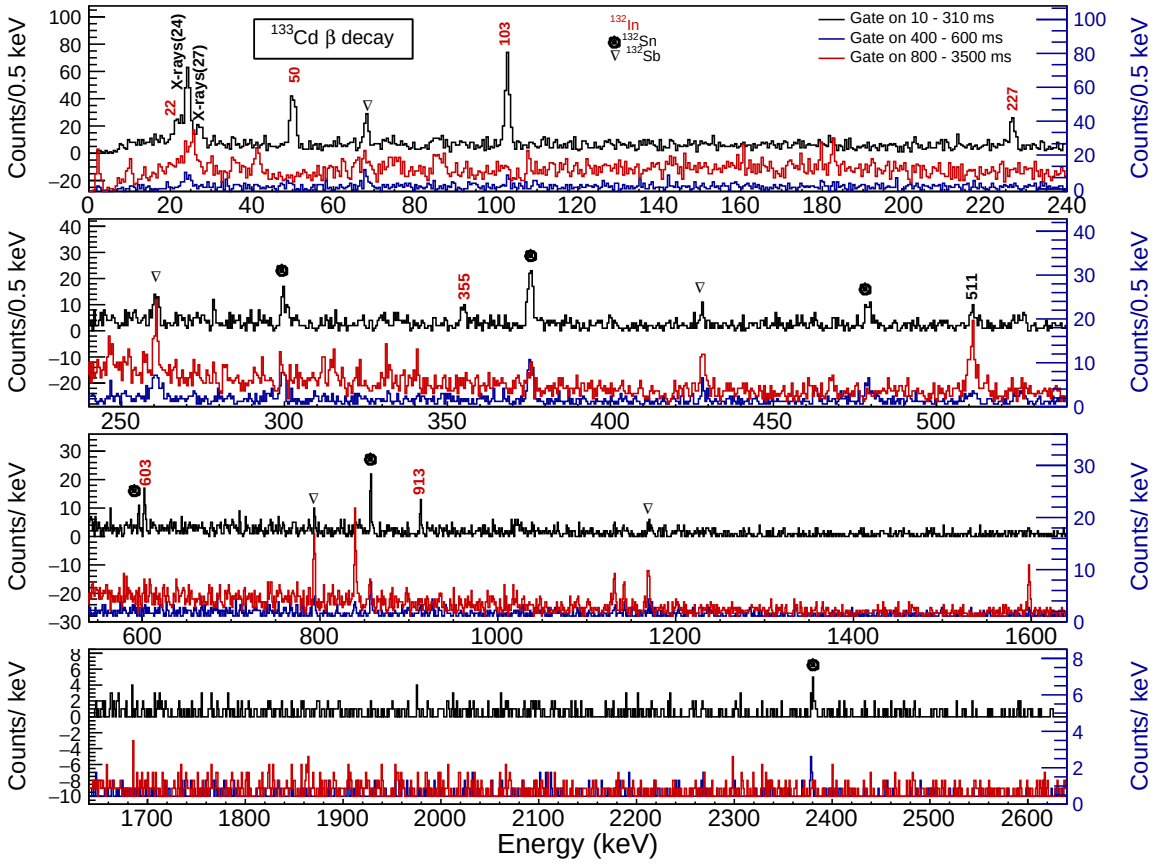


**Figure 7.11.** Beta-gated $\gamma$-ray energy spectrum following the decay of $^{133}$Cd. Three beam-gate conditions in the time reference of the protons is imposed to distinguish the observed $\gamma$-ray transitions of the different isotopes in the $A = 133$ $\beta$ decay chain. The $\gamma$ rays from the $\beta$n decay of $^{133}$Cd identified in this work are labeled in red. Transitions attributed to other isotopes within the $\beta$-decay chain are indicated with black symbols. The spectra corresponding to long-lived $\beta$ decay products of $^{133}$Cd are shown in a different scale for better visibility.

spectrum (shown in red in Fig. 7.11), indicating that it likely corresponds to the strong 85-keV transition in $^{132}$Sb populated in the $\beta$ decay of $^{132}$Sn. The clear presence in the spectrum of a low-energy, 22-keV, $\gamma$ line, is also noticeable. Its energy lies below the indium X-rays, with energies 24.3 and 27.1 keV. Since the detector efficiencies cannot be safely extrapolated to such low energies using the calibration curve presented in Subsec. 4.5, a conservative 50 % uncertainty is assigned to the 22-keV intensity.

The list of the observed $\gamma$ and X rays from $\beta$ decay of $^{133}$Cd, including their relative intensities, is given in Tab. 7.4. The intensities are normalized to the 103-keV $\gamma$ ray.

### 7.2.3 Beta-decay half-life of $^{133}$Cd

The most recent measurement of the $^{133}$Cd $\beta$-decay half-life yields 61(6) ms, reported in Ref. [PNL+22].The time distributions of the most intense 50-, 103-, and 227-keV $\gamma$-ray transitions observed in the $\beta$n-decay branch were analyzed, after subtraction of the Compton background. The time distribution of the summed events is presented in

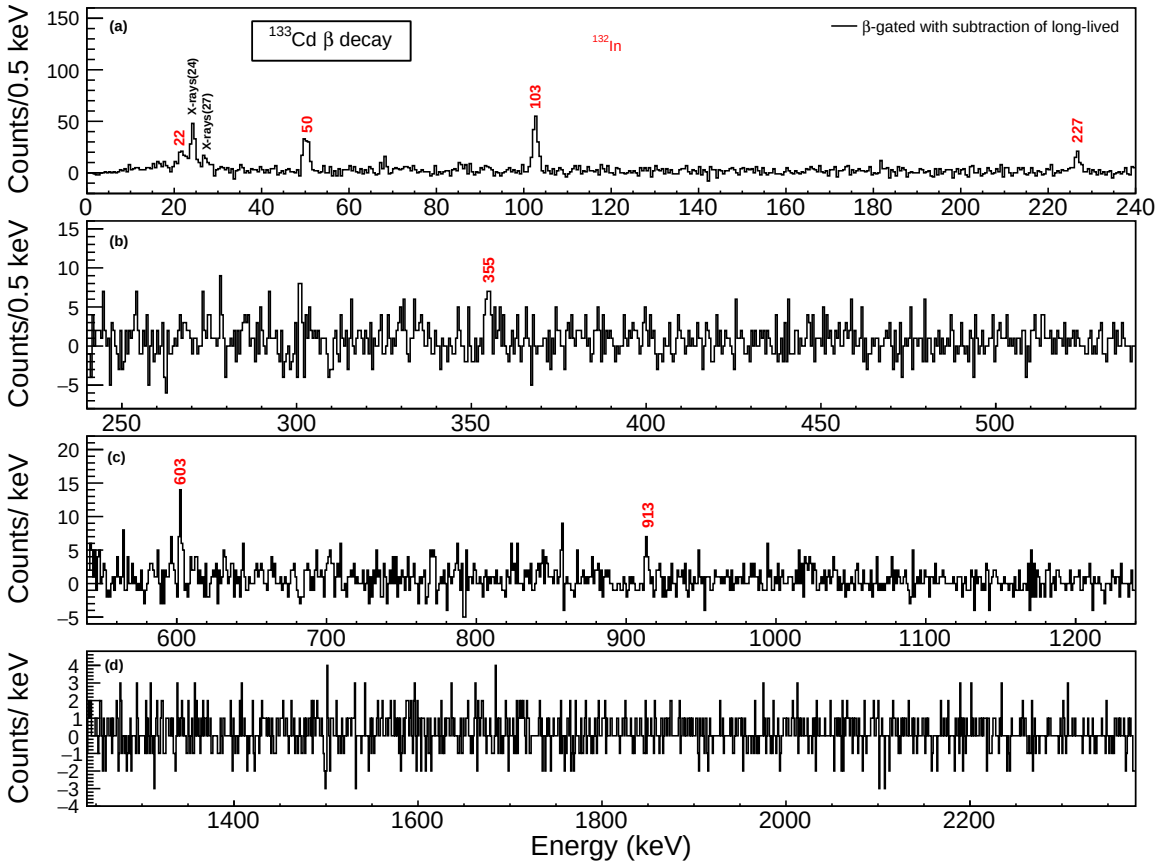


**Figure 7.12.** Beta-gated $\gamma$-ray energy spectra recorded following the decay of $^{133}$Cd in black. The black spectrum was constructed with a time window since proton impact and subtraction of long-lived to observe only $\gamma$ rays from the $\beta$ decay chain. The negative counts arise from oversubtraction of the most intense $\gamma$-ray in the the $\beta$ decay chain. The $\gamma$ rays from the $\beta$n decay of $^{133}$Cd identified in this work are labeled in red.

Fig. 7.13. The limited statistics prevents the extraction of a reliable half-life value. Nevertheless, the extracted time distribution can be used to cross check the identification of $\gamma$ rays associated to the $^{133}$Cd $\beta$-decay.

### 7.2.4 Beta-delayed neutron emission

Beta-delayed neutron emission branches are dominant in the decay of $^{133}$Cd, with $P_{1n}[^{133}\text{Cd}] = 86(7)\%$ and $P_{2n}[^{133}\text{Cd}] = 6(2)\%$ [PNL+22]. Hence, the direct $\beta$-decay branching ratio of $^{133}$Cd is expected to be $\approx 8(7)\%$. A thorough search was performed for the most intense $\gamma$ rays emitted after the $\beta$ decay of the $^{133g}$In and $^{133m}$In [PKF+19, BFK+20], but no evidence of $\gamma$ transitions in $^{133}$Sn was found. In addition to the weak direct $\beta$ branch, the branching ratios for the strongest transitions for each decay are very small. For example, the 3564-keV transition in the decay of $^{133g}$In has a 2% absolute intensity, while the 854-keV transition in the decay of $^{133m}$In accounts for just 1.4%. Thus the expected intensity of these transitions may well be below the experimental sensitivity.

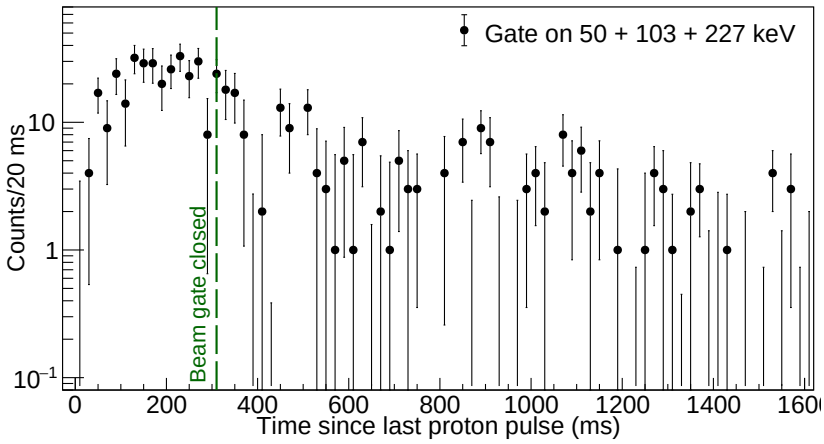


**Figure 7.13.** Time distribution analysis of the $^{133}$Cd ($7/2^-$) decay. The dark green vertical dashed line represents the end of the implantation. Time distribution gated on 50-, 103- and 227-keV transitions are shown.

In contrast, $\gamma$ lines from transitions in $^{132}$Sn such as those at 299 and 375 keV, are clearly observed in the spectra. These $\gamma$ rays most likely originate from the $\beta$ decay of $^{132}$In, produced by the strong $\beta$ delayed neutron branch of the decay of $^{133}$Cd. However, it is also possible that the observed $\gamma$ rays in $^{132}$Sn originate from the $\beta$-delayed neutron emission of $^{133}$In isomers, although their intensity is quite low, of the order of 5% [BFK$^+$20]. Unfortunately, all the observed transitions are also known to occur in the decay of $^{132}$In, preventing an unambiguous assignment.

In summary, it is not possible to provide a reliable estimate of the direct $\beta$-decay branch of $^{133}$Cd. Some of the observed $\gamma$-rays may be attributed to transitions in $^{133}$In, however, none of them could be unambiguously assigned to it.

### 7.2.5 Coincidence analysis

The total projection of the $\beta$-gated $\gamma\gamma$ coincidence spectra following the $\beta$-decay of $^{133}$Cd is shown in Fig. 7.14. The spectrum is generated with a time gate of 10 to 310 ms relative to the impact of the protons on the target to enhance the selection of the $^{133}$Cd decays. All the $\gamma$-rays listed in Tab. 7.4 are present in the spectrum, including the 22 and 903-keV lines.

Fig. 7.15 shows the $\beta$-gated $\gamma$-ray spectra in coincidence with $\gamma$- and X-ray transitions previously identified in the $\beta$ decay of $^{133}$Cd and presented in Tab. 7.4. The 50-, 103- and 227-keV $\gamma$-ray transitions are in mutual $\gamma\gamma$ coincidence and form a $\gamma$-ray cascade, which is also observed in the $^{132}$Cd decay (see Sec. 7.1). In addition, the 103- and 335-keV $\gamma$-ray transitions are also observed in mutual coincidence, and provide evidence of sequential $\gamma$-ray decay, while the 335-keV transition is not in coincidence with the 225-keV one.

The 50-keV $\gamma$-ray gate is of particular interest (see Fig. 7.15 (d)), as it exhibits the most intense $\gamma\gamma$ coincidence with the 22-keV $\gamma$-ray. Still it suffers from the limited

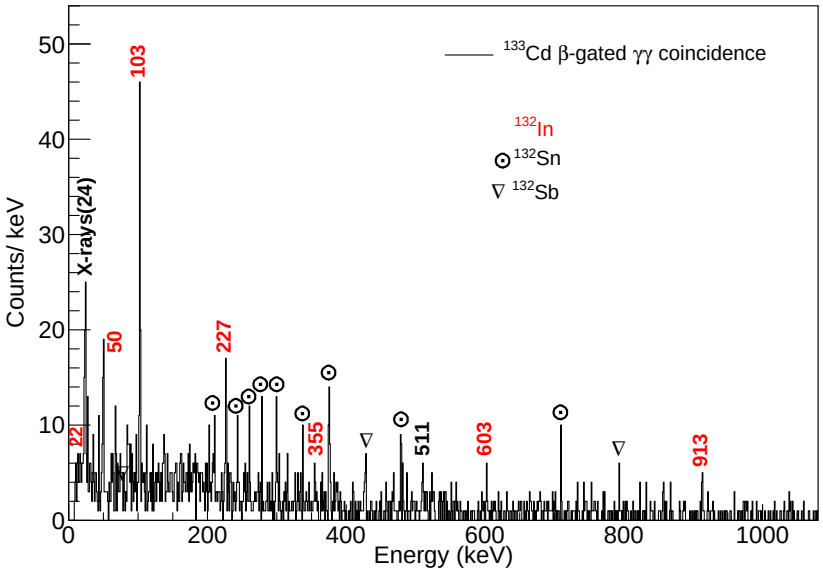


**Figure 7.14.** Total projection of the beta-gated $\gamma\gamma$ coincidence matrix showing $\gamma$-ray transitions in $^{132}$In following the $\beta$-delayed neutron emission of $^{133}$Cd, labeled in red. A time gate of 10–310 ms relative to the proton impact is applied.

statistics and the reciprocal coincidence is not observed in the 22-keV gate.

No $\gamma\gamma$ coincidences were observed for the 913- and 603-keV $\gamma$-ray transitions either. Since there is no firm evidence of their assignment to the $\beta$-delayed one neutron emission from $^{133}$Cd to $^{132}$In, and no coincidencent transitions were found, they will not be included in the proposed level scheme. Nonetheless they will be tentatively included as belonging to the $\beta$-delayed neutron emission branch populating $^{132}$In, as this is the most likely option given the $\gamma$ intensities involved.

In an attempt to identify potential new isomeric states, delayed $\gamma\gamma$ coincidence time gates were explored using successive time windows starting at 500 ns and extending up to 2500 ns in steps of 1000 ns. The $\beta$ condition and the restrictive 10–310 ms time gate relative to the proton impact was kept. The resulting projected $\gamma$ spectrum is shown in Fig. 7.16. No change in the line intensities from $\gamma$ rays associated with the decay of $^{133}$Cd is observed, and thus no evidence for isomeric transitions is found in the $\mu$s time range.

## 7.3 Nuclear structure of $^{132}$In

Once the experimental evidence from the direct $\beta$ and $\beta$-delayed neutron population of $^{132}$In is established, the construction of the level scheme is undertaken. Shell-model calculations are first discussed to support the spin-parity assignments.

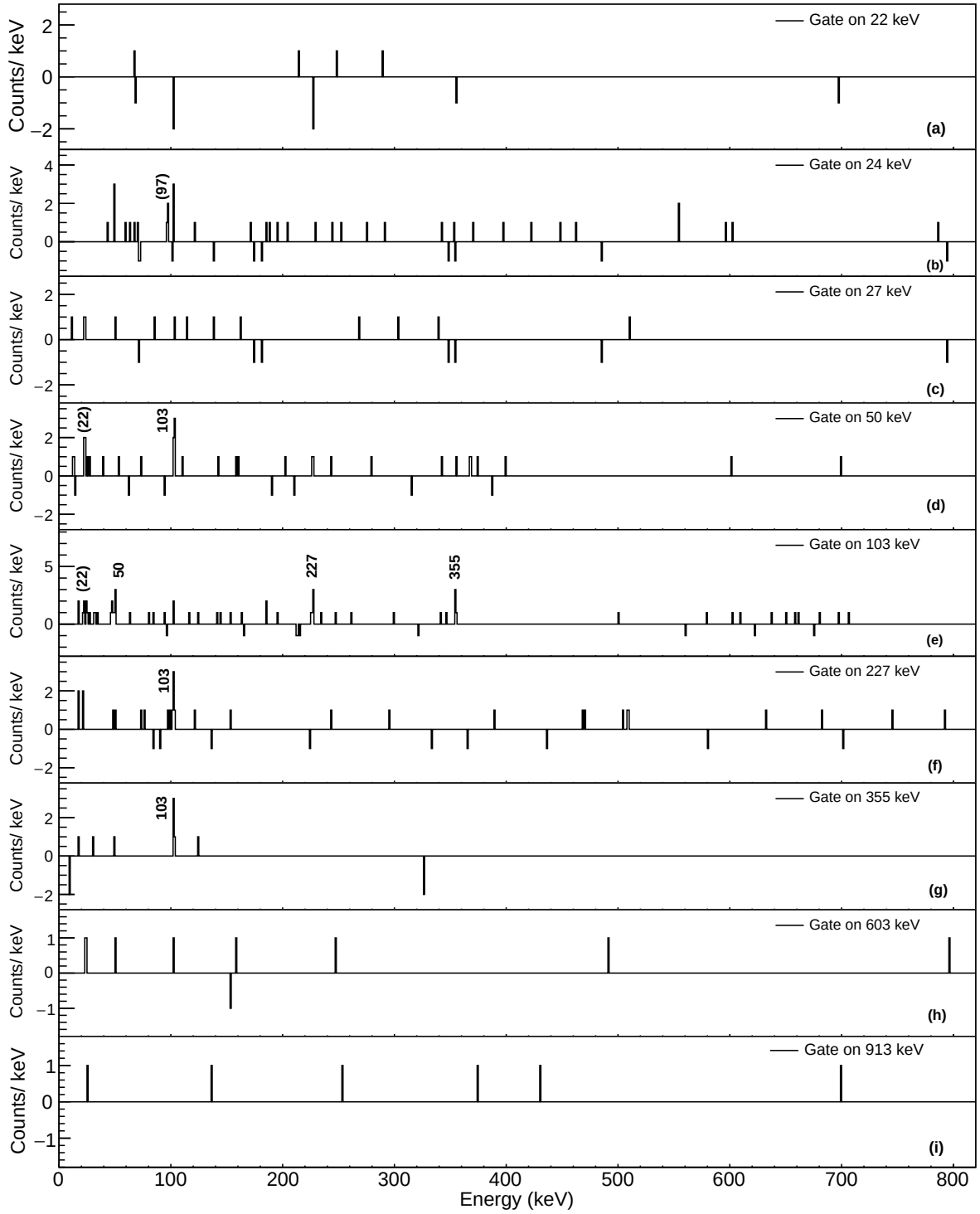


**Figure 7.15.** Beta-gated $\gamma\gamma$ coincidence spectra following the $\beta$-delayed neutron emission of $^{133}$Cd. A time window of 10–310 ms relative to the proton impact was applied to suppress background contributions. Panels (b) and (c) show X-rays associated with indium. Panels (a), (d), (e), (f), (g), (h) and (i) display coincidence spectra gated on the 22-, 50-, 103-, 227-, 354-, 603- and 913-keV $\gamma$-ray transitions respectively. Transitions labeled in brackets remain unassigned.

### 7.3.1 Shell-model calculations

Large-scale shell-model calculations were performed using the jj46Y16 interaction, where "jj" denotes the use of the jj-coupling scheme and the model space comprising

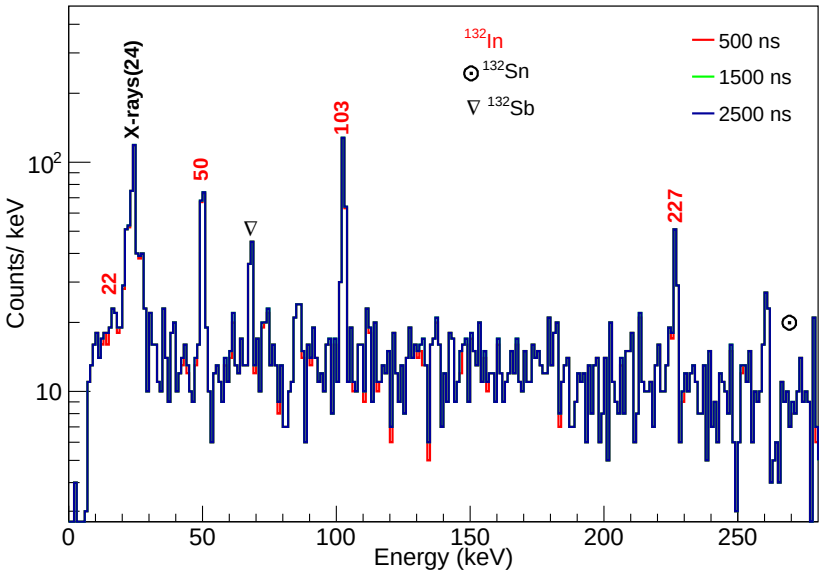


**Figure 7.16.** Beta-$\gamma$(t) delayed spectra measured for the $\beta$ decay of $^{133}$Cd with different time coincidence gates. The delayed coincidence was constructed using successive time windows starting at 500 ns and extending up to 2500 ns in steps of 1000 ns. The $\gamma$ rays from the $\beta$n decay of $^{133}$Cd identified in this work are labeled in red. A beam-gate condition of 10–310 ms relative to the proton impact was applied to enhance the selectivity for $\gamma$ rays associated with the decay of $^{133}$Cd.

four proton ($4\pi$) and six neutron ($6\nu$) orbitals. It is specifically tailored for nuclei in the southeast region of $^{132}$Sn, with the $\pi(0f_{5/2}, 1p_{3/2}, 1p_{1/2}, 0g_{9/2})$ proton orbitals and $\nu(1f_{7/2}, 2p_{3/2}, 2p_{1/2}, 0h_{9/2}, 1f_{5/2}, 0i_{13/2})$ neutron orbitals. The proton–proton interaction is derived from the jj45pna Hamiltonian, which in turn originates from the CD-Bonn potential via the G-matrix renormalization procedure. The neutron–neutron interaction is similarly taken from the CWG Hamiltonian, also based on the CD-Bonn force. A more detailed description of the jj46Y16 shell-model interaction can be found in Ref. [YLX+16]. The KSHELL code for nuclear shell-model calculations was used [Shi13].

The low-lying excited states in $^{132}$In calculated with the jj46Y16 interaction are shown in Fig. 7.17. The shell-model calculations predict excited states below 2 MeV based on particle-hole configurations. The occupation probabilities for the negative and positive parity states are summarized in Tabs. 7.5 and 7.6, repectively. These states are found to be remarkably pure, with negligible configuration mixing.

The obtained lowest-lying states are based on the $\pi g_{9/2}^{-1}\nu f_{7/2}$ configuration, as otherwise expected and reproduced by other calculations [JGG+16, YLX+16]. The calculated ground state has $7^-$ spin-parity. While no direct measurement is reported in the literature, a $(7^-)$ assignment for the g.s. of $^{132}$In is strongly supported by the feeding pattern observed in its $\beta$-decay [BFK+20]. Many of the excited states are quasi-degenerate and therefore the ordering of the levels should be taken with caution, specifically for the $4^-$, $5^-$ and $6^-$ states.

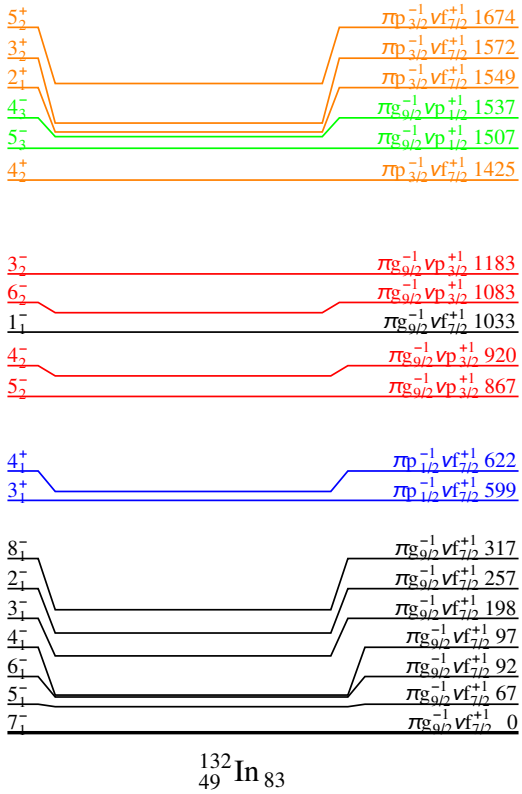


**Figure 7.17.** Low energies of excited states (in keV) in $^{132}$In using the jj46Y16 shell-model interaction. The dominant proton-neutron configurations for each state are annotated and represented in different colors. States belonging to the same multiplet are highlighted using the same color.

### 7.3.2 $^{132}$In level scheme

The level scheme of $^{132}$In has been established by combining the experimental information obtained from the $\beta$ decay of $^{132}$Cd, discussed in Sec. 7.1, and from the $\beta$-delayed neutron emission of $^{133}$Cd, presented in Sec. 7.2. Tentative spin and parity assignments for the populated states are inferred from $\beta$-decay selection rules and the observed $\gamma$-ray transitions connecting the levels. Shell-model calculations are used to support the assignments.

In the $\beta$ decay of $^{132}$Cd, the initial state is the $0^+$ ground state, identified predominantly by the $\pi g_{9/2}^{-2} \nu f_{7/2}^{2}$ configuration [HKP+00]. The decay pattern of $^{132}$Cd is expected to be dominated by the GT $\nu g_{7/2} \rightarrow \pi g_{9/2}$ transition [PKF+19, PSKB+21, XMG+23b, BFK+24]. Nonetheless, this transition creates a hole deep in the neutron shell, leading to highly-excited states with cross-shell $\pi g_{9/2}^{-1} \nu g_{7/2}^{-1} f_{7/2}^{2}$ configurations well above the neutron-separation energy. Competition between $\gamma$-ray decay with the neutron emission has been observed in this region [PKF+19, XMG+23b, BFK+24]. Contrary to this, the $^{132}$Cd $0^+$ decay should populate $1^+$ states, for which the de-excitation via neutron emission to low-lying states in $^{131}$In should not be so strongly hindered, since there are low-lying states

**Table 7.5.** Neutron orbital occupation numbers for the lowest negative-parity states in $^{132}$In, calculated using the jj46Y16 interaction. Only neutron configurations are reported, since all states have an identical proton structure characterized by $\pi g_{9/2}^{-1}$ hole (whose occupation number is 9). The values correspond to the dominant components of the wave functions for the first three negative-parity multiplets.

| $J^\pi$ | $\langle n_\nu \rangle$ | | | | | |
|---|---|---|---|---|---|---|
| | $0h_{9/2}$ | $1f_{7/2}$ | $1f_{5/2}$ | $2p_{3/2}$ | $2p_{1/2}$ | $0i_{13/2}$ |
| $7_1^-$ | 0.000 | 0.999 | 0.001 | 0.000 | 0.000 | 0.000 |
| $5_1^-$ | 0.000 | 0.989 | 0.001 | 0.006 | 0.003 | 0.000 |
| $6_1^-$ | 0.000 | 0.968 | 0.002 | 0.029 | 0.000 | 0.001 |
| $4_1^-$ | 0.001 | 0.971 | 0.003 | 0.017 | 0.009 | 0.000 |
| $3_1^-$ | 0.000 | 0.955 | 0.001 | 0.044 | 0.000 | 0.000 |
| $2_1^-$ | 0.003 | 0.974 | 0.023 | 0.000 | 0.000 | 0.000 |
| $8_1^-$ | 0.000 | 0.999 | 0.000 | 0.000 | 0.000 | 0.000 |
| $5_2^-$ | 0.001 | 0.005 | 0.003 | 0.966 | 0.025 | 0.000 |
| $4_2^-$ | 0.002 | 0.010 | 0.000 | 0.916 | 0.072 | 0.000 |
| $1_1^-$ | 0.000 | 1.000 | 0.000 | 0.000 | 0.000 | 0.000 |
| $6_2^-$ | 0.007 | 0.027 | 0.010 | 0.955 | 0.000 | 0.001 |
| $3_2^-$ | 0.023 | 0.039 | 0.045 | 0.893 | 0.000 | 0.000 |
| $5_3^-$ | 0.046 | 0.003 | 0.061 | 0.016 | 0.873 | 0.000 |
| $4_3^-$ | 0.040 | 0.010 | 0.063 | 0.053 | 0.834 | 0.000 |

**Table 7.6.** Proton and neutron orbital occupation numbers for the lowest positive-parity states in $^{132}$In, calculated using the jj46Y16 interaction. The values correspond to the dominant components of the wave functions for the first two positive-parity multiplets.

| $J^\pi$ | $\langle n_\pi \rangle$ | | | | $\langle n_\nu \rangle$ | | | | | |
|---|---|---|---|---|---|---|---|---|---|---|
| | $0f_{5/2}$ | $1p_{3/2}$ | $1p_{1/2}$ | $1g_{9/2}$ | $0h_{9/2}$ | $1f_{7/2}$ | $1f_{5/2}$ | $2p_{3/2}$ | $2p_{1/2}$ | $0i_{13/2}$ |
| $3_1^+$ | 6.000 | 3.938 | 1.065 | 9.998 | 0.000 | 0.996 | 0.001 | 0.001 | 0.000 | 0.002 |
| $4_1^+$ | 5.999 | 3.971 | 1.034 | 9.995 | 0.000 | 0.991 | 0.003 | 0.001 | 0.000 | 0.005 |
| $4_2^+$ | 5.998 | 3.033 | 1.977 | 9.991 | 0.000 | 0.989 | 0.000 | 0.001 | 0.000 | 0.009 |
| $2_1^+$ | 5.994 | 3.710 | 1.314 | 9.982 | 0.000 | 0.260 | 0.001 | 0.695 | 0.025 | 0.018 |
| $3_2^+$ | 5.997 | 3.078 | 1.937 | 9.988 | 0.000 | 0.973 | 0.011 | 0.002 | 0.001 | 0.012 |
| $5_2^+$ | 5.999 | 3.026 | 1.989 | 9.986 | 0.011 | 0.974 | 0.001 | 0.000 | 0.000 | 0.014 |

with similar spins to the ones populated in the $\beta$ decay. Therefore, this GT transition is expected to contribute mainly to the $\beta$-delayed neutron emission decay branch.

The GT branch expected to populate states below the neutron separation energy corresponds to the allowed $\nu p_{3/2} \rightarrow \pi p_{1/2}$ transition [HKP$^+$00]. This transition feeds the $1_1^+$ state in $^{132}$In, and is associated with the $\pi p_{1/2}^{-1} \nu p_{3/2}$ configuration located around 2 MeV according to shell-model calculations, see Fig. 7.17. For such a transition to occur, the initial $^{132}$Cd ground state would need to contain a sizable contribution of two proton holes in the $\pi p_{1/2}^{-2}$ orbital and two valence neutrons in the $\nu p_{3/2}^2$ orbital. On the contrary, it is expected that the $^{132}$Cd g.s. is dominated by the $\pi g_{9/2}^{-2} \nu f_{7/2}^2$ configuration [HKP$^+$00]. Therefore, the GT transition leading to the $1_1^+$ state in $^{132}$In is strongly suppressed due to the unfavorable overlap between the initial and final

wave functions.

FF transitions to low-lying states are predicted to play a significant role in the decay of all neighboring nuclei. In particular, the transition $\nu h_{11/2} \rightarrow \pi g_{9/2}$ has been identified in the decay of $^{131g}$In [BFK+24], $^{132}$In [BFK+20], $^{133g}$In [PS21, XMG+23b] and $^{131}$Cd [TJG+16]. In the case of $^{132}$Cd, this transition would lead to $\pi g_{9/2}^{-1}\nu h_{11/2}^{-1} f_{7/2}^{2}$ configurations above the neutron separation energy, contributing to the $\beta n$-decay branch. At low excitation energies, the most probable decay branch proceeds through FF transitions associated with the $\nu f_{7/2} \rightarrow \pi g_{9/2}$ transition [HKP+00, TJG+16, PKF+19], which will populate states within the $\pi g_{9/2}^{-1}\nu f_{7/2}$ multiplet. In particular, in the decay of $^{132}$Cd the $1^-$ member of this multiplet should be mostly populated by this FF transition.

The discussion now turns to $^{133}$Cd. Its ground state is tentatively assigned $(7/2^-)$ spin-parity based on the $\pi g_{9/2}^{-2}\nu f_{7/2}^{3}$ configuration, according to systematics and shell-model calculations [YLX+16]. Since the same orbitals that participate in $^{132}$Cd $\beta$-decay are also involved here, one can expect a similar contribution of the aforementioned GT and FF transitions. The relatively high initial spin of $^{133}$Cd will favour the population of the higher spin members of the low-lying $\pi g_{9/2}^{-1}\nu f_{7/2}$ multiplet. According to $\beta$-decay selection rules, allowed GT transitions from the $(7/2^-)$ ground state can populate final states in $^{133}$In with spin-parities $5/2^-$, $7/2^-$, or $9/2^-$. In contrast, FF transitions, which involve a change in parity, can populate positive-parity states ranging from $3/2^+$ to $11/2^+$. Following neutron emission from unbound states in $^{133}$In, the resulting states in $^{132}$In will depend on the orbital angular momentum $\ell$ of the $s = 1/2$ emitted neutron. In the more likely situation of neutrons emitted with $\ell = 0$, the populated states in $^{132}$In will have spin-parity in the range $2^-$ to $5^-$ after GT $\beta$ decay, and $1^+$ up to $6^+$ for FF transitions. If $\ell = 1$ neutrons are emitted, GT $\beta$-decay transitions will lead to $1^+ - 6^+$ states and FF transitions to $0^-$ and $7^-$ states. The most favoured $\beta$-delayed neutron banch will therefore populate negative parity states with spin $1 - 5$.

As discussed in the previous sections, the data reveals a $227 \rightarrow 103 \rightarrow 50$ keV cascade of sequential $\gamma$ rays populated in both $^{132}$Cd and $^{133}$Cd decays. The ordering of these transitions can be deduced from the comparison of the relative intensity of the $\gamma$-rays between both decays. Moreover, one can impose an extra constraint on the multipolarity of the transitions, by considering their total intensity once the internal conversion coefficients $\alpha_T$ are taken into account. They are included in Tab. 7.7 together with $\gamma$-ray intensities. Assuming an $E2$ character for the 50- and 103-keV transitions will lead to very high intensities, which in turn will then indicate large feeding to the states they de-excite. Guided by the shell model calculations, this will entail strong feeding to the lower-lying higher spin levels, in particular populated in the $^{132}$Cd $0^+$ decay, which is inconsistent with the assumption that most of the feeding goes to the $1^-$. On the other hand, assuming a $M1$ multipolarity, a similar total intensity for the 227-, 103- and 50-keV transitions in $^{132}$Cd decay is obtained, and within $2\sigma$ of the 561-keV transition. The similar intensities allow for the feeding to proceed to the low-spin states including the $1^-$ level, and then sequentially transmit along the band. The 561 keV transition, was only observed in coincidence with the 103 keV and 227 keV $\gamma$ rays (see Fig. 7.7), and is the weakest among them, supporting

**Table 7.7.** List of $\gamma$ rays observed following the $\beta$ decay of $^{132}$Cd and the $\beta$-delayed neutron emission branch from $^{133}$Cd. Theoretical internal conversion coefficients $\alpha_T$ are shown assuming pure $M1$ and $E2$ multipolarities [KBT+08]. Transition energies, relative $\gamma$ intensities ($I_\gamma$) normalized to 100 units for the 103-keV $\gamma$ ray, and total transition intensities ($I_T$) are reported for both isotopes. The $I_T$ were calculated assuming a pure $M1$ multipolarity (see text for details). The initial and final levels for each connecting transition are also given. The level excitation energies are offset by a quantity $Y$, an unknown energy shift common to all states.

| $E_\gamma$ (keV) | $\alpha_T(XL)$ | | $^{132}$Cd $\beta$ decay | | $^{133}$Cd $\beta$n decay | | $E_i - Y \rightarrow E_f - Y$ | |
|---|---|---|---|---|---|---|---|---|
| | $M1$ | $E2$ | $I_\gamma^a$ | $I_T$ | $I_\gamma$ | $I_T$ | (keV) | (keV) |
| 22.0(1) | 5.8 | 500 | – | – | 90(47) | 608(320) | 22.0(1) | 0 |
| 50.0(3) | 3.9 | 19 | 30(7) | 147(36) | 84(14) | 412(65) | 72.0(2) | 22.0(1) |
| 102.8(3) | 0.48 | 1.4 | 100 | 148 | 100 | 148 | 174.8(4) | 72.0(2) |
| 226.7(3) | 0.054 | 0.088 | 109(14) | 115(15) | 45(12) | 48(12) | 401.5(5) | 174.8(4) |
| 355.0(3) | – | – | – | – | 29(10) | 29(10) | 529.8(5) | 174.8(4) |
| 560.7(3) | – | – | 62(11) | 62(11) | – | – | 962.2(5) | 401.5(5) |
| 602.7(2)[b] | – | – | – | – | 40(10) | 40(10) | – | |
| 913.4(2)[b] | – | – | – | – | 39(14) | 39(14) | – | |
| 1301.1(2)[c] | – | – | 58(12) | 58(12) | – | – | – | |
| 1934.6(2)[c] | – | – | 78(17) | 78(17) | – | – | – | |

[a] For intensity per 100 decays of the parent, multiply values for $^{132}$Cd by 0.014(1).
[b] Assigned to the $^{133}$Cd $\beta$-n branch and not placed in the level scheme.
[c] Assigned to the $^{132}$Cd $\beta$ decay and not placed in the level scheme.

its placement as a $(1^-) \rightarrow (2^-)$ transition.

The ordering of the $\gamma$ rays, the lower energy transitions below the higher energy ones, is supported by the shell model calculations described above and by the state population in the $^{133}$Cd $\beta$-n branch. The direct coincidence between the 227- and 561-keV transitions is also clearly observed in the $\beta$-gated $\gamma\gamma$ coincidence spectra following the $^{132}$Cd $\beta$-decay. A sequence of levels at 962.2-, 401.5-, 174.8-, 71.9- and 22.0-keV, all of them with an offset by $Y$ keV, can be established, interconnected by the 560.7-, 226.7-, 102.9- and 49.9-keV $\gamma$ transitions.

The shell-model calculations also predict the $1_1^-$ state at an excitation energy around 1 MeV, which provides support for the tentative spin-parity assignment of $(1^-)$ for the level at 962.2 + $Y$ keV, since the excitation energy of the $Y$ level is expected to lie within a few tens of keV. Due to the uncertainties inherent to shell-model calculations, this cannot be regarded as conclusive, but helps the interpretation of the $\beta$ feeding to the 962.2 + $Y$-keV state.

Based on the above arguments the proposed $^{132}$Cd to $^{132}$In decay scheme is built and presented in Fig. 7.18. The $\beta$-decay feeding has been determined based on the intensity balance between feeding and de-exciting $\gamma$-rays for each energy level. Since the $\beta$ decay of the $0^+$ $^{132}$Cd to the $(7^-)$ state in $^{132}$In is highly forbidden, direct $\beta$ feeding to the ground state has been assumed to be zero. The $\log ft$ values are obtained from the $\beta$ feeding, the $Q_{\beta^-}$ value [NND25], and the experimentally measured

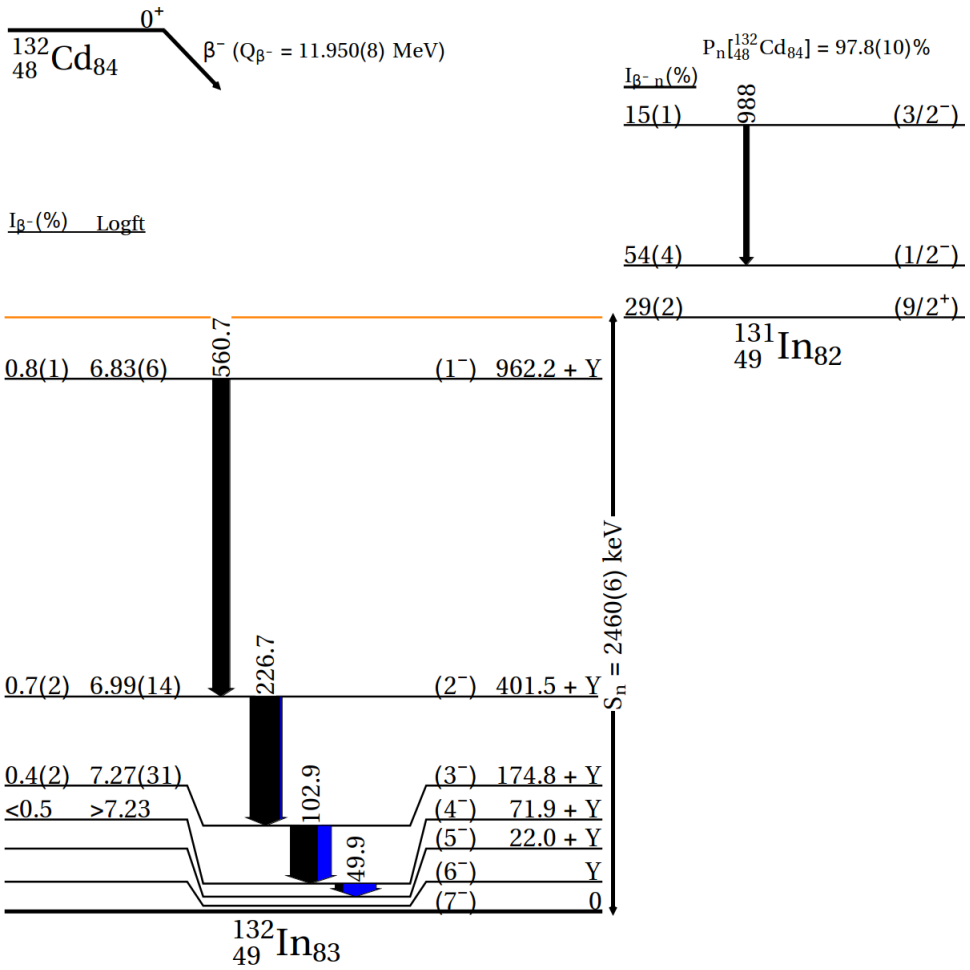


**Figure 7.18.** Proposed level scheme of $^{132}$In observed following the $\beta$ decay of the $^{132}$Cd $0^+$. Transition widths are proportional to their intensities, with the internal conversion fraction, assuming an pure $M1$ character, indicated in blue. For completion, the states populated in $^{131}$In via $\beta$-delayed neutron emission are shown on the right-hand side. The neutron separation energy ($S_n$) is not drawn to scale.

$\beta$-decay half-life [PNL+22]. The $\log ft$ value estimated in this work for the $(1^-)$ level is $\log ft = 6.83(6)$, corresponding to a $\beta^-$ feeding intensity of $I_{\beta^-} = 0.8(1)\%$. For the $(2^-)$ level, the extracted value is $\log ft = 6.99(14)$ with $I_{\beta^-} = 0.7(2)\%$. Both values are higher than those predicted by shell-model calculations in Ref. [HKP+00]. However, as discussed in the experimental systematics of Ref. [TMSZ23], these $\log ft$ values are consistent with first-forbidden transitions.

In the case of the population of the $^{132}$In structure by $\beta$-delayed neutron emission from $^{133}$Cd, the 50 keV $\gamma$-ray transition clearly exhibits the highest total intensity (see Tab 7.7). As previously discussed, the relatively high initial spin of $^{133}$Cd favors the population of the higher-spin members of the $\pi g_{9/2}^{-1}\nu f_{7/2}$ negative-parity multiplet. As a result, numerous states in $^{132}$In may be populated via $\beta$-delayed neutron emission following the decay of $^{133}$Cd, but the 50-, 103- and 227-keV $\gamma$-rays transitions form a cascade of $M1$ transitions between the low energy states and

the $\gamma$ transitions can be ordered based on the total intensity shown in Tab. 7.7. This leads to the interpretation of the 50-keV transition connecting low-lying states, such as $(4^-) \rightarrow (5^-)$, with the dominant feeding populating the $(4^-)$ level at $72+Y$ keV.

The shell-model calculations suggest that the $(6^-)$ level may lie above the $(4^-)$ level in energy. This would imply that the observed 50 keV $\gamma$-ray transition corresponds to a $(6^-) \rightarrow (4^-)$ transition. However, such a transition would have E2 character, requiring very large $\beta$ feeding, which is not compatible with a second-forbidden $\beta$ transition. Similar arguments can be made for the low-lying states, which favors states of sequentially decreasing spin connected by $M1$ transitions, consistent with the $^{132}$Cd $\beta$ decay discussed above.

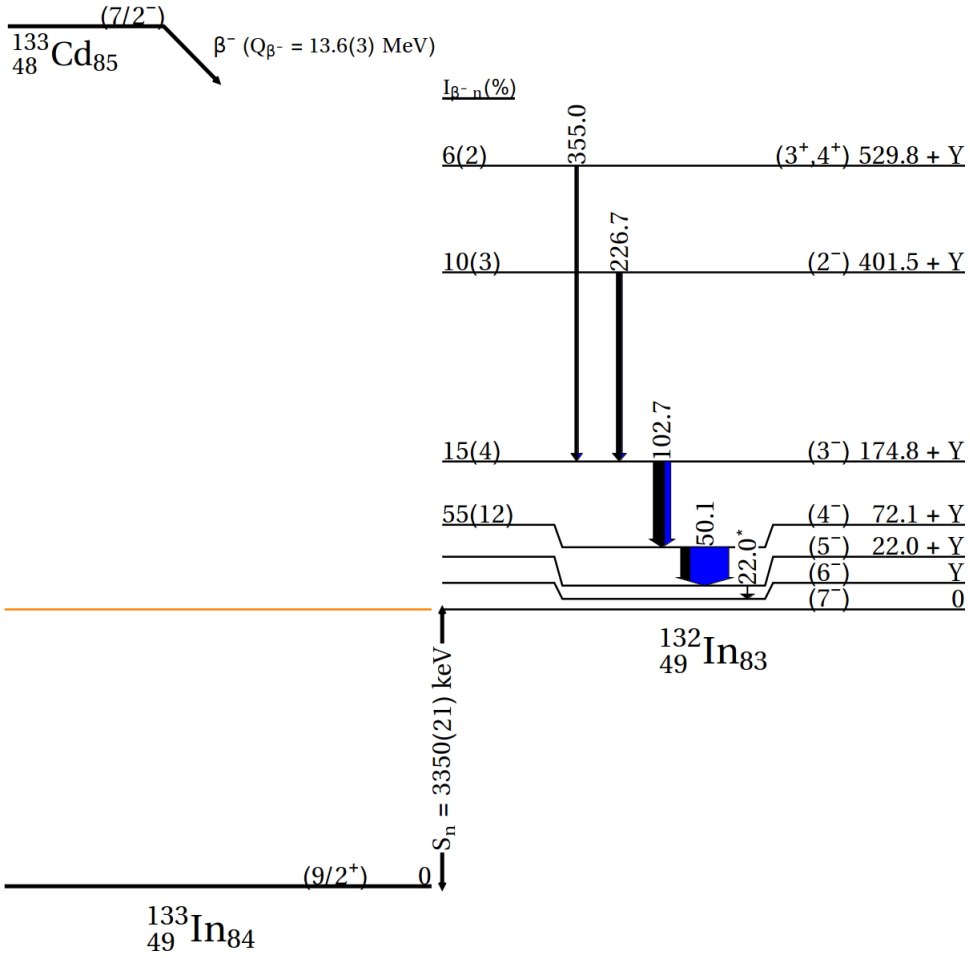


**Figure 7.19.** Proposed level scheme of $^{132}$In observed following the $\beta$ delayed neutron emission branch of the $^{133}$Cd $(7/2^-)$ $\beta$-decaying state. Transition widths are proportional to their intensities, with the internal conversion fraction, assuming a pure $M1$ character, indicated in blue. The 22-keV transition, marked with an asterisk, is placed in the decay scheme based on several assumptions discussed in the text. The neutron separation energy ($S_n$) is not drawn to scale.

The 355 keV $\gamma$-ray transition is observed solely in the $\beta$-delayed neutron emission of $^{133}$Cd. It appears only in coincidence with the 103 keV $\gamma$-ray transition (see Fig. 7.14),

which leads to its assignment directly on top of the 103-keV transition. Considering the result from the shell-model calculations, and also those in Refs. [JGG$^+$16, YLX$^+$16], the $\gamma$-ray is a strong candidate of a transition between one of the low-lying positive parity states (either $3^+$ or $4^+$) arising from the $\pi p^{-1}_{1/2}\nu f_{7/2}$ configuration and the negative ($3^-$) state of the $\pi g^{-1}_{9/2}\nu f_{7/2}$ multiplet. Beta-delayed neutron feeding from the ($7/2^-$) $^{133}$Cd g.s. to the ($3^+$, $4^+$) levels is possible, as discussed before. The absence of the 355-keV transition in the $\beta$-gated $\gamma$-ray spectrum following the $^{132}$Cd decay supports that it does not originate from negative-parity states.

No $\gamma$-ray transitions feeding the ($7^-$) ground state of $^{132}$In were observed in the $\beta\gamma\gamma$ coincidence analysis, and consequently, the excitation energy of the ($6^-$) state remains undetermined. Tentatively, the very low-energy 22 keV $\gamma$ transition, observed in the $\beta$-delayed neutron emission of $^{133}$Cd (see Fig. 7.11), is assigned to the ($5^-$) $\rightarrow$ ($6^-$) transition. Its tentative placement in the level scheme is based on the shell-model calculations, since it cannot be confirmed through direct coincidences with the 50 keV transition.

The proposed $^{133}$Cd ($7/2^-$) $\beta$-decay scheme is shown in Fig. 7.19. Only the transitions discussed above have been included. The $\beta$n-decay intensities have been normalized using the literature value of the one-neutron emission probability $P_{1n}$ = 86(7)% [PNL$^+$22].

Finally, the experimental level scheme of $^{132}$In obtained in this work is presented in Fig. 7.20. It includes both the $\gamma$ transitions and energy levels identified following the $\beta$ decay of the $^{132}$Cd $0^+$ ground state (in red), as well as those populated via $\beta$-delayed neutron emission from the ($7/2^-$) ground state of $^{133}$Cd (in blue). Levels and transitions common to both decays are depicted in black. The 22-keV transition is placed in the level scheme based on several assumptions, discussed above, not on coincidence relations. There is an ambiguity on the energy of the first-excited state, denoted as $Y$, which offsets all the known leveles, but is expected to be around 10 keV. The level energies are compared to the SM calculations from this work using the jj46Y16 interaction, as well as with two additional SM calculations from Ref. [JGG$^+$16].

## 7.4 Conclusions of the chapter

The nuclear structure of $^{132}$In, characterized as a proton hole–neutron particle configuration relative to the doubly magic $^{132}$Sn core, has been investigated through the $\beta$ decay of $^{132}$Cd and the $\beta$-delayed neutron emission of $^{133}$Cd. For the first time, it was possible to observe $\gamma$-ray transitions in $^{132}$In populated directly in the decay of $^{132}$Cd.

Owing to the increased yields obtained in this experiment compared to previous works, it has been possible for the first time to construct a level-scheme based on $\gamma\gamma$ coincidence analysis. A cascade of $M1$ transitions connecting the ($1^-$) to ($5^-$) states has been established, supported by $\gamma\gamma$ coincidences data. Large-scale shell-model calculations employing the jj46Y16 interaction provide guidance of the low-lying

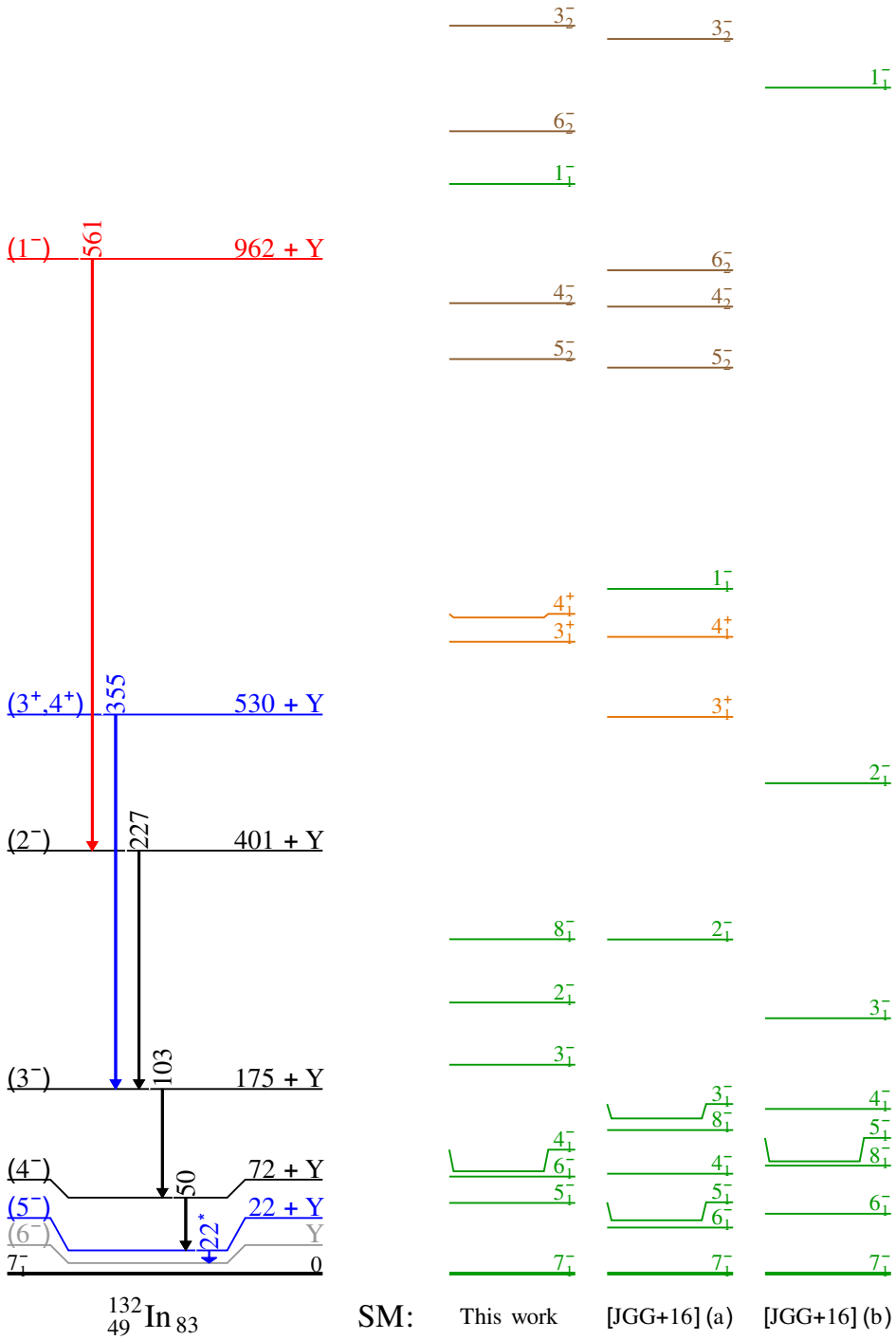


**Figure 7.20.** Proposed experimental level scheme of $^{132}$In (left) with the results of the SM. Transitions and levels observed exclusively following the $\beta$ decay of the $^{132}$Cd $0^+$ are shown in red. Those observed only via the $\beta$-delayed neutron emission from the $(7/2^-)$ ground state of $^{133}$Cd are indicated in blue. Levels and transitions common to both decays are depicted in black. The level labeled Y is shown in grey, as its placement is tentative and based on several assumptions (see text for further details). The 22 keV transition, marked with an asterisk, is placed in the decay scheme based on several assumptions discussed in the text. The SM results obtained in this work are presented together with (a) SM calculations using realistic effective interactions for $^{134}$Sb [JGG+16], as well as (b) SM estimates based on a scaling of TBMEs from the $^{208}$Pb region [JGG+16], both taken from Ref. [JGG$^+$16]. The dominant proton-neutron configurations for each state are represented in different colors. States belonging to the $\pi g_{9/2}^{-1}\nu f_{7/2}$ multiplet are shown in green, those associated with $\pi p_{1/2}^{-1}\nu f_{7/2}$ in orange, and those corresponding to $\pi g_{9/2}^{-1}\nu p_{3/2}$ in brown.

negative-parity states being dominated by $\pi g_{9/2}^{-1}\nu f_{7/2}$ configurations. The observed level-scheme and feeding patterns can be interpreted in terms of these particle-hole configurations, yielding a consistent picture from both $^{132}$Cd and $^{133}$Cd decays.

The $\beta$-feeding intensities and $\beta$-delayed neutron emission intensities for the $^{132}$Cd and $^{133}$Cd decays, respectively, have been calculated. A new $P_{1n} = 97.8(10)\%$ value has been determined for the first-time for $^{132}$Cd from $\gamma$-ray intensities.

Although the excited structure of $^{132}$In is notably improved in this study, important questions remain open, such as the connection of the observed states with the $^{132}$In ground state, which appears to be dominated by strongly converted low-energy transitions. Further studies focused on measuring these low-energy transitions and on conversion electron-spectroscopy would be strongly helpful to clarify the $^{132}$In structure.

# Chapter 8

# Conclusions

The evolution of nuclear shell structure in nuclei with large neutron-to-proton ratios remains an open question in nuclear physics. Experimental investigations in the vicinity of exotic doubly magic nuclei provide essential insights into how shell structure evolves and deliver benchmark data for large-scale shell-model calculations, which can then be applied to broader regions of the nuclear chart. The study of excited states in nuclei around $^{132}$Sn provides valuable constraints on the proton-neutron interaction, pairing correlations, and the onset of collective phenomena. In this context the addition of electromagnetic transition rates to the spectroscopic information has the added value of providing a sensitive tool to test the nuclear wavefunctions.

The $B(E2)$ transition strengths for even-even nuclei in the $^{132}$Sn region have revealed unexpected deviations from the seniority scheme arising from the coupling of valence nucleons in the vicinity of shell closures. A salient example is the anomalous $B(E2)$ enhancement in $^{136}$Sn [DTMW63, SAG$^+$07], which has been interpreted either as a reduction of neutron pairing or within a generalized multi-$j$ seniority approach [JM17]. However, such models fail to reproduce the enhanced $B(E2; 4^+ \rightarrow 2^+)$ in $^{134}$Sn [PS21]. Additional measurements in $^{134}$Sn and $^{130}$Cd suggest isospin-dependent effective charges [JGM$^+$24], while data in $^{130,132}$Te point to the influence of core excitations [KBA$^+$22]. Beyond $N = 82$, a sudden enhancement in $B(E2; 2^+ \rightarrow 0^+)$ has been observed, signaling the onset of collectivity [VJD$^+$19, AJA$^+$25], though higher-spin transitions indicate a subsequent reduction of collective behavior [HLN$^+$21]. Despite these advances, precise experimental $B(E2)$ data for tin isotopes below $^{132}$Sn remain scarce.

At higher excitation energies ($\approx$ 4 MeV), cross-shell particle-hole excitations of the $^{132}$Sn core become accessible [BDGE$^+$80, BDZ$^+$01, FHJ$^+$94, BFK$^+$20, WAG$^+$20], and their coupling to neighboring single-particle configurations governs the structure of high-energy levels [SVFM$^+$99, TJG$^+$16, PKF$^+$19, BFK$^+$24]. These excitations strongly impact $\beta$-decay, particularly southeast of $^{132}$Sn, where the Gamow-Teller $\nu g_{7/2} \rightarrow \pi g_{9/2}$ transition dominates. Their theoretical description requires large-scale shell-model calculations [DS21], whose reliability must be tested against experimental information on energies, lifetimes, and decay patterns. Precise $\beta$-decay studies, including half-lives and $\log ft$ values, are crucial to benchmark Gamow-Teller and

first-forbidden transitions [XMG+23a, XMG+23b, BFK+24, PKF+19].

In odd-odd nuclei the identification of multiplets is particularly complex due to the increased density of states. The indium isotopes with $Z = 49$ are of specific interest, since the proton hole with a strong predominance of the $\pi g_{9/2}$ configuration couples to the valence neutron, allowing the role of the neutron orbitals across $N = 82$ to be explored. The case of $^{132}$In with $N = 83$ is particularly interesting, since it allows one to probe the nuclear structure beyond the neutron shell closure, remaining one of the few nuclides accessible for spectroscopy in the south-west region of $^{132}$Sn. Its structure is largely tentative to date [JGG+16, Par23].

In this context, this PhD thesis presents new results on the structure of isotopes in the vicinity of the double shell closure at $Z = 50$ and $N = 82$. The nuclear structure of $^{128}$In, $^{128}$Te, and $^{128}$Sn, populated through the $\beta$-decay chain of $^{128}$Cd, have been investigated. For $^{128}$Sn, the level scheme has been greatly extended. Lifetime measurements of the excited states have been carried out for all four isotopes studied. In addition, the level scheme of $^{132}$In, populated for the first time via $\beta$ decay of $^{132}$Cd and via $\beta$-delayed neutron emission of $^{133}$Cd, has been expanded and revised to provide a more reliable description.

The experimental investigation was carried out at the ISOLDE facility at CERN, utilizing low-energy radioactive ion beams produced by fast neutron-induced fission of a $UC_x$ target. The results obtained during the two IS685 and IS685_II experimental campaigns demonstrate that the combination of the $UC_x$ target with a neutron converter, the quartz transfer line, and selective laser ionization using the RILIS technique enables the production of high-intensity and high-purity Cd beams. The measurements, performed at the ISOLDE Decay Station included high-resolution $\gamma$-ray spectroscopy and fast-timing measurements of the excited states.

The main results and achievements of this thesis are summarized in the following.

## High-purity beams of neutron-rich Cd isotopes at ISOLDE

The production yields of neutron-rich cadmium isotopes with mass numbers $A = 124$-133 have been determined from $\gamma$-ray spectroscopy following their $\beta$ decay, using known branching ratios for the relevant transitions. Corrections for the IDS transmission efficiency and for the isotope release fraction from the target were applied. The measurements from the IS685 and IS685_II experimental campaigns show that the neutron converter, the quartz transfer line, and selective laser ionization using the RILIS technique substantially suppresses isobaric contaminants and greatly improves isotopic selectivity. A fully functional target and ion source enabled a significant increase in the production rates in the second campaign, making the investigation of the $\beta$ decay of isotopes very scarcely produced possible, including $^{131,132,133}$Cd. The enhanced purity obtained in this work provides conditions for high-resolution $\gamma$ spectroscopy studies following the $\beta$ decay of neutron-rich Cd isotopes. Under the present experimental conditions, no contamination from Cs was detected, and In was

suppressed by more than three orders of magnitude relative to Cd. The results derived from this investigation have been published in the peer-reviewed journal *Acta Physica Polonica B* [LEBF$^+$25a], stemming from a presentation in an international conference. Additional results are discussed in the *ISOLDE 2025 Newsletter* [LEBF$^+$25b], distributed to the wider ISOLDE community.

## Lifetime measurements in $^{128}$In and $^{128}$Te

The fast-timing spectroscopy investigation of the $^{128}$Cd $\beta$-decay chain has provided the first sub-nanosecond lifetime measurements in $^{128}$In, together with new and more precise determinations of excited-state lifetimes in $^{128}$Te.

Using the centroid-shift method on $\beta\gamma\gamma(t)$ data, lifetimes in $^{128}$In were measured for the first time for the 315- and 489-keV levels from fits of the 462- and 857-keV $\gamma$-ray time spectra with a Gaussian–exponential response. The limited statistics prevented lifetime determinations for the 711- and 1173-keV states. The results yield $B(X\lambda)$ values for several transitions and support spin–parity assignments of $(2^-)$ for the 315- and 711-keV states, $(1^-)$ for 489 keV level, and confirm $1^+$ for 1173 keV state.

In $^{128}$Te, populated via the $\beta$ decay of the $5^+$ isomer in $^{128}$Sb, lifetimes of the yrast $6^+$, $4^+$, and $2^+$ yrast states were determined using $\beta\gamma(t)$ and $\gamma\gamma(t)$ techniques. The half-life of the $6^+$ state was measured with high precision, yielding $T_{1/2} = 461(2)$ ps. The $4^+$ state at 1497 keV was remeasured, yielding a mean lifetime of $\tau = 11(7)$ ps that challenges recent results [PBE$^+$22] and the $2^+$ state found to have a lifetime of $\tau = 9(8)$ ps, albeit with a large uncertainty. These measurements enabled the extraction of $B(E2)$ transition strengths along the yrast cascade. The results generally agree with shell-model predictions, with some deviations that may reflect limitations in the current effective interactions for this mass region. The results derived from this investigation have also been published in *Acta Physica Polonica B* [LEBF$^+$25a].

## Nuclear structure of $^{128}$Sn

A part of this thesis focused on the nuclear structure of $^{128}$Sn. Owing to the $\beta$ decay selectivity starting from $^{128}$Cd it was populated exclusively from the ground state of $^{128}$In. A detailed re-examination of the decay scheme led to the identification of 81 new $\gamma$ transitions and 30 new levels, substantially expanding the known level structure. New, more precise, values for the $\beta$-decay half-lives of the $^{128g}$Cd $0^+$ g.s. ($T_{1/2} = 256(5)$ ms) and the $^{128g}$In $(3^+)$ g.s. ($T_{1/2} = 814(9)$ ms), was obtained by analyzing the time distributions of the strongest $\gamma$-rays.

Using fast-timing techniques the lifetime of the $(4^+)$ state at 2001 keV was measured for the first time. A half-life of $T_{1/2} = 17(9)$ ps was determined using the centroid-shift method. The corresponding reduced transition probability

$B(E2;\ 4^+ \rightarrow 2^+) = 2.1(^{+2.3}_{-0.7})$ W.u. was found to be consistent with shell-model predictions and with the systematics of neighboring even–even Sn isotopes. The half-life of the $(5^-)$ state at 2121 keV was re-determined with significantly improved precision, yielding $T_{1/2} = 10.5(3)$ ns. An upper limit on the half-life of the 2378-keV state of 40 ps was obtained, and the extracted reduced transition probabilities from this state support a tentative $(4^-)$. Together, these measurements refine the understanding of level energies, transition multipolarities, and spin-parity assignments in $^{128}$Sn, testing the reliability of nuclear-structure models in the vicinity of the doubly magic $^{132}$Sn core.

The results derived from this investigation have been published in the peer-reviewed journal *Physical Review C* [LEFB+24].

## Nuclear structure of $^{132}$In

The nuclear structure of $^{132}$In has been investigated through the $\beta$ decay of $^{132}$Cd and the $\beta$-delayed neutron emission of $^{133}$Cd. For the first time, $\gamma$-ray transitions in $^{132}$In populated directly in the decay of $^{132}$Cd were observed. Owing to the production yields achieved in this experiment at ISOLDE, it was possible to construct a level scheme based on $\gamma\gamma$ coincidence analysis. A cascade of 4 $\gamma$-rays was identified. Aided by large-scale shell-model calculations using the jj46Y16 interaction, which indicate that the low-lying negative-parity states are dominated by proton-hole–neutron-particle configurations relative to the doubly magic $^{132}$Sn core, where the $\pi g_{9/2}^{-1}\nu f_{7/2}$ multiplet is the lowest in energy, they are assigned as $M1$ transitions connecting the $(1^-)$ to $(5^-)$ states. The proposed $\beta$-decay schemes and feeding patterns from both $^{132}$Cd and $^{133}$Cd decays are consistent with this interpretation. A level structure for $^{132}$In is proposed in this work.

The $\beta$-feeding intensities and $\beta$-delayed neutron emission probabilities for the decays of $^{132}$Cd and $^{133}$Cd, respectively, have been quantified. In particular, a new value of $P_{1n} = 97.8(10)\%$ was determined for $^{132}$Cd from $\gamma$-ray intensities. While the excited structure of $^{132}$In is significantly clarified in this study, open questions remain, especially regarding the connection between the observed states and the ground state, which appears to be governed by strongly converted low-energy transitions. Future investigations focused on these low-energy transitions and on conversion-electron spectroscopy will be essential to establish a better understanding of the $^{132}$In level structure.

A manuscript describing the current work on the nuclear structure of $^{132}$In is in preparation for submission to *Physical Review Letters*.

## Outlook

In conclusion, this PhD thesis exposes outstanding questions that should guide future experimental and theoretical efforts aimed at advancing the understanding of nuclear

structure around $^{132}$Sn and its implications for nuclear astrophysics. The present experimental results highlight the need for extensive shell-model calculations and the development of robust theoretical frameworks capable of accurately describing exotic nuclear configurations in the $Z < 50$, $N > 82$ region. Despite recent experimental progress, spectroscopic information in the $^{132}$Sn region remains incomplete. Complementary investigations may be undertaken using low-energy transfer reactions and high-energy knockout experiments, which would provide additional constraints on nuclear structure and enable a more comprehensive understanding of shell evolution in this mass region. The type of measurements presented in this work, which combine $\gamma$-ray spectroscopy and lifetime measurements via fast-timing methods, can be extended to other nuclei in the south $^{132}$Sn region.

# Bibliography


[AGT07] M. Arnould, S. Goriely, and K. Takahashi. *Phys. Rep.*, 450(4-6):97–213, 2007.

[AJA+25] J. Acosta, A. Jungclaus, M. Armstrong, M. Górska, T. Parry, Zs. Podolyák, P. Doornenbal, K. Wimmer, A. Gargano, N. Aoi, et al. *Phys. Rev. C*, 111:064316, 2025.

[Bat10] H. Bateman. *Proc.Cambridge Phil.Soc.*, volume 15. 1910.

[BBFH57] E. M. Burbidge, G. R. Burbidge, W. A. Fowler, and F. Hoyle. *Rev. Mod. Phys.*, 29(4):547, 1957.

[BBG+16] J. C. Batchelder, N. T. Brewer, C. J. Gross, R. Grzywacz, J. H. Hamilton, M. Karny, A. Fijalkowska, S. H. Liu, K. Miernik, S. W. Padgett, et al. *Phys. Rev. C*, 94(2):024317, 2016.

[BCE+07] E. Bouquerel, R. Catherall, M. Eller, J. Lettry, S. Marzari, and T. Stora. *Eur. Phys. J. Spec. Top.*, 150(1):277–280, 2007.

[BDGE+80] T. Björnstad, L.-E. De Geer, G. T. Ewan, P. G. Hansen, B. Jonson, K. Kawade, A. Kerek, W.-D. Lauppe, H. Lawin, S. Mattsson, et al. *Phys. Lett. B*, 91(1):35 – 37, 1980.

[BDSS78] M. J. Bechara, O. Dietzsch, M. Samuel, and U. Smilansky. *Phys. Rev. C*, 17:628–633, 1978.

[BDZ+01] P. Bhattacharyya, P. J. Daly, C. T. Zhang, Z. W. Grabowski, S. K. Saha, R. Broda, B. Fornal, I. Ahmad, D. Seweryniak, I. Wiedenhöver, et al. *Phys. Rev. Lett.*, 87:062502, 2001.

[Ben20] J. Benito. *Gamma and fast-timing spectroscopy of exotic tin isotopes around $^{132}Sn$.* PhD thesis, Universidad Complutense de Madrid, 2020.

[Ber18] N. Bernier. *Decay spectroscopy of neutron-rich cadmium around the N= 82 shell closure.* PhD thesis, University of British Columbia, 2018.

[BFK+20] J. Benito, L. M. Fraile, A. Korgul, M. Piersa, E. Adamska, A. N. Andreyev, R. Álvarez-Rodríguez, A. E. Barzakh, G. Benzoni, T. Berry, et al. *Phys. Rev. C*, 102:014328, 2020.

[BFK+24] J. Benito, L. M. Fraile, A. Korgul, M. Piersa-Siłkowska, A. Jaries, M. Stryjczyk, E. Adamska, R. Álvarez-Rodríguez, A. N. Andreyev, A. E. Barzakh, et al. *Phys. Rev. C*, 110:014328, 2024.

[BKL+18] C. Babcock, R. Klawitter, E. Leistenschneider, D. Lascar, B. R. Barquest, A. Finlay, M. Foster, A. T. Gallant, P. Hunt, B. Kootte, et al. *Phys. Rev. C*, 97(2):024312, 2018.

[BR14] B. A. Brown and W. D. M. Rae. *Nucl. Data Sheets*, 120:115–118, 2014.

[BSS+05] B. A. Brown, N. J. Stone, J. R. Stone, I. S. Towner, and M. Hjorth-Jensen. *Phys. Rev. C*, 72(2):029901, 2005.

[CCG+09] L. Coraggio, A. Covello, A. Gargano, N. Itaco, and T. T. S. Kuo. *Prog. Part. Nucl. Phys.*, 62(1):135–182, 2009.

[CCGI13] L. Coraggio, A. Covello, A. Gargano, and N. Itaco. *Phys. Rev. C*, 87:034309, 2013.

[CER25a] CERN. European organization for nuclear research. https://home.cern/, 2025. Accessed: November 26, 2025.

[CER25b] CERN RILIS database. https://riliselements.web.cern.ch/index.php, 2025. Accessed: November 26, 2025.

[CQZA16] Y. Y. Cheng, C. Qi, Y. M. Zhao, and A. Arima. *Phys. Rev. C*, 94(2):024321, 2016.

[CSA+20] B. J. Coombes, A. E. Stuchbery, J. M. Allmond, A. Gargano, J. T. H. Dowie, G. Georgiev, M. S. M. Gerathy, T. J. Gray, T. Kibedi, G. J. Lane, et al. In *EPJ Web Conf.*, volume 232, page 04003. EDP Sciences, 2020.

[DBT+99] G. Duchêne, F. A. Beck, P. J. Twin, G. De France, D. Curien, L. Han, C. W. Beausang, M. A. Bentley, P. J. Nolan, and J. Simpson. *Nucl. Instrum. Methods Phys. Res. A*, 432(1):90–110, 1999.

[DGX+25] P. Dyszel, R. Grzywacz, Z. Y. Xu, N. Kitamura, M. Karny, A. Korgul, M. Madurga, S. Neupane, A. Algora, A. N. Andreyev, et al. *Phys. Rev. Lett.*, 135:152501, 2025.

[DS21] Sangeeta Das and M. Saha Sarkar. *Nucl. Phys. A*, 1014:122262, 2021.

[DTMW63] Amos De-Shalit, Igal Talmi, H. S. W. Massey, and Eugene P. Wigner. *Phys. Today*, 16(9):67–67, 1963.

[Els34] W. M. Elsasser. *J. Phys. Radium*, 5(8):389–397, 1934.

[End81] P. M. Endt. *At. Data Nucl. Data Tables*, 26(1):47–91, 1981.

[ET15] Z. Elekes and J. Timar. *Nucl. Data Sheets*, 129:191–436, 2015.

[Eva21] A.M.E. Atomic Mass Evaluation. *Chin. Phys. C*, 45(3):030003, 2021.

[FBL+20] L. M. Fraile, J. Benlliure, M. Lhersonneau, J. R. Murias, V. Sánchez-Tembleque, J. M. Udías, A. Korgul, A. Fijalkowska, Z. Janas, M. Karny, et al. (CERN-INTC-2020-070 / INTC-P-585), 2020.

[FC79] B. Fogelberg and P. Carlé. *Nucl. Phys. A*, 323(2):205–252, 1979.

[FCG+17] V. Fedosseev, K. Chrysalidis, T. D. Goodacre, B. Marsh, S. Rothe, C. Seiffert, and K. Wendt. *J. Phys. G: Nucl. Part. Phys.*, 44(8):084006, 2017.

[FHJ+94] B. Fogelberg, M. Hellström, D. Jerrestam, H. Mach, J. Blomqvist, A. Kerek, L. O. Norlin, and J. P. Omtvedt. *Phys. Rev. Lett.*, 73:2413–2416, 1994.

[FHS81] B. Fogelberg, K. Heyde, and J. Sau. *Nucl. Phys. A*, 352(2):157–180, 1981.

[FMV+13] L. M. Fraile, H. Mach, V. Vedia, B. Olaizola, V. Paziy, E. Picado, and J. M. Udías. *Nucl. Instrum. Methods Phys. Res. A*, 701:235–242, 2013.

[Fog88] B. Fogelberg. In *Nucl. Data Sci. Technol.*, pages 837–840. Saikon Publishing Co., Ltd., 1988.

[Fra17] L.M. Fraile. *J. Phys. G*, 44(9):094004, 2017.

[GELF86] H. Göktürk, B. Ekström, E. Lund, and B. Fogelberg. *Z. Phys. A*, 324(1):117–118, 1986.

[GH78] M. L. Gartner and J. C. Hill. *Phys. Rev. C*, 18(3):1463, 1978.

[GLMP07] H. Grawe, K. Langanke, and G. Martínez-Pinedo. *Rep. Prog. Phys.*, 70(9):1525, 2007.

[Gug34] K. Guggenheimer. *J. Phys. Radium*, 5(6):253–256, 1934.

[HAC+19] C. J. Horowitz, A. Arcones, B. Cote, I. Dillmann, W. Nazarewicz, I. U. Roederer, H. Schatz, A. Aprahamian, D. Atanasov, A. Bauswein, et al. *J. Phys. G*, 46(8):083001, 2019.

[HCJH77] J.C. Hardy, L.C. Carraz, B. Jonson, and P.G. Hansen. *Phys. Lett. B*, 71(2):307–310, 1977.

[HDE+21] O. Hall, T. Davinson, A. Estrade, J. Liu, G. Lorusso, F. Montes, S. Nishimura, V.H. Phong, Phil J. Woods, J. Agramunt, et al. *Phys. Lett. B*, 816:136266, 2021.

[HEHJO98] A. Holt, T. Engeland, M. Hjorth-Jensen, and E. Osnes. *Nucl. Phys. A*, 634(1):41–56, 1998.

[HKP+00] M. Hannawald, K.-L. Kratz, B. Pfeiffer, W.B. Walters, V.N. Fedoseyev, V.I. Mishin, W.F. Mueller, H. Schatz, J. Van Roosbroeck, U. Köster, et al. *Phys. Rev. C*, 62(5):054301, 2000.

[HLN+21] G. Häfner, R. Lozeva, H. Naïdja, M. Lebois, N. Jovancevic, D. Thisse, D. Etasse, R. L. Canavan, M. Rudigier, J. N. Wilson, et al. *Phys. Rev. C*, 103, 2021.

[HXL+20] B.C. He, H.T. Xue, L. Li, Y.A. Luo, Y. Zhang, F. Pan, and J.P. Draayer. *Phys. Rev. C*, 101(1):014324, 2020.

[IBD+21] C. Izzo, J. Bergmann, K. A. Dietrich, E. Dunling, D. Fusco, A. Jacobs, B. Kootte, G. Kripkó-Koncz, Y. Lan, E. Leistenschneider, et al. *Phys. Rev. C*, 103(2):025811, 2021.

[IBJ+14] Ł. W. Iskra, R. Broda, R. V. F. Janssens, J. Wrzesiński, B. Szpak, C. J. Chiara, M. P. Carpenter, B. Fornal, N. Hoteling, F. G. Kondev, et al. *Phys. Rev. C*, 89(4):044324, 2014.

[Int25] International Atomic Energy Agency. LiveChart of Nuclides. https://www-nds.iaea.org/relnsd/vcharthtml/VChartHTML.html, 2025. Accessed: November 26, 2025.

[ISO21] ISOLDE. The isolde yield database, version 0.2. https://cern.ch/isolde-yields, 2021. Accessed: November 26, 2025.

[ISO25] ISOLDE. Isotope separator on-line device. https://isolde.cern/, 2025. Accessed: November 26, 2025.

[JAB+10] K. L. Jones, A. S. Adekola, D. W. Bardayan, J. C. Blackmon, K. Y. Chae, K. A. Chipps, J. A. Cizewski, L. Erikson, C. Harlin, R. Hatarik, et al. *Nature*, 465(7297):454–457, 2010.

[JGG+16] A. Jungclaus, A. Gargano, H. Grawe, J. Taprogge, S. Nishimura, P. Doornenbal, G. Lorusso, Y. Shimizu, G. S. Simpson, P.-A. Soderstrom, et al. *Phys. Rev. C*, 93(4):041301, 2016.

[JGM+24] A. Jungclaus, M. Górska, M. Mikołajczuk, J. Acosta, J. Taprogge, S. Nishimura, P. Doornenbal, G. Lorusso, G. S. Simpson, P. A. Söderström, et al. *Phys. Rev. Lett.*, 132, 2024.

[JGN+16] A. Jungclaus, H. Grawe, S. Nishimura, P. Doornenbal, G. Lorusso, G. S. Simpson, P.-A. Söderström, T. Sumikama, J. Taprogge, Z. Y. Xu, et al. *Phys. Rev. C*, 94(2):024303, 2016.

[JM17] Ashok Kumar Jain and Bhoomika Maheshwari. *Phys. Scr.*, 92(7):074004, 2017.

[KBA+22] D. Kumar, T. Bhattacharjee, S. S. Alam, S. Basak, L. Gerhard, L. Knafla, A. Esmaylzadeh, M. Ley, F. Dunkel, K. Schomaker, et al. *Phys. Rev. C*, 106, 9 2022.

[KBT+08] T. Kibédi, T. W. Burrows, M. B. Trzhaskovskaya, P. M. Davidson, and C. W. Jr. Nestor. *Nucl. Instrum. Methods Phys. Res. A*, 589(2):202–229, 2008.

[Ker72] A. Kerek. *Nucl. Phys. A*, 185(2):497–508, 1972.

[KGM+91] K.-L. Kratz, H. Gabelmann, P. Möller, B. Pfeiffer, H. L. Ravn, and A. Wöhr. *Z. Phys. A*, 340:419–420, 1991.

[KHCM72] A. Kerek, G.B. Holm, P. Carlé, and J. McDonald. *Nucl. Phys. A*, 195(1):159–176, 1972.

[Kli52] P. F. A. Klinkenberg. *Rev. Mod. Phys.*, 24(2):63, 1952.

[KMB+05] A. Korgul, H. Mach, B. A. Brown, A. Covello, A. Gargano, B. Fogelberg, R. Schuber, W. Kurcewicz, E. Werner-Malento, R. Orlandi, et al. In *Proc. 4th Int. Conf. Exotic Nuclei and Atomic Masses*, pages 123–124. Springer, 2005.

[KTG+05] U. Köster, E. Tengborn, T. J. Gilles, P. Delahaye, D. M. Seliverstov, R. Gernhäuser, L. M. Fraile-Prieto, J. Van de Walle, T. Behrens, T. Kröll, et al. In *AIP Conf. Proc.*, volume 798, pages 315–326, 2005.

[Kug00] E. Kugler. *Hyperfine Interact.*, 129(1):23–42, 2000.

[KWH+21] F.G. Kondev, M. Wang, W.J. Huang, S. Naimi, and G. Audi. *Chin. Phys. C*, 45(3):030001, 2021.

[LCD+97] J. Lettry, R. Catherall, P. Drumm, P. Van Duppen, A. H. M. Evensen, G. J. Focker, A. Jokinen, O. C. Jonsson, E. Kugler, H. Ravn, et al. *Nucl. Instrum. Methods Phys. Res. B*, 126(1-4):130–134, 1997.

[LEBF+25a] M. Llanos-Expósito, J. Benito, L. M. Fraile, A. Illana, J. Acosta, A. Algora, B. Andel, A. N. Andreyev, S. Antalic, M. Araszkiewicz, et al. *Phys. Rev. C*, 111(6):064310, 2025.

[LEBF+25b] M. Llanos-Expósito, J. Benito, L. M. Fraile, A. Illana, et al. *ISOLDE Newsletter*, pages 20–21, 2025. IS685 and IDS collaborations.

[LEFB+24] M. Llanos-Expósito, L. M. Fraile, J. Benito, J. Acosta, A. Algora, B. Andel, A. N. Andreyev, S. Antalic, R. A. Bark, C. Bernerd, et al. *Acta Phys. Pol. B Proc. Suppl.*, 17, 2024.

[LMF+16] R. Lică, H. Mach, L. M. Fraile, A. Gargano, M. J. G. Borge, N. Mărginean, C. O. Sotty, V. Vedia, A. N. Andreyev, G. Benzoni, et al. *Phys. Rev. C*, 93(4):044303, 2016.

[LPC+23] R. Lică, K. Phan, J. Cubiss, C. Page, and A. Illana. xia4ids: Xia dgf pixie-16 .ldf data file converter into root and gaspware format for ids. https://gitlab.cern.ch/ids/xia4ids, 2023.

[May49] M. G. Mayer. *Phys. Rev.*, 75(12):1969, 1949.

[MCB+17] S. Mukhopadhyay, B. P. Crider, B. A. Brown, S. F. Ashley, A. Chakraborty, A. Kumar, M. T. McEllistrem, E. E. Peters, F. M. Prados-Estévez, and S. W. Yates. *Phys. Rev. C*, 95(1):014327, 2017.

[MCP+14] M. Mumpower, J. Cass, G. Passucci, R. Surman, and A. Aprahamian. *AIP Adv.*, 4(4), 2014.

[MF95] H. Mach and B. Fogelberg. *Phys. Scr.*, 1995(T56):270, 1995.

[MFA+07] H. Mach, L. M. Fraile, O. Arndt, A. Blazhev, N. Boelaert, M. J. G. Borge, R. Boutami, H. Bradley, N. Braun, B. A. Brown, and et al. *Acta Phys. Pol. B*, 38(4):1213–1220, 2007.

[MGM89] H. Mach, R. L. Gill, and M. Moszyński. *Nucl. Instrum. Methods Phys. Res. A*, 280(1):49–72, 1989.

[Mie14] K. Miernik. *Phys. Rev. C*, 90(5):054306, 2014.

[MKM16] M. R. Mumpower, T. Kawano, and P. Möller. *Phys. Rev. C*, 94(6):064317, 2016.

[MM71] J. McDonald and S. G. Malmskog. *Nucl. Phys. A*, 176(3):526–534, 1971.

[MM89] M. Moszyński and H. Mach. *Nucl. Instrum. Methods Phys. Res. A*, 277(2-3):407–417, 1989.

[MNK97] P. Möller, J. R. Nix, and K.-L. Kratz. *At. Data Nucl. Data Tables*, 66(2):131–343, 1997.

[MSMA16] M. R. Mumpower, R. Surman, G. C. McLaughlin, and A. Aprahamian. *Prog. Part. Nucl. Phys.*, 86:86–126, 2016.

[MW85] G. J. Mathews and R. A. Ward. *Rep. Prog. Phys.*, 48(10):1371, 1985.

[NKK+20] D. A. Nesterenko, A. Kankainen, J. Kostensalo, C. R. Nobs, A. M. Bruce, O. Beliuskina, L. Canete, T. Eronen, E. R. Gamba, S. Geldhof, et al. *Phys. Lett. B*, 808:135642, 2020.

[NLP+22] C. Neacşu, R. Lică, G. Pascovici, C. Mihai, and S. Rothe. *Nucl. Instrum. Methods Phys. Res. A*, 1026:166213, 2022.

[NND25] NNDC. National Nuclear Data Center (NNDC). http://www.nndc.bnl.gov, 2025. Accessed: November 26, 2025.

[OPA+18] R. Orlandi, S. D. Pain, S. Ahn, A. Jungclaus, K. T. Schmitt, D. W. Bardayan, W. N. Catford, R. Chapman, K. A. Chipps, J. A. Cizewski, et al. *Phys. Lett. B*, 785:615 – 620, 2018.

[Par23] T. Parry. *Structure of Neutron-rich Nuclei in the $^{132}$Sn Region*. Doctoral thesis, University of Surrey, November 2023.

[PBE+22] Sarah Prill, Anna Bohn, Vera Everwyn, Guillaume Häfner, Felix Heim, Mark Spieker, Michael Weinert, Julius Wilhelmy, and Andreas Zilges. *Phys. Rev. C*, 105:034319, 2022.

[PJG+11] S. Pietri, A. Jungclaus, M. Górska, H. Grawe, M. Pfützner, L. Cáceres, P. Detistov, S. Lalkovski, V. Modamio, Z. Podolyák, et al. *Phys. Rev. C*, 83(4):044328, 2011.

[PKF+19] M. Piersa, A. Korgul, L. M. Fraile, J. Benito, E. Adamska, A. N. Andreyev, R. Álvarez-Rodríguez, A. E. Barzakh, G. Benzoni, T. Berry, et al. *Phys. Rev. C*, 99:024304, 2019.

[PNL+22] V. H. Phong, S. Nishimura, G. Lorusso, T. Davinson, A. Estrade, O. Hall, T. Kawano, J. Liu, F. Montes, N. Nishimura, et al. *Phys. Rev. Lett.*, 129(17):172701, 2022.

[PS21] M. Piersa-Silkowska. *Beta-decay studies of very neutron-rich indium isotopes*. Doctoral thesis, University of Warsaw, 2021.

[PSC+19] E. E. Peters, A. E. Stuchbery, A. Chakraborty, B. P. Crider, S. F. Ashley, A. Kumar, M. T. McEllistrem, F. M. Prados-Estévez, and S. W. Yates. *Phys. Rev. C*, 99(6):064321, 2019.

[PSKB+21] M. Piersa-Siłkowska, A. Korgul, J. Benito, L. M. Fraile, E. Adamska, A. N. Andreyev, R. Álvarez-Rodríguez, A. E. Barzakh, G. Benzoni, T. Berry, et al. *Phys. Rev. C*, 104:044328, 2021.

[RAS93] G. Rudstam, K. Aleklett, and L. Sihver. *At. Data Nucl. Data Tables*, 53(1):1–22, 1993.

[RM25] J. Rodríguez Murias. *Advanced scintillator readout for fast-timing experiments and its application to $A = 130$ nuclei*. Doctoral thesis, Universidad Complutense de Madrid, 2025.

[ROO25] ROOT Development Team. ROOT — data analysis framework. https://root.cern, 2025.

[RSR+18] D. Rosiak, M. Seidlitz, P. Reiter, H. Naidja, Y. Tsunoda, T. Togashi, F. Nowacki, T. Otsuka, G. Colo, K. Arnswald, et al. *Phys. Rev. Lett.*, 121(25):252501, 2018.

[RSSR+16] J.-M. Régis, N. Saed-Samii, M. Rudigier, S. Ansari, M. Dannhoff, A. Esmaylzadeh, C. Fransen, R.-B. Gerst, J. Jolie, V. Karayonchev, et al. *Nucl. Instrum. Methods Phys. Res. A*, 823:72–82, 2016.

[RWE+85] P. L. Reeder, R. A. Warner, M. D. Edmiston, R. L. Gill, and A. Piotrowski. In *Nuclei Off Line Stab.* ACS, 1985.

[SAG+07] G. S. Simpson, J. C. Angelique, J. Genevey, J. A. Pinston, A. Covello, A. Gargano, U. Köster, R. Orlandi, and A. Scherillo. *Phys. Rev. C*, 76, 2007.

[SBLW90] U. Stöhlker, A. Blönnigen, W. Lippert, and H. Wollnik. *Z. Phys. A*, 336(4):369–374, 1990.

[SFW89] Craig A. Stone, Scott H. Faller, and William B. Walters. *Phys. Rev. C*, 39:1963–1971, 1989.

[SGP+04] A. Scherillo, J. Genevey, J. A. Pinston, A. Covello, H. Faust, A. Gargano, R. Orlandi, G. S. Simpson, I. Tsekhanovich, and N. Warr. *Phys. Rev. C*, 70:054318, Nov 2004.

[SHH+75] J. C. Soares, P. Herzog, H. Hübel, A. Kluge, and W. Thomas. *Nucl. Phys. A*, 247(2):274–282, 1975.

[Shi13] N. Shimizu. *arXiv:1310.5431*, 2013.

[SMA15] R. Surman, M. Mumpower, and A. Aprahamian. In *Proc. Conf. Adv. Radioact. Isotope Sci. (ARIS2014)*, page 010010, 2015.

[SVFM+99] M. Sanchez-Vega, B. Fogelberg, H. Mach, R. B. E. Taylor, A. Lindroth, J. Blomqvist, A. Covello, and A. Gargano. *Phys. Rev. C*, 60:024303, 1999.

[SWW+05] J. Shergur, A. Wöhr, W. B. Walters, K.-L. Kratz, O. Arndt, B. A. Brown, J. Cederkall, I. Dillmann, L. M. Fraile, P. Hoff, et al. *Phys. Rev. C*, 71:064321, 2005.

[Tay17] S. Z. Taylor. GASPware-1: Data analysis package for nuclear spectroscopy. https://github.com/sztaylor89/GASPware-1, 2017.

[TJG+14] J. Taprogge, A. Jungclaus, H. Grawe, S. Nishimura, P. Doornenbal, G. Lorusso, G. S. Simpson, P.-A. Söderström, T. Sumikama, Z. Y. Xu, et al. *Phys. Rev. Lett.*, 112(13):132501, 2014.

[TJG+16] J. Taprogge, A. Jungclaus, H. Grawe, I.N. Borzov, S. Nishimura, P. Doornenbal, G. Lorusso, G.S. Simpson, P.-A. Söderström, T. Sumikama, et al. *Eur. Phys. J. A*, 52:1–10, 2016.

[TMSZ23] S. Turkat, X. Mougeot, B. Singh, and K. Zuber. *At. Data Nucl. Data Tables*, 152:101584, 2023.

[TYHO15] E. Teruya, N. Yoshinaga, K. Higashiyama, and A. Odahara. *Phys. Rev. C*, 92(3):034320, 2015.

[VCGF+17] V. Vedia, M. Carmona-Gallardo, L. M. Fraile, H. Mach, and J. M. Udías. *Nucl. Instrum. Methods Phys. Res., Sect. A*, 857:98–105, 2017.

[VGRM+22] A. R. Vernon, R. F. Garcia Ruiz, T. Miyagi, C. L. Binnersley, J. Billowes, M. L. Bissell, J. Bonnard, T. E. Cocolios, J. Dobaczewski, G. J. Farooq-Smith, et al. *Nature*, 607(7918):260–265, 2022.

[VJD+19] V. Vaquero, A. Jungclaus, P. Doornenbal, K. Wimmer, A. M. Moro, K. Ogata, T. Furumoto, S. Chen, E. Nácher, E. Sahin, et al. *Phys. Rev. C*, 99, 2019.

[VMF+15] V. Vedia, H. Mach, L. M. Fraile, J. M. Udías, and S. Lalkovski. *Nucl. Instrum. Methods Phys. Res., Sect. A*, 795:144–150, 2015.

[WAG+20] K. Whitmore, C. Andreoiu, F. H. Garcia, K. Ortner, J. D. Holt, T. Miyagi, G. C. Ball, N. Bernier, H. Bidaman, V. Bildstein, et al. *Phys. Rev. C*, 102:024327, 2020.

[WCS+20] B. S. Wang, S. A. Caldwell, N. D. Scielzo, A. Czeszumska, J. A. Clark, G. Savard, A. Aprahamian, M. T. Burkey, C. J. Chiara, J. Harker, et al. *Phys. Rev. C*, 101(2):025806, 2020.

[WHK+21] Meng Wang, Wen Jie Huang, Filip G Kondev, Georges Audi, and Sarah Naimi. *Chin. Phys. C*, 45(3):030003, 2021.

[WLWJ22] H.-K. Wang, Z.-H. Li, Y.-B. Wang, and B. Jiang. *Phys. Lett. B*, 833:137337, 2022.

[XMG+23a] Z. Y. Xu, M. Madurga, R. Grzywacz, T. T. King, A. Algora, A. N. Andreyev, J. Benito, T. Berry, M. J. G. Borge, C. Costache, et al. *Phys. Rev. Lett.*, 131:022501, 2023.

[XMG+23b] Z. Y. Xu, M. Madurga, R. Grzywacz, T. T. King, A. Algora, A. N. Andreyev, J. Benito, T. Berry, M. J. G. Borge, C. Costache, et al. *Phys. Rev. C*, 108:014314, 2023.

[YLX+16] C. Yuan, Z. Liu, F. Xu, P. M. Walker, Zs. Podolyák, C. Xu, Z. Z. Ren, B. Ding, M. L. Liu, X. Y. Liu, et al. *Phys. Lett. B*, 762:237–242, 2016.

# List of Figures

# List of Tables

# Scientific publications and conferences contributions

During this PhD Thesis the following investigations were published in international journals relevant in the field, or presented at international conferences.

## Scientific publications in indexed international journals

1. **M. Llanos-Expósito**, J. Benito, L.M. Fraile, A. Illana, J. Acosta, A. Algora, B. Andel, A.N. Andreyev, S. Antalic, M. Araszkiewicz, R.A. Bark, C. Bernerd, N. Bernier, B. Bhengu, M.J.G. Borge, A.J. Briz, K. Chrysafidis, T.E. Cocolios, T. Costache, J.G. Cubiss, U. Datta, H. De Witte, N. Encina, A. Esmaylzadeh, Z. Favier, D. Fernández, C. Ferrera, H.O.U. Fynbo, V. García-Távora, G. Georgiev, M. Górska, R. Heinke, J.L. Herraiz, P.M. Jones, I.J. Jolie, D.S. Judson, A. Jungclaus, M. Karny, A. Korgul, U. Köster, Th. Kröll, M. Labiche, S. Lalkovski, R. Lesch, M. Ley, R. Lică, M. Madurga, N. Mărginean, B.A. Marsh, K. Miernik, C. Mihai, M. Mikolajczuk, J. Mišţ, J.R. Murias, E. Nácher, C. Neacsu, V.M. Nouvalis, S. Ntshangase, B. Olaizola, J.N. Orce, C.A.A. Page, R.D. Page, J. Pakarinen, C. Papadakis, A. Perea, M. Piersa-Sitkowska, Z.S. Podolyak, M. Régis, I. Rogi, H. Rothe, B. Rozwoda, V. Sánchez-Tembleque, K. Solak, S. Stegemann, M. Stepaniuk, A. Stoica, M. Stryjczyk, O. Tengblad, A. Turturica, G. Turturica, J.M. Udías, S. Ujeniuc, P. Van Duppen, Ir. Vasilev, M. von Tresckow, N. Warr, Z. Yue, S. Zajda and IDS Collaboration. Structure of $^{128}$Sn selectively populated in the $\beta$ decay of the $^{128}$In ground state. *Phys. Rev. C, 111:064310, 2025.*

2. **M. Llanos-Expósito**, L.M. Fraile, J. Benito, J. Acosta, A. Algora, B. Andel, A.N. Andreyev, S. Antalic, R.A. Bark, C. Bernerd, N. Bernier, B. Bhengu, D. Bittner, M.J.G. Borge, J.A. Briz, K. Chrysafidis, T.E. Cocolios, C. Costache, J.G. Cubiss, H. De Witte, N. Encina, A. Esmaylzadeh, Z. Favier, D. Fernández, C. Ferrera, H.O.U. Fynbo, V. García-Távora, G. Georgiev, M. Górska, R. Heinke, J.L. Herraiz, A. Illana, P. Jones, D.S. Judson, A. Jungclaus, M. Karny, A. Korgul, U. Köster, Th. Kröll, M. Labiche, S. Lalkovski, R. Lesch, M. Ley, R. Lică, M. Madurga, N. Mărginean, C. Mihai, M. Mikolajczuk, J. Miśt, J.R. Murias, E. Nácher, C. Neacsu, V.M. Nouvalis, S. Ntshangase, B. Olaizola, J.N. Orce, C. Page, J. Pakarinen, P. Papadakis, A. Perea, M. Piersa-Silkowska, Z.S. Podolyak, J. Rogi, S. Rothe, V. Sánchez-Tembleque, K. Solak, S. Stegemann, M. Stepaniuk,

A. Stoica, M. Stryjczyk, O. Tengblad, A. Turturica, G. Turturica, J.M. Udías, S. Ujeniuc, P. Van Duppen, Ir. Vasilev, M. von Tresckow, N. Warr, Z. Yue, S. Zajda and IDS Collaboration. Fast-timing investigation of $A = 128$ isobars populated in the $\beta$-decay of $^{128}$Cd. *Acta Phys. Pol. B Proc. Suppl., 17:3-A7, 2024.*

3. J. Rautasalo, I.,A. Jarise, M. Stryjczyk, A. Kankainen, H. Bandé, M. Araszkiewicz, O. Beluskaia, A.,M. Bruce, S. Cazzanrozzo, S. Chintakayala, V.,S. Doshie, T. Eronen, A. Fijałkowska, L.,M. Fraile, P. Graczykowska, S.,Z. Ge, D.,D. Grigorova, I.,G. Jarosova, A. Korga, T. Krakowska, J. Kurpeta, S. Lalkowski, **M. Llanos-Expósito**, D.,I.,D. Moore, L.,M. Motilla, V. Mougeot, H. Penttilä, A. Reggio, W. Ratanasakuludko, J.,T. Saarn, K. Solak. Probing the quantum phase transition near $N \approx 60$ via mass measurements of technetium isotopes. *Phys. Rev. C, 112:064302, 2025.*

4. P. Dyszel, R. Grzywacz, Z. Y. Xu, N. Kitamura, M. Karny, A. Korgul, M. Madurga, S. Neupane, A. Algora, A. N. Andreyev, M. Araszkiewicz, R. A. Bark, J. Benito, N. Bernier, M. J. G. Borge, M. Caballero, P. Chuchala, T. E. Cocolios, C. Costache, J. G. Cubiss, H. DeWitte, J. E. Escher, D. Fernandez-Ruiz, A. Fijalkowska, L. M. Fraile, H. O. U. Fynbo, J. Gouge, J. L. Herraiz, A. Illana, P. M. Jones, D. S. Judson, P. Kamińska, T. Kawano, K. Kolos, M. Labiche, R. Lică, **M. Llanos-Expósito**, G. G. DeLorenzo, N. Marginean, I. Michelon, C. Mihai, E. Nácher, C. Neacsu, J. S. Nielsen, B. Olaizola, J. N. Orce, C. A. A. Page, R. D. Page, J. Pakarinen, A. Perea, M. Piersa-Siłkowska, Zs. Podolyák, J. S. Prieto, M. Rajabali, J. Shaw, A. I. Sison, K. Solak, M. Stryjczyk, O. Tengblad, P. G. T. Vicente, N. Warr, J. Wilson, Z. Yue, S. Zajda. First $\beta$-delayed two-neutron spectroscopy of the r-process nucleus $^{134}$In and observation of the $i_{13/2}$ single-particle neutron state in $^{133}$Sn. *Phys. Rev. Lett., 135:152501, 2025.*

5. B. Olaizola, A. Illana, J. Benito, D.P. Suárez-Bustamante, G. Del Piccolo, A. Algora, B. Andel, A.N. Andreyev, M. Araszkiewicz, Y. Ayyad, R.A. Bark, T. Berry, M.J.G. Borge, K. Chrysafidis, T.E. Cocolios, C. Costache, J.G. Cubiss, P. Van Duppen, Z. Favier, L.M. Fraile, H.O.U. Fynbo, F. Galtarossa, G. Georgiev, P.T. Greenlees, R. Grzywacz, L.J. Harkness-Brennan, R. Heinke, M. Huyse, P. Ibáñez, K. Johnston, P.M. Jones, D.S. Judson, J. Konki, A. Korgul, U. Köster, J. Kurcewicz, M. Labiche, M. Lazarus, R. Lică, **M. Llanos-Expósito**, M. Madurga, N. Mărginean, P. Mihai, R.E. Mihai, J.R. Murias, E. Nácher, C. Neacsu, A. Negret, V.M. Nouvalis, J. Ojala, J.N. Orce, C.A.A. Page, R.D. Page, J. Pakarinen, J. Papadakis, S. Pascu, A. Perea, M. Piersa-Sitkowska, A.M. Plaza, Z.S. Podolyák, W. Poklepa, V. Pucknell, P. Rakhila, C. Raison, E. Rapisarda, K. Rezynkina, F. Rotaru, K. Schomacker, M. Siciliano, C. Sotty, M. Stryjczyk, O. Tengblad, J.M. Udías, V. Vedia, S. Viñals, R. Wadsworth, N. Warr, H. Witte, D. Yates, Z. Yue. The $^{76}$Cu conundrum remains unsolved. *Phys. Lett. B, 860:139551, 2025.*

6. G. Zhang, M. Polettini, D. Mengoni, G. Benzoni, Z. Huang, M. Górska, A. Blazhev, L.M. Fraile, A. Gargano, G. De Gregorio, F. Nowacki, G. Akgöz, U. Ahmed, O. Aktas, M. Al-Aqeel, B. Alayed, H.M. Albers, A. Algora, S. Alhomaidhi, F. Amjad, C. Appleton, T. Arici, M. Armstrong, B.Q. Arnés, A.

Astier, M. Balogh, A. Banerjee, D. Bazzacco, J. Benito García, S. Bottoni, P. Boutachkov, A. Bracco, A. Bruce, D. Brugnarra, C. Bruno, F. Camera, B. Cederwall, M. Cicerchia, M.M.R. Chishti, A. Corsi, M.L. Cortes, D. Cox, F.C.L. Crespi, B. Das, T. Davidson, G. de Angelis, T. Dickel, M. Doncel, A. Ertoprak, A. Esmaylzadeh, L. Gaffney, F. Galtarossa, E.R. Gamba, D. Garbe, D. Genna, A. Gerl, A. Goadsuff, A. Gottardo, A. Gozzellino, T. Grahn, J. Ha, E. Haettner, O. Hall, L. Harkness-Brennan, P. Heggen, C. Hornung, Y. Hrabar, S.P. Hu, N. Hubbard, K.E. Ide, A. Illana, S. Jazrawi, P.R. John, I. Jolie, C. Jones, Y. D. Joss, D.S. Judson, V. Karayonchev, E. Kazantseva, R. Kern, G.G. Kiss, L. Knafla, R. Knöbel, I. Kojouharov, A. Korgul, W. Korten, R. Koseoglou, D. Kostyleva, T. Kurtukian-Nieto, G. Kosir, N. Kurz, S. Luki, M. Labiche, S.M. Lenzi, S. Leoni, G.-S. Li, Z. Liu, **M. Llanos Expósito**, R. Lozeva, J.B. Lu, M. Luoma, G. Mantovani, T. Marchi, M. Mazzocco, R. Menegazzo, T.J. Mertzimekis, M. Mikolajczuk, B. Million, A.K. Mistry, I. Mukha, E. Nácher, D.R. Napoli, B.S. Nara Singh, S.E.A. Orrigo, R.D. Page, P. Papadakis, G. Pasqualato, J. Pellumaj, S. Pelios, M.B. Pérez Vidal, C.M. Petrache, V. Petrovici, N. Pietralla, S. Pietri, S. Pigliapoco, Z.S. Podolyák, C. Porzio, A. Raggio, F. Recchia, P.H. Regan, J.S.M. Régis, P. Reiter, K. Rezynkina, E. Rocco, J. Rodríguez Murias, H. Rösch, P. Roy, B. Rubio, M. Rudigier, P. Roussel-Chomaz, E. Sahin, L.G. Sarmiento, M.-M. Satrazzani, H. Schaffner, Ch. Scheidenberger, L. Sexton, A. Sharma, M. Siciliano, J. Simpson, J. Smallcombe, P.P. Söderström, D. Soldera, A. Sood, F. Soramel, H.-B. Sun, H.B. Sun, A.V. Swecicz, N. Szegedi, Y.K. Tanaka, J.J. Valiente-Dobón, K. Veselou, A. Vogt, M. von Tresckow, M. Vedia, H. Watanabe, M. Weick, W. Werner, M. Wieland, O. Wieland, K. Wimmer, A. Wodrig, D. Wolf, A. Zanutta, M. Zbrzeźniak, Z. Zliliani. Approaching $^{100}$Sn: Structural evolution in $^{98,100}$Cd via lifetime measurements. *Phys. Lett. B, 863:139378, 2025.*

7. E. Şahin, V. Werner, A.K. Mistry, M. Rudigier, K. Nomura, J. Jolie, N. Pietralla, P.H. Regan, G. Akgöz, H.M. Albers, U. Ahmed, Ö. Aktas, A. Algora, S. Alhomaidhi, C. Appleton, T. Arici, M. Armstrong, A. Banerjee, J. Benito, G. Benzoni, A. Blazhev, P. Boutachkov, A.M. Bruce, B. Cederwall, M.M.R. Chishti, M.L. Cortés, F. Crespi, B. Das, T. Davinson, T. Dickel, M. Doncel, A. Ertoprak, A. Esmaylzadeh, L.M. Fraile, E.R. Gamba, J. Gerl, M. Górska, J. Ha, E. Haettner, O. Hall, H. Heggen, C. Hornung, N. Hubbard, S. Jazrawi, P.R. John, C.E. Jones, V. Karayonchev, E. Kazantseva, R. Kern, L. Knafla, I. Kojouharov, P. Koseoglou, G. Kosir, D. Kostyleva, N. Kurz, N. Kuzminchuk, **M. Llanos-Expósito**, R. Lozeva, D. Mengoni, T.J. Mertzimekis, M. Mikolajczuk, A.I. Morales, I. Mukha, J.R. Murias, B.S. Nara Singh, S.E.A. Orrigo, J. Pellumaj, S. Pélissier, S. Pietri, S. Pigliapoco, Z.S. Podolyák, M. Polettini, K. Rezynkina, H.A. Rösch, H. Schaffner, Ch. Scheidenberger, L. Sexton, P.-A. Söderström, Y.K. Tanaka, J.J. Valiente-Dobón, P. Vasileiou, J.V. Vasiljević, J. Vesic, H. Weick, J. Wiedeking, A. Wieland, A. Yaneva, G. Zhang, J. Zhao, A. Zyriilov. Collectivity at the prolate–oblate transition: The $2_1^+$ lifetime of $^{190}$W. *Phys. Lett. B, 857:138976, 2024.*

8. K. Miernik, A. Korgul, W. Poklepa, J.N. Wilson, G. Charles, S. Czajkowski, P. Czyż, A. Fijałkowska, L.M. Fraile, P. Garczyński, K. Hauschild, C. Hiver, T. Kurtukian-Nieto, M. Lebois, **M. Llanos**, A. Lopez-Martens, K.M. Deby Treasa,

J. Ljungvall, I. Matea, J. Mielczarek, J.R. Murias, G. Pasqualato, A. Skruch, K. Solak, K. Stoyachev, I. Tsekhanovich. Fission of $^{215}$Fr studied with $\gamma$ spectroscopic methods. *Phys. Rev. C, 108:054608, 2023.*

9. A.K. Mistry, H.M. Albers, T. Arici, A. Banerjee, G. Benzoni, B. Cederwall, J. Gerl, M. Górska, O. Hall, N. Hubbard, I. Kojouharov, J. Jolie, T. Martinez, Zs. Podolyák, P.H. Regan, J.L. Tain, A. Tarifeño-Saldivia, H. Schaffner, V. Werner, G. Akgöz, J. Agramunt, U. Ahmed, Ö. Aktas, V. Alcayne, A. Algora, S. Alhomaidhi, F. Amjad, C. Appleton, M. Armstrong, M. Balogh, K. Banerjee, P. Bednarczyk, J. Benito, C. Bhattacharyya, P. Black, Á. Blazhev, S. Bottoni, P. Boutachkov, A. Bracco, A.M. Bruce, M. Brunet, C.G. Bruno, I. Burrows, F. Calvino, R.L. Canavan, D. Cano-Ott, M.M.R. Chishti, P. Coleman-Smith, M.L. Cortés, G. Cortes, F. Crespi, T. Davinson, A. De Blas, T. Dickel, M. Doncel, A. Ertoprak, A. Esmaylzadeh, B. Fornal, L.M. Fraile, F. Galtarossa, A. Gottardo, V. Guadilla, A. Ha, E. Haettner, G. Hãfner, H. Heggen, P. Herrmann, C. Hornung, S. Jazrawi, P.R. John, A. Jokinen, C.E. Jones, D. Kahl, V. Karayonchev, E. Kazantseva, R. Kern, L. Knafla, R. Knöbel, P. Koseoglou, G. Kosir, D. Kostyleva, N. Kurz, N. Kuzminchuk, M. Labiche, J. Lawson, J. Lazarus, S.M. Lenzi, S. Leoni, **M. Llanos-Expósito**, R. Lozeva, A. Maj, J.K. Meena, E.S. Mendoza, R. Menegazzo, D. Mengoni, T.J. Mertzimekis, M. Mikolajczuk, B. Million, M. Mont-Geli, A.I. Morales, P. Morral, I. Mukha, J.R. Murias, E. Nácher, N. Naparalla, D.R. Napoli, B.S. Nara-Singh, D. O'Donnell, S.E.A. Orrigo, R.D. Page, P. Palier, M. Pallas, J. Pellumaj, S. Pelonis, H. Penttila, E. Perea de Rada, R.M. Pérez-Vidal, C.M. Petrache, N. Pietralla, S. Pietri, S. Pigliapoco, M. Polettini, C. Porzio, V.B.E. Pucknell, F. Recchia, P. Reiter, K. Rezynkina, S. Rinta-Antila, E. Rocco, H.A. Rösch, P. Roy, B. Rubio, M. Rudigier, P. Roussel-Chomaz, E. Sahin, Ch. Scheidenberger, L. Sexton, P.-A. Söderström, A. Smith, R. Smith, Y.K. Tanaka, J.J. Valiente-Dobón, P. Vasileiou, J.V. Vasiljević, J. Vesic, H. Weick, M. Wiebusch, J. Wiederhold, O. Wieland, H.J. Wollersheim, P.J. Woods, A. Yaneva, T. Zanon, G. Zhang, J. Zhao, R. Zidarova, G. Zimba, A. Zyriilov. The DESPEC setup for GSI and FAIR. *Nucl. Instrum. Methods Phys. Res. A, 1033:166662, 2022.*

10. N. Mont-Geli, A. Tarifeño-Saldivia, L.M. Fraile, S. Viñals, A. Perea, M. Pallàs, G. Cortés, G. García, E. Nácher, J. L. Tain, V. Alcayne, O. Alonso-Sañudo, A. Algora, J. Balibrea-Correa, J. Benito, M.J.G. Borge, J.A. Briz, F. Calviño, D. Cano-Ott, A. De Blas, C. Domingo-Pardo, B. Fernández, R. García, J. Gómez-Camacho, E.M. González-Romero, C. Guerrero, J. Lerendegui-Marco, **M. Llanos**, T. Martínez, T. Martínez-Nouvilas, E. Mendoza, J.R. Murias, S.E.A. Orrigo, A. Pérez de Rada, V. Pesudo, J. Plaza, J.M. Quesada, A. Sánchez, V. Sánchez-Tembleque, R. Santorelli, O. Tengblad, J.M. Udías, D. Villamarín. Commissioning of miniBELEN-10A, a moderated neutron counter with a flat efficiency for thick-target neutron yields measurements. *EPJ Web Conf., 290:01003, 2023.*

11. N. Mont-Geli, A. Tarifeño-Saldivia, L.M. Fraile, S. Viñals, A. Perea, M. Pallàs, G. Cortés, E. Nácher, J.L. Tain, V. Alcayne, A. Algora, J. Balibrea-Correa, J. Benito, M.J.G. Borge, J.A. Briz, F. Calviño, D. Cano-Ott, A. De Blas, C. Domingo-Pardo,

B. Fernández, R. García, G. García, J. Gómez-Camacho, E.M. González-Romero, C. Guerrero, J. Lerendegui-Marco, **M. Llanos**, T. Martínez, E. Mendoza, J.R. Murias, S.E.A. Orrigo, A. Pérez de Rada, V. Pesudo, J. Plaza, J.M. Quesada, A. Sánchez, V. Sánchez-Tembleque, R. Santorelli, O. Tengblad, J.M. Udías, D. Villamarín. miniBELEN: a modular neutron counter for $(\alpha, n)$ reactions. *EPJ Web Conf., 284:06004, 2023.*

# Conference and workshop presentations

1. Mazurian Lakes Conference, Ełk, Poland, September 2–9, 2023.
   Talk: *Fast-timing spectroscopy in the $^{128}$Cd, $^{128}$In, $^{128}$Sn $\beta$-decay chain*
   Authors: **M. Llanos-Expósito**, J. Benito, L.M. Fraile and IS685 collaboration

2. ISOLDE Workshop and Users meeting, Geneva, Switzerland, November 29–December 1, 2023.
   Talk: *Fast-timing spectroscopy in the $^{128}$Cd, $^{128}$In, $^{128}$Sn $\beta$-decay chain*
   Authors: **M. Llanos-Expósito**, J. Benito, L.M. Fraile and IS685 collaboration

3. Nuclear Structure and Dynamics (NSD 2024), Valencia, Spain, May 27 – June 1, 2024.
   Talk: *Fast-timing spectroscopy in the $^{128}$Cd, $^{128}$In, $^{128}$Sn $\beta$-decay chain*
   Authors: **M. Llanos-Expósito**, J. Benito, L.M. Fraile and IS685 collaboration

4. XVI Jornadas CPAN, Madrid, Spain, November 19–21, 2024.
   Talk: *New $\beta$-decay spectroscopy of $^{133,132}$Cd*
   Authors: **M. Llanos-Expósito**, J. Benito, L.M. Fraile and IS685 collaboration

5. III IPARCOS Congress, Madrid, Spain, December 11, 2024.
   Talk: *First $\beta$-decay spectroscopy of $^{132}$Cd*
   Authors: **M. Llanos-Expósito**, J. Benito, L.M. Fraile and IS685 collaboration

6. ISOLDE Decay Station (IDS) collaboration meeting, Madrid, Spain. March 11–12, 2025.
   Talk: *$\beta$-decay spectroscopy of neutron-rich Cd isotopes (Status report for IS685_II)*
   Authors: **M. Llanos-Expósito**, J. Benito, L.M. Fraile and IS685 collaboration

7. Fast25 Workshop: Fast timing for nuclear structure and applications, Madrid, Spain, March 12–14, 2025.
   Talk: *Fast-timing spectroscopy in the $^{128}$Cd $\beta$-decay chain*
   Authors: **M. Llanos-Expósito**, J. Benito, L.M. Fraile and IS685 collaboration

8. ISOLDE Workshop and Users meeting, Geneva, Switzerland, December 3–5, 2025.
   Poster: *Production of intense, high-purity beams of neutron-rich Cd isotopes at ISOLDE*
   Authors: **M. Llanos-Expósito**, J. Benito, L.M. Fraile, A. Illana and IS685 collaboration

9. École Joliot-Curie (EJC 2021), Saint-Pierre d'Oléron, France, October 3–8, 2021.
   Poster: *High-resolution gamma and Fast-Timing spectroscopy of nuclei $^{135,136}$Sb*
   Authors: **M. Llanos-Expósito**, J. Benito, L.M. Fraile and IS441 collaboration